ASSESSMENT OF FRP-CONFINED CONCRETE: UNDERSTANDING BEHAVIOR AND ISSUES IN NONDESTRUCTIVE EVALUATION USING RADAR

by

José Alberto Ortega

B.S., Civil Engineering
Texas A&M University (2002)

Submitted to the Department of Civil and Environmental Engineering
in Partial Fulfillment of the Requirements for the Degree of

MASTER OF SCIENCE IN CIVIL AND ENVIRONMENTAL ENGINEERING

at the

MASSACHUSETTS INSTITUTE OF TECHNOLOGY

February 2006

Signature of Author ______________________________
Department of Civil and Environmental Engineering
January 20, 2006

Certified by ______________________________
Oral Büyüköztürk
Professor of Civil and Environmental Engineering
Thesis Supervisor

Accepted by ______________________________
Andrew J. Whittle
Professor of Civil and Environmental Engineering
Chairman, Departmental Committee on Graduate Studies

Assessment of FRP-Confined Concrete: Understanding Behavior and Issues in Non-destructive Evaluation using Radar

by

José Alberto Ortega

Submitted to the Department of Civil and Environmental Engineering
on January 20, 2006 in Partial Fulfillment of the Requirements for the Degree of
Master of Science in Civil and Environmental Engineering

ABSTRACT

Increase in the use of fiber-reinforced polymer (FRP) composite materials for strengthening and retrofitting of concrete columns and bridge piers has urged the development of an effective non-destructive evaluation (NDE) methodology. Radar technologies have shown great potential for assessing the structural and material integrity of FRP-confined concrete systems. In developing such technology, an interdisciplinary approach must be pursued by integrating contributions of various engineering fields. Under this framework, this thesis aims at establishing fundamental knowledge in two particular research areas: the mechanics and damage behavior of FRP-confined concrete and the characterization of electromagnetic (EM) properties for concrete and FRP materials. Research on mechanics and damage behavior of FRP-confined concrete involved a thorough literature survey on the state-of-the-art understanding of the subject and the execution of an experimental program for load-deformation characterization of FRP-confined concrete cylindrical specimens subjected to monotonic axial compressive loads. Based on the experimental results and comparative studies with recent analytical models, the experimental program was extended to the characterization of specific damage levels using a volumetric deformation metric. Visual inspection of the concrete core of specimens previously loaded to levels close to ultimate failure revealed the existence of significant residual volumetric strains, which upon the removal of the FRP jacket could provoke severe concrete cracking and catastrophic failure. Research on dielectric property characterization of concrete and FRP materials led to the development of an integrated methodology for estimating the complex permittivity of low-loss materials in general using free-space measurements of EM wave transmission. Such development required theoretical modeling of EM wave propagation through dielectric media and experimental measurements of transmission coefficients. Validation studies were performed using Teflon, Lexan, and Bakelite materials whose dielectric properties are established in literature. The methodology was then applied to concrete and FRP materials. Establishing minimum criteria for specimen dimensions and optimal frequency bandwidths is still required before the proposed methodology can be used in field applications. Additionally, exploratory research on the assessment of FRP-confined concrete using radar technologies was conducted. Preliminary results indicate potential of such technologies for detecting features related to the presence of rebar, air cavities, delaminations, and mechanical damage in FRP-confined concrete columns.

Thesis Supervisor: Oral Büyüköztürk
Title: Professor of Civil and Environmental Engineering

ACKNOWLEDGMENTS

I would like to express my most sincere gratitude and appreciation to my advisor, Prof. Oral Büyüköztürk, for his guidance, encouragement, and patience throughout the completion of my SM education and thesis work. Not only have I been part of his work group and conducted valuable research, but I have also learned from him many valuable scholarly skills.

I am thankful to the National Science Foundation (Grant CMS-0324607) and MIT - Lincoln Laboratory Advanced Concepts Committee (Grant ACC-376) for their financial support to this research. In particular, I am sincerely thankful to Dennis Blejer from MIT - Lincoln Laboratory for introducing me to the radar aspects of this project. His mentorship, friendship, and valuable comments are greatly appreciated. I also want to thank Tzu-Yang Yu and Alex Eapen for their collaboration with the dielectric property characterization and radar measurement aspects of this thesis. I am also sincerely thankful to Prof. J. Bryan Evans, postdoctoral student Xiaohui Xiao, and graduate student Nicholas Austin from the Department of Earth, Atmospheric, and Planetary Sciences for their mentorship and collaboration with the visual and microscopic observation studies of the internal structure of FRP-confined concrete specimens.

Gratitude is extended to Fyfe Co. LLC for kindly providing the FRP materials for conducting this research. In particular, I would like to thank Mr. Scott Arnold for his valuable comments and guidance regarding the preparation of FRP materials. I would like to also thank Mr. Stephen W. Rudolph for his constant support with laboratory work and his resourcefulness for tackling experimental research issues. My sincere appreciation is extended to all my superb UROP students: Cody Edwards, Joseph O'Connor, LaToya McKinley, Carrie McDonough, and Hillary Dyer, who collaborated with me throughout the development of this research. Special thanks are given to Cody for all his hard work and creativity, and to LaToya for entrusting me part of her summer research experience at MIT.

I would like to wholeheartedly thank all of my co-workers in the research group: Dr. Oguz Gunes, Dr. Ching Au, Dr. Erdem Karaca, and Tzu-Yang Yu. I would not be living this amazing experience at MIT to its fullest without their friendship, encouragement, and wisdom. I cherish every moment, activity, and experience that I have shared with all and each of them.

And of course, I want to thank all of those whose love makes the difference in my life. To my parents, Alberto and Magdalena, and brothers, Andrés and Ernesto, for being the light, joy, and fuel of my existence. To my wonderful and sweet girlfriend, Carenina, for being my constant inspiration and support. To my best friends, KC and Eduardo, for always being there for me. And to La Cúpula for making my music dreams come true.

TABLE OF CONTENTS

LIST OF FIGURES

LIST OF TABLES

Chapter 1

Introduction

Civil infrastructure is one of the most valuable assets in any country. In the United States, the nation's infrastructure, which was generally built in 1950s, is now approaching the service life, and in need of urgent repair and retrofit. Approximately 27% of the nations' 600,000 bridges were reported to be structurally deficient or functionally obsolete (ASCE 2005). Rehabilitation and upgrading of existing structures are estimated to cost about $212 billion, prompting the urgent need for finding rapid and cost-efficient assessment and repair technologies. In the past decades, the use of fiber-reinforced polymer (FRP) composite materials has experienced substantial growth in structural strengthening and retrofitting applications worldwide. With improved mechanical and durability properties, FRP composite jacketing systems have emerged as an alternative to traditional strengthening and repair of reinforced concrete columns and bridge piers. A large number of civil infrastructure projects from the public and private sectors have opted for FRP technologies. Although substantial research has been conducted in the area of mechanical behavior characterization of FRP-confined concrete column elements, several research issues such as improving the current understanding of damage processes in the concrete core as well as developing reliable non-destructive evaluation techniques for these systems require further investigation.

1.1 Damage in FRP-Confined Concrete Systems

Over the past decade, extensive research has been devoted to the understanding of the mechanical behavior of FRP-confined concrete systems. In particular, the main emphases of such studies have been the investigation of failure modes and ultimate conditions or stages of damage. However, mechanical processes leading to damage or failure of the concrete core are not well understood (Lau and Zhou 2001, Mirmiran and Yunmei 2001).

Furthermore, recent studies have identified that a concrete column could appear safe without showing any visible signs of substantial damage in the FRP jacket and yet containing a damaged concrete core (Au and Büyüköztürk 2005). Thus, there is a pressing need for better understanding of the damage extent and evolution phenomena in FRP-confined concrete systems before they can be used widely and reliably.

1.2 Integrity Assessment of FRP-Confined Concrete

Existing evaluation methods for FRP-confined concrete systems such as visual inspection and sample extraction are labor intensive, time consuming, and destructive to structures. Other methods such as acoustic emission would require the continuous monitoring of the structure in order to detect changes in performance or structural integrity. In addition, these methods are unable to provide sufficient information regarding the extent of damage or the presence of defects such as air cavities or FRP/concrete delaminations. Non-destructive evaluation (NDE) methods using radar technologies have the potential for assessing the concrete conditions inside the FRP jacket. The development of an effective radar NDE methodology is needed to match the growing industrial applications of FRP jacketing systems for concrete columns and bridge piers.

1.3 Interdisciplinary Approach for Developing a Radar NDE Methodology for FRP-Confined Concrete

Developing of a robust damage assessment methodology using radar for FRP-confined concrete systems would require synthesizing knowledge being developed in distinct research areas such as structural engineering, materials science, electrical engineering, and applied mathematics. Figure 1-1 shows a diagram of the different research components of an interdisciplinary effort required for developing a radar NDE methodology for FRP-confined concrete systems. This thesis work is devoted to providing some of the necessary "building blocks" envisioned in the proposed interdisciplinary and synergistic approach. The contributions of this thesis are framed in the research efforts undertaken by the Infrastructure Science and Technology (IST) Group at the MIT Civil and Environmental Engineering Department. Integration of the contributions of this thesis and the results of future research endeavors could potentially lead to the development of a radar NDE technology suited for field applications. By assessing the damage condition or the presence of construction defects in FRP strengthened or retrofitted columns or bridge piers via efficient non-destructive means, effective decisions could be made regarding time, extent, and cost of repair after the occurrence of a seismic event or other processes causing damage to concrete infrastructure.

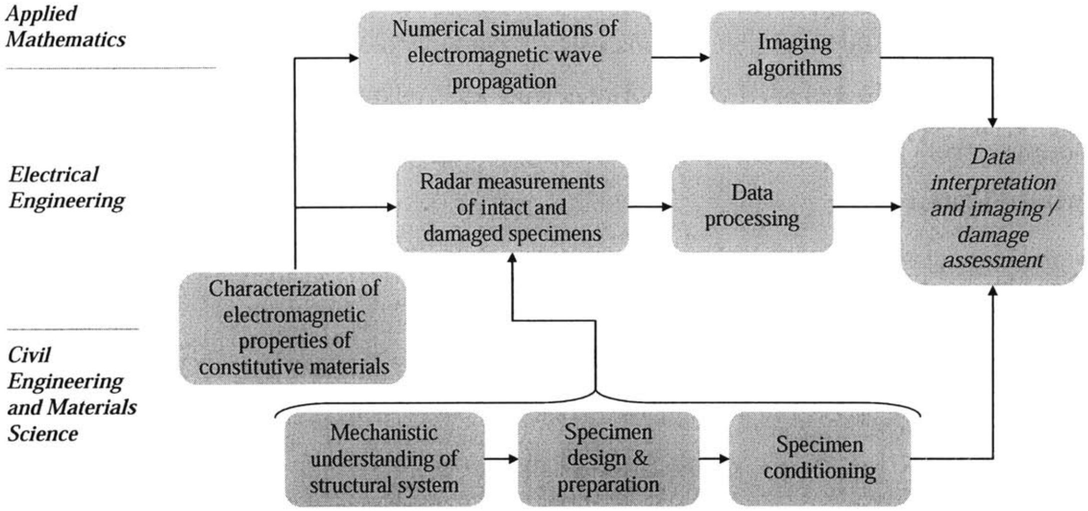

Figure 1-1 Interdisciplinary approach for developing a robust radar NDE methodology

1.4 Research Objective

Based on the framework sketched in Figure 1-1, the two main objectives of this thesis are:

- Investigation of the mechanics and damage behavior of FRP-confined concrete subjected to compressive loadings with an emphasis on the mechanistic understanding of intermediate stages of damage.
- Development of a methodology for characterizing the electromagnetic properties of low-loss materials using free-space radar measurements of EM wave trasmission. This methodology targets the characterization of dielectric properties of low-loss (less electrically conductive) construction materials such as concrete and certain FRP composites used in civil engineering applications.

Achievement of these two main objectives would fulfill tasks 1 and 2, which are schematically shown in Figure 1-2, of the overall research approach for developing a radar NDE methodology for assessing FRP-confined concrete column elements.

An additional objective of this thesis is to describe the methodology, experimentation, and results of preliminary radar measurements of defective and damaged FRP-wrapped concrete specimens using inverse synthetic aperture radar (ISAR) measurement techniques. These laboratory measurements simulate what it is envisioned for a NDE methodology suited for field applications using radar technologies for the assessment of concrete columns strengthened or retrofitted with FRP materials. Achievement of this exploratory work is one of the first steps for fulfilling task 3, which is schematically shown in Figure 1-2.

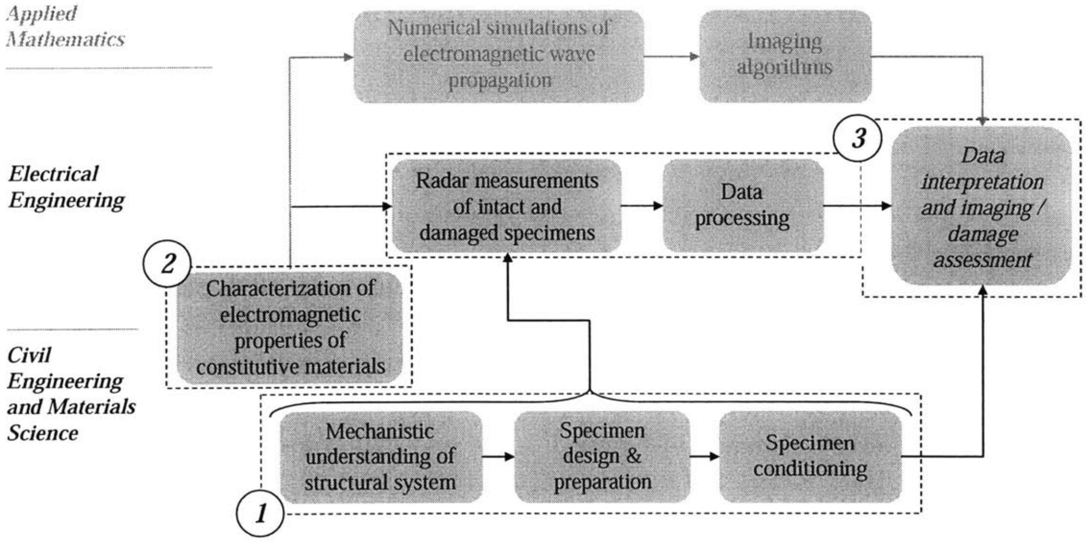

Figure 1-2 Research Objectives

1.5 Research Approach

1.5.1 Mechanics and Damage Behavior Characterization Studies

In order to investigate the mechanics and damage behavior of FRP-confined concrete column elements, a thorough literature review and a comprehensive experimental program were conducted. The literature review on the mechanical and damage behaviors of concrete column elements subjected to active or passive confinements was conducted to highlight specific aspects related to the damage evolution in FRP-confined concrete systems which have not being thoroughly treated by ongoing research. The experimental program focused on the study of the uniaxial compressive behavior of un-reinforced concrete cylinders wrapped with glass fiber-reinforced polymer (GFRP) jackets. Normal strength concrete was used throughout these studies. Concrete cylinders were wrapped with GFRP jackets using wet lay-up installation procedures. GFRP composites were used due to expected ultimate load capacities of GFRP-wrapped concrete specimens and limitations imposed by the experimental set-up for compression tests. In addition, the interdisciplinary nature of this research work imposed various other constraints on the selection of materials such as the use of non-carbon FRP fabrics and on the selection of specimen dimensions. Specimens were tested under monotonic uniaxial compression. Comparisons between state-of-the-art numerical modeling and experimental data on load-deformation behaviors were also conducted for enhancing the understanding obtained throughout the experimental program and for developing expertise in the accurate control of imposed loads to achieve specifically selected damage levels. This former goal is directly related to the preliminary radar measurement studies for detection of damage in FRP-wrapped concrete specimens. Visual assessment of the integrity of concrete cores was conducted through bisection procedures and microscopic observations.

1.5.2 Characterization of Electromagnetic Properties

It is recognized that electromagnetic property characterization of low-loss materials such as concrete may encounter difficulties if the properties are to be inferred from radar measurements of transmitted signals only. However, the experimental set-up required to perform such measurements results advantageous in terms of specimen preparation and flexibility for potential field applications. Based on these considerations, an integrated methodology for determining the complex permittivity (dielectric constant and loss factor) for low-loss materials using free-space radar measurements was developed. The methodology consists of an estimation procedure of the dielectric constant using time difference of arrival information for transmitted EM wave signals and a root-searching technique based on parametric system identification along with an error criterion to estimate the corresponding loss factor. Experimental measurements of EM wave transmission in terms of transmission coefficients for various materials were conducted. Validation of the methodology was performed using Teflon, Lexan, and Bakelite, materials for which dielectric properties are well established. The methodology was then extended to the characterization of concrete and FRP materials. Additionally, studies of EM wave transmission measurements through various types of glass and carbon FRP materials were conducted to enhance understanding of EM wave propagation, scattering, and transmission phenomena.

1.5.3 ISAR Radar Measurements

Exploratory ISAR measurements of various intact and damaged or defective FRP-confined concrete specimens were conducted under laboratory conditions using a wideband radar system. Measurements were collected over two bandwidths: X-band (8 – 12 GHz) and Ku-band (12 – 18 GHz). Three types of specimens were measured. The first type of specimens consisted of plain concrete, reinforced concrete, and FRP-wrapped concrete cylinders with artificially introduced air voids that simulate air cavities and delaminations found in defective FRP-confined concrete structural elements. The second type of specimens consisted of FRP-wrapped concrete cylinders that were previously subjected to different levels of damage through uniaxial compressive loadings. Manufacturing and damage conditioning of these specimens relied on the knowledge developed throughout the studies of mechanical and damage behaviors of FRP-confined concrete. The third type of specimens consisted of plain concrete with steel rebar embedded at different locations. Radar measurements were conducted for this type of specimens to test the ability of the ISAR methodology for detecting rebar. Frequency-angle, range-angle, and ISAR imagery were generated using the radar measurement data to detect features of defective and damaged specimens and to contrast them with the results from undamaged specimens. Cross-correlation studies were also conducted to compare radar measurements of intact and defective specimens.

1.6 Thesis Organization

Due to the multi-disciplinary nature of the work accomplished, this thesis document is organized in the following manner.

Chapter 1 presents an introduction to this thesis. The motivation, problem statement and research needs, research objective, and research approach are discussed. The objective of this chapter is to provide the reader with the "big picture" of this work, which encompasses several studies on different engineering areas such as civil and structural engineering, material science, and electrical engineering.

Chapter 2 introduces the reader to background information on FRP composite materials and their applications to civil engineering and infrastructure. Particular attention is given to the use of FRP composites for strengthening and retrofitting of concrete structures. This chapter also provides a comprehensive overview of non-destructive evaluation techniques used for damage assessment of concrete structures, with an emphasis on potential applications to FRP-confined concrete column elements.

Chapter 3 is devoted to the investigation of the mechanics and damage behavior in FRP-confined concrete systems. A theoretical survey on active and passive confinement of concrete subjected to multi-axial stress states is presented. An experimental program is also implemented to develop data for load-deformation behavior of FRP-confined concrete cylindrical specimens. After developing this data, a consistent metric for characterizing specific damage levels in the FRP-confined concrete system was established. The results from visual and microscopic observations of the concrete core of FRP-confined concrete specimens are also reported.

Chapter 4 presents a comprehensive study on electromagnetic properties of concrete and FRP materials. The importance of understanding such properties is stated as a link between the material composition of FRP-confined concrete systems studied in Chapter 3 and the radar measurements and signal processing studies related to the non-destructive evaluation of those systems described in Chapter 5. A new methodology for characterizing the dielectric properties of low-loss materials, which may be applicable to concrete, FRP, and other construction materials, is described in this chapter. Development of the methodology, experimental and theoretical results, and the advantages and limitations of this methodology are discussed.

Chapter 5 presents the results of exploratory research related to the implementation of a radar NDE methodology for assessing FRP-confined concrete laboratory specimens. Radar measurements of intact specimens, mechanically damaged specimens, defective specimens, and specimens with rebar are described and analyzed. Various signal processing and imagery techniques are applied for interpreting the radar measurements and to contrast characteristic features between various specimens.

As noted by the reader, Chapters 3, 4, and 5 are devoted to three independent studies, each of them in different engineering research areas. However, the author has attempted to draw links between the analyses and results presented in these chapters as the goals of each specific study enhance and complement the overall research objectives described in Chapter 1. It is worth noticing that these three chapters provide the necessary background information in the particular research area at the introductory levels.

In Chapter 6, a summary of the research performed, conclusions, and recommendations for future work are provided.

Chapter 2

FRP Composites in Infrastructure Rehabilitation: Applications and Non-Destructive Evaluation

The aim of this chapter is to provide the necessary background information relevant to the scope of this thesis work. Due to the interdisciplinary nature of the research herein presented, several topics across the subject areas of structural engineering, materials science, and electrical engineering are introduced. The first sections of this chapter are devoted to providing a detailed overview of the mechanical and durability aspects of fiber-reinforced polymer (FRP) composite materials followed by a discussion on specific applications for strengthening and retrofitting of concrete structures. The later sections of this chapter are devoted to presenting developments and challenges for non-destructive evaluation (NDE) of concrete structural elements retrofitted with FRP composites. Several types of NDE techniques are discussed and evaluated. Special emphasis is given to applications to these techniques to FRP-confined concrete column elements.

2.1 Overview of FRP Composite Materials

FRP composites are defined as the combinations of high strength and stiffness fibers in a polymeric matrix material with distinct interfaces between them. Thus, each of the constituents retains their mechanical and chemical properties while exhibiting enhanced combined properties. Generally, the fibers are considered as reinforcements and serve as the principal members for sustaining loads and controlling strains. The polymeric matrix material governs the thermal stability. Other roles of the matrix material are:

- Bind the fibers together
- Provide the physical shape of the composite
- Protect the fibers from aggressive environments

- Transfer and redistribute stresses between fibers, plies, and in areas of load or geometrical discontinuities (Tuttle 2004).

The properties of FRP materials are directly related to the properties of the constituents, the relative quantities of the constituents, and the manufacturing process of the composite material. Appropriate control and selection of these variables is the key feature of FRP composites. An optimum selection of fiber, matrix, and interface conditions can lead to the manufacturing of a composite with enhanced mechanical and durability properties comparable or better than many conventional materials.

2.2 Constituent Materials in FRP Composites

2.2.1 Fiber Reinforcements

Fibers are used in composites because of their light weight, high stiffness, and high strength. Fibers are stronger than the corresponding bulk material due to the preferential orientation of molecules along the fiber direction and the reduced number of defects in the fiber. In the case of unidirectional composites, fibers are used as continuous reinforcement by aligning large numbers of them in order to form a thin plate called lamina, layer, or ply (Barbero 1999). A unidirectional lamina shows its maximum strength and stiffness along the fiber direction and its minimum properties perpendicular to the fiber direction. Alternative fiber orientations are also manufactured when similar properties are desired in specific orientations. The most common fibers in FRP composites are glass, carbon, and aramid. The choice of a specific fiber type is dependent on the mechanical and environmental properties required for the application in mind, as well as the cost of the fibers.

Glass Fibers

Glass fibers replicate the properties of typical glass such as hardness, corrosion resistance, inertness, improved flexibility, lightweight, and low-cost. Due to this array of properties, glass fibers are the most commonly used type in low-cost industrial applications. The enhanced strength of glass fibers is related to the low number and small size of defects on the surface of the fiber. All glass fiber types show similar stiffness values but different strength and environmental resistance values. E-glass fibers (E stands for electrical) are used in applications where high tensile strength and improved chemical and electrical resistance are required. E-glass fiber reinforcement is the preferred choice for structural applications due to the combination of mechanical properties, corrosion resistance, and low cost, which could range between $1 - $6/lb (Gunes 2004). S-glass fibers (S stands for structural) have the highest strength; however, their use in structural large applications is limited due to their high costs. In general, glass fibers are isotropic. Selected mechanical and physical properties of typical E-glass and S-glass fibers are listed in Table 2-1.

Carbon Fibers

Carbon fibers are characterized by their lightweight, high strength, and chemical resistance. The properties of carbon materials depend on the raw material and the manufacturing process. The main two raw materials used are polyacrylonitrile (PAN) and pitch. Pitch fibers are less expensive but show lower strength values than PAN fibers. Maximum operating temperatures of carbon fibers vary from 315 °C to 537 °C (Schwartz 1992). Carbon fibers show improved stiffness values compared to glass fibers, while providing better fatigue resistance characteristics to the composite by reducing the amount of strain in the polymer matrix for a given load (Barbero 1999). Carbon fibers are good electrical conductors, and hence, galvanic corrosion could take place if carbon fiber composites are in electrical contact with metals. One important limiting factor for the wide use of carbon fibers is their elevated cost, which could range between $9 - $20/lb (Gunes 2004). Another issue that may affect the use of carbon fibers in certain structural applications is their lower ultimate strain capacity compared to glass and aramid fibers. Selected mechanical and physical properties typical of low-modulus, intermediate-modulus, and ultra-high-modulus fibers are listed in Table 2-2.

Aramid Fibers

Aramid fibers are the most commonly known organic type of fibers. Examples of aramid fibers are produced by DuPont under the trade name of Kevlar. Aramid fibers are the ideal choice for impact and ballistic protection because of their high energy absorption characteristics during failure. Additional attractive properties of aramid fibers are their high tensile-to-weight ratio and high modulus-to-weight ratio, which makes them specially suited for aircraft and body armor applications. Some of the disadvantages of aramid fibers are their low compressive strength, creep development, moisture absorption, and sensitivity to UV light. Mechanical properties of aramid fibers also vary with temperature, with a 75-80% reduction in tensile strength at 177 °C compared to room temperature (Barbero 1999). Various types of aramid fibers offer distinctive material properties, being Kevlar 49 the most widely used. Selected mechanical and physical properties of Kevlar 49 are presented in Table 2-3.

Property	E-Glass	S-Glass
Specific gravity	2.6	2.5
Young's modulus, GPa (Msi)	72 (10.5)	87 (12.6)
Tensile strength, MPa (ksi)	3450 (500)	4310 (625)
Tensile elongation, %	4.8	5.0
Coefficient of thermal expansion, um/m/°C (uin/in/°F)	5.0 (2.8)	5.6 (3.1)

Table 2-1 Typical properties of glass fibers (Tuttle 2004)

Property	Low modulus	Intermediate modulus	Ultra-high modulus
Specific gravity	1.8	1.9	2.2
Young's modulus, GPa (Msi)	230 (34)	370 (53)	900 (130)
Tensile strength, MPa (ksi)	3450 (500)	2480 (360)	3800 (550)
Tensile elongation, %	1.1	0.5	0.4
Coefficient of thermal expansion, um/m/°C (uin/in/°F)	-0.4 (-0.2)	-0.5 (-0.3)	-0.5 (-0.3)

Table 2-2 Typical properties of commercially available carbon fibers (Tuttle 2004)

Property	Kevlar 49
Specific gravity	1.44
Young's modulus, GPa (Msi)	124 (18)
Tensile strength, MPa (ksi)	3700 (535)
Tensile elongation, %	2.8
Coefficient of thermal expansion, um/m/°C (uin/in/°F)	-2.0 (-1.1)

Table 2-3 Typical properties of Kevlar 49 fibers (Tuttle 2004)

2.2.2 Forms of Fiber Reinforcement

FRP composite materials are produced in various forms depending on the volume fraction, length, orientation, and type of fibers in the matrix (Hull and Clyne 1996). The fibers may be either discontinuous or continuous and can be aligned in one or more directions or randomly distributed in two or three dimensions. Figure 2-1 shows samples of forms of fiber reinforcement that are used in composites.

Discontinuous fibers are short in length and are obtained by chopping continuous fibers. The orientation of short fibers is not controlled and they are assumed to be randomly distributed. Composites made with short fibers arranged randomly have nearly isotropic properties in the plane of the laminate. In general, short fiber composites are used for lightly loaded structural applications, whereas continuous fiber composites are considered high-performance materials.

Fiber reinforcements are produced in small diameters to optimize their mechanical performance. Since these so called monofilaments are extremely fragile, they are supplied in bundles. The appropriate terminology for identifying these bundles varies based on the type of fiber (Gunes 2004). Collections of untwisted continuous glass or aramid fibers are called strands, whereas similar arrangements of carbon fibers are called tows. Tow or twisted strands are called filament yarns, and a bundle of strands or yarns is called a roving. Figure 2-2 schematically illustrates these basic forms of reinforcements.

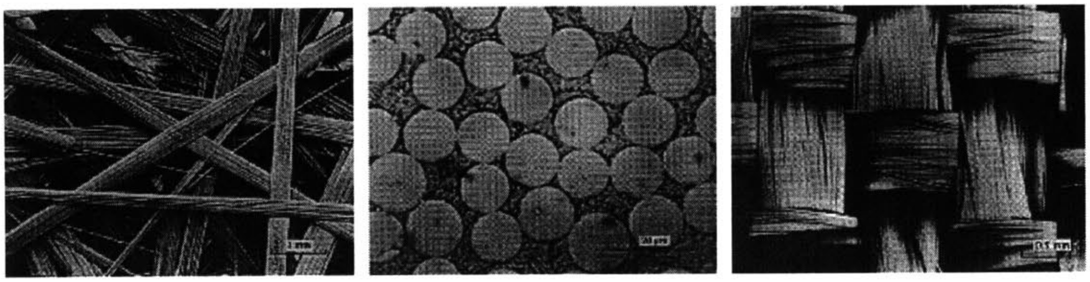

(a) continuous-unidirectional (b) continuous-woven (c) short-random

Figure 2-1 Different types of FRP composites based on fiber length and orientation (Hull and Clyne 1996)

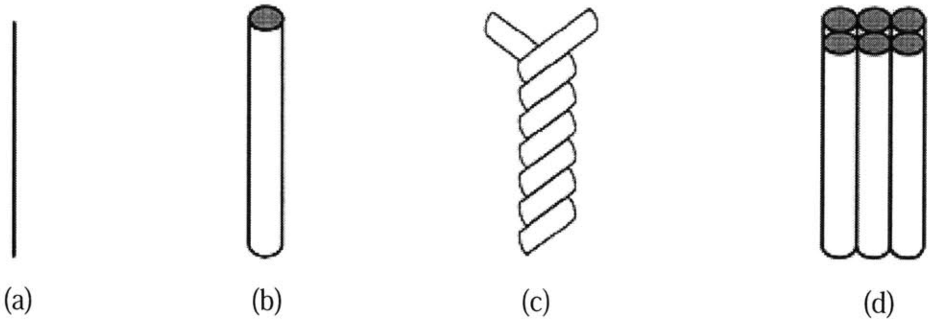

Figure 2-2 Schematics of basic fiber forms
(a) single fiber, (b) strand or two, (c) filament yarn, (d) roving
(Gunes 2004)

Rovings and tows are used to produce complex forms of fiber reinforcements using technologies developed for the textile industry: weaving, braiding, and knitting. These forms of reinforcement are collectively referred to as fabrics, and are commonly used for structural strengthening applications. Advantages of the mentioned fabric reinforcement forms are oriented strength, high reinforcement ratios, and conformability to curved shapes. Due to advances in manufacturing processes, fabrics can be manufactured from almost any type of fiber, using several weaving techniques, and with controllable thicknesses ranging from 0.025 *mm* to 10 *mm*.

2.2.3 Matrices

Matrix types are divided into two general groups: thermoplastics and thermosets. In thermoplastic matrices, the polymer molecules are held in place by weak secondary bonds with no chemical linking. Consequently, the matrix can be repeatedly melted and reshaped upon heat application. On the contrary in thermosetting matrices, the molecules are chemically joined by cross-linking, forming three-dimensional network structures. These matrices set at specific temperatures (room temperature or above) and cannot be melt or reshaped by subsequent heat application. Selected properties of various matrix types are provided in Table 2-4.

Matrix	Density ($Mg\ m^{-3}$)	Young's Modulus (GPa)	Poisson's Ratio	Tensile Strength (GPa)	Failure Strain %
Thermosets					
Epoxy resin	1.1 - 1.4	3.0 - 6.0	0.38 - 0.40	0.035 - 0.100	1.0 - 6.0
Polyesters	1.2 - 1.5	2.0 - 4.5	0.37 - 0.39	0.04 - 0.09	2.0
Thermoplastics					
Nylon	1.14	1.4 - 2.8	0.3	0.06 - 0.07	40 - 80
Polypropylene	0.9	1.0 - 1.4	0.3	0.02 - 0.04	300
PEEK	1.26 - 1.32	3.6	0.3	0.17	50

Table 2-4 Selected properties for different types of polymeric matrices
(Hull and Clyne 1996)

In structural applications, composites are usually manufactured using thermoset resins such as polyester and epoxy. Polyester resins are the most widely used material in the composites industry due to their low cost, ease of handling, and adequate balance between mechanical, electrical, and chemical properties. However, epoxy resins are preferred for structural applications due to their superior mechanical properties and resistance to corrosive environments. Epoxy resins also provide excellent adhesion to a wide range of fiber types due to their inherent polar nature. Other advantages of epoxy resins are low levels of shrinkage attained upon curing, high toughness resistance due to cross-linking, and no release of volatile byproducts that cause air voids during the curing process. Some disadvantages of epoxy resins are their tendency to absorb moisture in the uncured and cured states, as well as a relatively low elongation to failure.

2.2.4 Manufacturing Methods

The manufacturing methods utilized for making composites for infrastructure applications can be classified as automated manufacturing process and hand lay-up (Peters 1998). Automated manufacturing processes include techniques such as pultrusion, resin transfer molding, compression molding, and filament winding. Hand lay-up, also called wet lay-up, is the simplest technique for producing reinforced polymer laminates. This manual process is suited for FRP strengthening or retrofit applications on site. Important aspects related to the implementation of this technique are adequate surface preparation, selection of the adhesive material and bonding, and quality control.

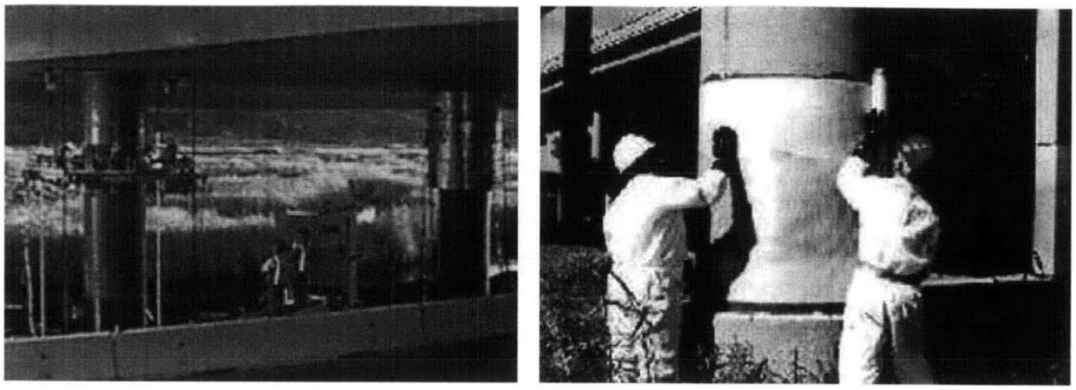

(a) Automatic filament winding (b) hand lay-up

Figure 2-3 Examples of manufacturing methods (Gunes 2004)

Important advantages of this technique when used for structural applications are low cost, flexibility, and ease of the process. Figure 2-3 shows examples of two manufacturing processes.

2.3 Mechanical and Durability Characteristics of FRP Composites

Mechanical characteristics discussed in this section include elastic modulus, strength, energy absorption, impact resistance, thermal expansion, and fatigue resistance. Selected mechanical properties for several unidirectional laminates are presented in Table 2-5. Environmental durability aspects are also addressed in this section.

Property	Boron - Epoxy	HS Carbon - Epoxy	HM Carbon - Epoxy	Kevlar 49 - Epoxy	E-Glass - Epoxy
Specific gravity	1.99	1.54	1.63	1.38	1.80
Tensile strength (MPa)					
Fiber axis	1585	1448	827	1379	1130
Transverse axis	63	62	86	28	96
Modulus (GPa)					
Fiber axis	207	128	207	76	39
Transverse axis	19	9	14	6	5
Shear properties					
Strength (MPa)	131	60	72	60	83
Modulus (GPa)	6.4	5.7	5.9	2.1	4.8
Poisson's ratio	0.21	0.25	0.20	0.34	0.30

Table 2-5 Typical mechanical properties of unidirectional laminates (Schwartz 1997)

2.3.1 Elastic Modulus

FRP composites are known to showing various degrees of anisotropy depending on fiber orientation. As shown in Figure 2-4 (a), the tensile strength and modulus of a unidirectional fiber-reinforced laminate are maximum when aligned with the fiber axis direction. Assuming strain compatibility between the fiber and matrix components, the elastic modulus of the composite in the longitudinal direction, E_{cl} is given by (Ward and Sweeney 2004):

$$E_{cl} = V_f E_f + (1 - V_f) E_m \tag{2.1}$$

where V_f = fiber volume fraction, and E_f and E_m = elastic modulus of the fibers and matrix, respectively. Eq. 2.1 represents the upper bound or Voigt average modulus (Ward and Sweeney 2004). For the case where the laminate is loaded in the transverse direction, as shown in Figure 2-4 (b), the elastic modulus of the composite in the transverse direction, E_{ct} based on the iso-stress assumption is given by (Ward and Sweeney 2004):

$$E_{ct} = \frac{E_f E_m}{E_m V_f + E_f (1 - V_f)} \tag{2.2}$$

which provides the lower bound or Reuss average modulus. Figure 2-4 (c) shows graphically the laminate stiffness as function of loading direction and fiber volume fraction.

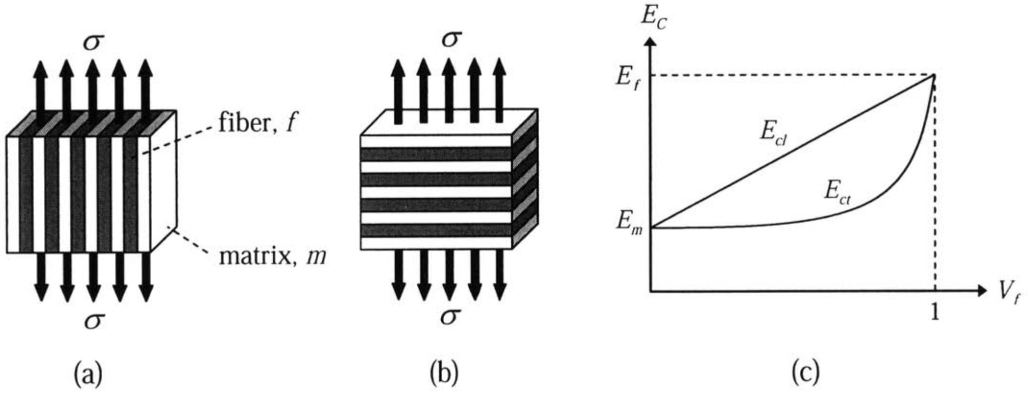

Figure 2-4 Voigt and Reuss bounds of laminate stiffness
(a) elastic modulus in longitudinal direction, (b) elastic modulus in transverse direction, (c) laminate stiffness as function of loading direction and fiber volume fraction

2.3.2 Strength

The application of arbitrary stress states to a unidirectional laminate can lead to failure by various failure processes such as tension in the fiber direction, tension in the transverse direction, and shear in the fiber direction (Hull and Clyne 1996). The strength of the composite laminate parallel to the fiber direction, σ_{lu} is given by:

$$\sigma_{lu} = V_f \sigma_{fu} + (1 - V_f)\sigma_{mfu} \tag{2.3}$$

where σ_{fu} is the fiber strength and σ_{mfu} is the stress in the matrix at fiber failure strain. The strength of the composite laminate in the transverse direction, σ_{tu} is given by:

$$\sigma_{tu} = \sigma_{mu}\left[1 - 2\sqrt{\frac{V_f}{\pi}}\right] \tag{2.4}$$

where σ_{mu} is the tensile strength of the matrix. A simple analytical solution for shear strength prediction as function of fiber content is not available. Based on finite difference analysis for $V_f \leq (\sim 0.7)$, the shear strength is expected to have a similar value to the shear strength of the matrix.

2.3.3 Energy Absorption

Although the behavior of FRP composites is characterized as linearly elastic based on their tensile stress-strain responses, their heterogeneous nature provide several energy dissipation mechanisms on the microscopic scale comparable to yielding processes found in structural metals (Jang 1994). Such mechanisms include matrix microcracking or crazing, fiber rupture, interfacial debonding, and fiber pull-out. Depending on the intensity and type of loading, these failure processes allow the composite laminate to display a gradual deformation rather than catastrophic failure.

2.3.4 Impact Resistance

In unidirectional composite laminates, the maximum impact resistance is exhibited when fibers are orientated in the direction of the maximum stress. Aramid and E-glass fibers offer significant impact resistance due to their high ultimate tensile strength.

2.3.5 Thermal Expansion

Carbon and aramid FRP composites have negative coefficients of thermal expansion, while that of glass FRP is positive (Barbero 1998). Resins display an expansive behavior upon heating. These differences in thermal expansion properties are of significance in relation to residual stress development. For instance in the case of a carbon/epoxy FRP composite, the thermal shrinkage of carbon fibers and the thermal expansion of the epoxy resin give rise to an overall near-zero coefficient of thermal expansion.

2.3.6 Fatigue Resistance

Fatigue behavior is commonly presented through the relationship between stress and number of loading cycles (*S-N* curve). This characterization is primarily dependent on the properties of the constituent materials. Figure 2-5 presents a comparison of the fatigue behavior for glass FRP (GFRP), Kevlar FRP (KFRP), and carbon FRP (CFRP). Studies directed by Curtis (in Holloway 1993) on the strain life of four CFRP types with different stiffness properties and the same matrix suggested that there were not significant differences in terms of their fatigue behavior. However, the same study revealed that different epoxy matrices alter the observed fatigue behavior by enhancing static strengths at the expense of steeper decays in the S-N curves after certain number of cycles.

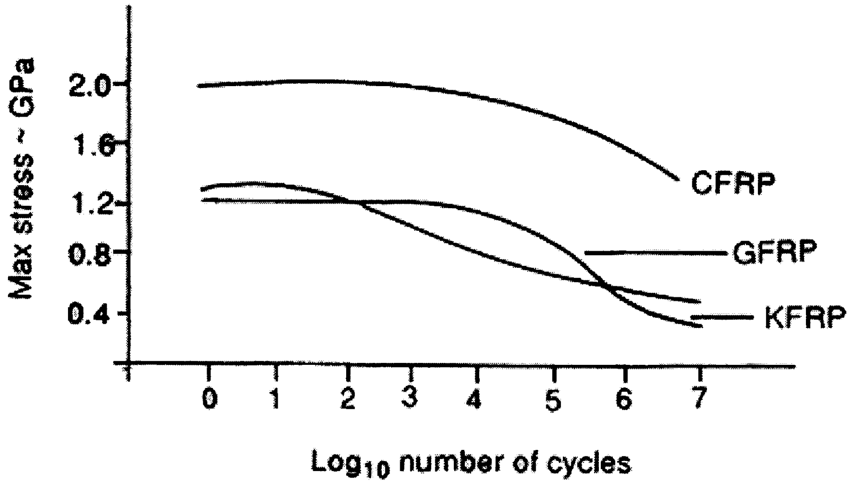

Figure 2-5 Typical S-N curves for unidirectional composites (Holloway 1993)

For the case of a GFRP cross-ply laminate (0°/90° orientations), fatigue due to damage accumulation would cause a rapid stiffness reduction, which is directly related to the increment in density of transverse ply cracks. This stage of rapid stiffness reduction is followed by a linear region of reduced rate of crack density in the transverse direction, delaminations in the ply interface, and fiber breakage in the 0° direction. The third stage is governed by a rapid reduction in stiffness due to macro-crack formations. Figure 2-6 shows the development of damage and stiffness reduction for a symmetrical 0°/90° GFRP laminate.

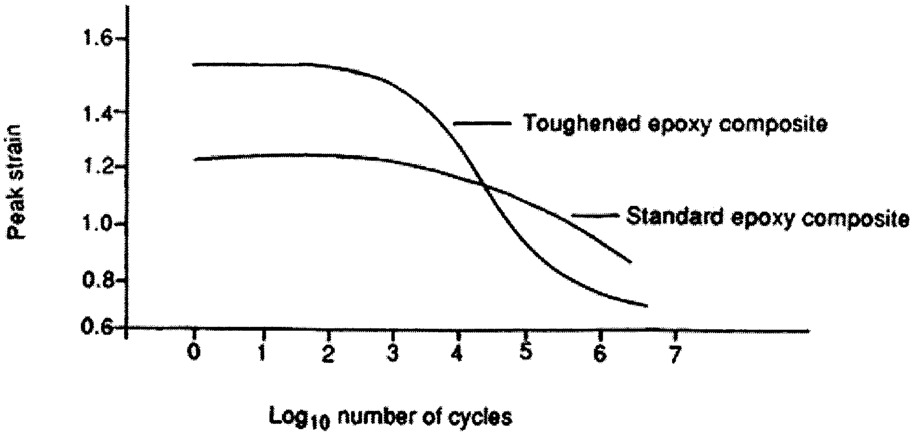

Figure 2-6 Development of damage and stiffness reduction in a 0°/90° GFRP laminate (Holloway 1993)

2.3.7 Environmental Durability

Environmental factors such as temperature cycles, moisture and chemical attack, and ultraviolet (UV) radiation are major concerns when evaluating the adequacy of FRP composites for specific structural applications. Although these materials have not been widely used for a long enough time, they are known to be more durable than other conventional structural materials such as steel, reinforced concrete (RC), and wood. However, depending on the specific type of fiber and matrix, certain environmental factors can cause degradation in the mechanical performance of the composite. For instance, recent studies have shown that moisture could accelerate debonding in FRP-bonded concrete systems when subjected to peel and shear loadings (Au 2005, Au and

Büyüköztürk 2006). UV radiation is also known to cause degradation in polymers by scission of the polymer chains.

2.4 Structural Strengthening and Retrofitting of Reinforced Concrete Structures

2.4.1 Rehabilitation Needs of Existing Infrastructures

Civil infrastructures are the most valuable assets in any country. In the United States, the nation's infrastructure, which was generally built in 1950s, is now approaching the service life, and is in need of urgent repair and retrofit. An infrastructure assessment survey conducted by the American Society of Civil Engineers (ASCE 2005) revealed that the overall condition of the United State's infrastructure could be categorized as poor to mediocre. As of 2003, approximately 27% of the nations' 600,000 bridges were reported to be structurally deficient or functionally obsolete. It is expected that the cost to eliminate all bridge deficiencies will be $9.4 billion a year for the next 20 years. Revisions to seismic design codes are also an important contributor to categorizing thousands of existing structures as substandard. Recent major earthquakes in urban areas of the United States (1989 Loma Prieta, 1994 Northridge), Japan (1995 Kobe), Turkey (1999 Kocaeli and Duzce), and Taiwan (2000 Chi Chi) have exposed the inadequacy of old seismic design codes. Considering the cost of repairing and retrofitting all damaged and substandard structures, it is apparent that reliable and cost-effective retrofit technologies are needed.

FRP composite systems have emerged as an alternative to traditional construction and strengthening and repair of existing infrastructure. The emerging field of renewal engineering may best describe the role of FRP composites in civil engineering and infrastructure (Van Den Einde *et al.* 2003). The renewal of civil structural inventory can be divided into (1) rehabilitation, including all applications geared towards the repair, strengthening, and retrofit of structures, and (2) new construction with all FRP solutions or new composite systems. Due to their enhanced properties and cost-effectiveness, FRP composites have the potential to influence numerous aspects of the construction industry. Figure 2-7 shows a diagram of the current use of FRP composites in the renewal of civil

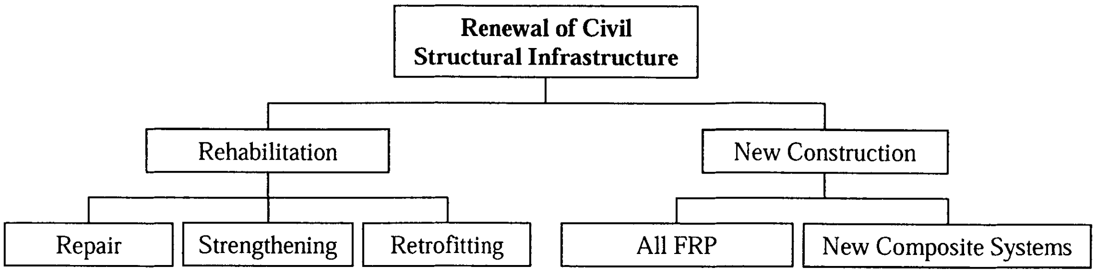

Figure 2-7 Use of FRP composites in civil infrastructure
(Van Den Einde *et al.* 2003)

infrastructure. The structural effectiveness of FRP composite materials has also been demonstrated by numerous studies, although further research is needed to fully understand complementary performance aspects such as complex loading conditions, long-term durability, environmental degradation, and in-situ monitoring and structural assessment. In the following section, the state-of-the-art in developments and applications of FRP composites in civil infrastructure is further described.

2.4.2 State-of-the-Art in Developments and Applications of FRP Composites

FRP composite materials have been used for repair, strengthening, and retrofitting of structural members in a variety of experimental and field projects since the 1980s. Early research and application of these materials were concentrated in Switzerland, Japan, and Germany. In the 1990s, other countries such as the United States, Canada, and Saudi Arabia joined the research efforts and continue advancing the understanding of the performance of FRP composite systems with respect to analysis, design, application, and durability aspects. With reductions in cost of FRP composites and the eminent need to strengthen existing infrastructure worldwide, external bonding and wrapping using FRP composites for strengthening and repair of structural members, especially in reinforced concrete applications, has emerged as a promising alternative method (Teng *et al.* 2003). Additionally, the ease of application of these materials makes them tremendously attractive for use in civil engineering applications in cases where dead weight, space, and time constraints are common.

The choice of the strengthening or retrofit system depends on the type of structural member, which typically derives into three categories: flexural strengthening, shear strengthening, and confinement strengthening. Flexural strengthening of beams is achieved by bonding FRP plates or sheets to the soffits of the concrete beam. Figure 2-8 shows several methods of beam strengthening in flexure with FRP composite plates.

Shear strengthening of concrete beams include bonding FRP composites on the sides of the beam and bonding U-wraps to cover both sides and the soffits using various anchorage schemes. FRP plates and sheets have been used for shear strengthening applications. Because of the improved mechanical properties of FRP composites in the direction of the main fibers, their orientation could be designed as to best reinforce the beam.

Column strengthening using FRP composites has proven to be a very effective solution for increasing the strength of concrete columns, in particular, circular columns (Nanni and Bradford 1995, Demers and Neale 1999, Xiao and Wu 2000, Au and Büyüköztürk 2005). Additionally, this technique has been widely used for seismic retrofit of columns, where improvements in shear strength and ductility are the main concerns (Van Den Einde *et al.* 2003). FRP sheets with the main fibers oriented in the hoop direction have been used for this application. Apart from the in-situ wrapping of columns with FRP sheets using the wet lay-up process, prefabricated FRP tubes and shells have also been used.

At the present time, deployment of FRP composite strengthening solutions is found worldwide. Projects involving such technology include the strengthening of silos, pylons,

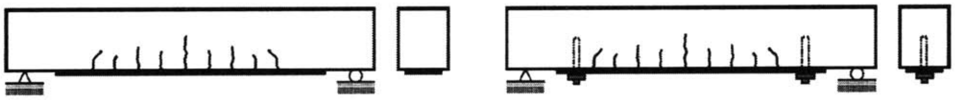

(a) FRP reinforcement bonded to soffit

(b) anchorage with bolts

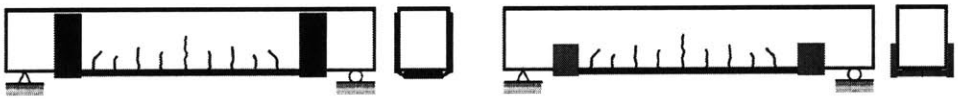

(c) anchorage with U-wraps

(d) anchorage with L-shaped plates

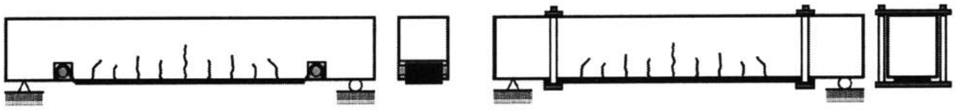

(e) anchorage with near surface mounted rods

(f) anchorage with mechanical clamps

Figure 2-8 Methods of beam strengthening in flexure with FRP composite (Gunes 2004) and transmission towers, rehabilitation of shop and office buildings, seismic strengthening of bridge piers, flexural strengthening of bridge decks and girders, strengthening of brick walls and masonry domes, among others (Fyfe Co. LLC 2005, Sika Group 2005). In the following section, FRP strengthening of columns elements is further discussed.

2.4.3 Applications of FRP Composites for Strengthening and Retrofitting of Concrete Column Members

For the case of reinforced concrete (RC) columns, structural problems that are mitigated with strengthening and retrofit measures include lack of flexural strength and ductility due to poor design of longitudinal reinforcement and lap-splices, inadequate confinement of potential plastic hinge zones, lack of shear strength, poor design of column-beam joints and footing connections, and inadequate strength capacity due to changes in design codes or as a result of seismic events (Xiao *et al.* 2001). Conventional retrofit solutions include addition of RC sections for external confinement of the concrete core, and use of steel jackets. Steel jacketing can be considered as a tubed column system, where the tube or jacket is designed to function as transverse reinforcement. While steel jacketing is a commonly accepted practice for structural repair and strengthening of RC columns, it is relatively time consuming and is susceptible to environmental degradation.

A key application of FRP composites in the forms of wraps or jackets is the confinement of RC columns in order to improve their strength and ductility characteristics. In FRP-confined concrete systems, the FRP is primarily loaded in tension in the hoop direction while the concrete is loaded in triaxial compression, a situation in which both materials are used to their best advantages. As a result of the confinement effect, both the strength and the ultimate strain capacities of the concrete can be greatly enhanced, while the high tensile strength of the FRP is being fully utilized. Although both materials exhibit brittle behaviors separately, FRP-confined concrete exhibits improved deformation capabilities (Teng and Lam 2004).

Several composite jacketing systems have been developed and validated in laboratory and field conditions. In-situ installed FRP jacketing involves hand or automated machine placement of glass or carbon fabrics saturated with an epoxy polymer on the surface of the concrete column. The advantages of this type of FRP jacket systems are their compatibility with various column geometries and the ease of installation. However, these systems may require special attention regarding quality control of the installation and the curing of the FRP jacket. Another category of FRP jackets is referred to as prefabricated jacketing systems. These prefabricated jackets are manufactured by putting together fiber sheets with fiber strands in order to form a composite laminate. This laminate is then saturated with epoxy resin and placed into a specially designed form, thus creating a prefabricated FRP jacket shell (Xiao *et al.* 2001).

Design Example for Calculating the Increase of Concrete Compressive Strength based on FRP Wrapping

To illustrate common practice for increasing the compressive strength of concrete columns using FRP wrapping, a design example is presented in this section. The design example is obtained from Fyfe Co. LLC, an established US manufacturer in the area of structural strengthening and retrofitting using FRP composites (Fyfe Co. LLC 1999). Design recommendations and equations are based on structural engineering principles and experimental data collected through numerous research studies. According to the manufacturer, this sample design serves as a general guideline; however, it should not be applied to individual projects without the supervision of the structural engineering and the collaboration of the composite manufacturer.

The calculation of the compressive strength increase in concrete based on wrapping with a Tyfo® jacket with the main fibers oriented in the hoop direction is based on the following equation:

$$\frac{f'_{cc}}{f'_c} = 2.25\sqrt{1 + 7.94\frac{f_l}{f'_c}} - 2\frac{f_l}{f'_c} - 1.254 \tag{2.5}$$

where:

f'_{cc} = confined concrete strength

f'_c = compressive strength of plain concrete

f_l = confining stress = $0.26\rho_j \phi f_{uj}$

ρ_j = confinement ratio for circular section = $4t_j / D$

t_j = jacket thickness

D = diameter of the concrete column

$\phi = 0.25$, factor for sustained design stress to prevent creep effects

f_{uj} = tensile strength of composite jacket

For the case of a 600 *mm* diameter column with a compressive strength of 24 *MPa* retrofitted with a two-layer Tyfo® SEH-51 fabric jacket (custom weave, unidirectional glass and aramid hybrid fabric, thickness = 1.3 *mm* / layer of SEH-51, tensile strength = 414 *MPa*), the increase of compressive strength is calculated:

$$f_l = 0.26\left(4 \cdot \frac{2.6}{600}\right)(0.25)(24) = 0.466MPa$$

$$\frac{f'_{cc}}{f'_c} = 2.25\sqrt{1 + 7.94\frac{0.466}{24}} - 2\frac{0.466}{24} - 1.254 = 1.12$$

Thus, the resulting increase in compressive strength of the FRP-confined concrete column is approximately of 12%. Further discussion on the mechanics and performance of concrete column elements confined with FRP composite jackets is presented in Chapter 3 of this thesis.

2.5 Non-Destructive Evaluation of FRP Retrofitted Concrete Structures

In order to meet the challenges of the growing industrial applications of FRP jacketing systems for concrete columns and bridge piers, a reliable NDE technology that is capable of assessing the structural integrity of the FRP/concrete composite system, and in particular the condition of the concrete inside the FRP jacket needs to be developed. In a study performed at MIT (Au 2001, Au and Büyüköztürk 2005), it was identified that concrete crumbling and delaminations between the FRP jacket and concrete could occur under various degrees of confinement provided by the FRP jacket. Figure 2-9 (a) shows the local crumbling failure of concrete in a FRP-confined concrete cylindrical specimen with high level of lateral confinement. Levels of high confinement are often characterized by column strengthening purposes, should there be an opportunity of functionality or an upgrade for seismic solutions (Nanni 1993, Priestley and Seible 1996). Figure 2-9 (b) shows a global shear crack failure of concrete in a specimen with little lateral confinement. Low levels of confinement are provided using minimal number of FRP plies. Applications of such type include repairing of columns that undergo rebar corrosion and concrete spalling (Fyfe Co. LLC 1999). Both scenarios are equally common in industrial practices (Howie and Karbhari 1995).

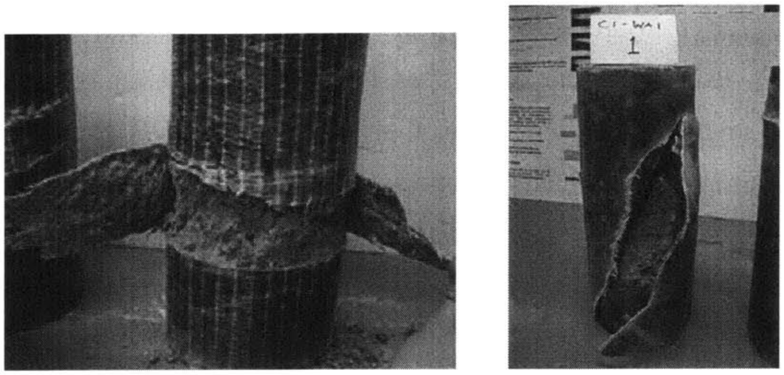

(a) Local concrete crumbling (b) global shear cracking

Figure 2-9 Failure mechanisms in FRP-confined concrete (Au 2001)

2.5.1 Challenges in NDE of FRP-Confined Concrete Structures

NDE of concrete structures is a challenging task. Some of the challenges that NDE technologies face in field applications are the following:

- Concrete is a highly heterogeneous material, which is generally produced in the field with limited quality control. The grain size distribution and properties of constituent materials are significantly variable.
- Complex physical geometries and limited accessibility to the concrete member are common in the concrete structures.
- Environment effects such as temperature, moisture, and wind may induce errors in the field data.
- Capability of handling layered materials system, especially sub-surface defects such as FRP-concrete debonding, air voids, concrete crumbling.
- Possible reflection and attenuation of signals from material interfaces and certain FRP materials.

- Handling of the equipment should be carefully considered when developing a successful NDE technique for field conditions. Equipment set-up and recording of measurements should not require highly skilled operators.
- NDE techniques should be efficient in terms of time. Assessment of civil infrastructure is a task that requires measurements of large numbers of structures and structural areas.
- Need to clearly understand the differences in terms of material types, nature of structures, and on-site conditions when applying existing NDE techniques to the construction industry compared to applications in other industries (*e.g.* aerospace).

In the next sections, brief descriptions of NDE methods applied to concrete structures are provided, followed by a discussion of application issues, advantages, and disadvantages of each particular method. Finally, an assessment of the feasibility of these methods for their application to FRP/concrete systems is presented.

2.5.2 NDE Technologies for Civil Infrastructure

Several NDE technologies have been under investigation and development for potential deployment for civil engineering infrastructure applications.

Radiography is a NDE technique used to obtain a shadow image of a solid using penetrating radiation (*e.g.* X-rays or Gamma-rays) (Cartz 1995). X-rays and Gamma-rays are forms of electromagnetic radiation with corresponding wavelengths which are small enough to penetrate all materials with some absorption and scattering during transmission (Halmshaw 1991). The transmitting rays strike a detector, typically a photographic film, and expose it similarly as light exposes a film in a typical camera. For the case of concrete, the obtained image is a two-dimensional projection, providing information about the physical characteristics of concrete such as density, composition, and inclusions through the different degrees of attenuation. This technique has been used to assess the location and condition of steel reinforcement, detect air voids, and delaminations, and to inspect the grouting of post-tensioned concrete (Mitchell 1991).

Computerized tomography (CT) refers to the reconstruction of cross-sectional image of an object based on its projections. Projections are obtained using a scanner by rotating the object or detector 360° at specific increments. The projections are then coherently superimposed to obtain a cross-sectional image of the object (Kak and Sianey 1988).

Applications of CT imaging techniques of concrete have been implemented to determine the density variations inside concrete, location of rebars and air voids, and their corresponding sizes. Figure 2-10 shows an image of a hollow cylinder of 20 *cm* diameter with a central hole, and a smaller hole (5 *mm* diameter). Computerized tomography is also used for the study of fracture mechanisms in concrete-based materials. High resolution three-dimensional X-ray computerized tomography techniques could be used to measure internal damage and crack growth in concrete specimens subjected to compressive loading conditions.

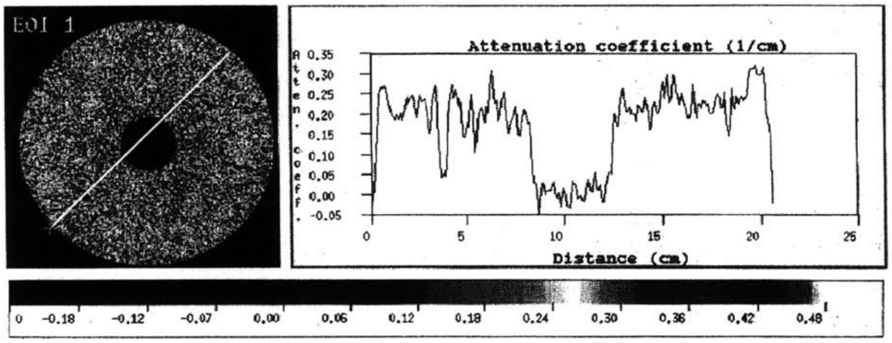

Figure 2-10 Tomography image of a hollow concrete cylinder and one-dimensional profile of attenuation coefficient along a white line (Martz *et al.* 1991)

Infrared thermography (IR) techniques are most commonly used in military applications, NDE of materials, and medical diagnosis. These technologies are based on the principle that subsurface anomalies or defects in the material under test result in localized differences in surface temperature caused by different rates of heat transfer at the defect zones. Thermography perceives the emission of thermal radiation from the material surface, and produces a visual signal related to this thermal radiation, which in turn can be related to the size of an internal anomaly. Most infrared thermography applications use a camera in conjunction with an infrared-sensitive detector which images the contrasts of heat radiation (Büyüköztürk 1998). Infrared thermography techniques have been applied within certain limitations to NDE of civil infrastructure. Currently, they have been used to determine the existence of air voids, delaminations, and debonding in reinforced concrete systems. Some civil engineering applications of infrared thermography technologies include bridges, highways, sewer systems and pipes, aqueducts, asphalt pavements, and indoor and outdoor thermography of buildings (Ljungberg 1994). Figure 2-11 shows a wall covered by pre-cast concrete panels. Thermography was used to detect separation of panels from the wall.

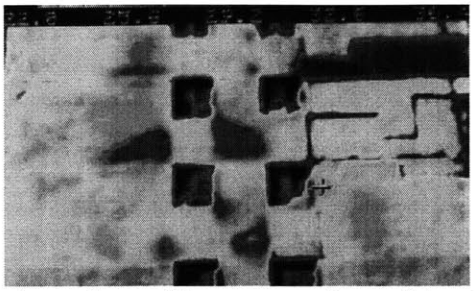

Figure 2-11 A computer-enhanced tomogram of a wall in a building under repair (Stanley and Balendran 1994).

Acoustic techniques such as impact-echo (IE), acoustic emission (AE), spectral analysis of surface waves (SASW), and ultrasound are based on elastic wave propagation in solid materials. Sound propagation occurs in the form of compression (P) waves, shear (S) waves in the solid, and surface waves (also called Rayleigh waves, R) along the surface. The acoustic emission technique is a passive condition monitoring technique that allows for testing of the structure while in service. Acoustic emission is related to pulses generated due to changes in elastic strain energy that occur locally in the material structure resulting from deformation and fracture processes. Ultrasonics involves the transmission of ultrasound waves into the concrete element using a transducer in contact with the surface of the element. The scattered signals are then recorded and interpreted to be used for image reconstruction. Acoustic imaging techniques are widely used in the evaluation of concrete structures. Several ultrasonic techniques are used for determination of concrete slab thickness (Krause *et al.* 1995) and measurement of elastic modulus (Blitz and Simpson 1996). Additionally, acoustic techniques are used for detection and imaging of voids (Jalinoos and Olson 1995).

The principle of the *radar method* is to generate and transmit electromagnetic pulses or waves towards a target medium. The electromagnetic (EM) wave propagation phenomenon in free-space and through other media can be described by Maxwell's coupled curl and divergence equations (Kong 1990). By incorporating the electromagnetic properties of the material target and the appropriate boundary conditions, a unique solution of the forward problem can be obtained using these equations (Büyüköztürk and Rhim 1994). At the instance when transmitted EM waves encounter another medium with different EM properties, a portion of that transmitted energy is reflected from the boundary, while the rest is transferred into the new medium undergoing some refraction depending on the properties of the new medium and the angle of incidence (Büyüköztürk 1998). Consequently, the scattered signals recorded at the receiver contain information about the target's EM properties (Büyüköztürk and Rhim 1995a, Büyüköztürk and Rhim 1995b). Radar techniques such as ground penetrating radar (GPR) have been extensively used in large scale applications, which include determination of thickness of glaciers, finding petroleum deposits, locating sewer lines and buried objects, assessment of bed profiles of lakes and rivers, and subsurface characterizations. In civil engineering applications, radar have been implemented in the inspection of highways and bridge decks (Chung *et al.* 1992), detection of cavities behind concrete tunnel linings (Fenning and Brown 1995), and detection and quantification of scour around bridge piers (Bungey *et al.* 1995, Davidson *et al.* 1995).

For a more complete discussion the advantages and limitations of the NDE methodologies herein discussed, the reader is referred to Büyüköztürk (1998).

2.5.3 NDE Methods Applied to FRP-Confined Concrete Systems

While radiography and computerized tomography have not been applied to FRP bonded concrete systems, infrared thermography, acoustic emission, and radar microwave techniques have been initially developed for this particular application. The following paragraphs discuss the results, advantages, and disadvantages of these techniques for the problem at hand.

Infrared Thermography

Work on condition assessment of FRP-wrapped concrete elements has been carried out by Starnes (Starnes *et al.* 2003) at MIT. The objective of this work was to provide the knowledge foundation for the potential application of infrared thermography to detect defects in FRP/concrete layered systems. Several testing parameters were investigated such as thermal input, amplitudes of signals, surface temperatures, FRP and concrete properties, and defect dimensions. Both numerical and experimental approaches were considered. The studies confirmed that the detection of voids at the FRP-concrete interface is possible, and that flaw depths and flaw widths may be predicted when working under controlled laboratory conditions.

Disadvantage

- Forced convection due to high wind speeds and atmospheric attenuation might have significant effects on the thermal response of the object and on the temperature recordings of the infrared detector, and therefore the obtained measurements may not be conclusive.

Acoustic Emission

Mirmiran *et al.* (1999) investigated the applicability of acoustic emission (AE) techniques to hybrid FRP-concrete columns and attempted to correlate AE parameters to stress states in the concrete core. Two types of AE data can be recorded with this technique: 1) AE parameters such as hit count, rise time, energy, amplitude and frequency content; and 2) AE waveforms. The rate and cumulative counts are used to determine damage levels in the concrete (Berthelot and Robert 1987). Frequency content and signal rise time allow for distinguishing between different damage mechanisms (Tanigawa *et al.* 1977). Other features of the AE technique is the correlation to the Felicity and Kaiser effects. The Felicity effect is the appearance of AE signals at stress levels below a previous maximum load. The Kaiser effect is the absence of detectable signals until a previous maximum load is exceeded. The results of this study on over 40 concrete-filled FRP tube specimens with different lengths, cross-section areas, and FRP jacket types and thicknesses subjected to uniaxial compression showed potential correlations between AE activity and damage extend in the specimens. The relation between the rate of change of cumulative AE counts and the applied load could help quantify accumulated damage. Figure 2-12 shows a typical variation of AE counts versus time along with the load-history for a FRP tubed specimen (6 layers of GFRP). Large AE counts are recorded at the initial phases of compression, followed by a low level of counts, and finally a rapid increase in the final stages of damage. Longer specimens and specimens with ticker FRP jackets showed higher AE activity. Figures 2-13 and 2-14 show the effects of jacket thickness on

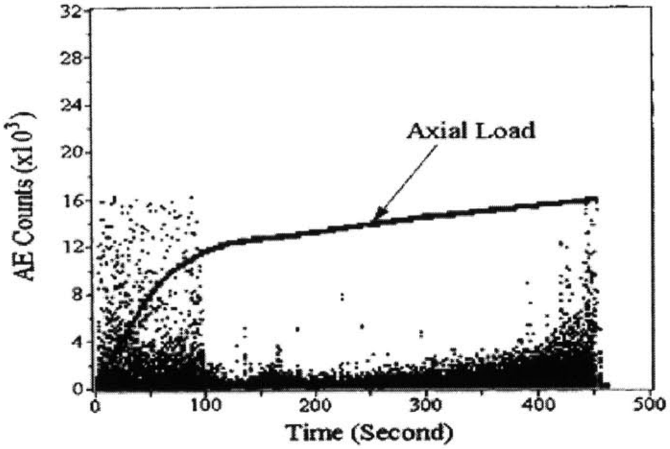

Figure 2-12 Typical variation on AE counts during compression (Mirmiran *et al.* 1999)

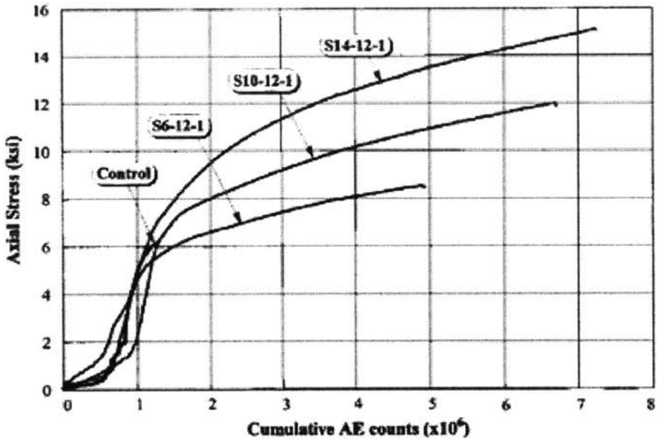

Figure 2-13 Effect of jacket thickness on cumulative AE counts (Mirmiran *et al.* 1999)

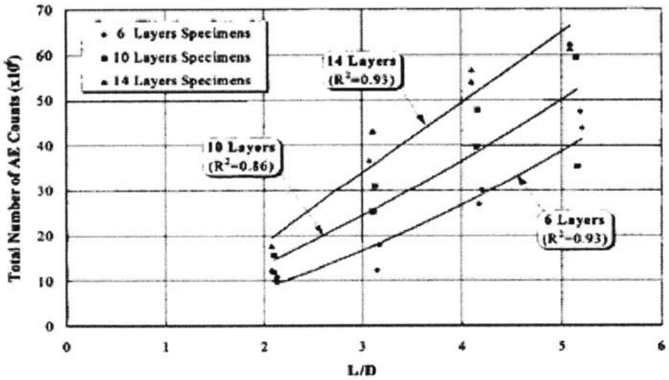

Figure 2-14 Effect of column size and jacket thickness on AE counts (Mirmiran *et al.* 1999)

cumulative AE counts and the effects of column size (length/diameter ratio) and jacket thickness on AE counts, respectively. It was proposed that the Felicity ratio can be used to investigate damage extent while the Kaiser effect was not present during cyclic loading.

Advantages

- AE techniques could result advantageous for structural health monitoring purposes. There are several AE parameters that could potentially be used for correlation with damage levels and mechanisms in FRP-concrete structures.
- In principle, the AE sensors could be positioned in key locations throughout the FRP-retrofitted column based the expected loading conditions.
- The technique also provides real-time recordings, which could be potentially processed and analyzed on-site given the availability of adequate monitoring equipment.

Disadvantages

- The same disadvantages of acoustic imaging methods apply in this specific case. The use of sensor in direct coupling with the FRP jacket could potentially lead to misinterpretations of AE signals due to the variety of FRP jacket threads and fabrics and their non-homogeneous surfaces. While in this study the FRP tubes were made of filament wound of unidirectional E-glass fibers, FRP retrofitting techniques such as hand lay-up are more commonly used for field applications. Surface quality and epoxy impregnation procedures vary considerably between these techniques.
- The signal-to-noise ratio is another limiting factor for this technique. Further studies in terms of de-noising algorithms and the use of selected frequency filters must be undertaken before this technique can be used reliably.
- While the AE emission technique has shown potential for real-time monitoring of FRP-confined concrete columns, NDE assessment of damage or defects in the concrete core without previous monitoring is still needed.

Due to the important information extracted from these results, further discussion of the AE method for damage monitoring in FRP-confined concrete is provided in Section 3.3.4.

Radar Microwave – Zoughi and Bakhtiari (1990)

Zoughi and Bakhtiari (1990) developed a microwave NDE methodology for detecting delaminations in layered dielectric slabs. The methodology relies on the phase properties of measured EM wave reflection coefficients. The layered material system, however, must be backed by a conduction plate. Applicability of the technique is limited to lossy dielectric materials provided adequate penetration of EM waves into the different dielectric material layers. The experimental set-up consisted of a microwave sweep oscillator, a network analyzer, and isolator devices. The dielectric samples were placed in the far-field to obtain a uniform plane wave scenario. Experimental measurements at X-band frequencies were obtained on bi-layer materials combinations of plexiglass and synthetic rubber as a function of increasing air gap (delamination). The experimental results were in good agreement with theoretical estimates.

Advantages

- The experimental set-up is relatively simple and could be applied to cases in which the specific arrangement of layered dielectric slabs and a conducting plate are used.
- A similar approach could be used for determining thicknesses of dielectric slabs (Zoughi and Lujan 1990).

Disadvantages

- The need of a conducting plate as part of the layered material system imposes a condition which might not be satisfied for a significant number of FRP/concrete systems such as FRP-confined concrete columns or FRP-retrofitted beams.
- Interpretation of phase information obtained from reflection coefficients is dependent on the a priori knowledge of the permittivity properties of the slabs under investigation.

Radar Microwave – Feng et al. (2002)

Feng *et al.* (2002) have developed an EM imaging technology for detecting air voids and debonding between the FRP jacket and concrete column. The proposed technology is based on the analysis of reflections of a continuous EM wave sent toward and reflected from the FRP-concrete medium. To mitigate the significant difference in signal intensity between the reflections from voids and debonding compared to that from the FRP jacket, a lens focusing approach was proposed. This approach focuses the EM waves onto a point at the FRP-concrete interface using dielectric lenses specifically manufactured.

Advantage

- Readings for reflections of EM waves using the lens focusing set-up provided evidence of manufactured voids and debonding defects.

Disadvantages

- All tests were conducted using specimens with one or two voids artificially introduced with known locations and size. No tests were conducted on damaged concrete previously subjected to mechanical loads to realistically search for damage levels and/or locations.
- Data processing scheme is elementary (simply a representation of raw data), which ultimately does not provide any information about the depth location of the defects.
- The microwave lens is a passive device and may suffer from power attenuation.
- The experimental set-up requires measurements in a point-by-point basis using a predefined grid, as seen in Figure 2-15, which might make this method not suitable for field application.

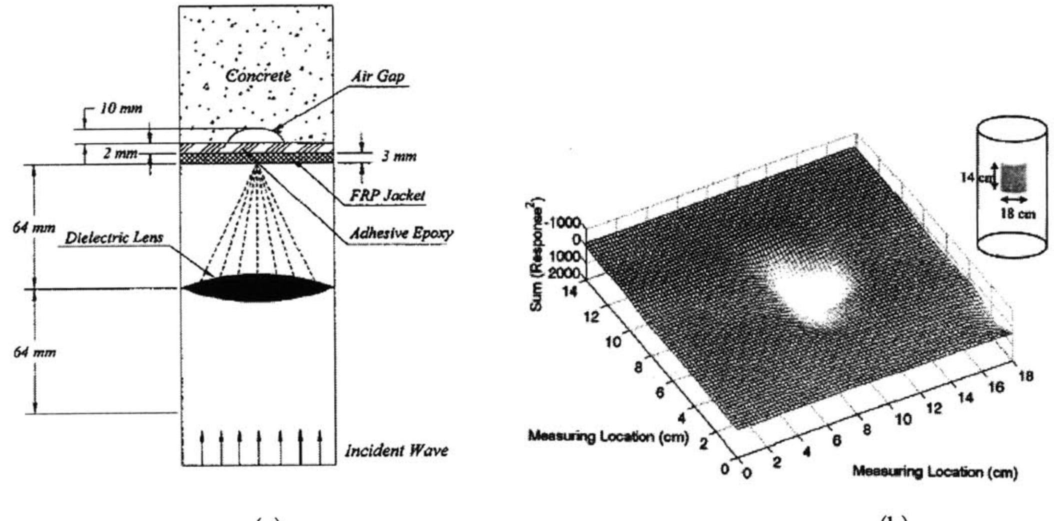

(a) (b)

Figure 2-15 (a) Schematic of numerical modeling, (b) Results of scanned image of a void caused by a hole in the concrete surface (Feng *et al.* 2002).

2.5.4 Radar Microwave – APS-CW Technique for NDE of FRP-Confined Concrete Columns

A recent development from the IST Group (IST Group 2005) called the Automatic Progressive Stepping – Converging Wave (APS-CW) technique has been proposed as an alternative to the lens focusing method previously discussed. The proposed method focuses the measured EM waves by means of data processing of the coherent scattering signals recorded at multiple locations around test specimens. At each location, a horn antenna transmits wide-band EM waves with a beam pattern covering partial areas of interest. With a predetermined step size (or number of antenna locations), the antenna moves circumferentially in a progressive manner. The proposed method is implemented in laboratory conditions using an Inverse Synthetic Aperture Radar (ISAR) approach. In the ISAR set-up, the object rotates using a turntable, while the radar set-up is stationary. The ISAR set-up is more efficient for laboratory conditions, while it is equivalent to the APS-CW method. Figure 2-16 illustrates the APS-CW technique with a mono-static set-up for the assessment of a typical FRP-confined concrete column, where P_1 through P_N represent the measurement points. Exploratory research on the laboratory application of this radar NDE methodology is presented in Chapter 5 of this thesis, which documents its preliminary implementation for the detection of artificial defects and mechanical damage in FRP-confined concrete specimens.

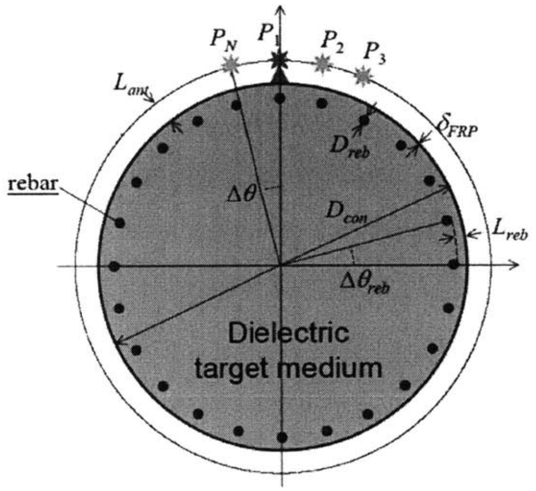

Figure 2-16 Schematic of the APS-CW technique

Chapter 3

Mechanics and Damage Behavior in FRP-Confined Concrete

The objective to this chapter is to shed light on the topic of the mechanics and damage behavior in FRP-confined concrete systems. While extensive research on the global mechanical behavior and ultimate response conditions of FRP-confined concrete column elements under compressive loads has been conducted in the past two decades, definitive postulates regarding the levels or extent of damage in the concrete core are still lacking. This chapter begins with a review of general cases of multi-axial stress states in concrete systems. Topics such as active and passive confinement of concrete and deformation behavior and damage characterization of concrete under multi-axial stress states are presented and reviewed. A brief description of FRP-confined concrete column systems is then presented, followed by a comprehensive review of the state-of-the-art work for FRP-confined concrete in terms of load-deformation behaviors, analytical modeling, and failure mode characterization. Existing research addressing damage extent and evolution in these systems is also reviewed. Experimental studies on mechanical behavior of FRP-wrapped concrete cylinders were conducted. The first objective of these experiments was to develop a physical and mechanistic understanding of the behavior of a particular FRP-confined concrete system composed of plain concrete cylinders wrapped with glass FRP (GFRP) fabrics. Based on these results, the experimental program was then extended to the conditioning of the mentioned laboratory specimens at specific intermediate levels of mechanical damage. Observations of intact and mechanically damaged concrete cores using visual inspection and optical microscopy techniques are detailed in this chapter. Knowledge developed through these studies directly contribute to the interdisciplinary research approach postulated in Chapter 1 regarding the development of a radar NDE methodology for damage assessment of FRP-confined concrete column elements.

3.1 Multi-Axial Stress States in Concrete

Before a detailed discussion of the mechanical behavior of FRP-confined concrete systems, adequate understanding of the mechanics and damage behavior of plain concrete subjected to multi-axial states of stress is needed. In particular, multi-axial compression of plain concrete is examined in the following sections since such general stress state is encountered when investigating the mechanical behavior of FRP-confined concrete column members subjected to compressive loads.

3.1.1 Modeling Concrete under Multi-Axial Compression

In order to understand the behavior of concrete subjected to multi-axial compression, van Mier (1997) used a simple model referred to as particle stack model. In Figure 3-1 (a), a cluster of interacting aggregate particles imbedded in a matrix material is shown. Concrete can be modeled as a stack of particles which will develop splitting tensile forces in the material structure upon application of external compressive stresses. Such splitting forces are presumed to act as the driving forces for processes leading to fracture. In a closer look, the interactions between four aggregate particles subjected to a biaxial compression stress state are presented in Figure 3-1 (b).

In contrast to the uniaxial compression case (*i.e.* $P_2 = 0$), the application of an external compressive stress σ_2 mitigates the wedge splitting forces resulting from the

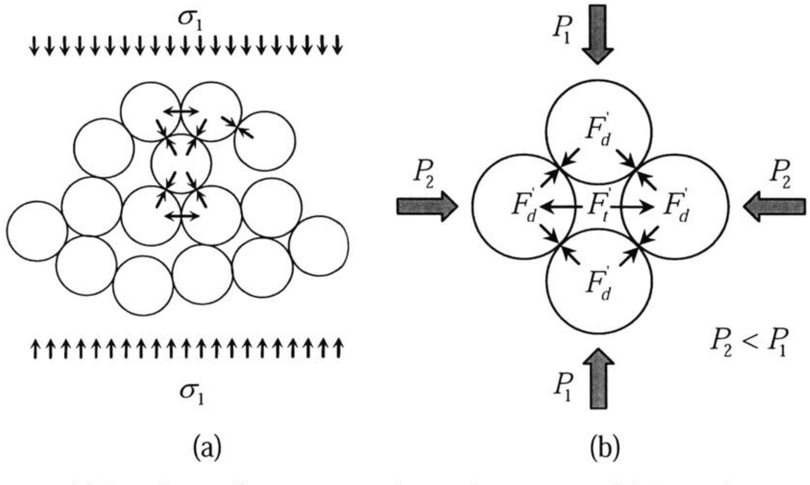

Figure 3-1 (a) Load transfer in a particle stack scenario (b) Particle interactions under biaxial compression (van Mier 1997) application of the perpendicular stress σ_1. For a triaxial compressive stress state, the same mechanism is developed when another confining stress σ_3 is applied in the out-of-plane direction. In this case, splitting tensile forces are further reduced due to the confinement effect provided by stresses σ_2 and σ_3. Thus, a higher external stress σ_1 will be required to produce failure in the composite system.

3.1.2 Nonlinear Stress-Strain Behavior for Uniaxial and Triaxial Compressive Stress States

The stress-strain behavior of concrete, which is considered a quasi-brittle material, is affected by the development of micro- and macrocracks in the body of the material. Even before concrete is subjected to external loading, large numbers of microcracks are present at the interfaces between coarse aggregates and mortar. The microcracking phenomenon is produced as a result of various mechanisms such as segregation, shrinkage, and thermal expansion in the cement paste. Further microcracking processes may occur at the aggregate-cement paste interface, which is regarded as the weakest interface in the concrete composite system, upon the application of external loading. Visibility of microcrack development is then directly related to the application of further external loads. Progression of microcracks becomes a leading factor to nonlinear stress-strain behavior of concrete (Chen and Han 1988).

Figure 3-2 shows typical axial stress – axial strain and axial stress – lateral strain curves for a uniaxial compression test. According to Kotsovos and Newman (1977), there are three distinct deformation stages generally observed in the mentioned test. The first stage extends from the unloaded state up to 30% of the compressive strength of concrete, $f_c^{'}$. The stress-strain behavior for this stage is characterized as linearly elastic since cracks existing in concrete prior loading remain approximately unchanged. The second stage extends between 30% to 75% of $f_c^{'}$. This stage is characterized by increases in length, width, and number of bond cracks. However, crack propagation is still considered stable until reaching a stress level of 75% of $f_c^{'}$, which is generally labeled as the onset of unstable fracture propagation. Material nonlinearity becomes evident in this second stage due to significant crack development. The third stage extends from 75% of $f_c^{'}$ until

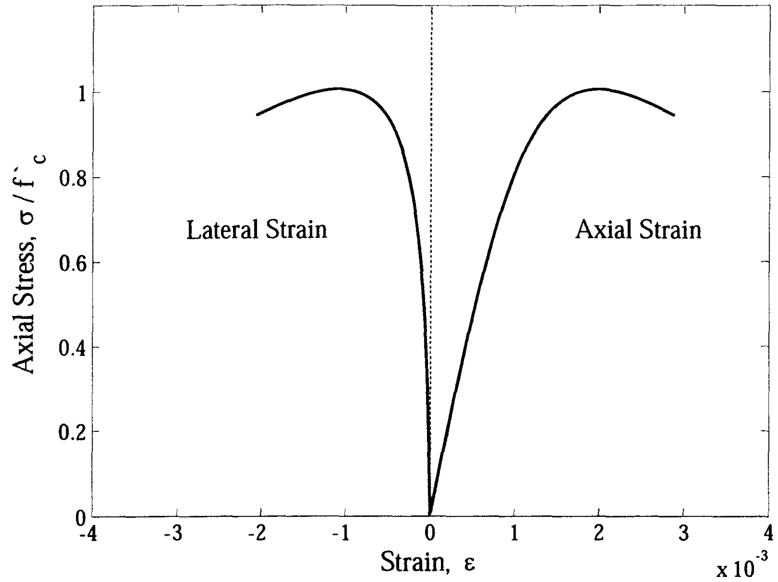

Figure 3-2 Typical stress-strain curves for uniaxial compression

failure of the specimen. At this stage, unstable fracture of concrete is primarily related to crack development in the mortar. Mortar cracks join bond cracks at the surface of adjacent aggregates forming crack zones. The previously smooth deformation behavior may now be distorted, and subsequent deformations tend to be localized. At last, major cracks develop parallel to the applied load to finally cause global failure of the specimen. While the previous discussion applies to the case of uniaxial compression, the three deformation stages (*i.e.* linear elastic stage, inelastic stage, and localized stage) can also be qualitatively identified in multi-axial loading cases for moderate confinement levels. Figure 3-3 shows the axial stress – axial strain $(\sigma_1 - \varepsilon_1)$ and the axial stress – lateral strain $(\sigma_1 - \varepsilon_2)$ curves for concrete subjected to various levels of confining (lateral) pressure (Palaniswamy and Shah 1974). The results were obtained from testing of cylindrical specimens using a triaxial cell. Due to symmetry, the cylinders were subjected to constant lateral pressures, $\sigma_2 = \sigma_3$. Based on the experimental results, it is concluded that the confining pressure significantly alters the deformation behavior of the concrete specimens. Larger strains were observed in the case of confined concrete specimens in comparison to the uniaxial compression case (Chen and Han 1988).

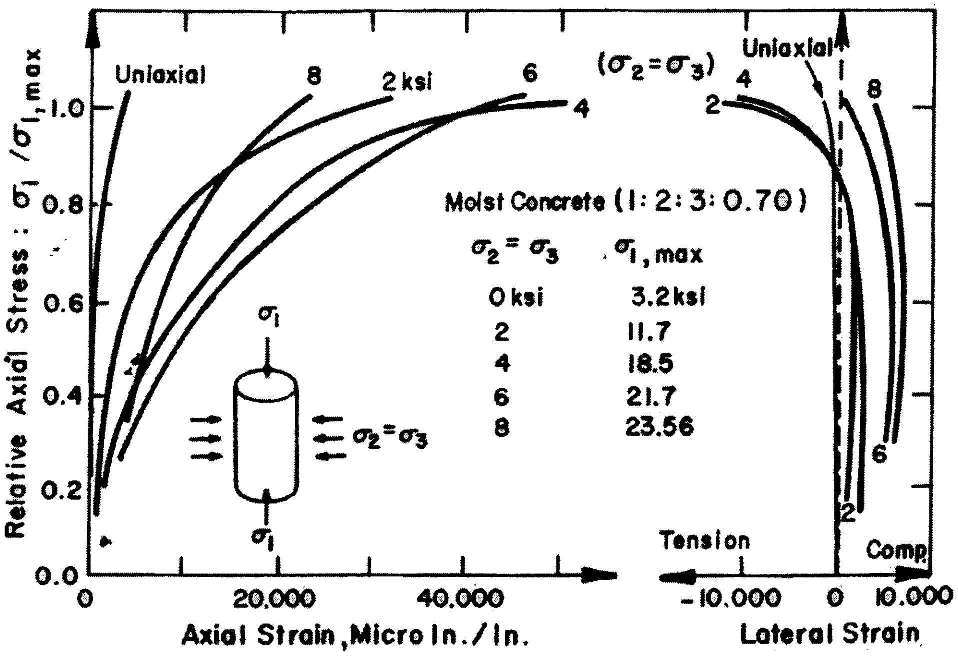

Figure 3-3 Stress-strain curves under multi-axial compression (Palaniswamy and Shah 1974)

3.1.3 Active and Passive Confinement in Concrete

In addition to these introductory sections aiming at establishing an adequate theoretical background of the mechanical and damage behaviors of FRP-confined concrete through introducing general concepts of multi-axial stress states in concrete, the topics of active and passive confinement must also be clearly defined and understood. Research endeavors such as those of Palaniswamy and Shah (1974), Richart *et al.* (1928), Mills and Zimmerman (1970), Pantazopoulou (1995), and Imran and Pantazopoulou (1996) have focused on the study of compressive behavior of concrete under active confinement. Active confinement is accomplished by maintaining a constant level of confinement stress in the concrete specimen. An example of an active confinement test is the compressive testing of concrete cylinders using a triaxial cell. Figure 3-4 shows a schematic of a triaxial cell testing device. Such device allows for the application of confinement stress through pressurized oil, while allowing the application of axial loading.

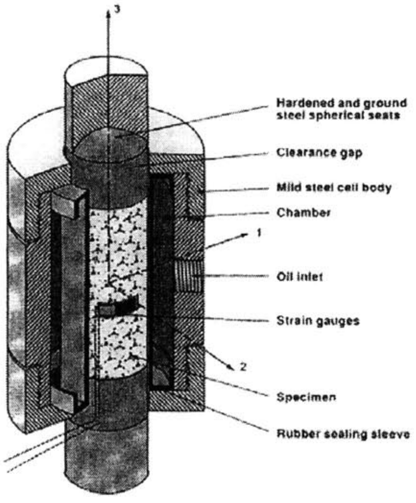

Figure 3-4 Triaxial testing device (Imran and Pantazopoulou 1996)

Active confinement of concrete was first studied by Richart *et al.* (1928), who proposed the well-known empirical formulas:

$$f'_{cc} = f'_c + 4.1 \cdot f_l \tag{3.1}$$

$$\varepsilon_{cu} = \varepsilon_{co}\left(1 + 20.5\frac{f_l}{f'_{co}}\right) \tag{3.2}$$

where f'_{cc} = ultimate confined compressive strength of concrete, f'_c = unconfined compressive strength of concrete, f_l = lateral (radial) confining pressure on the concrete core, ε_{cu} = peak confined axial strain, and ε_{co} = unconfined peak axial strain of concrete. While later experimental research results and analytical modeling efforts suggest modifications, the basic forms of these expressions are still used.

For the cases of conventional reinforced concrete (RC) and FRP-confined concrete, the confining action is of the passive type. Confining pressure is activated by the transverse dilation of the concrete core resulting from principal axial strains (Poisson's effect). Passive confinement could also be characterized as constant and variable through the axial load history (Harries and Kharel 2003). Constant confining pressure is found in concrete reinforced by conventional transverse steel, where this confining material behaves in a plastic manner. Variable confining pressure is found in FRP-confined concrete, where the FRP confining material has a considerably high stiffness. A more elaborate discussion on the mechanical behavior of concrete subjected to compressive loads and passively confined using FRP composites as the confining materials is presented in Section 3.2.

3.1.4 Deformation Behavior and Damage Characterization of Concrete under Multi-Axial Stress States

After studying and differentiating the effects of active and passive confinement types on concrete behavior, the role of deformation in damage characterization for multi-axial stress states is discussed. The mechanical response of concrete to triaxial stresses is governed by several material, load, and geometric parameters. However, the understanding and modeling of such response has not been a simple task due to the failure in appropriately isolating all significant parameters. According to Imran and Pantazopoulou (1996), previous research has primarily focused on strength parameters, which resulted in the established practice of defining the triaxial response in stress coordinates (*e.g.* yield and failure envelopes). Only a small number of comprehensive experimental results on deformation and damage characteristics have been reported in existing research.

Research results have demonstrated that damage in concrete caused by microcracking is exhibited by volumetric expansion or dilation of the material (Pantazopoulou and Mills 1995, Imran and Pantazopoulou 1996, van Mier 1997), which can be quantified in terms of volumetric strains (*i.e.* volume increment per unit of initial volume). However, partial or total restraint against expansion through the imposition of boundary conditions has a significant influence on the internal states of stress in the material (Pantazopoulou 1995, Imran and Pantazopoulou 1996). In order to quantify the residual stiffness and strength of concrete subjected to arbitrary stresses and boundary conditions, analytical models have been proposed based on strain measurements and kinematic restraint information (Pantazopoulou 1995). Thus, volumetric strain measurements capturing the volume changes in concrete developed through mechanical loading are considered important quantifiers of the history of damage accumulated in the material microstructure.

In order to illustrate how the progressive damage in the microstructure characterizes the response of concrete to mechanical loading through cracking and volumetric expansion processes, the results obtained by Imran and Pantazopoulou (1996) for a compressive experimental study plain concrete under triaxial stress and active confinement are presented. The test program was specifically focused on the deformation aspects of the mechanical response and damage buildup, and it consisted of 130 different tests. Testing was performed on plain concrete cylindrical specimens using a triaxial cell device. Core samples of 115 *mm* length by 56 *mm* length were extracted from larger cylindrical specimens to ensure homogeneity of the concrete material. While enclosed in the cell, a specimen was loaded axially under displacement control. The main parameters considered in this study were: water-to-cement ratio (*w/c*) of the concrete mix, moisture content, level of confining stress, and load path. The results of the investigation revealed a consistent relationship between the volumetric strain history and the characteristics of the compressive axial stress – axial strain curves. Figure 3-5 presents a schematic of the shape of the volumetric strain curves for axially loaded concrete subjected to different confinement levels, where σ_3 = compressive stress in the axial direction, ε_3 = axial strain, $\varepsilon_v = \varepsilon_1 + \varepsilon_2 + \varepsilon_3 =$ volumetric strain, $\varepsilon_{A3} =$ area strain or strain of cross section supporting the load at an axial strain of ε_3, and $\nu =$ Poisson's ratio.

Under ideal elastic conditions, the volumetric strain ε_v is contractive for the case of uniaxial stress, and it is given by $(1-2\nu)\varepsilon_3$ (refer to Figure 3-5). However, the $\varepsilon_v - \varepsilon_3$ relationship becomes nonlinear during the actual response of concrete, and eventually becomes expansive beyond the point termed $\varepsilon_3^{\ 0}$. The descending branch of the axial stress – axial strain curve is associated with the phase of volumetric expansion. Additionally, the area strain ε_{A3} increases at an associated rate compared to the rate of softening of the stress – strain curve. The area strain represents the coordinate bound between the $\varepsilon_v - \varepsilon_3$ curve and a 45 degree line in the contractive quadrant. Based on these concepts, $\varepsilon_3^{\ 0}$ represents the critical point where the area strain is equal in magnitude to the imposed axial strain, separating the regions of volumetric compaction and volumetric dilation. Consequently, $\varepsilon_3^{\ 0}$ characterizes a strain threshold beyond which the strength of the concrete decreases from its ultimate value (Pantazopoulou and Mills 1995).

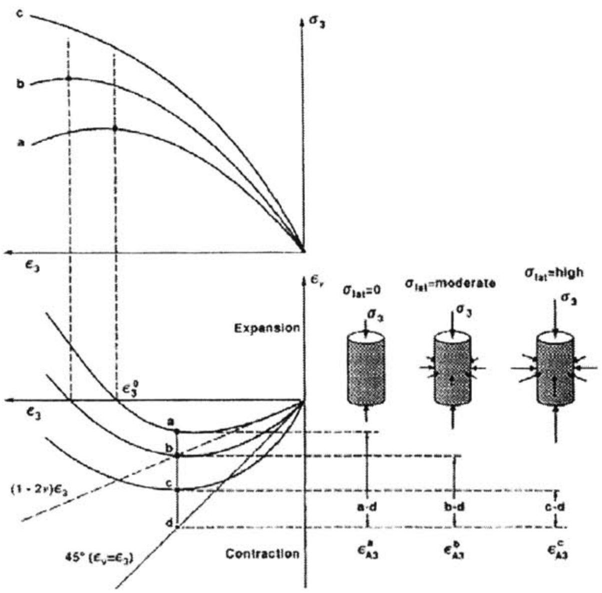

Figure 3-5 Geometry of volumetric strain plots for axially loaded concrete subjected to different levels of confinement (Imran and Pantazopoulou 1996)

Although this previously mentioned study dealt with the investigation of compressive behavior of concrete under active confinement, important information can be inferred from the research results. The strength of concrete specimens tested under triaxial states of stress was primarily limited by the initiation of volumetric expansion. Hence, establishment of the volumetric changes (volumetric strains) becomes one of the key variables in characterizing the mechanical and damage behaviors of concrete material.

3.2 Concrete Confined with FRP Composite Materials

3.2.1 Confinement Mechanics of Circular Column Elements

The confining action in a FRP-confined concrete column element can be schematically illustrated in Figure 3-6. From mechanical analysis, the lateral (radial) confining pressure acting on the concrete core, f_l is defined as:

$$f_l = \frac{2 f_h t}{D} \tag{3.3}$$

where f_h = tensile stress in the hoop direction of the FRP jacket, t = thickness of the FRP jacket, and D = diameter of the confined concrete core. Eq. 3.3 is a rearranged version of the well-known vessel formula which assumes a constant hoop stress over the thickness of the confining material (in this case, the FRP jacket). This solution is restricted to a thin wall scenario, with $2t/D << 1$ (Gere 2000). Assuming that the FRP jacket is stressed in hoop tension only and based on the linear elastic behavior on FRP, the hoop stress in the FRP jacket is proportional to the hoop strain by:

$$f_h = E_{FRP}\varepsilon_h \tag{3.4}$$

where E_{FRP} = elastic modulus of the FRP laminate.

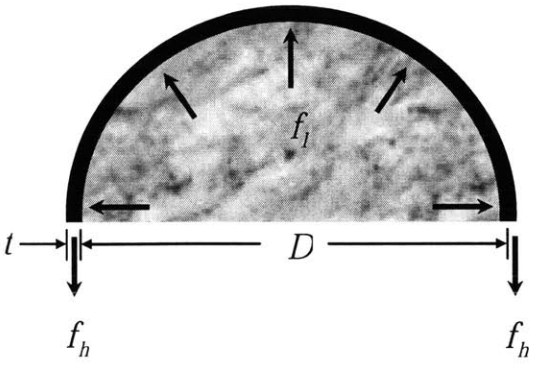

Figure 3-6 Lateral (radial) and hoop stresses present in confining action

3.2.2 Stress-Strain Response

Extensive research has been conducted to characterize the stress-strain response of FRP-confined concrete column members. For the vast majority of test results, it is well established that such response features a monotonically ascending bi-linear shape. This type of stress-strain response is termed as increasing type (Lam and Teng 2003, Au and Büyüköztürk 2005). Test specimens featuring the mentioned response reach their ultimate compressive strength and ultimate strain at the same point and are also significantly improved in comparison with the ultimate stress and strain found in unconfined concrete. However, a post-peak descending branch has also been observed by several researchers (Demers and Neale 1994, Xiao and Wu 2000, Au and Büyüköztürk 2005). This type of stress-strain response, which is termed as increasing-decreasing type, is characterized by minimal strength enhancement, and it was observed by Au and Büyüköztürk (2005) when studying the effects of FRP ply orientation and mix configurations in FRP-confined concrete. The increasing and increasing-decreasing types of stress-strain behaviors are sketched in Figure 3-7.

For the case of load-deformation behavior of the increasing type, the FRP-concrete composite system shows a strain hardening action at the composite system level. The distinctive bi-linear behavior is characterized by a second branch in the stress-strain curve with reduced stiffness compared to the first branch. The point of transition between the two branches of the stress – strain curve has been noted as kink point (Howie and Karbhari 1995, Lau and Zhou 2001, Au and Büyüköztürk 2005). Beyond the kink point, a steady increase in stress is observed and continues until complete failure of the specimen under test. Another important issue when investigating the behavior of FRP confined concrete is the choice of fiber reinforcement. As already noted in Chapter 2, FRP jackets for civil engineering applications are commonly manufactured out of carbon (CFRP) or glass (GFRP) reinforcing fibers. Due to their different strength and deformation properties, the stress-strain responses for CFRP and GFRP-confined concrete differ considerably. Lam and Teng (2004) conducted a series of experiments to investigate ultimate performance conditions in terms of compressive strength and strain for carbon and glass FRP-confined concrete specimens. Selected results from the experiments are shown in Figure 3-8. Due to the inherent differences in the material properties (CFRP

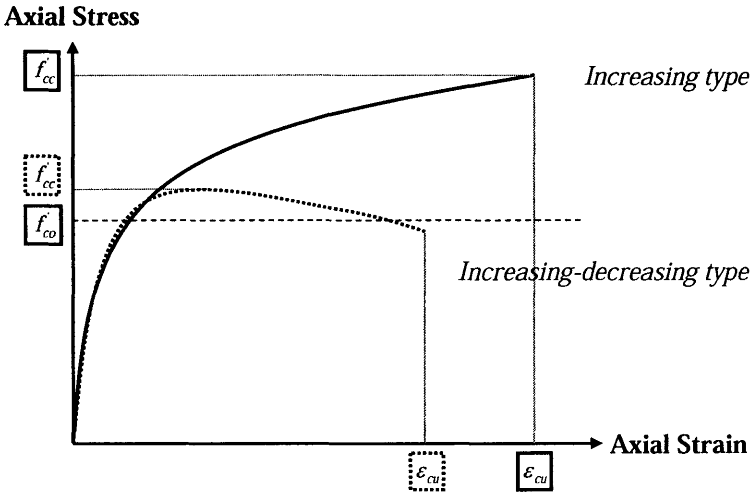

Figure 3-7 Stress-strain curves for FRP confined concrete for increasing and decreasing types (Lam and Teng 2003)

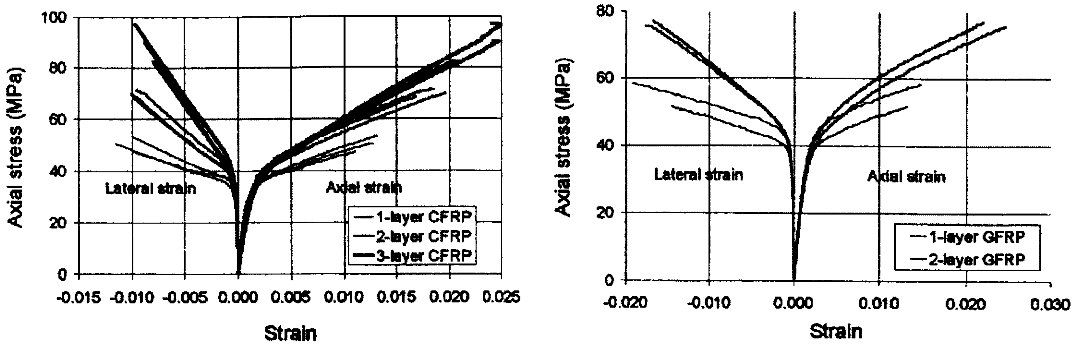

(a) (b)

Figure 3-8 Stress-strain curves for FRP-confined concrete (a) CFRP-wrapped cylinders (b) GFRP-wrapped cylinders (Lam and Teng 2004)

elastic modulus and tensile strength are higher than those of GFRP) and thickness values (thicker GFRP plies) between the CFRP and GFRP composites used in the mentioned studies, it is observed that different load-deformation behaviors are obtained. In practical applications, the use of either composite material for strengthening or retrofitting purposes depends on the specific needs of the project in terms of degree of access to the structural element, target level of confinement, ease of installation, cost of the project, among other considerations. A detailed discussion regarding the particular choice of GFRP for the experimental aspects of this thesis work is provided in Section 3.4.

3.2.3 Failure Modes of FRP-Confined Concrete

Based on a recent study by Au and Büyüköztürk (2005), both brittle and ductile behaviors were observed at ultimate failure states, where the composite system failure was characterized by a sudden reduction in load resistance. In that study, various ply and mix configurations consisting of uni-directional and bi-directional GFRP composite materials were investigated. Specimens with a load-deformation behavior of the increasing type showed a brittle failure mode due to rupture of the FRP in the hoop direction. These specimens were manufactured with at least one uni-directional GFRP ply. FRP jacketing using uni-directional fibers, either CFRP or GFRP, is the most commonly deployed in field applications, and thus, laboratory experiments using such fiber direction configuration have been the most widely conducted. Rupture of the FRP jacket due to hoop tension is the well-known failure mode for the mentioned FRP-confined concrete types of specimens, although premature failure due to debonding of the FRP at the overlap joint has also been reported (Lam and Teng 2003). Ductile failure has been encountered in FRP jackets manufactured with angular fiber wrap configurations, which also show a load-deformation behavior of the increasing-decreasing type. Substantial post-peak straining has been observed for axial and radial directions. Reorientation of angular fibers to align with the hoop stress direction allowed for a more compliant radial dilation (Au 2001).

3.3 Review on Damage Evolution of FRP-Confined Concrete

As it has been discussed in the previous sections, extensive work has been conducted by the research community to further improve the understanding of the mechanical behavior and ultimate failure conditions of FRP-confined concrete column elements. However, studies dealing with specific issues such the extent and evolution of the damage processes in the concrete core of the FRP-confined specimen under compression loads are still at initial stages. Existing research addressing these research issues, from various research angles and perspectives, are discussed in this section.

3.3.1 Bi-Linear Behavior of FRP-Confined Concrete and Mechanisms of Confinement

Existing research has generally established the bi-linear character of the stress-strain response of FRP-confined concrete cylindrical specimens subjected to uniaxial compression. It is commonly recognized that the first region of the stress-strain curve is mainly affected by the strength properties of the concrete core due the low level of passive confinement provided by the FRP jacket resulting from the minimal lateral expansion of the specimen under test. However in the second region of the stress-strain curve, the concrete core is commonly believed to be cracked or substantially damaged, allowing the fully activation of the FRP wrapping system (Karbhari and Gao 1997, Toutanji 1999, Lau and Zhou 2001). It has also been hypothesized that a gradually failed brittle zone between the matrix and the aggregates takes place for a load level corresponding to the compressive strength of plain concrete, and that aggregates are heaved and the concrete core becomes a non-cohesive medium for load levels exceeding the compressive strength of plain concrete (Berthet *et al.* 2005).

3.3.2 Kinking Point

Having established the general bi-linear character of the stress-strain response for FRP-confined concrete, researchers have identified the need for better understanding the transition point between the two regions, which has been referred to as kink point (refer to Section 3.2.2). The kink point becomes the stage at which significant axial stiffness reduction begins, as illustrated in Figure 3-9. Au and Büyüköztürk (2005) proposed that this significant reduction in axial stiffness may be a product of the damage occurring at the concrete core level since the FRP jacket is intact, at least from the visual inspection point of view. As noted in that study, the accurate characterization of the kink point is essential for the proper design of FRP-wrapped concrete columns since today's practices in this field mainly consider terminal stress-strain responses under uniaxial compression. Design stresses beyond the kink point stress might not be justified under other different loading conditions (*e.g.* seismic, cyclic).

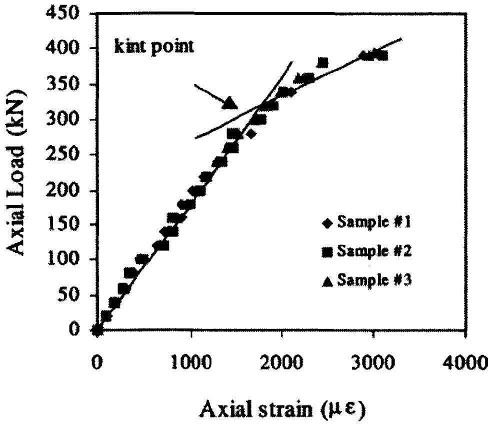

Figure 3-9 Kink point in stress-strain response for GFRP-confined concrete under uniaxial compression (Lau and Zhou 2001).

3.3.3 Localized Damage

For the case of one layer of GFRP-wrapped concrete cylinder specimens, Au and Büyüköztürk (2005) observed severe concrete crushing focalized at the mid-height section of the cylinders, while the concrete core and the FRP jacket above and below the mentioned zone seemed to remain intact. This behavior was attributed to the differential shortening behavior, which is a product of the increase in stiffness at the FRP overlap region in one of the sides of the specimen. Close to ultimate failure, concrete rubbles pushed against the strained fabric locally, which was followed by fiber rupture. The FRP jacket opened up locally, allowing crushed concrete to spall off. Some concrete was also adhered to the fractured portion of FRP after complete failure, as observed in Figure 3-10. Based on the findings of this study, mechanical damage in the concrete core could be localized depending on the size of the specimen, FRP jacket configuration, and loading conditions. However, visual inspection after ultimate failure of the FRP-confined concrete cylinders provided some physical understanding of the state of damage in the concrete core.

Figure 3-10 Localized damage zone in FRP-confined concrete (Au 2001)

3.3.4 Monitoring of Damage Evolution using Acoustic Emission Techniques

Monitoring of damage in FRP-confined concrete using acoustic emission techniques has provided some valuable inside regarding the damage processes occurring in the concrete core and FRP jacket when the specimen is subjected to compressive loading (Mirmiran *et al.* 1999). The cited work used concrete-filled FRP tubes for their experimental program. While this construction technique also uses the same principle of FRP confinement, its mechanical behavior differs from other types of FRP confinement due to the substantial longitudinal stiffness inherent to the tube structure (Lam and Teng 2003). Thus, direct comparability with other FRP retrofitting techniques of concrete columns such as hand lay-up may not be accurate. However, the damage evolution traits observed in this cited work are in line with the proposed damage evolution discussions previously presented. For a brief introduction of the work of Mirmiran *et al.* (1999), refer to Section 2.5.3. Three stages of damage evolution as functions of applied compressive load were experimentally identified, as seen in Figure 3-11. This figure shows a plot of cumulative AE counts versus axial load for a concrete cylinder encased in 6-ply GFRP tube. The three proposed stages in the damage response are:

- *Stage 1:* The initial stage corresponds to a swift propagation of microcracks within the concrete core. A large number of AE counts are observed.
- *Stage 2:* This stable stage is characterized by a gradual increase in AE counts. Existing cracks open at a rate controlled by the stiffness of the FRP tube rather than appearance of new crack formation processes.
- *Stage 3:* This unstable stage is characterized by a rapid increase of AE counts near failure. Several processes take place such as growth of internal cracks, flow of resin, shear cracks in the FRP tubes, and pore compaction in the concrete core.

Having developed a comprehensive theoretical understanding of the state-of-the-art research on FRP-concrete systems regarding several topics such as general stress states in concrete under multi-axial compressive loads, mechanics of concrete under FRP confinement, its load-deformation behaviors, ultimate failure modes, and various research

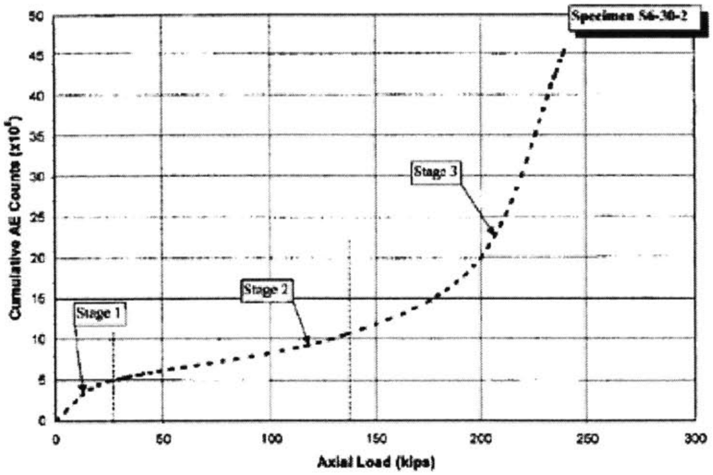

Figure 3-11 Typical variation of cumulative AE counts versus axial load (Mirmiran *et al.* 1999)

initiatives addressing the damage development, evolution, and characterization in such systems, an experimental program dealing with the mechanical behavior and damage characterization of FRP-confined concrete is described in the following sections.

3.4 Experimental Studies on Characterization of Mechanical Behavior of FRP-Confined Concrete

3.4.1 Objective and Overview

This experimental work aims at examining and characterizing the mechanical behavior of FRP-confined concrete members subjected to monotonic concentric axial compressive loading. In particular, this study focuses on normal strength, plain concrete cylindrical specimens wrapped with a one-ply GFRP jacket mounted using wet lay-up installation procedures. The objectives of this experimental study are to obtain an adequate understanding of the mechanical and deformation behaviors of the particular FRP-confined concrete system previously mentioned and to show that specimens manufactured using the procedures hereafter described display a consistent and repeatable performance behavior for the case of monotonic concentric axial loading. The results from achieving the two mentioned objectives will serve as the basis for damage conditioning of the same type of GFRP-concrete specimens and subsequent damage assessment using visual and microscope observations of specimen cross-sections (Section 3.8) and the exploratory radar NDE technology described in Chapter 5.

Test Matrix

Characterization of the mechanical behavior of FRP-confined concrete was performed according to the test matrix described in Table 3-1. In addition to FRP-wrapped specimens, plain concrete specimens were also tested to draw comparisons between the two different types of specimens in terms of strength and deformation behavior. Detailed descriptions of material selection, specimen configuration, instrumentation, and loading conditions related to the compression tests of the specimens described in Table 3-1 are provided in the following sections.

Specimen Type	Individual Notation
Plain concrete	PC01, PC02, PC03
FRP-confined concrete	CC01, CC02, CC03, CC04

Table 3-1 Test matrix for characterization of mechanical behavior of plain and FRP-wrapped concrete specimens

Sign Conventions

As it will be observed in the forthcoming sections, measurements of both axial and lateral (radial) strains were performed. For simplicity and clarity, these measurements are sometimes presented in plots simultaneously. Axial shortening is assigned positive values, while lateral dilation is assigned negative values. The sign conventions will also apply to any subsequent calculations based on these measurements (*e.g.* stress-strain plots, volumetric deformations).

Units

The SI unit system is used for consistency with the radar measurements, dielectric materials property assessment, and electromagnetic wave propagations aspects of this thesis. The following conversion factors may be useful to reader for comparison with the English unit system:

$$1\,MPa = 145.04\,lbf/in^2$$
$$1\,N = 0.22481\,lbf$$
$$1\,mm = 0.03937\,in$$
$$1\,kg/m^3 = 0.062426\,lbm/ft^3$$

3.4.2 Material Selection

Concrete

Normal strength concrete was used throughout the mechanical studies (described in this chapter), electromagnetic property characterization studies (described in Chapter 4), and radar NDE assessment studies (described in Chapter 5). The concrete was produced using mix proportions of Portland cement Type I / sand / coarse aggregate = 1.0 / 2.5 / 3.2 by weight with a water-to-cement ratio, $w/c = 0.60$. Adequate workability and consistency was achieved during the production of the concrete and no admixtures were included in the mixing process. The average 28-day compressive strengths from 100 *mm* diameter by 200 *mm* length cylinder tests and the corresponding standard deviations for each batch of concrete are presented in Table 3-2. The concrete mix characteristics are in line with the works of Rhim (1995) and Au (2001) related to non-destructive evaluation of concrete using wideband microwave techniques and behavior of FRP-confined concrete, respectively. Similar mechanical and electromagnetic properties of concrete between these previous works and the present work are crucial to the use and extension of the existing knowledge base. One important requirement that was accomplished in this work was the need for adequate consistency in material characteristics and mechanical performance among all specimens. This aspect becomes imperative in our efforts to develop fundamental knowledge in terms of damage detection and assessment of FRP-confined concrete systems through studies of artificially-introduced damage (such as air cavities or delaminations) and mechanically-introduced damage scenarios.

Batch	*Mean, μ [MPa]*	*Sta Dev, σ [MPa]*
1	25.8	1.2
2	26.8	1.4
3	25.2	2.0
4	25.0	1.7

Table 3-2 28-day compressive strength values for all concrete batches

Capping Material

Due to the vertical orientation of the molds during specimen manufacturing, the top end of the cylinders used in this study did not have a reasonably flat and smooth surface. Additionally, compressive loading testing requires all cylindrical specimens to have parallel top and bottom surfaces in order to approximately provide a uniaxial loading scenario. Consequently, cylindrical specimens were capped with gypsum-plaster as stipulated in ASTM C617 - 98 (2003). Careful preparation of the capping was necessary to satisfy the 6 *mm* maximum average thickness of the cap.

Cylinder Molds

Two types of molds were used in this study. Cylindrical specimens used for 28-day compressive strength testing for the purposes of checking consistency among batches were cast on 100 *mm* diameter by 200 *mm* length reusable plastic molds in accordance to ASTM C39/C39M - 04 (2004). Cylindrical specimens used for mechanical behavior characterization, both plain and FRP-wrapped specimens, were cast on non-standard 150 *mm* diameter by 380 *mm* length molds. These molds were manufactured using disposable cardboard tubing and a reusable wooden base. The mentioned molds served to provide a poor finish to the specimen surfaces, which in turn would provide adequate bonding between the concrete and FRP materials. The wooden base was design to tightly fit on the tube and thus prevent water leakage.

FRP Composites

All FRP composite materials used in this study were manufactured by Fyfe Co. LLC. The jacketing system used for mechanical behavior characterization of FRP-confined concrete was Tyfo® SEH-51A Composite. This system consists of Tyfo® S epoxy and Tyfo® SEH-51A reinforcing fabric. Tyfo® SEH-51A is a custom wave, unidirectional glass fabric with yellow glass cross fibers at 90°. Tyfo® S is a two-component epoxy matrix material used for bonding applications. The mix ratio prescribed for the epoxy system is 100 component A / 34.5 components B, by weight. The suggested minimum curing time for the epoxy is 72 hours at room temperature. Typical properties of this composite system are provided in Tables 3-3 through 3-5 (Fyfe Co. 2002).

Tensile strength, *GPa*	3.24
Tensile modulus, *GPa*	72.4
Ultimate elongation, %	4.5
Density, g/cm^3	2.55
Weight, g/m^2	915
Fiber thickness, *mm*	0.36

Table 3-3 Typical dry fiber properties

Property	Typical Test Value	ASTM Method
Tg 60° C, post cure 24 hours	82° C	D-4065
Tensile strength, *MPa*	72.4	D-638, Type I
Tensile modulus, *GPa*	3.18	D-638, Type I
Elongation, %	5.0	D-638, Type I
Flexural strength, *MPa*	123.4	D-790
Flexural modulus, *GPa*	3.12	D-790

Table 3-4 Epoxy material properties

Property	Typical Test Value	Design Value	ASTM Method
Ultimate tensile strength in primary fiber direction, *MPa*	575	460	D-3039
Elongation at break, %	2.2	2.2	D-3039
Tensile modulus, *GPa*	26.1	20.9	D-3039
Ultimate tensile strength 90° to primary fiber, *MPa*	25.8	20.7	D-3039
Laminate thickness, *mm*	1.3	1.3	-

Table 3-5 Composite gross laminate properties

3.4.3 Specimens

Cylinder Configuration

The choice for the concrete cylinder configuration was determined after a detailed analysis of several constraints imposed by the interdisciplinary character of this research work. Although this chapter deals with the mechanical response characterization of FRP-confined concrete cylindrical specimens, their geometric and material configurations have a direct impact on the radar NDE exploratory studies described in Chapter 5.

In terms of the geometric configuration, both the diameter and height of the specimens were chosen based on the following considerations. Because of the inherent characteristics of the compressive test set-up used in this study, an elastic mismatch and the presence of frictional forces between the steel plates and the end caps of the cylindrical specimens would interfere with the uniaxial loading character of the test. The mentioned phenomenon imposes additional constraints in the system leading to complex stress states near the ends of the cylinder caps. This is commonly recognized as the main factor for shear cone formation in cylinder compression tests, which ideally would fail under vertical fracture if subjected to pure uniaxial compressive loads. Based on experimental findings developed by several researchers for uniaxial compression testing of concrete prism elements with steel plates, van Mier (1997) concluded that reasonable results could be obtained when the aspect ratio of the specimens is between 2.5 and 3.0. While a direct comparison may not be appropriate, equivalent cylindrical specimens with a height-to-diameter ratio of 2.5 could represent optimal for the proposed work.

Another important factor influencing the response and performance of the FRP-wrapped concrete cylinders is the radius of curvature. Previous research (Yang *et al.* 2001, De Lorenzis and Tepfers 2003, Lam and Teng 2004) has identified the influence of the radius of curvature on the tensile strength of FRP composite jacket. Results indicated that the tensile strength of the laminate decreased with decreasing corner radius (Yang *et al.* 2001). Consequently, the choice for the diameter of the cylinder specimens should be as large as possible to avoid the mentioned losses in strength capabilities of the FRP composite wraps. Directly related to the choice of specimen diameter is the capacity available from the loading device in use. As it will be noted in Section 3.4.5, the Baldwin loading frame could provide compressive forces up to 890 *kN.* Based on the experience gathered from the work of Au (2001) and on the results of preliminary analytical modeling of FRP-confined concrete, the choice of a 150 *mm* diameter cross-section could ensure an adequate strength analysis of the FRP-confined concrete cylinder specimens.

Lastly, important geometrical constraints are related to the experimental set-up used for the radar NDE measurement aspects of this project. As it will be discussed in Chapter 5, radar measurements required the FRP-confined concrete cylinders to have large dimensions in order maximize radar cross section (RCS) signals, while at the same time keep the weight of the specimens bellow 45 *kg* (due to the maximum weight allowed on top of a Styrofoam tower supporting the specimen during measurements). After analysis of all the mentioned geometry-related criteria, cylindrical specimens of 150 *mm* diameter by 380 *mm* length were chosen for mechanical behavior characterization of FRP-confined concrete.

In terms of the material configuration, the choices of plain concrete cylinders or reinforced concrete cylinders were analyzed. Although in field applications reinforced concrete is the necessary choice for column applications, laboratory experimentation with reinforced concrete might not be a feasible choice. Demers and Neale (1999) concluded in their study that compressive testing on FRP-confined plain concrete specimens was sufficient to achieve their research objectives due to the lesser contribution of transverse steel reinforcement in FRP-confined RC concrete specimens as long as the stirrup spacing was medium to large. Consequently, plain concrete specimens are selected for the herein discussed experimental program.

FRP Wrapping Configuration

The choice of one layer of Tyfo® SEH-51A Composite system for confining the concrete specimens is substantiated from two different points of view. From the mechanics point of view, mechanical properties and the number of layers or plies of the FRP laminate directly affect the strength and deformation responses of FRP-confined concrete. Based on previous experience and preliminary analytical modeling, the strength of a specimen manufactured with one layer of GFRP (in this case, Tyfo® SEH-51A) wrapped around the proposed 150 *mm* by 380 *mm* concrete cylinders would almost match the maximum load provided by the loading frame used in this study, and thus it becomes the limiting constraint on the number of plies that could be used. Another aspect related to the FRP wrapping configuration is the appropriate choice for the overlap length. Fyfe Co. LLC suggests an overlap length of at least 150 *mm* in the primary fiber direction (Fyfe Co. LLC 2005). Such overlap length is assumed effective for appropriate epoxy bond strength and shear transfer developments. However, for the case of a 150 *mm* diameter cylinder, the proposed overlap length would be unrealistic from the perspective of developing a uniformly distributed stress state in the hoop direction of the wrapped specimen. Based on previous experience, an overlap of 75 *mm* would ensure appropriate performance of the specimens, although some minor differential displacements are expected.

From the non-destructive evaluation point of view, the choice of the fiber used for jacketing has a significant influence on the application of a specific type of NDE methodology. Obvious choices for FRP retrofitting of concrete columns are GFRP and CFRP composites. However, the application of radar NDE techniques on CFRP jackets presents additional challenges. As it is discussed in Section 4.5.1, wave propagation through one layer of CFRP fabric shows significant signal attenuation. Consequently, the choice of a glass-based material is justified.

Concrete Casting Procedures

All concrete cylinder specimens were cast in four batches. For each batch, six 150 *mm* × 380 *mm* cylindrical specimens and nine 100 *mm* × 200 *mm* cylindrical specimens were cast. All casting procedures were in accordance with ASTM C192/C192M - 02 (2002). A power-driven concrete mixer was used. Plastic sheets were used to cover the specimens to keep them moist until demolding. The cast specimens were allowed to cure for a 24-hour period in the molds. After demolding, the specimens were submerged in a water bath for a 7-day curing period, after which they were left to cure at room temperature until completing the 28-day curing period. Compressive tests on 100 *mm* × 200 *mm* cylinders were conducted within eight hours after the 28-day curing period. The results of compression tests are tabulated in Table 3-2. Specimens were then capped and wrapped with FRP composite.

FRP Composite System Installation

The installation of the FRP composite system onto the concrete cylinders was conducted in accordance with the Quality Control Manual for the Tyfo® Fibrwrap® System (Fyfe Co. 2005). Additionally, relevant questions about specific installation issues were appropriately addressed by the engineering team at Fyfe. Co. LLC. The first step in the installation process was the surface preparation. For the case of column applications, the surface shall be free from fins, sharp edges, and protrusions that could cause air voids or damage the fibers. Although large voids or uneven surfaces would have to be filled with epoxy filler, small pinholes or micro-bubbles in the concrete surface do not require special detailing, which implied that our specimens did not require any epoxy filling. The surfaces had to be free of moisture before application. The specimens were hand cleaned to remove any dust. Following the cleaning process, one prime coat of thickened Tyfo® S epoxy was applied to the concrete surface. To prepare the epoxy matrix, the two components were uniformly mixed with a mechanical mixer for approximately five minutes at 400 *rpm* (see Figure 3-12). Based on the experience of the manufacturer, the expected workable time for the epoxy mix is approximately three hours. After application of the prime coat, the specimens were left to cure for approximately one hour.

The second step in the installation procedure was the fabric saturation. The FRP fabric sheets were cut to the appropriate lengths. Because of the size of the experimental program, manual saturation was suggested without compromising the quality of the final outputs. The pre-cut fabric sheets were placed in a saturation bath frame. The epoxy was then worked into the fabrics using a paint roller.

The last step was the saturated fabric installation using the wet lay-up technique.

(a) (b)

Figure 3-12 FRP composite system installation (a) Mixing of epoxy resin
(b) Samples curing after installation of epoxy jacket

After the fabrics were saturated with epoxy from both sides, they were rolled in such a way that during installation the fabrics will be unrolled while being placed around the concrete cylinder with a constant pull. Hand pressure was applied to ensure good adhesion between the saturated fabric and the prime coated concrete surface and to prevent the formation of air voids. The cylinders were watched for approximately one hour to check that overlaps were perfectly adhered. As suggested by the manufacturer, the specimens were allowed to cure at room temperature for 72 hours.

3.4.4 Instrumentation

The data acquisition system consisted of a desktop computer, data acquisition software, and a connection box, which served as the interface between all measuring devices and the computer. This system collected displacement and load measurements from all linear variable displacement transducers (LVDTs), extensometers, and the load cell in real time with a logging time step of one second. The basic measurement principle for all devices was the differences in voltage due to load and displacement changes. All the devices were calibrated and tested before the experiments. A picture of the data acquisition is presented in Figure 3-13.

Two Trans-Tek LVDTs were used to record the radial expansion of the cylinder specimens. The LVDTs were mounted on especially-designed spring systems. A sketch of the spring system is shown in Figure 3-14. Measurements of radial expansion were recorded with the LVDTs at mid-height and at 50 *mm* bellow mid-height level. Axial displacements were recorded with two 90 *mm* extensometers, one placed on the overlap region, and the other place 180° apart from the first one. Both extensometers were placed at mid-height level with the aid of rubber bands to prevent any slippage. A picture of the instrumentation mounted on a FRP-confined concrete specimen is provided in Figure 3-15.

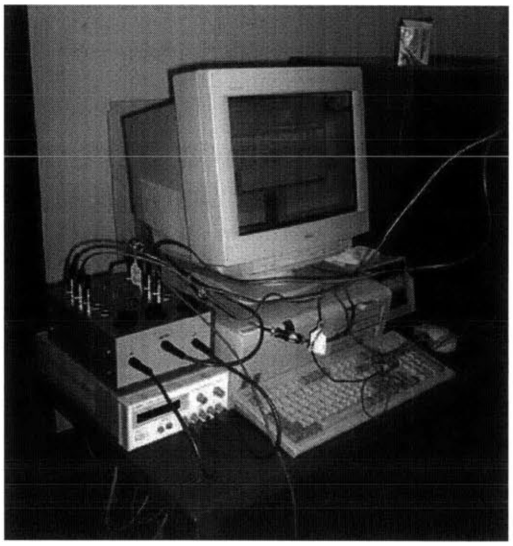

Figure 3-13 Data acquisition system

3.4.5 Loading

Compressive load testing under monotonic conditions was accomplished with the aid of a Baldwin 890 *kN* loading frame. The load frame operates based on hydraulic principles and it is controlled through a computer interface. During testing, the crosshead remains stationary while the platform moves upward to provide compressive loads. The steel plate attached to the crosshead of the loading frame can be adjusted to be fixed or released for free rotational motion. For the case of this work, the plate was allowed free motion in

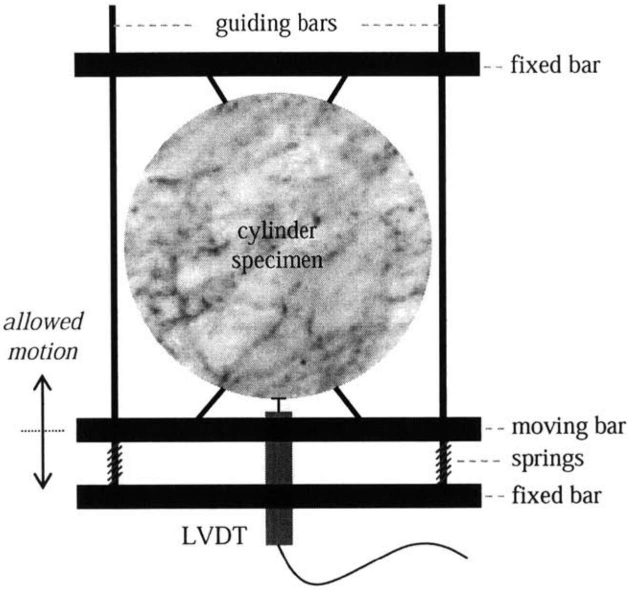

Figure 3-14 LVDT mounting system

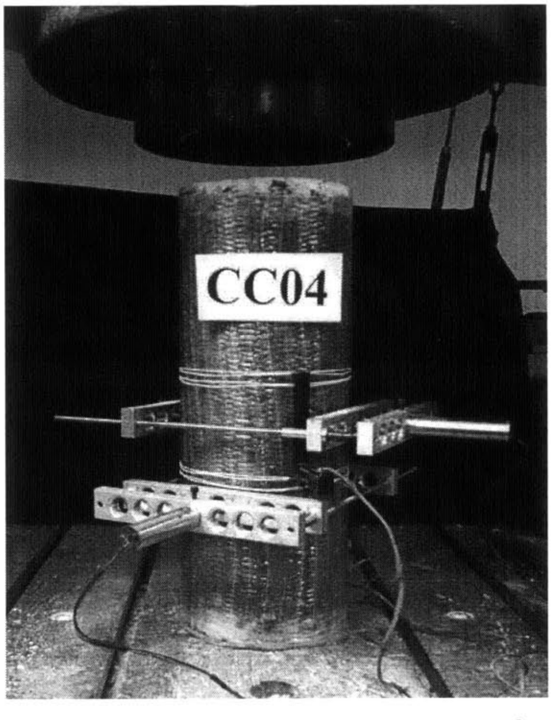

Figure 3-15 Set-up for instrumentation mounted on a FRP-confined concrete specimen

order to capture any differential motions due to the overlap in the FRP jacket. The two basic modes of operation are load-control and displacement-control testing. For this study, displacement-control was chosen in order to capture the plastic deformation of the FRP-confined concrete specimens. The load displacement rate was adjusted to 1.27 *mm/min*. Figures 3-16 shows a picture of the loading frame.

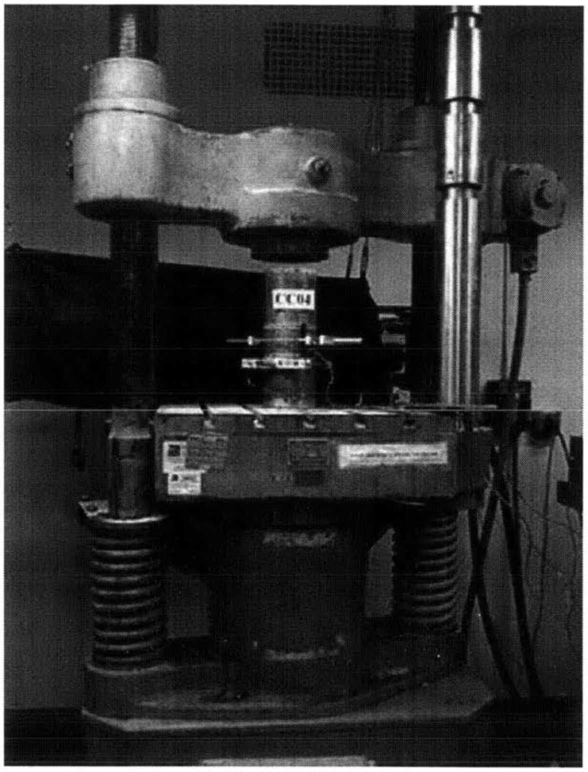

Figure 3-16 Baldwin loading frame

3.5 Experimental Results of Mechanical Behavior of FRP-Confined Concrete

3.5.1 Load-Deformation Behavior

The fundamental tool for characterizing the mechanical performance of the plain concrete and FRP-wrapped concrete specimens is the construction of the stress-strain curves using the data from axial load, axial deformation, and lateral deformation measurements. Figures 3-17 through 3-20 show the stress-strain curves for the specimens detailed in Table 3-1. The PC-series correspond to plain concrete specimens, and the CC-series

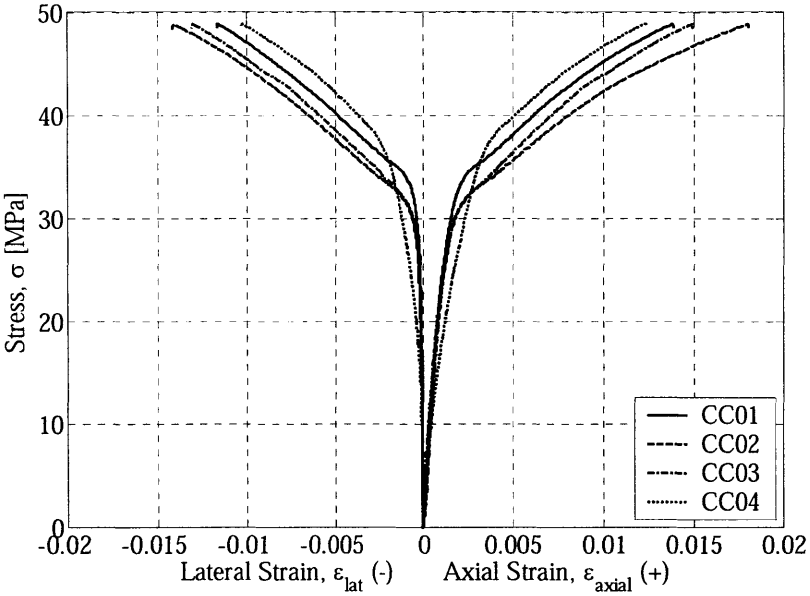

Figure 3-17 Axial stress – axial strain and axial stress – lateral strain curves for FRP-wrapped concrete specimens

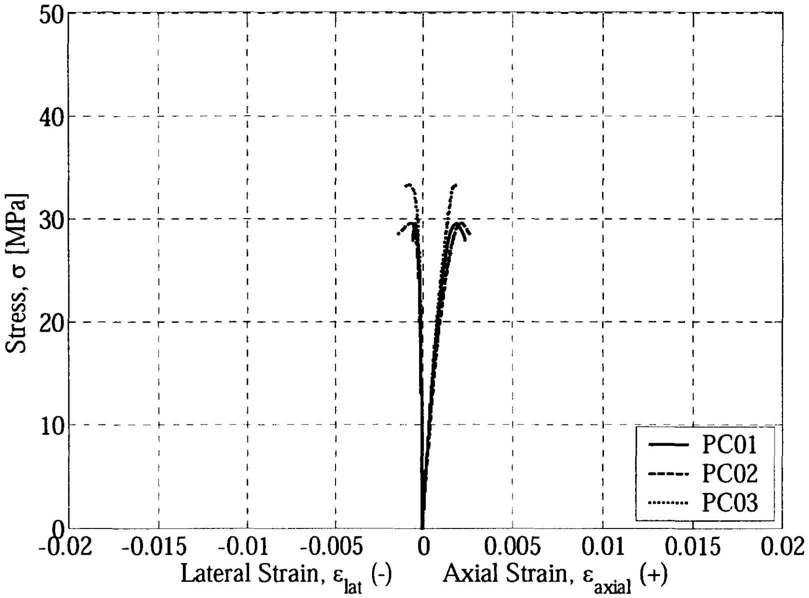

Figure 3-18 Axial stress – axial strain and axial stress – lateral strain curves for plain concrete specimens

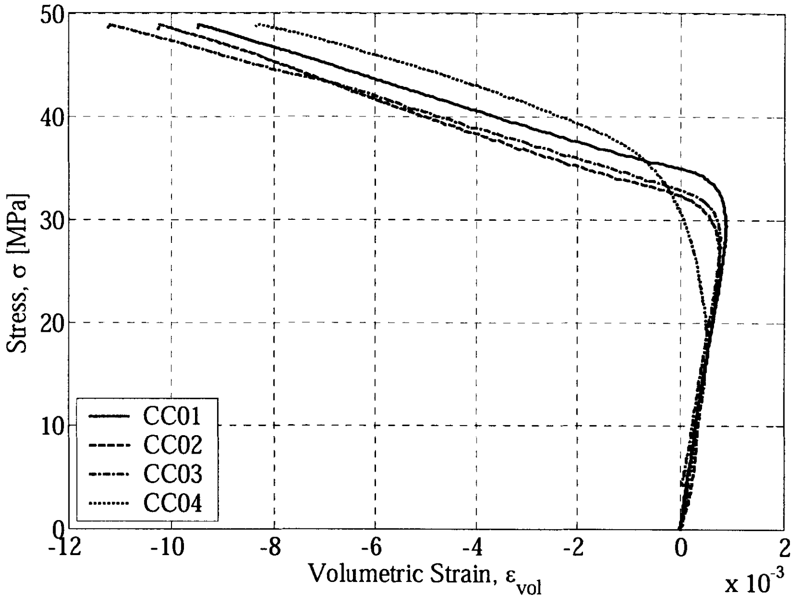

Figure 3-19 Axial stress – volumetric strain curves for FRP-wrapped concrete specimens

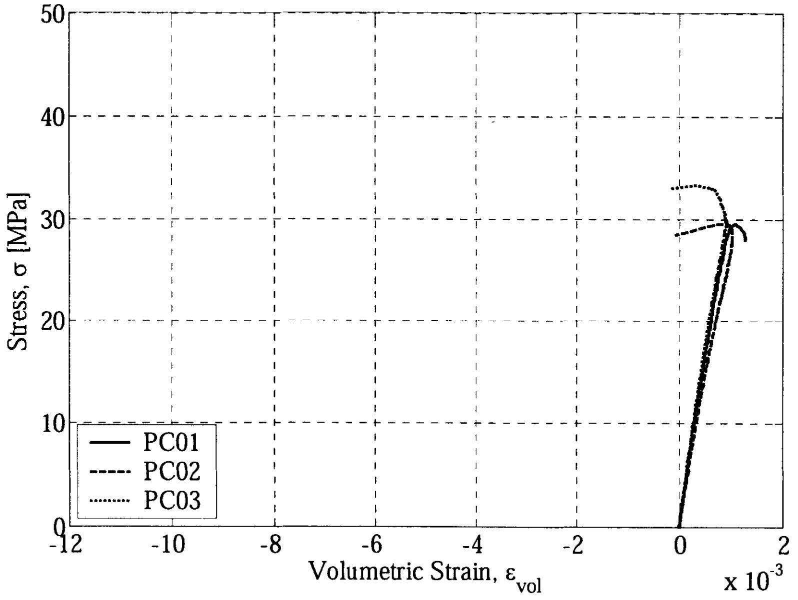

Figure 3-20 Axial stress – volumetric strain curves for plain concrete specimens

correspond to FRP-wrapped concrete specimens. In Figures 3-17 and 3-18, the curves whose strains are positive correspond to axial stress – axial strain behavior, while the curves whose strains are negative correspond to axial stress – lateral (radial) strain behavior. Physically, the specimens undergo axial shortening and radial dilation under axial compressive loading. While these deformations could be intuitively related to negative and positive values respectively, the sign convention used in Figures 3-17 and 3-18 is widely used to depict the axial and lateral deformation behaviors. The computation of axial stresses, axial strains, and lateral strains was based on the concepts of engineering stresses and engineering strains in which the load and deformation changes are characterized in terms of the original geometry of the specimen (*i.e.* original cross-section areas and original lengths). Values for axial deformation were obtained by averaging the measurements of the two extensometers located at the mid-section of the specimen. Values for radial deformation were obtained by averaging the measurements of the two LVDT devices.

Figures 3-19 and 3-20 show plots of axial stress – volumetric strain behavior. Volumetric strains were computed from the axial and lateral strain measurements. By definition, the volumetric strain for a specimen of cylindrical geometry is:

$$\varepsilon_{vol} = \varepsilon_{axial} + \varepsilon_{radial} + \varepsilon_{hoop} \tag{3.5}$$

Based on mechanics principles and symmetry arguments, it can be shown that the lateral (radial) strain is equal to the hoop strain, thus:

$$\varepsilon_{vol} = \varepsilon_{axial} + 2\varepsilon_{radial} \tag{3.6}$$

3.5.2 Maximum Stresses and Strains

Table 3-6 provides a summary of the maximum stresses and strains developed in the specimens under test. A key aspect in these characterization studies of global stress-strain behavior is the fact that FRP-confined concrete specimens, which were listed in Table 3-1, could not be loaded up to ultimate failure that is commonly characterized by fiber rupturing and catastrophic collapse of the jacketed system. This situation is reflected in the values for ultimate stresses and strains of FRP-wrapped concrete specimens (CC specimen series). The reason for this limitation is directly related to the capacity of the available loading frame used in this experimental study. The Baldwin loading frame has a capacity of 890 *kN* (described in Section 3.4.5). Strengthening of the plain concrete specimens with one ply of GFRP composite material resulted in an increased capacity surpassing the maximum load available from the loading frame. It was decided that testing must stop once the load level reached 890 *kN*. From additional studies, it was determined that FRP-wrapped concrete specimens ultimately failed at relative short periods of constant-loading after the maximum load available from the loading frame was reached. Testing the FRP-confined concrete samples up to load levels slightly lower than ultimate loading does not significantly alter the objectives of the proposed research since this thesis work aims at the understanding of the damage development and evolution in FRP-confined concrete specimens and to mechanical conditioning these type of specimens in a repeatable and consistent manner for later assessment through visual inspection, microscope observations, and radar NDE technologies. No availability of experimental data on ultimate loads and deformations partially affected the analytical modeling component of this work, discussed in Section 3.6

Specimen	Axial Stress [MPa]	Axial Strain [mm/mm]	Lateral Stress [mm/mm]	Volumetric Strain [mm/mm]
PC01	29.5	0.0019	-0.0004	0.0011
PC02	29.6	0.0022	-0.0007	0.0008
PC03	33.3	0.0018	-0.0007	0.0003
CC01	48.4*	0.0139	-0.0117	-0.0095
CC02	48.3*	0.0181	-0.0142	-0.0102
CC03	48.5*	0.0149	-0.0131	-0.0112
CC04	48.6*	0.0124	-0.0103	-0.0083

** Strength capacity of specimen exceeded the maximum load supplied by load frame*

Table 3-6 Maximum stress and strain values for specimens under test

3.5.3 Differential Shortening Behavior

Another important aspect related to the results of the mechanical behavior characterization of plain concrete cylinders wrapped with one layer of GFRP composite is the overlap strengthening phenomena, which was previously observed in the experimental work of Au and Büyüköztürk (2005). Figure 3-21 shows the axial stress –

axial strain curve for specimen CC01. It is observed that axial strain values measured by the extensometer on the bond overlap region are smaller than those measured opposite to the overlap region. Thus, differential shortening behavior occurred during uniaxial compression testing. Based on the data collected from the four FRP-confined concrete specimens, an average value for the differences between the two measured axial strains corresponded to approximately 20%. This type of response was expected due to the wrapping of the concrete specimens with only one ply of FRP. In practice, retrofitting with FRP composite fabrics would require several plies for adequate confinement. If several individual fabrics are used for the retrofitting job, these are placed such that bond overlaps are distributed around the circumference of the column, which ideally would mitigate differential deformation effects.

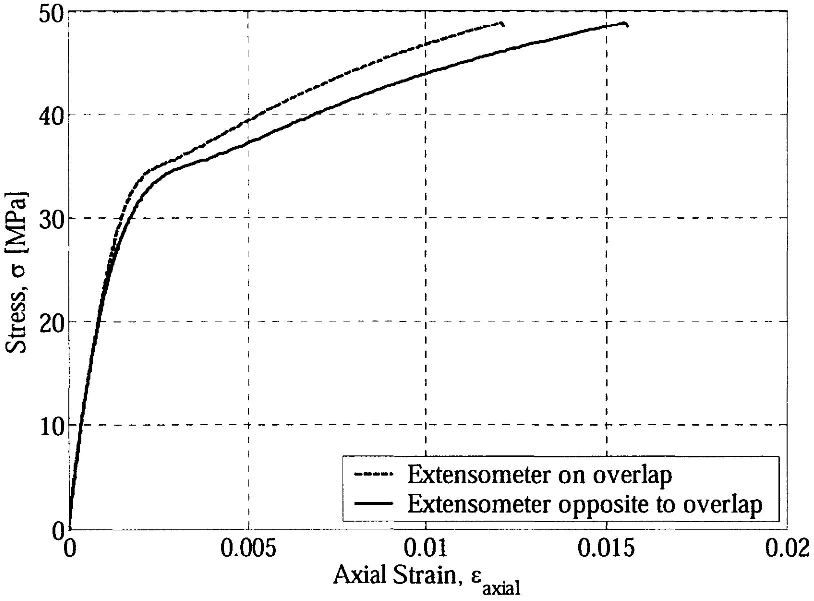

Figure 3-21 Overlap strengthening on one-ply FRP-wrapped concrete, specimen CC01

3.5.4 Analysis of Mechanical Behavior

From the results presented in Table 3-6, the enhancement in strength and deformation characteristics of plain concrete specimens when wrapped with one layer of GFRP composite is clearly observed. The stress-strain behavior of the FRP-confined concrete specimens showed the distinctive bi-linear form as it is commonly observed in existing research (refer to Section 3.2.2). The kink point was clearly observed at a stress level slightly above 30 *MPa*. At the kink point, a drastic change in the stiffness behavior of the composite system occurred. Furthermore, this change in stiffness behavior is experimentally related to the large dilatational lateral strain values developed after the kink point for all specimens under test. The best way to understand this behavior is to focus on the volumetric strain development plotted in Figure 3-19. Up to a load level of approximately 30 *MPa*, both plain concrete and FRP-confined concrete specimens follow similar axial stress – volumetric strain responses. The effect of the FRP wrapping appears minimal up to that point, except for specimen CC04. Plain concrete specimens failed at 30 *MPa* showing no signs of significant dilation behavior. On the contrary, FRP-confined concrete specimens displayed changes in volumetric deformation, shifting from a compaction-dominated behavior up to the kink point to a dilation-dominated behavior. For load levels higher than approximately 35 *MPa*, these specimens underwent significant volumetric dilations. Thus, the net effect of axial shortening due to axial compressive loads is dominated by the lateral expansion due to the confinement provided by the FRP jacket. It is important to notice that the dilatational behavior herein discussed is only related to the specific case of FRP wrapping with one ply of GFRP fabric. FRP jacket configurations with two or more plies may result in significantly different behaviors, some of which are characterized by continuous compaction for the cases of large numbers of FRP plies (Teng and Lam 2004).

One of the important aspects in the stress-strain behavior studies is the observed consistency and repeatability in performance among the FRP-confined concrete specimens. As already mentioned in Section 3.4.1, one of the goals of these experiments was to manufacture specimens with highly similar characteristics in terms of mechanical performance. It has been noted in existing literature that scattering in experimental results could be expected when investigating the mechanical responses of GFRP-confined concrete specimens (Au 2001, Lam and Teng 2003). Thus, these results provide the necessary reliability when expanding this work to the investigation of intermediate stages of mechanical damage, in which accurate control over load-deformation behaviors is necessary for adequate conditioning of specimens for selected mechanical damage levels. These studies are presented in Section 3.7

3.6 Analytical Modeling of Mechanical Behavior of FRP-Confined Concrete

Extensive analytical modeling of FRP-confined concrete (Saadatmanesh *et al.* 1994, Miyauchi *et al.* 1997, Saafi et al. 1999, Spoelstra and Monti 1999, Samaan *et al.* 1998, Toutanji 1999, Shahawy *et al.* 2000, Xiao and Wu 2000, Harries and Kharel 2002, Moran and Pantelides 2002, Lam and Teng 2003) has been carried out over the past decade to advance the understanding of its mechanical behavior when subjected to compressive load scenarios. For practical applications, adequate modeling of FRP-confined concrete stress-strain behavior is necessary for the reliable design of structural column elements. In this section, the performances of three representative existing models are evaluated in view of the experimental results obtained and presented in the previous section. As it was already mentioned, a limitation of the experimental work related to characterizing the stress-strain behavior was the inability to load the FRP-confined concrete specimens up to ultimate conditions due to the maximum load capacity of the loading frame. Thus, a complete stress-strain curve could not be measured. However, comparisons of the three analytical stress-strain models herein described with the experimental results will deliver important knowledge of the fundamental mechanical behavior and trends of FRP-confined concrete. Due to the different notations for equation parameters used among researchers, a common notation has been adopted in this work for easier comparison between different models. Additionally, all formulations herein presented are referenced to SI units.

3.6.1 State-of-the-Art in Stress-Strain Modeling

Three analytical models of the axial stress – axial strain behavior of FRP-confined concrete systems are described in this section. These models correspond to the works of Samaan *et al.* 1998, Spoelstra and Monti 1999, and Lam and Teng 2003. While the descriptions of these models will provide sufficient information regarding the overall principles of each model, the reader is referred to the mentioned journal publications for further details of each formulation.

Samaan et al. 1998

Modeling of the stress-strain curve was based on the work of Richard and Abbott (1975), which assumed a four-parameter relationship of the following form:

$$f_{cc} = \frac{(E_1 - E_2)\varepsilon_{cc}}{\left\{1 + \left[\frac{(E_1 - E_2)\varepsilon_{cc}}{f_o}\right]^n\right\}^{1/n}} + E_2\varepsilon_{cc} \tag{3.7}$$

where: f_{cc} and ε_{cc} = concrete axial stress and strain respectively, E_1 and E_2 = slopes of the first and second portions of the curve, f_o = reference plastic stress at intercept of second slope with the stress axis, and n = curve shape factor which controls the transition between the two main segments of the curve. The ultimate stress state is defined by the relationship between the compressive strength of concrete, $f_c^{'}$ and the effective lateral confinement stress provided by the FRP, f_l as follows:

$$f_{cc}^{'} = f_c^{'} + k_1 f_l \tag{3.8}$$

where k_1 = coefficient of effectiveness, $f_l = \frac{2 f_{FRP} t}{d}$, f_{FRP} = tensile strength of the FRP jacket, t = thickness of the jacket, and d = diameter of the concrete core. Samaan *et al.* proposed that although several models use a constant value for the k_1 parameter, confinement effectiveness decreases at high levels of confinement. Thus, this parameter was defined as:

$$k_1 = 6.0 f_l^{-0.3} \ [MPa] \tag{3.9}$$

The first slope of this model is assumed to be uniquely dependent on the strength of unconfined concrete. The secant modulus formula proposed by Ahmad and Shah (1982) for estimating the elastic modulus was used:

$$E_1 = 3{,}950\sqrt{f_c^{'}} \ [MPa] \tag{3.10}$$

The second slope was estimated based on the assumption that for stress states surrounding the unconfined strength of plain concrete and beyond microcrack propagation results in a complete activation of the FRP jacket. Therefore, the second slope is mainly dependent on the stiffness of the FRP jacket and less dependent on the unconfined strength of concrete.

$$E_2 = 254.61\, f_c'^{0.2} + 1.3456 \frac{E_{FRP} t}{d} \; [MPa] \tag{3.11}$$

where E_{FRP} = elastic modulus of the FRP in the hoop direction. The intercept stress is related to the unconfined concrete strength and the confining pressure as follows:

$$f_o = 0.872\, f_c' + 0.371\, f_l + 6.258 \; [MPa] \tag{3.12}$$

The ultimate strain of the composite system is defined as:

$$\varepsilon_{cu} = \frac{f_{cc}' - f_o}{E_2} \tag{3.13}$$

The curve-shape factor n was set to 1.5. The calibration of this model was based on experimental results of FRP-encased concrete specimens.

Spoelstra and Monti 1999

This stress-strain model of concrete with elastic confinement follows an incremental-iterative formulation. The confined concrete model developed by Mander *et al.* 1988 serves as the theoretical basis for this formulation. The Mander *et al.* model defines the confined concrete stress as:

$$f_{cc} = \frac{\bar{f}_{cc} \cdot x \cdot r}{r - 1 + x^r} \tag{3.14}$$

where:

$$x = \frac{\varepsilon_{cc}}{\bar{\varepsilon}_{cc}} \tag{3.15}$$

$$r = \frac{E_c}{E_c - E_{\sec}} \tag{3.16}$$

$$E_{\sec} = \frac{f_{cc}'}{\bar{\varepsilon}_{cc}} \tag{3.17}$$

$$\bar{\varepsilon}_{cc} = \varepsilon_{co}\left[1 + 5\left(\frac{\bar{f}_{cc}}{f_c'} - 1\right)\right] \tag{3.18}$$

where ε_{co} = ultimate compressive strain of unconfined concrete, and $E_c = 4{,}730\sqrt{f_c'}$. The compressive strength of FRP-confined concrete is defined in terms of a constant confining pressure as follows:

$$\bar{f}_{cc} = f_c'\left[2.254\sqrt{1 + 7.94\frac{f_l}{f_c'}} - 2\frac{f_l}{f_c'} - 1.254\right] \tag{3.19}$$

However, this model is suitable for a confining action such as that created by steel where a constant confining pressure is more realistic during material yielding phases. As described in previous sections, FRP confinement is a type of passive confinement, and thus, pressures are increasing as the axial load on the FRP-confined specimen increases. Spoelstra and Monti proposed this behavior could be better represented by axial compressive stresses, f_{cc} and lateral strains, ε_l which are dependent on updated values of axial strains, ε_{cc} and confining pressures, f_l. Mathematically, this can be represented as:

$$\varepsilon_l(\varepsilon_{cc}, f_l) = \frac{E_c\varepsilon_{cc} - f_{cc}(\varepsilon_{cc}, f_l)}{2\beta f_{cc}(\varepsilon_{cc}, f_l)} \tag{3.20}$$

where β is related to a concrete property definition proposed by Pantazopoulou and Mills (1995) used in characterizing uniaxial compression behavior of unconfined concrete. An alternative estimate of this parameter is given by:

$$\beta = \frac{E_c}{|f_c'|} - \frac{1}{|\varepsilon_{co}|} \tag{3.21}$$

Calculating the lateral strain, ε_l allows for corresponding calculation of the current lateral confining pressure by:

$$f_l = E_{FRP}\varepsilon_l \tag{3.22}$$

This updated lateral pressure is then used in an iterative scheme until convergence to an stable value occurs. This procedure is repeated for each axial strain value, ε_{cc}. The iterative procedure can be summarized as follows:

1. Impose a value for ε_{cc}
2. Update value of lateral confining pressure: $f_l\big|_{iter=i} = f_l\big|_{iter=i-1}$

3. Calculate $\bar{f}_{cc}\left(f_l\big|_{iter=i}\right)$ using Eq. 3.19
4. Calculate current stress state $f_{cc}\left(f'_{cc}\big|_{iter=i}\right)$ using Eq. 3.14
5. Update lateral strain $\varepsilon_l\left(f_{cc}\big|_{iter=i}\right)$ from Eq. 3.20
6. Update f_l using Eq. 3.22
7. Check for convergence $f_l\big|_{iter=i} = f_l\big|_{iter=i-1}$. If convergence is not achieved, then repeat steps 2 through 7.

Finally, the ultimate stress and strain states are calculated using the Mander *et al.* model and the definition of the maximum confinement pressure available through the FRP jacket. The following set of equations provides the necessary parameters for such calculations:

$$f_{lu} = \frac{2\, f_{FRP} t}{d} \tag{3.23}$$

$$\hat{f}_{cc} = f'_c\left[2.254\sqrt{1+7.94\frac{f_{lu}}{f'_c}} - 2\frac{f_{lu}}{f'_c} - 1.254\right] \tag{3.24}$$

$$\hat{\varepsilon}_{cc} = \varepsilon_{co}\left[1+5\left(\frac{\hat{f}_{cc}}{f'_c}-1\right)\right] \tag{3.25}$$

$$E_{\sec,u} = \frac{E_c}{1+2\beta\dfrac{f_{FRP}}{E_{FRP}}} \tag{3.26}$$

$$E_{\sec} = \frac{\hat{f}_{cc}}{\hat{\varepsilon}_{cc}} \tag{3.27}$$

Using Eqs. 3.23 through 3.27, we obtain:

$$\varepsilon_{cu} = \hat{\varepsilon}_{cc}\left[\frac{E_{\sec}\left(E_c - E_{\sec,u}\right)}{E_{\sec,u}\left(E_c - E_{\sec}\right)}\right]^{1-\frac{E_{\sec}}{E_c}} \tag{3.28}$$

$$f'_{cc} = E_{\sec,u}\varepsilon_{cu} \tag{3.29}$$

Lam and Teng 2003

The proposed model was built upon the analysis of large database of FRP-confined concrete studies available in the open literature. The main assumptions of this model are the following:

- The stress-strain behavior is characterized by a parabolic first segment and a linear second segment
- The tangent modulus at zero axial strain is that of unconfined concrete and stiffness properties of the subsequent parabolic segment are influenced by the FRP jacket
- A smooth transition between the two segments is accomplished
- The ultimate condition for the FRP-confined concrete specimen is defined by a point for which the ultimate compressive strength and ultimate axial strain are met.

The proposed model is defined by the following set of equations:

$$f_{cc} = \begin{cases} E_c \varepsilon_{cc} - \dfrac{(E_c - E_2)^2}{4 f_o} \varepsilon_{cc}^2 & 0 \le \varepsilon_{cc} \le \varepsilon_t \\ f_o + E_2 \varepsilon_{cc} & \varepsilon_t \le \varepsilon_{cc} \le \varepsilon_{cu} \end{cases} \qquad (3.30)$$

where f_o = intersection point of the second segment with the stress axis, ε_t = strain at the transition of the two segments, E_2 = slope of the linear second segment. Additionally, the last two parameters are defined as:

$$\varepsilon_t = \frac{2 f_o}{E_c - E_2} \qquad (3.31)$$

$$E_2 = \frac{f_{cc}^{'} - f_o}{\varepsilon_{cu}} \qquad (3.32)$$

Three parameters need further definition, namely f_o, $f_{cc}^{'}$ = ultimate compressive strength of FRP-confined concrete, and ε_{cu} = ultimate axial strain. Extensive analysis of these parameters was conducted in order to explicitly incorporate the effects of FRP jacket stiffness contributions and FRP rupture behaviors in these systems, which significantly differs to those characterized by material tests such as flat coupon tests. Using the dataset of compressive behavior of glass, carbon, and aramid FRP-confined concrete specimens, the following expression were developed:

$$f_o = f_c^{'} \qquad (3.33)$$

$$f'_{cc} = f'_c\left(1 + 2\frac{f_l}{f'_c}\right) \tag{3.34}$$

$$\varepsilon_{cu} = \varepsilon_{co}\left[1.75 + 6.00\left(\frac{f_l}{f'_c}\right)\left(\frac{f_{FRP}}{E_{FRP}\varepsilon_{co}}\right)^{0.45}\right] \tag{3.35}$$

The above set of equations has been adjusted to the values of GFRP experiments, which differ from the results obtained for other types of FRP jacketing.

3.6.2 Performance of Existing Models and Comparison with Experimental Data

After describing each of the three analytical models for FRP-confined concrete column members, their performances are evaluated in the context of the experimental results presented in Section 3.5. Table 3-7 summarizes all the geometric and mechanical property values corresponding to the plain concrete and FRP composite jacket that are necessary for the evaluation of the analytical models. Figure 3-22 shows the comparison of the stress-strain behaviors predicted by each of the three analytical models with the experimental data corresponding to the four FRP-wrapped concrete specimens previously introduced in Table 3-2.

It is observed that while predictions of the ultimate stress and strain conditions differ significantly among the three models, the overall shapes of the stress-strain curves are highly similar. As mentioned in Section 3.6.1, the aim of this comparative study between analytical models and the generated experimental data is not the analysis of ultimate stress-strain states or conditions, but instead, such comparative study could further enhance the understanding of the mechanical behavior of FRP-confined concrete systems. Representative analytical models such as the three works mentioned in this section are developed based on large arrays of experimental observations and comparisons with other previous research efforts. The close comparisons between the experimental data described in Section 3.5 and the analytical predictions presented in this section provide a reliable framework for the study of intermediate damage stages in FRP-confined concrete. Based on the experimental expertise developed in manufacturing and testing, a test matrix of FRP-wrapped concrete cylinder specimens which are conditioned under different levels of compressive mechanical loads is developed in Section 3.7. These conditioned specimens will be used for the damage characterization studies using visual and microscopic observations and a radar NDE technology.

Ultimate strain, unconfined concrete	ε_{co} =	0.002 mm/mm
Compressive strength, unconfined concrete	f_c' =	30.8 MPa
Diameter of specimen	d =	152 mm
Thickness of FRP jacket	t =	1.3 mm
Ultimate tensile strength in hoop direction	f_{FRP} =	460 MPa
Tensile elastic modulus	E_{FRP} =	20,900 MPa

Table 3-7 Input parameters for evaluation of analytical models

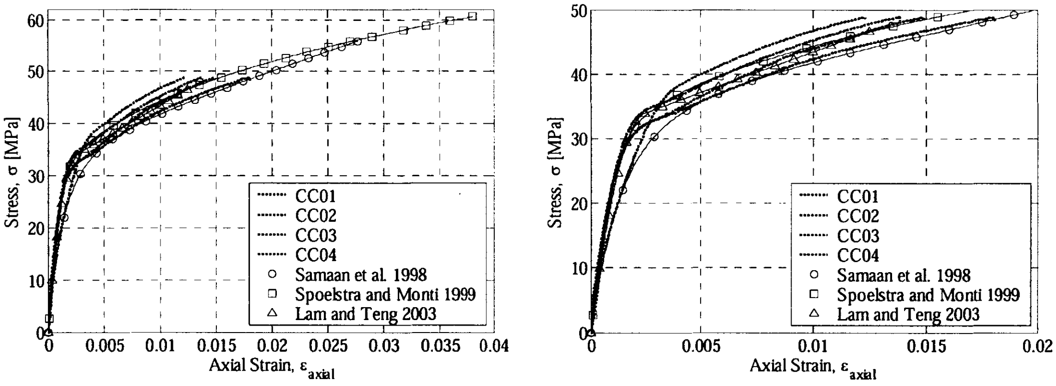

(a) (b)

Figure 3-22 Comparison of analytical models with experimental results
(a) Normal view (b) Close up to zone of interest

3.7 Characterization of Damage Stages in FRP-Confined Concrete

Damage assessment of complex systems such as the case of concrete wrapped with FRP composites subjected to diverse loading scenarios could encounter several potential difficulties related to the appropriate choices of damage quantification parameters, the implementation of sound measuring techniques, and more fundamentally, the knowledge of the exact types of behaviors, responses, or features that are being quantified. Based on the literature review presented in previous sections, damage behavior of FRP-confined concrete systems was shown to be closely related to its load-deformation response, which in experimentation could be quantified in terms of axial, lateral, and volumetric strain histories. The test program described in the previous section helped enhancing the understanding of mechanical behavior of FRP-confined concrete cylinder specimens subjected to monotonic axial compression loads from an experimental point of view. Based on the developed knowledge from the experimental and theoretical studies, characterization of damage stages in FRP-confined concrete is accomplished through the use of volumetric deformation information. Volumetric stress-strain measurements are regarded as important information related to the damage accumulation and evolution in the FRP-confined concrete system under compressive loads (refer to Section 3.1.4). Based on the consistent mechanical behavior of FRP-confined concrete observed in the experiments (refer to Section 3.5) and the research conclusions found in existing literature (refer to Section 3.3), the following specific deformation stages in the volumetric stress-strain behavior of the FRP-confined concrete specimens tested in this current work are identified:

1. *Intact sample*: The FRP-confined concrete specimen is load-free
2. *Maximum volumetric contraction*: The deformation of the FRP-confined concrete specimen is mainly due to the axial shortening contribution.
3. *No apparent volumetric change*: The net contributions of axial shortening and lateral expansion equate to zero. The stress level at this stage directly corresponds to the kink stress noted in previous discussions.
4. *Volumetric expansion*: The FRP-confined concrete specimen undergoes clear volumetric expansion. It is hypothesized from existing research that the concrete core has already failed at this deformation level.
5. *Close to ultimate failure*: FRP-confined concrete is close to reaching its ultimate load bearing capacity. In our particular experiments, the FRP jacket did not rupture at this deformation level.

These different deformation stages are schematically shown in Figure 3-23. Due to the consistent load-deformation response of the tested FRP-confined concrete specimens, deformation stages 3 through 5 could be correlated to different stages of damage in the

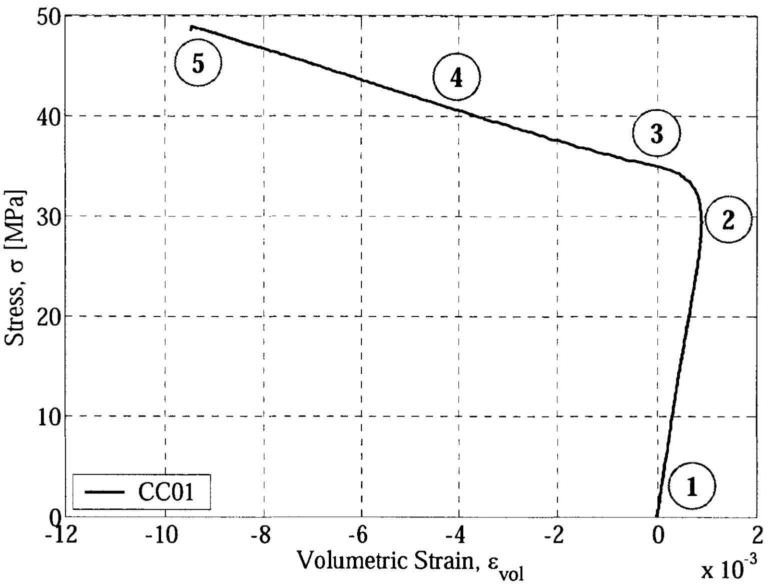

Figure 3-23 Characterization of deformation stages for FRP-confined concrete specimens

specimen. While the FRP jacket may not show any signs of deterioration or damage, the concrete core experiences several stages of deformation ranging from pure dilation (stage 2) to pure expansion or dilation (stages 4 and 5). The key incentive for developing this characterization scheme based on volumetric deformation measurements of FRP-confined concrete specimens is to establish a reliable benchmark for two studies which are included in this thesis work. The first study refers to visual and optical microscopic observations of the concrete matrix for selected damage stages (refer to Section 3.8). The second study refers to the non-destructive evaluation of selected FRP-confined concrete specimens using a broadband radar methodology (refer to Chapter 5). The series of specimens that were mechanically conditioned to selected damage levels for use in the two mentioned studies are discussed in the next sections.

5.7.1 Test Matrix

The test matrix of samples that will be used in microscope and radar studies for damage assessment of FRP-confined concrete is presented in Table 3-8. Two specimens were conditioned for each damage level: one sample for each damage assessment study.

Specimen Type	Damage Stage	Individual Notation	Number of Specimens
FRP-confined concrete	1	MD1	2
FRP-confined concrete	3	MD3	2
FRP-confined concrete	5	MD5	2

Table 3-8 Test matrix of specimens conditioned through mechanical loading to specific damage stages

5.7.2 Load-Deformation Behavior and Conditioning of Specimens

The load deformation responses for each of the two MD3 and MD5 types of specimens are presented in Figures 3-24 through 3-26. The conditioning levels for each of the specimens were determined as in Figure 3-23. Such conditioning levels were achieved by subjecting the specific FRP-confined concrete specimen to monotonic axial compression loads as described in Section 3.4.5. Once the stress level corresponding to the specific damage stage was reached, the experiment was immediately stopped and the load subsequently released.

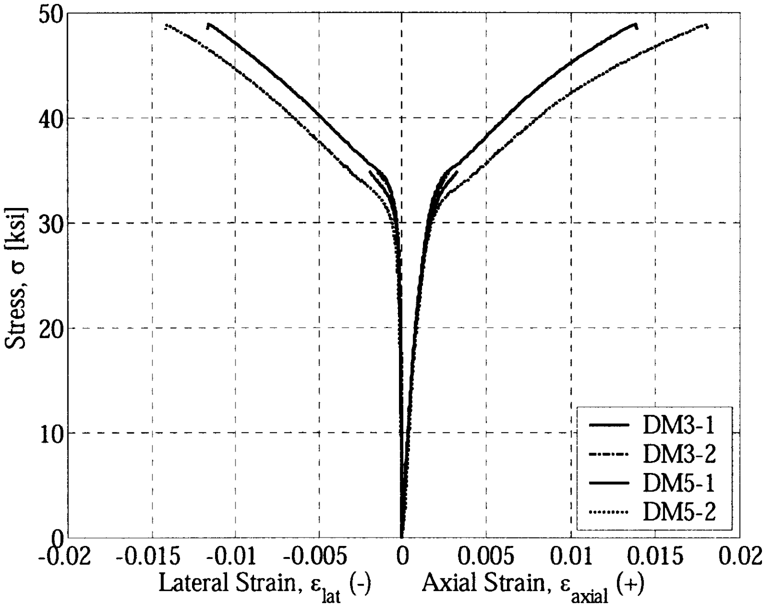

Figure 3-24 Axial stress – axial strain and axial stress – lateral strain curves for FRP-wrapped concrete specimens conditioned under compressive load

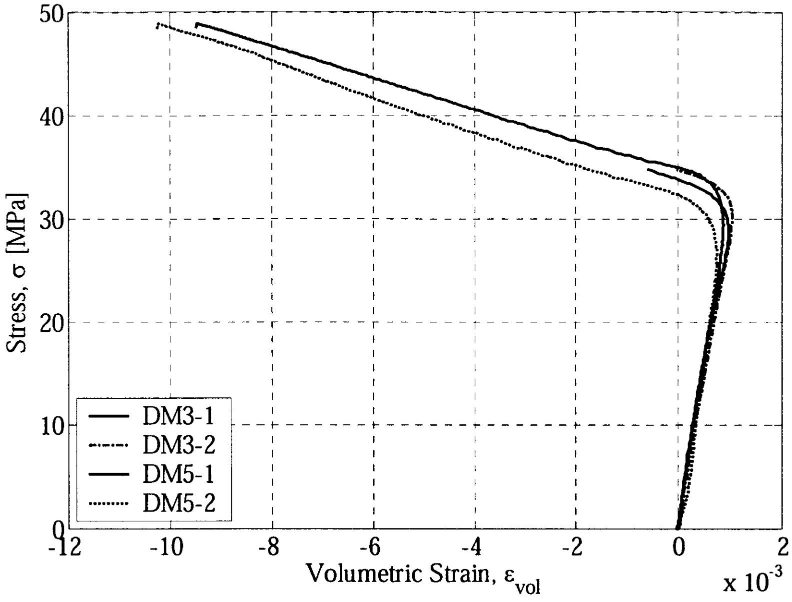

Figure 3-25 Axial stress – volumetric strain curves for FRP-wrapped concrete specimens conditioned under compressive load

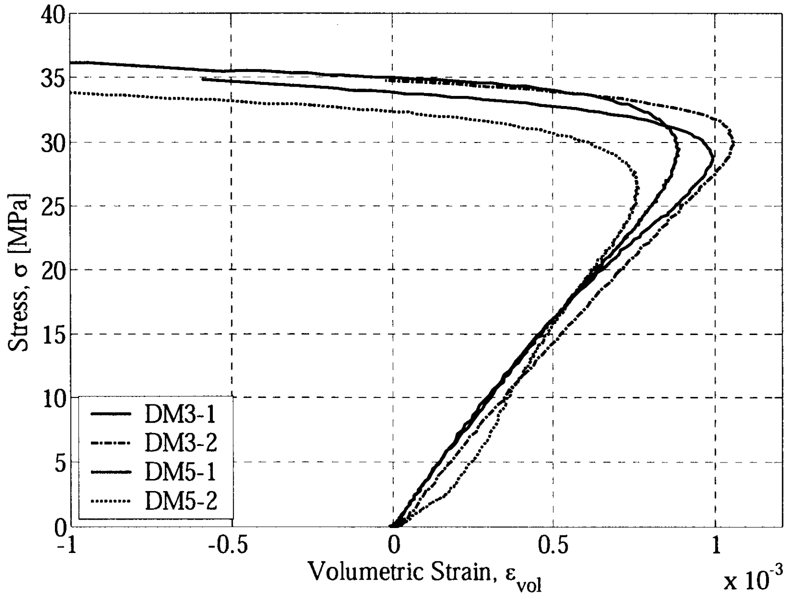

Figure 3-26 Close up of axial stress – volumetric strain curves for FRP-wrapped concrete specimens conditioned under compressive load

3.8 Bisection Procedures and Microscopic Observations for Determination of Mechanical Damage in FRP-Confined Concrete

3.8.1 Objective

The objective of these studies is to investigate the concrete core condition of selected FRP-confined concrete specimens through visual assessment of their cross-sections. Assessment of concrete cores was performed through visual inspection and via optical microscopic observations once specimens were bisected. In what follows, a brief summary of previous research related to the inspection of concrete matrices through bisection procedures and microscope techniques, the particulars of the experimental procedures used in this work to assess concrete core conditions of FRP-confined concrete specimens, and the results of the visual and microscope inspections are discussed.

3.8.2 Background Information on Internal Observations of Concrete

While extensive research for concrete materials has been conducted in several areas such as mechanical, chemical, and structural properties and behaviors of these materials, there is still some uncertainty with regards to the physical understanding of the internal processes that lead or control such properties or behaviors. Experimental and theoretical understanding of controlling mechanisms such as fracture, slip, crushing, crack propagation, friction, pore growth and dilation are commonly inferred from indirect measurements and surface observations (in Karihaloo and Jefferson 2001). Research on the particular area of internal observations of concrete matrices after induced damage has developed over the years in order to bring answers to the missing link between visual observation and understanding of the actual phenomena under investigation and development of measurement techniques and theoretical models.

Hsu *et al.* (1963) investigated the microcracking phenomenology for plain concrete specimens through direct microscope observations and x-ray photographs. The objective of this work was to relate the microcracking evolution to the shape of the stress-strain response for plain concrete specimens subjected to uniaxial compression loads. Some of the main results of this work were related to the understanding of how microcracking, bond cracking, and continuous cracking processes take place in the concrete matrix leading to ultimate failure of tested specimens. Several other later experimental studies (van Mier 1991, Hornain *et al.* 1996, Ammouche *et al.* 2001, Karihaloo 2001) for concrete were conducted for understanding damage evolution in the microstructure using advanced visualization techniques under several loading conditions such as compression and fracture. Visualization techniques range from using common optical microscopes with $\times 10$ to $\times 80$ zoom capacities to using scanning electron microscopy (SEM) techniques. In summary, most of the defects and cracks found in several studies are of characteristic lengths in the scale of micrometers to tenths of micrometer. However, most of the studies focus on crack formation and propagation in fracture experiments.

3.8.3 Experimental Procedures

Bisection of FRP-Confined Concrete Specimens

The bisection procedures were carried out using a wet saw located in Building 54, MIT campus. The wet saw is capable of producing smooth cuts through rocks and other solids due to relatively low and consistent operating speeds. The cutting blade has a diameter of 600 *mm*. The bottom of the machine was filled with water in order to keep the blade wet through out the experiment and to allow for reduced friction between the surface of the blade and the material's surface. Photographs of the equipment are provided in Figure 3-27. The specimen is positioned on the wet saw as seen in Figure 3-27, and the cutting procedure is executed. Cutting one cross-section of the by 150 *mm* diameter by 380 *mm* length FRP-wrapped concrete specimens lasted for approximately 1.5 *h*. The end result was a very smooth cut across the cross-section of the specimens. Examples of the bisected specimens are shown in Figure 3-28.

Cross-sections of approximately 25 *mm* in height (disk configuration) were extracted from each specimen for further treatment before microscopy studies. Using a table saw, each cross-section was cut into smaller portions that would fit in the microscope device. Figure 3-29 shows the results of the mentioned procedure for MD1 and MD5 cross-sections. Having completed the bisection and sawing procedures, microscope observations were conducted.

Figure 3-27 Photographs of equipment used for bisection of specimens

Figure 3-28 Examples of specimens after cutting procedure

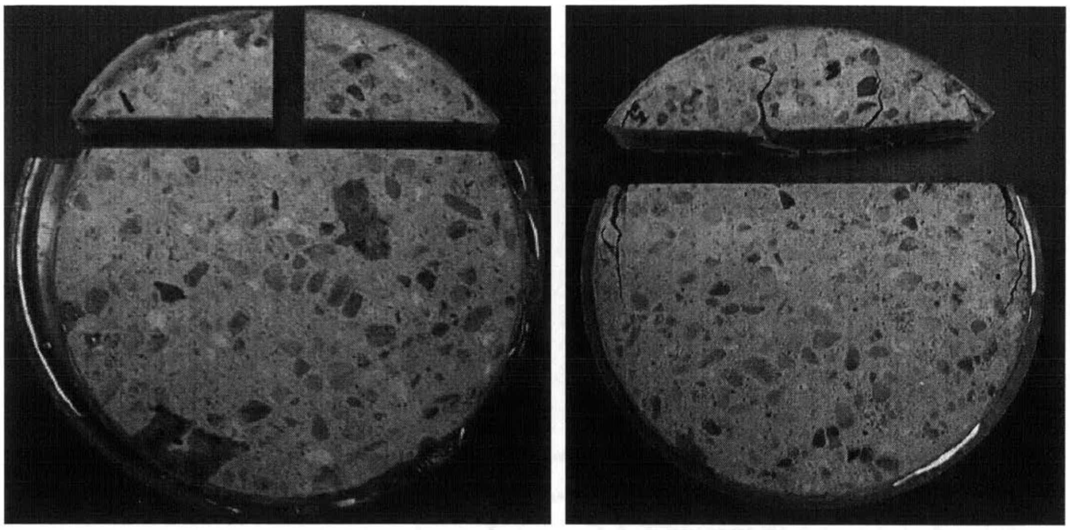
(a) (b)

Figure 3-29 Bisected cross-sections and portions of specimens (a) MD1 and (b) MD5

3.8.4 Results of Bisection Procedures and Optical Microscopic Observations

Observations during Bisection Procedures

After specimens were bisected according to the previously mentioned procedures, visual inspection of the uncovered cross-sections was performed. All surfaces appeared alike to the naked eye and no apparent differences in terms of grain or cement matrix distribution were noticed. However, specimen MD5 (subjected to damage level 5) seemed to show a deteriorated surface texture as several large aggregate particles fell out of their positions in the concrete matrix with the handling of the specimen. Another important finding was related to the time for drying after the specimens were cut and set aside. The exposed surfaces of specimens MD1 and MD3 dried faster than that of specimen MD5. It was observed that water diffused into the concrete matrix of the later specimen and complete drying of the surface lasted for a longer period of time. This behavior was consistent for all surfaces created after bisection procedures were executed.

Another important finding that shed light on the different responses between specimens was the observed behavior of the cross-sections during the sawing of smaller sections for later microscopic observations. One can notice in Figure 3-29 (b) that severe cracking had taken place for specimen MD5. The observed cracking comes as a result of the longitudinal cut made on the cross-section. As the sawing procedure was taking place, the FRP jacket wrapped around the cross-section showed a pre-stressed nature. This was confirmed upon final stages of sawing. Once the FRP jacket was cut at both ends, it snapped back as if releasing stresses present in the hoop direction. The smaller portion (top part of the sample in Figure 3-29 (b)) showed severe cracking in the mid-section due to the stress release in the FRP jacket. The corresponding behavior was also observed in the larger portion of the specimen (bottom part of the sample in Figure 3-29 (b)) in which the FRP jacket also shortened after the mentioned stress release. This action could only be physically accommodated by redistributing the stresses in the concrete matrix which ultimately created cracking due to tension stresses. On the contrary specimens MD1 and MD3 did not show fracture formation, and intact sections could be created after sawing, as observed in Figure 3-29 (a).

Observations using Optical Microscopy

Prepared specimen sections were observed using a LEITZ Metallux II optical microscope with $\times 10$ to $\times 40$ optical zoom capabilities. Only small pieces sectioned from the complete cross-sections were investigated. Observations were conducted at several locations in each sample in order to understand the nature of the different concrete matrices of specimens MD1, MD3, and MD5. After exhaustive observations, no significant differences were detected. Representative images of the concrete matrix for specimen MD5 seen under the $\times 10$ and $\times 40$ lens are presented in Figure 3-30. The pictures were taken using a Cannon EOS 20D camera. The microscope and camera equipment were readily available at Rock Mechanics Laboratory on Building 56, MIT Campus. Grains (identified with darker color in the images) appeared intact, and the mortar matrix (identified with lighter color in the images) showed consistent features throughout the observations. Using the $\times 40$ zoom, one could assess the grain/mortar interfaces. For the vast majority of observations, such interface appeared intact, and no signs of microcracking could be observed.

3.8.5 Conclusions

Important understanding was gained regarding the condition or state of the concrete core

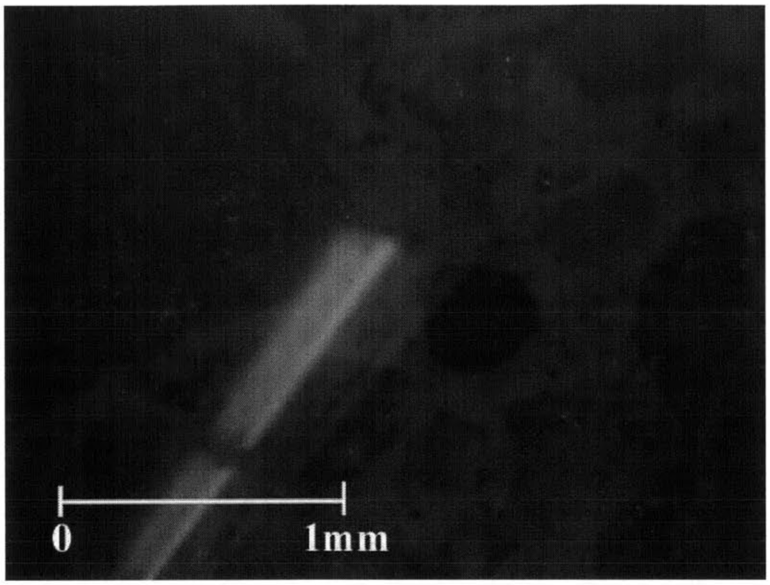

(a)

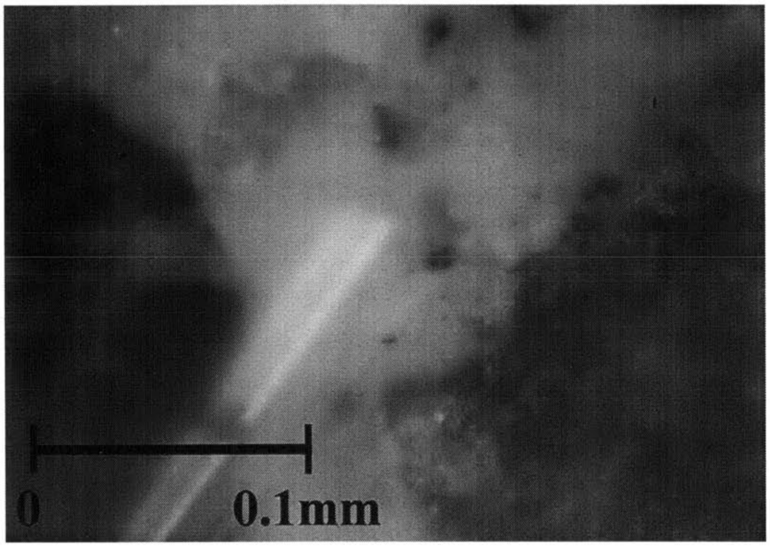

(b)

Figure 3-30 Optical microscopic images for the concrete matrix of specimen MD5 using (a) $\times 10$ zoom and (2) $\times 40$ zoom of intact and mechanically damaged FRP-confined concrete specimens through bisection procedures and optical microscopic observations. During the bisection procedures, loosening of aggregates and increased water absorption of the cross-section of specimen MD5 were observed. Although the concrete core appeared intact for all specimens, the concrete matrix in MD5 might have lost part of its cohesiveness. This behavior could be explained by assuming that the binding of the aggregates through the mortar matrix must have changed and deteriorated during the compression loading experiments. The mechanisms related to material integrity inherent to an intact concrete matrix could have evolved into other mechanisms governed by the confinement action of the FRP jacket. The effect of the confining action of the FRP jacket on the concrete matrix was corroborated during the sawing procedures for partitioning of cross-sections for microscopic observations. Release of residual stresses present in the FRP jacket of specimen MD5 was observed at the moment the FRP jacket was cut loose. Contraction of the FRP caused the concrete to fracture in order for a new equilibrium state to be reached. Specimen MD3 did not show a similar behavior to MD5 although it was subjected to significant compression loads (specimen MD3 was subjected to approximately 70% of the load imposed on specimen MD5).

Although differences between specimens MD1 and MD3 and specimen MD5 were observed during the bisection procedures, optical microscopy experiments did not reveal any apparent differences. Concrete matrices seemed to have similar features in terms of grain integrity, mortar matrix integrity, and porosity distribution. Thus, no visible mechanisms of failure could be deduced from the microscopic observations. Damage processes such as microcracking, which from the understanding gain through the literature review is one of the main drivers for structural collapse of the concrete matrix, would have to be investigated at smaller scales. The use of scanning electron microscopy (SEM) techniques could allow further understanding of what damage processes are present at the different damage states in FRP-confined concrete subjected to compressive loads.

Chapter 4

Electromagnetic Properties of Concrete and FRP Composite Materials

While applications of FRP composites for strengthening and retrofitting of concrete structures are growing rapidly, characterization and fundamental understanding of electromagnetic (EM) properties of concrete and FRP materials is constantly under development. Furthermore, existing research has shown that characterization of certain construction materials such as concrete present some challenges due to wave dispersion and attenuation effects. For the purposes of characterizing the electromagnetic properties of concrete and FRP composites, an integrated methodology has been developed based free-space radar measurements of EM wave transmission. The results and knowledge established in this study represent a crucial advancement in the interdisciplinary approach outlined in Chapter 1 for developing a robust radar NDE technology for assessment of FRP-confined concrete. In applications of radar technologies for NDE purposes, characterization and understanding of the electromagnetic properties of the materials under investigation becomes crucial due to the essential role such properties play in the wave propagation and scattering phenomena as well as in the analysis and interpretation of radar measurements.

4.1 Fundamentals of Electromagnetic Wave Theory

The term microwave is used to define all EM radiation waves for frequencies ranging from 0.3 to 300 gigahertz (*GHz*) (McIntire 1986). These frequencies correspond to a range of free-space wavelengths ranging from 1.0 *m* to 0.001 *m*, respectively. In vacuum, microwaves travel at the velocity of light, $c = 2.997 \times 10^8\, m/\sec$. Microwaves occupy the section of the electromagnetic spectrum between radio waves and infrared radiation. Microwaves are commonly used for communications, radio and television signals, microwave ovens, radar (radio detecting and ranging), and non-destructive evaluation. The range of microwave frequencies is subdivided into bands. The designations of each band according to the Institute of Electrical and Electronics Engineers (IEEE 1984) Standard 521-1984 are presented in Table 4-1.

Band Designation	Frequency Range (GHz)
HF	0.003 - 0.03
VHF	0.03 - 0.3
UHF	0.3 - 1
L	1 - 2
S	2 - 4
C	4 - 8
X	8 - 12
Ku	12 - 18
K	18 - 27
Ka	27 - 40

Table 4-1 Radar frequency band designations (IEEE 1984)

Electromagnetic waves emitted by radars are harmonic in time. The electric and magnetic field strengths of an electromagnetic wave vary sinusoidally with time and distance. If the frequency of the source is denoted by f, the electric and magnetic fields have the following forms:

$$E_x = E_0 \cos(\omega t - kR) \tag{4.1}$$

$$H_y = H_0 \cos(\omega t - kR) \tag{4.2}$$

where:

E_x = electric field, (volts/meter, V/m)

H_y = magnetic field, (amperes/meter, A/m)

E_0 = maximum amplitude of the electric field

H_0 = maximum amplitude of the magnetic field

$\omega = 2\pi f$ = angular frequency of the wave

$k = {}^{2\pi}\!/_{\lambda}$ = wave number

λ = wavelength

R = distance measured from a specific origin

Mathematically, it is convenient to describe EM waves using complex representation,

$$E_x = E_0 e^{j(\omega t - kR)} \tag{4.3}$$

$$H_y = H_0 e^{j(\omega t - kR)} \tag{4.4}$$

where $j = \sqrt{-1}$. From complex notation, the representations of Eqs. 4.1 and 4.2 are the real parts of Eqs. 4.3 and 4.4, respectively. The negative sign in the second term inside the exponentials of Eqs. 4.3 and 4.4 is interpreted as a positive phase angle. The electric and magnetic fields of EM waves are perpendicular to each other and to the direction of propagation, as shown in Figure 4-1. Thus, electric and magnetic fields are vector quantities having intensity as well as a direction.

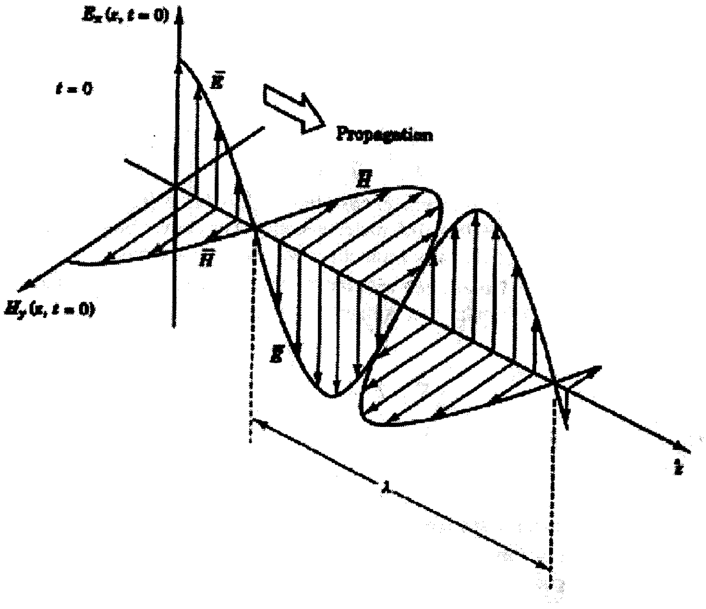

Figure 4-1 Electric and magnetic field vectors for a uniform plane wave (Staelin *et al.* 1994)

4.1.1 Maxwell's Equations and Constitutive Relationships

Propagation of electromagnetic waves in free-space and in any media is governed by a set of coupled partial differential equations called Maxwell's equations (Kong 1990). These equations fundamentally describe the relations of electric and magnetic fields to each other and to the position and motion of charged particles. Maxwell's equations in differential form are written as:

$$\nabla \times \overline{E}(\overline{r},t) = -\frac{\partial \overline{B}(\overline{r},t)}{\partial t} \text{ (Faraday's law)} \tag{4.5}$$

$$\nabla \times \overline{H}(\overline{r},t) = \frac{\partial \overline{D}(\overline{r},t)}{\partial t} + \overline{J}(\overline{r},t) \text{ (Ampere's law)} \tag{4.6}$$

$$\nabla \times \overline{D}(\overline{r},t) = \rho(\overline{r},t) \text{ (Gauss's law)} \tag{4.7}$$

$$\nabla \times \overline{B}(\overline{r},t) = 0 \text{ (Gauss's law)} \tag{4.8}$$

where the field variables are:

$\overline{E}$ = electric field (volts/meter, *V/m*)
$\overline{H}$ = magnetic field (amperes/meter, *A/m*)
$\overline{B}$ = magnetic flux density (tesla, *T*)
$\overline{D}$ = electric displacement (coulombs/meter^2, C/m^2)
$\overline{J}$ = electric current density (amperes/meter^2, A/m^2)
ρ = electric charge density (coulombs/meter^3, C/m^3)

Except for the scalar charge density $\rho(\overline{r},t)$, all fields are vector fields. After analysis of Maxwell's equations, which are media independent, there are three scalar equations for each curl equation, Eqs. 4.5 and 4.6, and one for each divergence equation, Eqs. 4.7 and 4.8. However, the divergence equations can be derived from the curl equations (Staelin *et al.* 1994). Thus, there are a total of six independent equations. In terms of independent scalar-field variables in Maxwell's equations, there is a total of twelve unknowns, one for each component of $\overline{E}$, $\overline{D}$, $\overline{H}$, and $\overline{B}$ in three dimensions. Consequently, the six independent equations from the set of Maxwell's equations are not sufficient to solve for the twelve unknowns. The six remaining equations that are needed to solve the problem at hand are called constitutive relations. Physically, the constitutive relations provide information about the media in which electromagnetic fields occur (*e.g.* free-space, water, plasma). A homogeneous and isotropic medium can be characterized by its complex permittivity, ε (farads/meter, *F/m*) and complex permeability, μ (henries/meter, *H/m*) as follows:

$$\overline{D} = \varepsilon \overline{E} \tag{4.9}$$

$$\overline{B} = \mu \overline{H} \tag{4.10}$$

There are three independent equations obtained from Eqs. 4.9 and 4.10. Theoretically, both the permittivity and permeability must be determined to characterize a homogenous and isotropic material. However, common materials such as concrete, FRP, and other construction materials are nonmagnetic, which means that their permeability is very close to that of free-space, $\mu_0 = 4\pi \times 10^{-7}$ *H/m*. Therefore, determination of the complex permittivity is sufficient to characterize the mentioned materials, which are then termed as dielectric materials.

4.1.2 Definitions of Electromagnetic Properties

Dielectric Constant

The complex permittivity for a dielectric medium is described as:

$$\varepsilon = \varepsilon' - j\varepsilon'' \tag{4.11}$$

where ε' and ε'' are the real and imaginary parts of the complex permittivity, respectively. Dividing both sides of Eq. 4.11 by the free-space permittivity, $\varepsilon_0 = 8.854 \times 10^{-12}$ *F/m*, which is a real quantity, the complex permittivity could be also expressed in a dimensionless form:

$$\varepsilon_r = \varepsilon_r' - j\varepsilon_r'' \tag{4.12}$$

where the subscript r means relative to free-space permittivity. The real part of the complex permittivity is referred to as dielectric constant. Physically, the dielectric constant provides an indication of how polarizable the medium is, or alternatively, how much energy is stored in the medium when an electric field is imposed on it.

Loss Factor

The imaginary part of the relative complex permittivity, ε_r'' in Eq. 4.12 is referred to as loss factor. The loss factor is a measure of how lossy or dissipative a medium is when subjected to an external electric field, and it is usually much smaller than the dielectric constant. The ratio of the energy lost to the energy stored in a material is referred to as loss tangent:

$$\tan\delta = \frac{\varepsilon_r''}{\varepsilon_r'} \tag{4.13}$$

Mathematically, a medium is referred to as a good conductor if $\tan\delta >> 1$ and a good insulator if the reverse is true. It is important to note that the dielectric constant and loss factor are not constant quantities, since they are highly dependent on several factors such as frequency, temperature, moisture content, and composition of the material.

4.1.3 Significance of Electromagnetic Properties in Microwave Propagation, Scattering, and NDE

The interaction of a material with electromagnetic fields is entirely dependent on the material's electromagnetic properties. The amount of EM wave reflection and transmission at material boundaries, velocity and wavelengths of waves inside the material, and degrees of wave intensity attenuation are elements of microwave propagation and scattering that are determined by the electromagnetic properties. A set of simplified mathematical expressions describing EM wave propagation in free-space are subsequently provided, since the previously mentioned elements of microwave propagation and scattering are based on derived versions of these expressions.

For the case of a time-harmonic uniform plane EM wave in free-space propagating in the z-direction with an electric field $\bar{E}$ pointing in the x-direction, the solution to the wave equation form of Maxwell's equations has the form:

$$\bar{E} = \bar{x}E_0 \cos(\omega t - k_0 z) \tag{4.14}$$

where E_0 is the magnitude of the electric field and k_0 is the wave number which is determined from the dispersion relation for free-space:

$$k_0^{\;2} = \omega^2 \mu_0 \varepsilon_0 \tag{4.15}$$

The spatial period of the EM wave is referred to as wavelength, λ given by:

$$\lambda = \frac{2\pi}{k_0} = \frac{2\pi}{\omega\sqrt{\mu_0 \varepsilon_0}} \tag{4.16}$$

As already mentioned in Section 4.1, this wave representation is periodic both in time and space. In order to trace a certain point on the EM wave, one has to move in space at a velocity such that the field intensity is constant (*i.e.* $\omega t - k_0 z = \text{constant}$). Thus, an expression for the wave velocity in free-space can be obtained by differentiating the displacement with respect to time, as follows:

$$v = \frac{dz}{dt} = \frac{\omega}{k_0} \tag{4.17}$$

where the right hand side of Eq. 4.17 can be obtained from the dispersion relation in Eq. 4.15:

$$\frac{\omega}{k_0} = \frac{1}{\sqrt{\mu_0 \varepsilon_0}} \equiv c \tag{4.18}$$

where c represents the velocity of EM waves in free-space.

Velocity and Wavelength of Microwaves inside Dielectric Media

In dielectric materials such as concrete and other construction materials, EM waves travel with velocities lower than the velocity in free-space depending on the dielectric properties of the material. Correspondingly, their wavelengths are also shorter than their corresponding ones in free-space. Generalizing the free-space dispersion relation in Eq. 4.15, we obtain:

$$k^2 = \omega^2 \mu \varepsilon \tag{4.19}$$

After calculating the square root of Eq. 4.19, substituting the complex permittivity from Eq. 4.11, and noting that the permeability for most construction materials is to close to that of free-space, μ_0, (refer to Section 4.1.1), the complex wave number k is expressed as:

$$k = \omega \sqrt{\mu_0 \varepsilon'} \sqrt{1 - j \tan\delta} \tag{4.20}$$

Applying the Taylor expansion $\sqrt{1-x} \cong 1 - x/2$ for small x, Eq. 4.20 is approximated for small loss tangent values (Kong 1990):

$$k \cong \omega \sqrt{\mu_0 \varepsilon'} \left(1 - j \frac{\tan\delta}{2} \right) \quad \text{for } (\tan\delta << 1) \tag{4.21}$$

Based on this approximation, the velocity of microwaves in construction materials, given by replacing the real part of Eqs. 4.21 in 4.17, can be approximated as:

$$v \cong \frac{1}{\sqrt{\mu_0 \varepsilon'}} \quad \text{for } (\tan\delta << 1) \tag{4.22}$$

or more conveniently, it can also be expressed in terms of the free-space velocity and the dielectric constant of the material using Eq. 4.12:

$$v \cong \frac{c}{\sqrt{\varepsilon_r{}'}} \text{ for } (\tan\delta << 1) \tag{4.23}$$

Following the same approximations and noting that $\omega = 2\pi f$, where f is the frequency in Hz, the microwave wavelength inside a construction material is given by:

$$\lambda \cong \frac{2\pi c}{\omega\sqrt{\varepsilon_r{}'}} = \frac{c}{f\sqrt{\varepsilon_r{}'}} \text{ for } (\tan\delta << 1) \tag{4.24}$$

Attenuation and Penetration Depth

Microwaves dispersing in a lossy material experience a decrease in field amplitude. The rate of decrease is dependent on the conductivity of the medium, which in turn is directly dependent on the loss factor. The significance of microwave attenuation in NDE applications is that inhomogeneities or defects located at certain depths inside the material under test may remain undetected since their reflections may decay below noise levels. The degree of wave attenuation in lossy media is often expressed in terms of a penetration depth parameter, d_p which is defined as the distance over which the wave amplitude decays by $1/e$, and it is expressed as (Kong 1990):

$$d_p \cong \frac{2}{\sigma}\sqrt{\frac{\varepsilon'}{\mu_0}} \text{ for } (\tan\delta << 1) \tag{4.25}$$

where $\sigma = \sigma(f) =$ conductivity of the dielectric medium. Attenuation and penetration depth responses are often functions of frequency, which suggests that there are limits to frequency ranges that can be used in microwave radar applications for predetermined depths. Higher frequencies above the mentioned limits will not provide additional useful NDE information due to wave attenuation. However as it will be discussed in Chapter 5, resolution in microwave radar measurements is directly proportional to working frequencies and frequency bandwidths. Consequently, the trade-off between penetration capability of the NDE radar technology and the achieved resolution becomes an optimization problem.

4.2 Characterization of Dielectric Properties of Concrete and FRP Materials

4.2.1 State-of-the-Art for Dielectric Property Characterization

The appropriate measurement and characterization of dielectric properties is significantly important due to the influence of dielectric properties in non-destructive monitoring and evaluation of materials undergoing physical or chemical changes (Venkatesh and Raghavan 2005). Property characterization of dielectric materials could be accomplished through the application of various available measuring techniques. A brief review of selected techniques is presented hereafter.

Capacitor Model – Parallel Plate Capacitor Technique

The complex permittivity of materials can be measured using a perfect capacitor model. The specimen is placed between two parallel plates made of perfect conductive materials, and a uniform electric field over a large volume of space is generated (Al-Qadi *et al.* 1995). This technique requires the specimen to be of a certain shape, with flat surfaces on the two sides contacting the two parallel plates. The constraints on the shape of specimen and measurement condition limit the use of this technique, making it appealing for laboratory rather than in situ material characterization.

Resonator/Oscillator Model – Resonant Cavity Technique

The resonant cavity technique is proposed by the American Society for Testing and Materials (ASTM) as standard D252 (ASTM 2001). Baker-Jarvis *et al.* (1998) performed measurements of dielectric properties of low-loss materials whose loss tangent is less than 0.005 using closed and open cavity resonator methods to determine the real and imaginary parts of the complex permittivity. This technique can provide accurate results compared to other broadband techniques, but the results are obtained for single frequencies only. This implies the need for significant measurement effort when a wide range of frequency responses is expected. Additionally, this technology cannot measure sample sizes greater than the resonator capacity.

Transmission Line Model – Open-Ended Coaxial Probe Technique

The coaxial probe technique is based on the use of a cut-off section of a transmission line. The material is measured by placing the probe on its machined flat surface. The EM fields at the end of the probe change when the probe comes in contact with the material, and thus the material's permittivity can be computed from the measured reflected signals (Gershon *et al.* 1999). The coaxial probe technique requires intimate contact between the probe and the specimen to eliminate measurement errors induced by air gaps. The surface area, homogeneity, and thickness of the material are also constrained for the use of this technique. For example, Arai *et al.* (1995) suggested that the specimen surface roughness should be less than $0.5\mu m$ to minimize the air gap error. This technique is ideal for liquid and semi-solids, but could encounter difficulties in the characterization of materials with rough surfaces.

Transmission Line Model – Rectangular Waveguide Technique

The waveguide technique is categorized as a type of two-port measurement (transmission line) techniques. A material sample needs to be machined to fill in the contact area of the waveguide, and the EM wave transmission through the material is measured. The complex relative permittivity, ε_r^* and complex relative permeability, μ_r^* of the specimen are determined using the formula provided by Nicholson and Ross (1970). Waveguides can only operate in designated frequency bands associated with certain wave propagation modes. Several different samples are needed when measurements are conducted over a large frequency range. Inaccuracies in the measurements may occur due to air gaps between the waveguide and the specimen (Deshpande *et al.* 1997).

Free-Space Technique

In principle, free-space techniques are non-contact and non-destructive, and they require little sample preparation. Broadband characterization on isotropic or anisotropic materials under various incident angles, polarizations, and temperature conditions can be accomplished by this technique. The free-space technique can be further categorized into reflection-transmission (Maurens *et al.* 1992), reflection-only (Ghodgaonkar *et al.* 1989, Seo *et al.* 2004), and transmission-only (Aurand 1995) methods, depending on the corresponding experimental set-ups. Two types of measurements can be made using the free-space technique: reflection coefficients and transmission coefficients.

Estimation of dielectric properties based on reflection data could encounter potential difficulties when the radar operates at high frequencies. For instance, multiple reflections occurring at boundaries between layers in multi-layered systems need to be treated, and surface conditions of the material become crucial for wave reflection at high frequencies. In contrast, the use of transmission coefficient in the estimation of dielectric properties avoids these difficulties. However, the measurement of transmission coefficients cannot uniquely determine the complex permittivity of lossy construction materials such as concrete due to multiple combinations of the real and imaginary parts of the complex permittivity for the same transmission coefficient at single frequencies (Ghodgaonkar *et al.* 1989, Zhang and Huang 1999, Jose *et al.* 2000, Millard *et al.* 2002).

4.3 Development of Integrated Methodology for Determining Dielectric Properties of Concrete and FRP Materials

Based on the previous discussion, several experimental methods can applied to the measurement of material dielectric properties. Although each method has its own features and constraints, among these, the free-space technique appears to be more applicable for in situ measurements. In free-space measurements, transmission and reflection coefficients of the material under test can be measured, depending on the measurement scheme.

In order to find the value of complex permittivity, both the real and imaginary parts must be determined. Since there are two unknowns in the complex permittivity, two conditions are required for a mathematical determination. A unique determination of the complex permittivity may not be accomplished even with the availability of complex transmission coefficient from measurements. This is because one cannot explicitly derive relationships between the real and imaginary parts of the complex permittivity with the respective real and imaginary parts of complex transmission coefficient. Typical approaches to solve this problem are the use of root-searching or optimization techniques, which search for the most reasonable (optimal) combination within a given range of parameter values. An error evaluation criterion is often needed to resolve the object function. For lossless materials such as Teflon (related to poor or no conductivity, which is also related to loss factor), a unique optimal combination can be expected after the application of root-searching techniques at a single frequency. However, for lossy materials such as concrete and other construction materials, multiple combinations of real and imaginary parts of complex permittivity for the same transmission coefficient at single frequencies are observed (Ghodgaonkar *et al.* 1989, Zhang and Huang 1999, Jose *et al.* 2000, Millard *et al.* 2002).

The objectives of this chapter is to introduce an integrated methodology for determining unique combinations of complex permittivity for low-loss materials such as concrete, FRP, and other construction materials in general using free-space transmission coefficient measurements. The proposed methodology has been recently developed by the Infrastructure Science and Technology Group at MIT (Büyüköztürk *et al.* 2005).

4.3.1 Components of the Methodology

The methodology consists of two main components: (1) an estimation procedure of the real part of complex permittivity based on time difference of arrival (TDOA) information, and (2) a root-searching procedure of possible combinations of real and imaginary parts of the complex permittivity based on a theoretical representation of transmission coefficient (which is derived from EM wave theory), parametric system identification (SI), and an error sum of squares (SSE) criterion. Figure 4-2 illustrates the overview of the methodology. Each of the components is discussed in detail in the remainder of this section. The description of the theoretical representation of transmission coefficients is introduced first, as it provides the required framework for developing the TDOA estimation procedure.

4.3.2 Theoretical Representation of Transmission Coefficient

The EM wave transmission analysis is based on theoretical transmission coefficients for a two-dimensional model of EM uniform plane wave propagation through a dielectric medium proposed by Kong (1990). A schematic of this model is provided in Figure 4-3. By solving Maxwell's equations (refer to Section 4.1.1) and applying energy conservation principles with appropriate dispersion relations for the particular case at hand, the expression of the complex transmission coefficient T^* for transverse electric (TE) waves is given as follows:

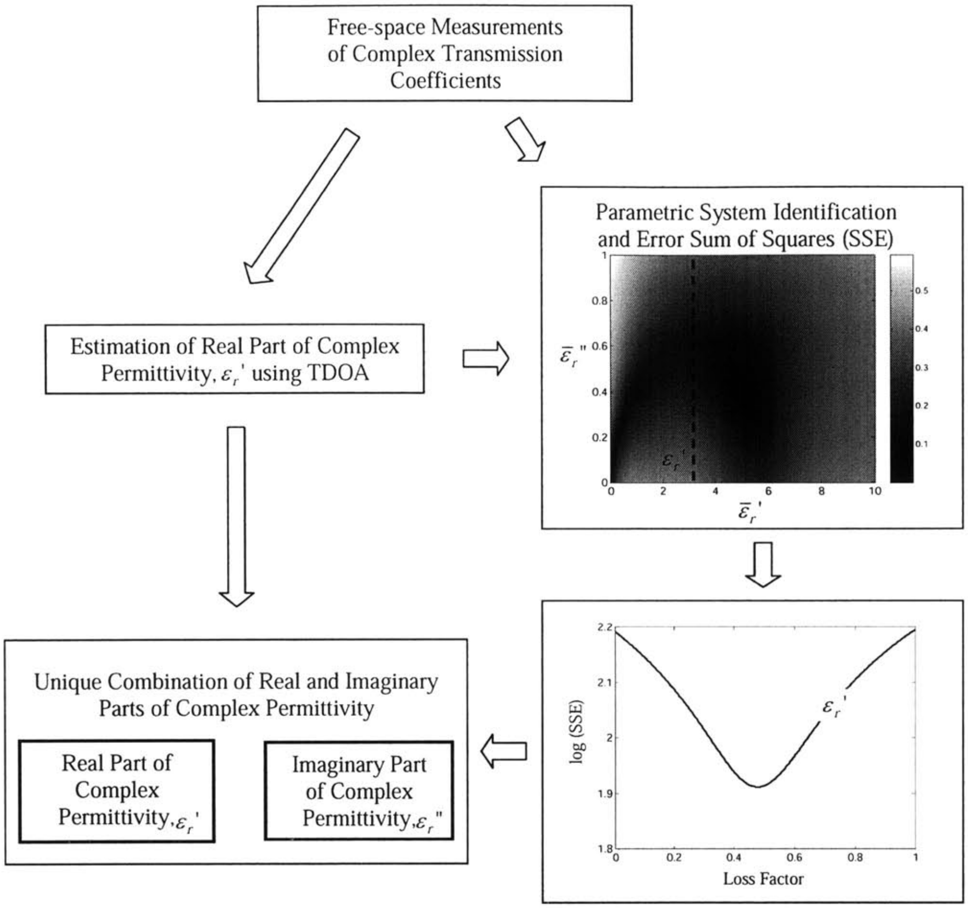

Figure 4-2 Overview of the proposed methodology for dielectric property characterization (Büyüköztürk *et al.* 2005)

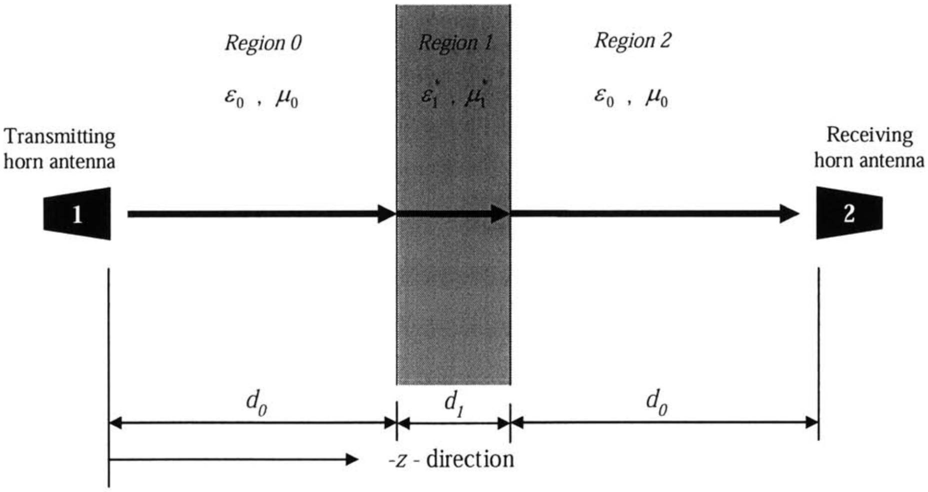

Figure 4-3 Two-dimensional model for EM wave transmission analysis

$$T^{*}=\frac{4e^{j(k_{1z}-k_{0z})d_1}}{(1+p_{01})(1+p_{10})\left(1+R_{01}R_{10}e^{j2k_{1z}d_1}\right)} \qquad (4.26)$$

where,

$$k_{0z}=\omega\sqrt{\varepsilon_0\mu_0}\cos\theta$$

$$k_{1z}=k_0\sqrt{\varepsilon_r^{*}-\sin^2\theta}$$

$$p_{01}=\frac{k_{1z}}{k_{0z}}=\frac{1}{p_{10}}=\frac{\mu_0 k_{1z}}{\mu_1^{*}k_{0z}}$$

$$R_{01}=\frac{1-p_{01}}{1+p_{01}}=\frac{1}{R_{10}}$$

d_1 = thickness of the specimen

ω = wave angular frequency

θ = angle of incidence

μ_0 = the permeability of free-space

μ_r^{*} = the complex relative permeability of the specimen

ε_0 = the permittivity of free-space

$\varepsilon_r^{*}=\varepsilon_r^{'}-j\varepsilon_r^{''}$ = complex relative permittivity of the specimen, $\varepsilon_r^{'}$ and $\varepsilon_r^{''}$ are its real and imaginary parts, respectively.

The EM wave propagation phenomenon through a dielectric material specimen is modeled as a two-dimensional problem. The use of this model is justified by the choice of an appropriate corresponding experimental set-up, in which uniform plane wave conditions are achieved by satisfying the far field condition (which is discussed in Section 4.4.2). Additionally, the assumption of material homogeneity in the theoretical model leads to a global description of dielectric properties for the specimen under investigation.

4.3.3 Estimation Procedure based on Time Difference of Arrival (TDOA)

The TDOA technique is used to estimate the dielectric constant of a low-loss (less conductive) material using experimental measurements of transmission coefficients. This technique is conceptually based on the same two-dimensional theoretical model for EM wave propagation previously described. For the case of normal incidence, the time domain representation of an EM plane wave is (Stone 1996):

$$E_i = E_0\left(t - \frac{z}{c}\right) \tag{4.27}$$

where E_i = incident wave propagating in the z-direction, E_0 = amplitude of the signal, t = propagation time, z = propagation direction, and c = speed of light. An illustration of the EM transmission through the dielectric medium is presented in Figure 4-4.

Considering only the first peak response in the transmission measurement, the first transmitted pulse is represented as:

$$E_{t1}(t) = T_{01}T_{10}E_0\left(t - \frac{z}{c} - \Delta t\right) \tag{4.28}$$

where T_{01} and T_{10} are transmission factors accounting for the EM wave transmission through both faces (front and back) of the plate specimen. Here, Δt is the time difference of arrival. In this formulation the first-peak assumption holds since the loss is considered primarily due to energy absorption in the specimen rather than transmission losses. The difference in arrival time due to the presence of the specimen is found by setting the argument in Eq. 4.28 to be zero, thus:

$$t - \frac{z-d}{c} - \frac{d\sqrt{\varepsilon_r^{'}}}{c} = 0 \tag{4.29}$$

Note that Eq. 4.29 is a simplified velocity representation since the wave velocity in the medium is assumed to be $c/\sqrt{\varepsilon_r{}'}$, which is applicable when the loss factor of the specimen is small (refer to Eq. 4.23). Further discussion on the accuracy of this simplification is available in Section 4.6.2 later in this chapter. Assuming that $z = 0$ at the first boundary of the dielectric medium, and after rearranging, it is found that:

$$\Delta t = \frac{d}{c}\left(\sqrt{\varepsilon_r^{'}} - 1\right) \tag{4.30}$$

where Δt constitutes the additional propagation time (or time difference of arrival) between the transmitting and receiving antennas over the time corresponding to the measurement when the specimen is not present. The estimation of Δt is achieved by processing the measured transmission coefficient from frequency-domain to time-domain using inverse Fourier transformation. Eq. 4.30 can be used as a tool for assessing the dielectric constant of the specimen by estimating its time difference of arrival using a set of experimentally measured transmission coefficients over a certain frequency band. The expression of dielectric constant can be derived from Eq. 4.30 as follows:

$$\varepsilon_r' = \left(1 + \frac{c \cdot \Delta t}{d}\right)^2 \tag{4.31}$$

The accuracy of the Δt estimation depends on the frequency bandwidth of the signal being processed (further discussion presented in Section 4.6.2) and the accurate measurement of the specimen thickness. This estimate will be the basis for the identification of the complex permittivity that characterizes the dielectric material specimen.

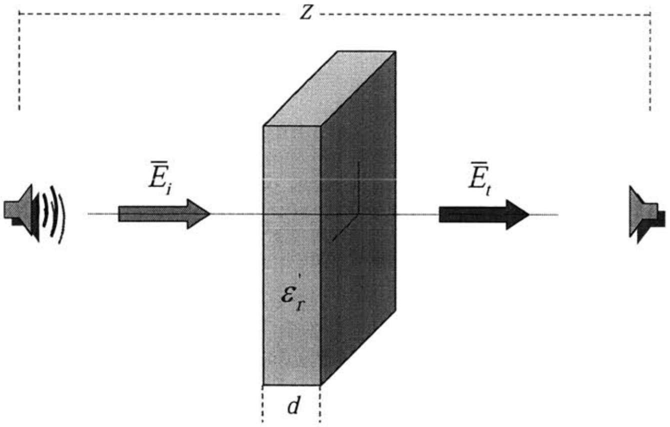

Figure 4-4 Illustration of theoretical framework for TDOA estimation

4.3.4 Root-Searching Procedure of Combinations of Dielectric Constant and Loss Factor based on Parametric SI and SSE Criterion

As noted by other research studies (Ghodgaonkar *et al.* 1989, Zhang and Huang 1999, Millard *et al.* 2002), the complex permittivity cannot be explicitly represented in terms of the S-parameter S_{21}^*, which is a measured value of EM wave transmission. Furthermore, the exact solution for the complex permittivity is not straightforward due to the multiple roots associated with Eq. 4.26 for lossy materials (Jose *et al.* 2000). In order to solve this problem, a root-searching procedure involving the use of parametric system identification (SI) and an error sum of squares (SSE) criterion are proposed. Parametric SI refers to the use of a mathematical model to characterize the behavior of a system based on experimental information (Venkatesh and Dahleh 2001). Parametric SI is applied for generating an array of theoretical estimations of transmission coefficients. Thereafter, the SSE criterion is introduced for estimating the error between the theoretical estimations and the measured transmission coefficients.

Experimental measurements must be conducted in coherent condition, where the measured complex S-parameter S_{21}^* equals the complex transmission coefficient, T^*. The coherent condition provides a non-distorted phase in the measurement of S_{21}^* (between antennas 1 and 2, Figure 4-3) such that amplitude attenuation within the specimen does not contribute to the transmission coefficient. The magnitude of complex transmission coefficient is expressed in decibels (dB) as:

$$T_{dB} = 10 \cdot \log\left(S_{21}^* \cdot \overline{S}_{21}^*\right) \tag{4.32}$$

where T_{dB} is a real number and $\overline{S}_{21}^*$ is the complex conjugate of S_{21}^*. It is observed from Eq. 4.26 that the complex transmission coefficient is a function of frequency, thickness of the dielectric specimen, and the complex permittivity (dielectric constant and loss factor), as well as the magnitude of complex transmission coefficient, thus:

$$T_{dB} = T_{dB}\left(\omega, d, \varepsilon_r', \varepsilon_r''\right) \tag{4.33}$$

The measured T_{dB} can be calculated by substituting the measured S_{21}^* into Eq. 4.32 to yield T_{dB}^m from the measurements. Figure 4-5 shows an example of T_{dB}^m values as functions of frequency corresponding to EM transmission measurements on a concrete slab specimen.

The estimated/predicted T_{dB}, denoted by T_{dB}^p, can be calculated by substituting theoretical T^* into Eq. 4.32. In order to graphically illustrate the characteristics of the wave propagation through a dielectric medium, Figures 4-6 through 4-8 show the effects of varying layer thickness, dielectric constant, and loss factor values on the predicted (theoretical) transmission coefficient. Parametric SI is carried out by generating a set of T_{dB}^p from possible combinations of ε_r' and ε_r''. From these possible combinations, those which will result in minimum difference between T_{dB}^m (measurement) and T_{dB}^p (theory)

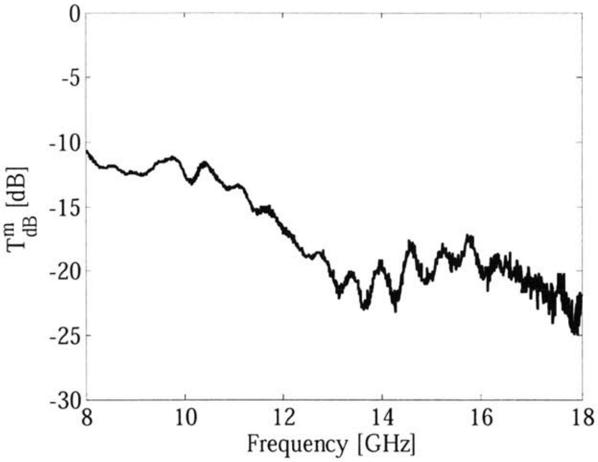

Figure 4-5 Experimentally measured transmission coefficient for a concrete slab specimen

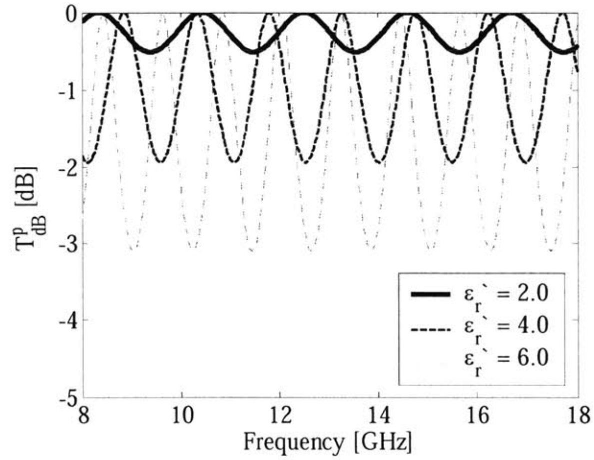

Figure 4-6 Effect of dielectric constant on predicted transmission coefficient (layer thickness d_1 = 50 mm, loss factor ε_r'' = 0.0)

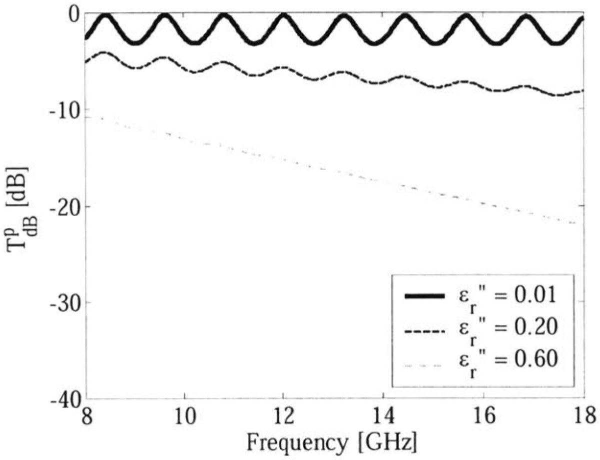

Figure 4-7 Effect of loss factor on predicted transmission coefficient (layer thickness d_1 = 50 mm, loss factor $\varepsilon_r^{'}$ = 6.0)

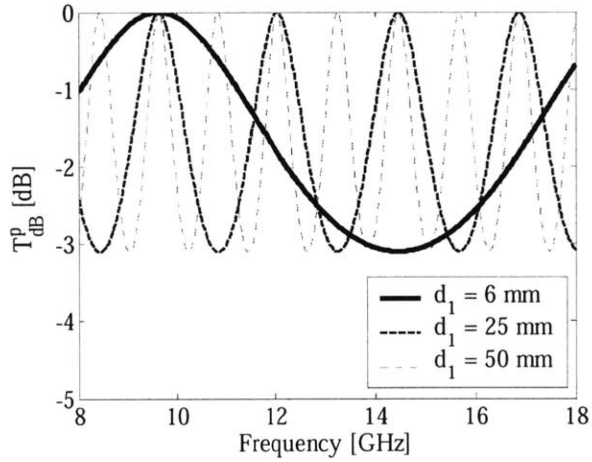

Figure 4-8 Effect of layer thickness on predicted transmission coefficient (dielectric constant $\varepsilon_r^{'}$ = 6.0, loss factor $\varepsilon_r^{''}$ = 0.0)

will be the estimates closest to the actual physical values. Estimation error between T_{dB}^{m} and T_{dB}^{p} is evaluated using an error sum of squares (SSE) criterion. Each combination of $\varepsilon_r^{'}$ and $\varepsilon_r^{''}$ generates a corresponding SSE value, which is expressed by:

$$SSE\left(\varepsilon_r^{'},\varepsilon_r^{''}\right)=\sum_{i=1}^{n}\left|T_{dB}^{m}\left(\omega_i\right)-T_{dB}^{p}\left(\omega_i,\varepsilon_r^{'},\varepsilon_r^{''}\right)\right|^2 \tag{4.34}$$

where n is the number of frequencies in the measured frequency band. With the assistance of the SSE criterion, an error surface is generated for various combinations of $\varepsilon_r^{'}$ and $\varepsilon_r^{''}$, as shown in Figure 4-9 for the same concrete specimen previously introduced in Figure 4-5. Using the estimated dielectric constant obtained through the TDOA technique, a corresponding error curve containing various combinations of loss factor can be located from the error surface, as shown in Figure 4-10. The optimal loss factor is determined by selecting the one with minimum error on the curve. Hence, the root-searching procedure is accomplished.

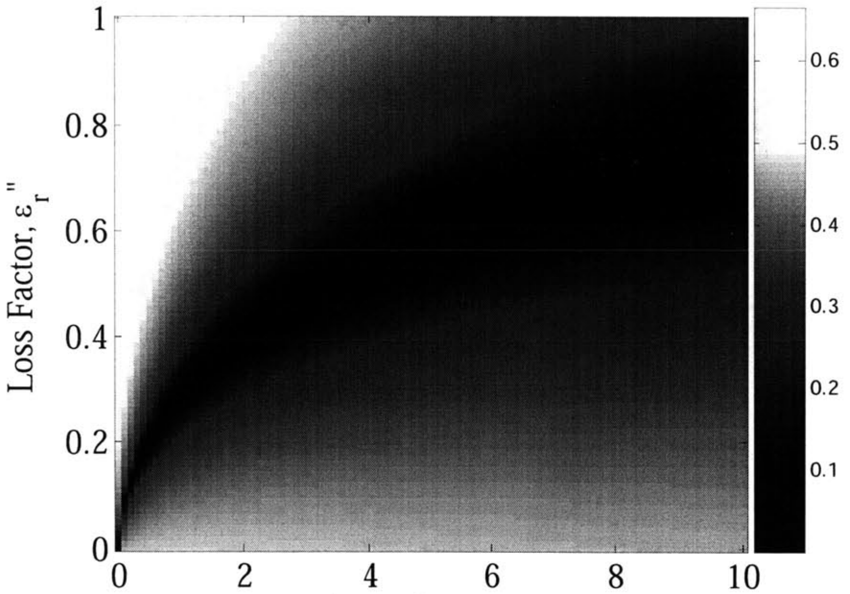

Figure 4-9 Estimation error surface using parametric SI and SSE criterion for concrete slab specimen. Color coding represents log(SSE)

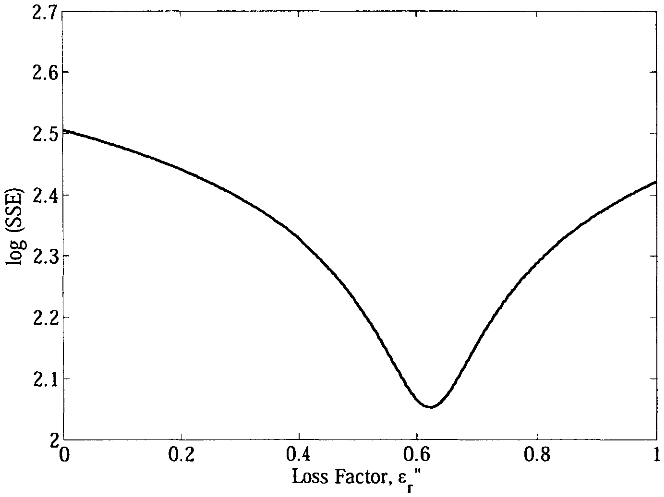

Figure 4-10 Result of root-searching procedure for identification of loss factor for concrete slab specimen

4.4 Experimental Program for Dielectric Property Measurements

In order to implement the methodology described in Section 4.3, experimental measurements of transmission coefficients were conducted for several materials, some of which have been previously documented in existing literature in terms of their dielectric properties to serve as benchmark results. Concrete and various FRP composite specimens were used in this study. In this section, details of the experimental set-up and measurement parameters, specimen descriptions, and results of the implementation of the methodology for dielectric property characterization are presented.

4.4.1 Sample Description

Plate-type specimens of 305 by 305 mm^2 cross-section with varying thicknesses were used. The selected width and height of the specimens meet the requirement for radar measurements in far field condition, which is further discussed in the Section 4.4.2. Table 4-1 shows the details of the text matrix used for this study such as the material used for manufacturing each specimen, the plate thickness, and the angle of incidence used in radar measurements. The concrete specimen was manufactured using mix proportions of Portland cement Type I / sand / coarse aggregate = 1.0 / 2.5 / 3.2 by weight with a water-to-cement ratio, $w/c = 0.60$. The concrete mix used in this study is the same used throughout the mechanical and radar studies of FRP-confined concrete presented in Chapters 3 and 5. All FRP materials were obtained from Fyfe Co. LLC. Three glass-based and one carbon-based FRP composite systems were used. All reinforcing fabrics were saturated with Tyfo® S Epoxy. The reinforcing fabrics were: Tyfo® SEH-51A – custom wave, unidirectional glass fabric with yellow glass cross fibers at 90°, Tyfo® WEB – made of 0° and 90° bi-directional weaved glass fibers with equal fiber content in both directions, Tyfo® BC – made of bi-directional weaved glass fibers oriented at ± 45 ° directions, and Tyfo® SCH-41 – custom wave, unidirectional carbon fabric with glass cross fiber for added stability. The FRP samples were manufactured by extruding a 3660 mm^2 (1 ft^2) square from the different types of fabrics, which were then saturated with Tyfo® S epoxy. The specimens were cured for seven days before testing. Benchmark materials were Teflon, Lexan, and Bakelite, whose dielectric properties have been already established in existing research literature.

Specimen Material	Thickness [mm]	Incidence Angle during Measurement
Teflon	6.0	0°, 30°
Lexan	6.0	0°, 30°
Bakelite	6.0	0°, 30°
Tyfo® SEH-51A (1 layer)	1.5	30°
Tyfo® WEB (1 layer)	1.5	30°
Tyfo® BC (1 layer)	1.5	30°
Tyfo® SCH-41 (1 layer)	1.5	30°
Concrete	50.0	0°
Concrete + 1 Layer of Tyfo® SEH-51A	51.5	0°

Table 4-1 Test matrix for dielectric property characterization

4.4.2 Experimental Configuration and Measurement Parameters

The experimental set-up used in this work to measure the transmission of EM waves through a dielectric material involved a network analyzer and a pair of horn antennas. The network analyzer was a Hewlett Packard Model 8510C that was operated in stepped-frequency mode. This equipment is located at the Mini-Chamber facility, Building 1715 at MIT – Lincoln Laboratory. The objective of the experiments was to obtain the complex transmission coefficients for a broad range of frequencies. Pictures of the measuring equipment are presented in Figure 4-11.

Far field conditions were necessary to ensure accuracy and validity of the radar measurements. The far field condition is required to ensure that the wave front is approximately plane, which is directly related to the theoretical methodology herein used for dielectric property characterization. Far field conditions also minimize complex wave behavior in near-field between the horn antennas and the specimen. For the case of a horn antenna of rectangular cross-section and characteristic dimension *w*, far field condition is guaranteed by (Blejer, D., personal communication, 2005):

$$R > \frac{2w^2}{\lambda} \tag{4.35}$$

where R = distance from the horn antenna to the FRP sample, and λ = microwave wavelength. Considering the highest frequency of 18 GHz for the proposed experiments, it was calculated that the specimen should be placed at least 0.5 *m* away from the horn antennas to satisfy far field condition, and the minimum area of the slab specimens should be greater than 160 cm^2 for adequate illumination. The applied experimental set-up meets these requirements. Direct coupling between the horn antennas was also eliminated in this experimental set-up due to the use of the network analyzer. The unwanted coupling between antennas is measured in free-range and stored in the phase angle information collected by the network analyzer. This information is then used in the calibration of all consequent measurements (Cullen 1987).

The radar measurements of complex transmission coefficients were collected using two different measurement schemes: EM wave propagation at normal (0°) incidence and EM wave propagation at an angle of 30° from normal incidence, as depicted in Figure 4-12. The alternative 30° incidence angle was used to reduce the noise levels in the signals, which would aid for a better understanding of the wave transmission capabilities of dielectric specimens under test. However, only measurements at normal incidence are used for dielectric property characterization, since the use of normal incidence is in line with the framework developed for estimating time differences of arrival and theoretical transmission coefficients.

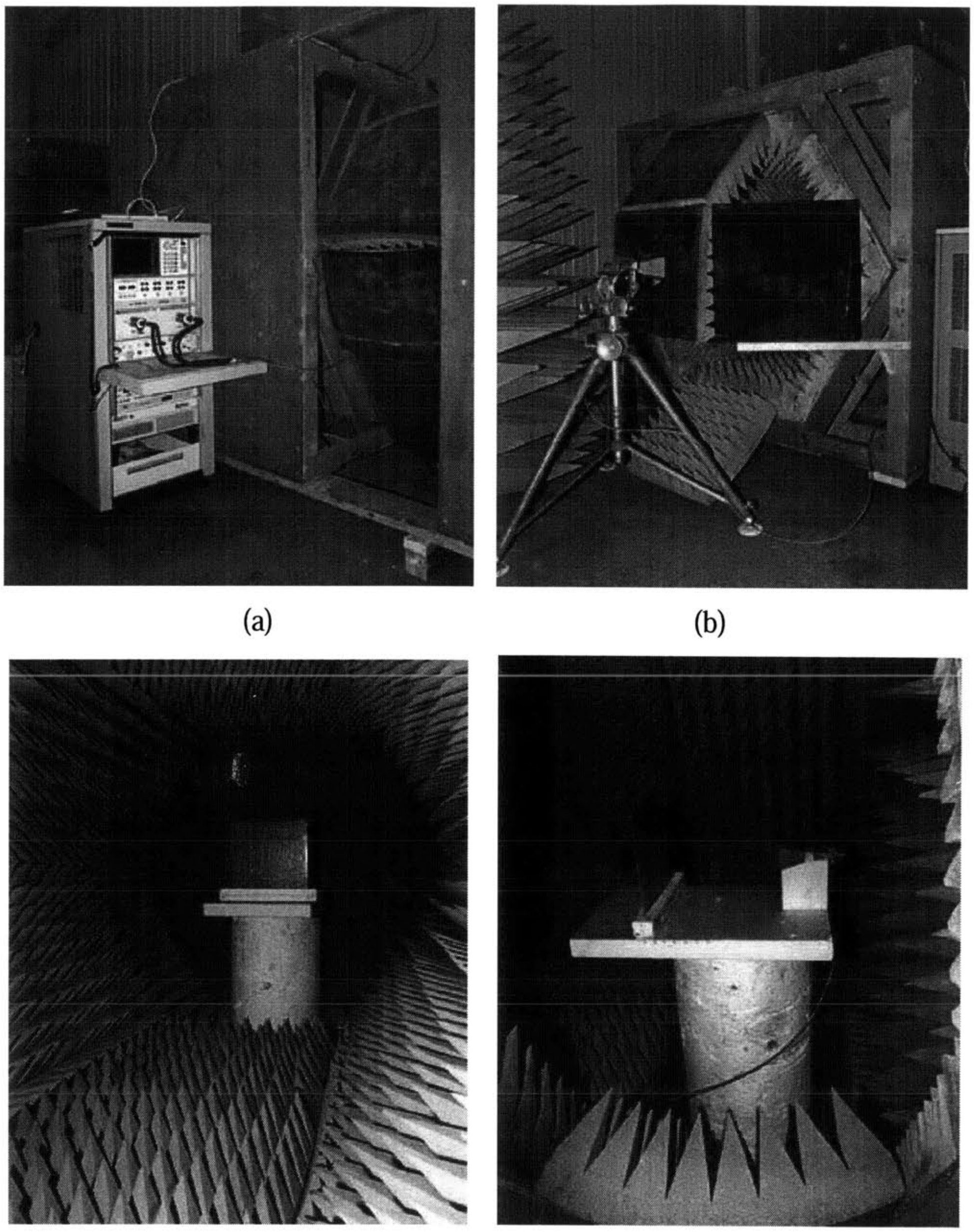

(a) (b)

(c) (d)

Figure 4-11 Experimental set-up for dielectric property measurements
a) Network analyzer, b) Transmit horn, c) FRP sample, d) FRP sample and receive horn
(Pictures courtesy of Dennis Blejer)

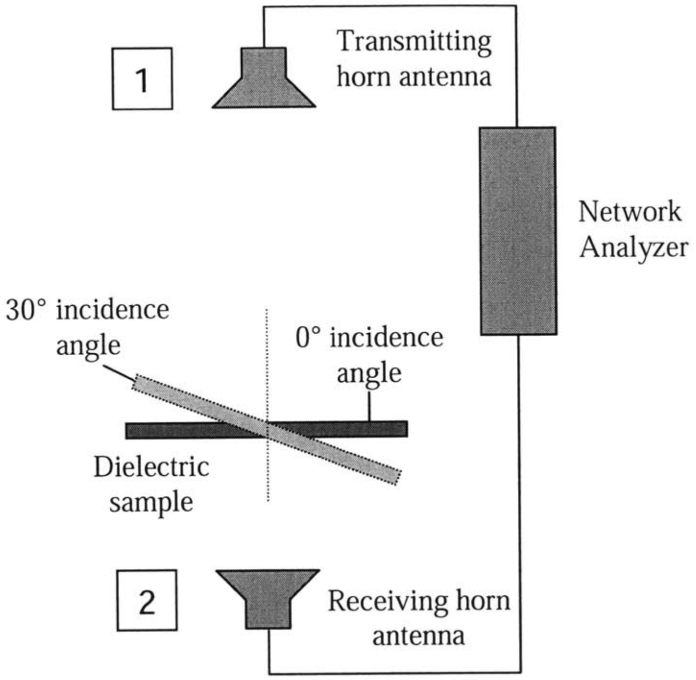

Figure 4-12 Radar measurement schemes for EM wave propagation at 0° and 30° incidence

Transmission measurements were collected in X-band through Ku-band (8-12 and 12-18 *GHz*) with a frequency step of 12.5 *MHz*. A typical set of measurements consisted of signal amplitudes, phase angles, and their corresponding frequencies. The amplitude and phase information were combined using complex notation:

$$S_{21} = \left[10^{\frac{amplitude}{20}} \cos(phase) \right] + j \cdot \left[10^{\frac{amplitude}{20}} \sin(phase) \right] \tag{4.36}$$

Non-calibrated data in the form of Eq. 4.36 was then properly calibrated using free-range measurements, which were conducted in the absence of the specimen. The calibrated complex transmission coefficient was:

$$S_{21}^{*} = \frac{S_{21}}{S_{21}^{free-range}} \tag{4.37}$$

Finally, the magnitude of complex transmission coefficient was expressed in decibels yielding T_{dB}^{m} by application of Eq. 4.32.

4.5 Experimental Results and Characterization of Dielectric Properties

4.5.1 Measurements of Transmission Coefficients

Figure 4.13 shows the results of transmission coefficient measurements for all materials for the 8-18 GHz frequency band. The transmission coefficients are presented in a dB scale. From the information obtained from these measurements, it was concluded that glass-based FRP (GFRP) specimens were highly transmissive, with transmission losses of approximately up to 4 dB. In contrast, carbon-based FRP (CFRP) specimen did not allow significant EM wave transmission, with transmission losses of approximately 30 dB. Additionally, from the measurements of the various GFRP composite laminates at 30° incidence angle, it is observed that the transmission coefficient curves show similar trends. Thus, based on this observation and their high transmissivity characteristics, GFRP composite materials are suited for the application of the dielectric property characterization methodology developed in this study. On the other hand, characterization of dielectric properties on CFRP composites becomes challenging due to their low transmission of EM waves when using a radar microwave method. In view of these results, the subsequent computations and discussions focus on only one type of FRP composite: Tyfo® SEH-51A. This fabric is representative of the GFRP laminates herein studied, and also it is the type of GFRP that was used in the FRP-confined concrete mechanical investigations presented in Chapter 3 and the damage assessment investigations using radar presented in Chapter 5.

Concrete, which is characterized as a low-loss material in dry conditions, registered transmission losses ranging from 10 to 30 dB. Transmission measurements through the concrete specimen and the concrete specimen bonded with 1 layer of Tyfo® SEH-51A showed comparable values for power loss, which further validates the transmissive character of GFRP composites in radar NDE applications. These results become significantly important in view of the developments presented in Chapter 5 with regards to damage assessment of GFRP-confined concrete elements using radar NDE. In contrast with CFRP and concrete, all benchmark materials (Teflon, Lexan, Bakelite) showed moderate transmission losses.

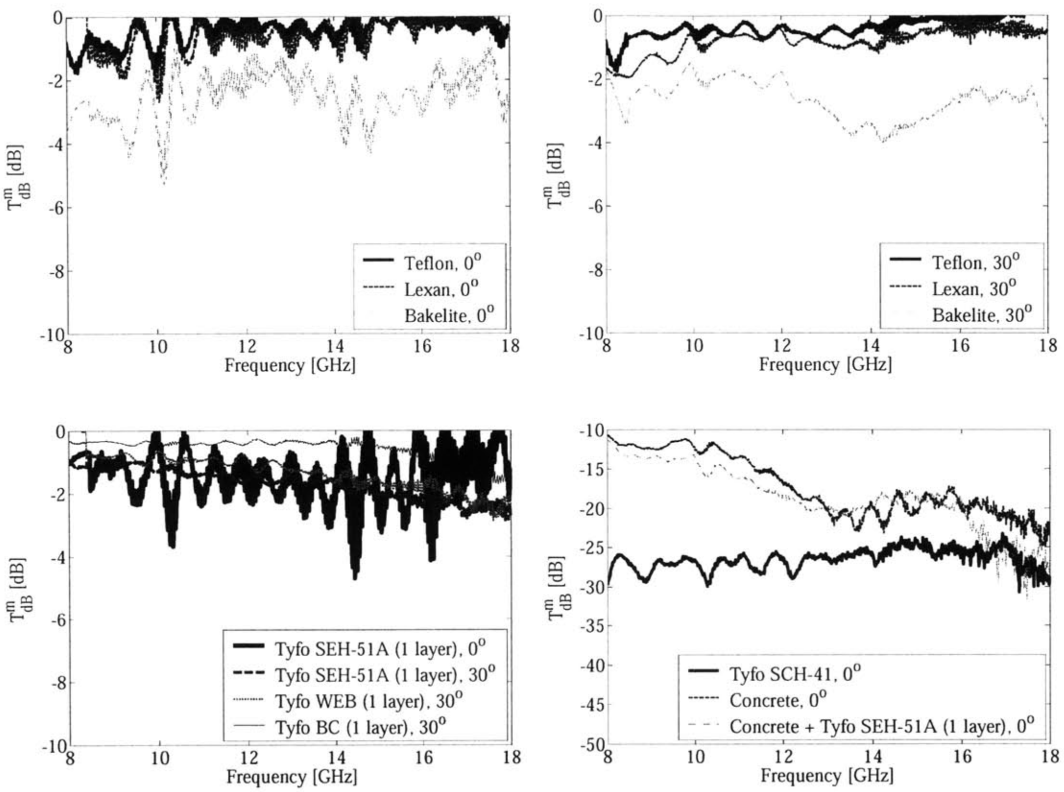

Figure 4-13 Radar measurements of transmission coefficients

4.5.2 Estimation of the Dielectric Constant using TDOA

The TDOA technique was used to estimate the dielectric constants of materials under investigation from both X- and Ku- bands. After performing inverse Fourier transformation of the experimental transmission coefficient data for the 8-18 GHz frequency band, the time difference of arrival values, Δt, for the materials considered in this study were calculated. Figure 4.14 shows the results for the inverse Fourier transformation of transmission coefficient information for free-space and for the concrete slab specimen previously introduced in Figure 4-5 and the procedure of how Δt was estimated. The results for time difference of arrival values are tabulated in Table 4-2. Using the time difference of arrival information, application of Eq. 4.31 yielded estimates for dielectric constants, which are also tabulated in Table 4-2. For the case of one layer of Tyfo® SEH-51A, the TDOA technique could not provide reliable results due to the small thickness of the specimen. Further discussion on this item is presented in Section 4.6.2

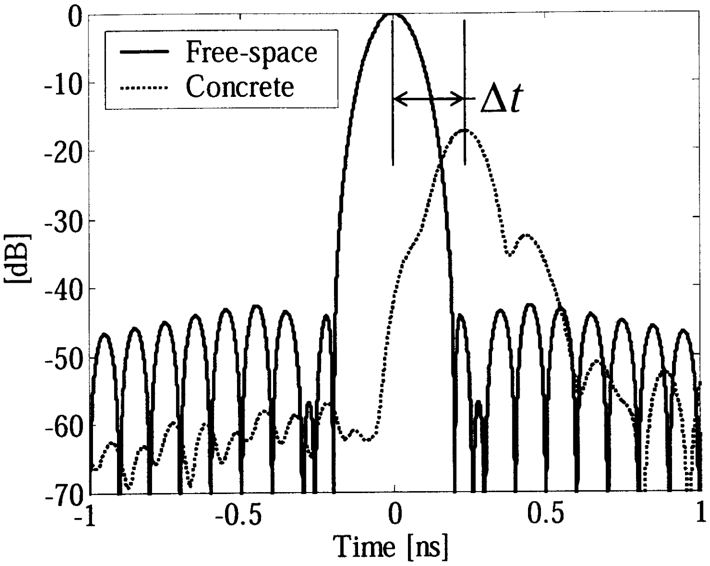

Figure 4-14 Estimation of time difference of arrival (TDOA)

Material	Δt [ns]	Estimated Dielectric Constant
Teflon	0.007	1.79
Lexan	0.012	2.48
Bakelite	0.030	5.95
Tyfo® SEH-51A (1 layer)	-	-
Concrete	0.235	5.69

Table 4-2 Dielectric constant estimations based on TDOA for 8-18 GHz

4.5.3 Root-Searching Results for Loss Factor

Following the root-searching procedure, optimal loss factor values were calculated by extracting an error curve using TDOA information from the error surfaces generated by parametric SI and SSE criterion, as it was illustrated in Section 4.3.4. The loss factor corresponding to the minimum SSE on the error curve is identified as the most appropriate value or characterization. The estimated loss factors thus found are provided in Table 4-3 for the test materials. Figures 4-15 and 4-16 show the implementation of parametric SI, SSE criterion, and root-searching procedures used to obtained the data in Table 4-3.

Material	Estimated Dielectric Constant	Estimated Loss Factor	Dielectric Constant from Literature	Loss Factor from Literature
Teflon	1.79	0.04	2.0 [1]	0.0008 [1]
Lexan	2.48	0.04	2.8 [2]	-
Bakelite	5.95	0.28	3.6 [1]	0.2 [1]
Concrete	5.69	0.62	4.4 - 7.2 [3]	0.3 - 0.7 [3]

[1] Harrington 2001, [2] Power Corporation 1996, [3] Rhim and Büyüköztürk 1998

Table 4-3 Characterization of complex permittivity for all test materials

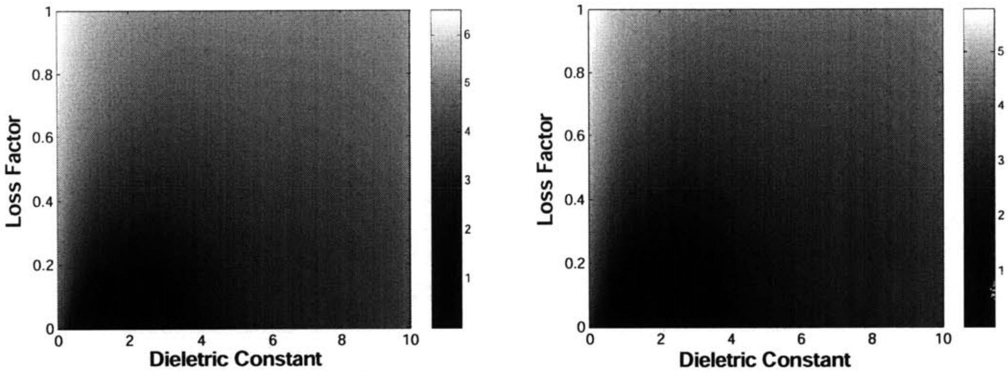

(a) Teflon (b) Lexan

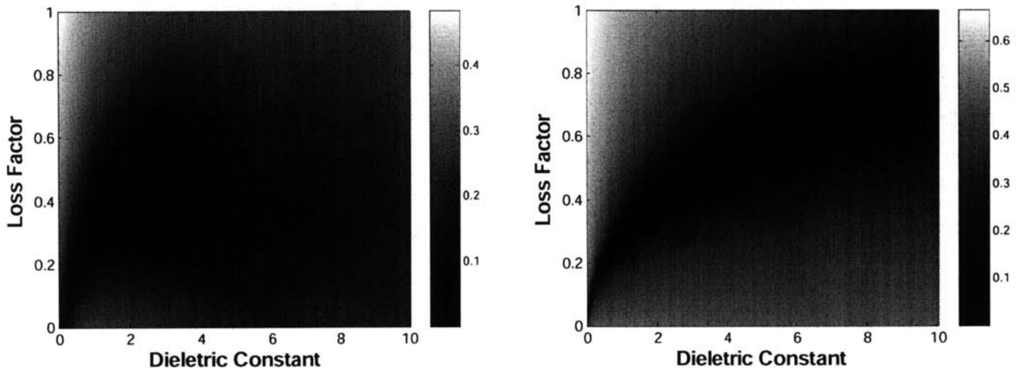

(c) Bakelite (d) Portland cement concrete

Figure 4-15 Estimation error surfaces using parametric SI and SSE criterion

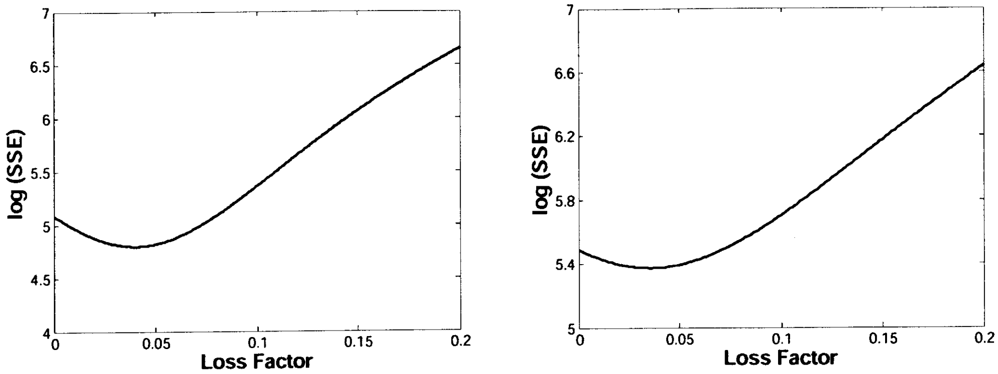

(a) Teflon

(b) Lexan

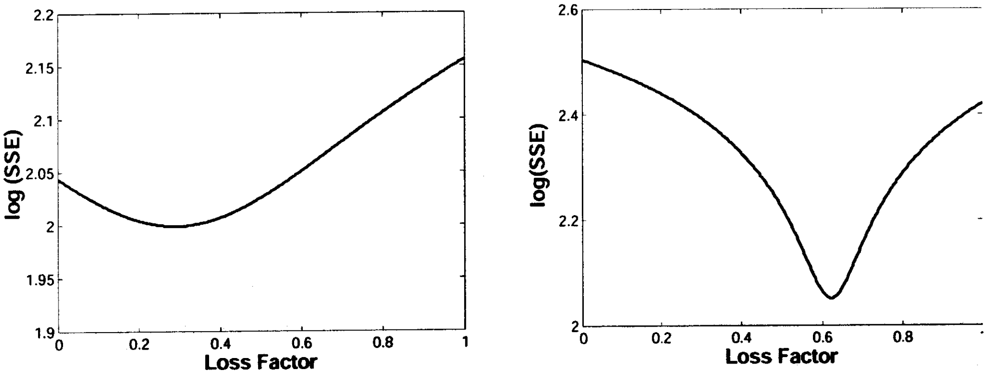

(c) Bakelite

(d) Portland cement concrete

Figure 4-16 Results of root-searching procedure for identification of imaginary part of complex permittivity

4.6 Discussion of Results

From the results for benchmark materials Teflon, Lexan, and Bakelite, it was found that a unique combination of real and imaginary parts of the complex permittivity can be obtained through the application of the proposed methodology. For low-loss materials such as concrete, the problem of non-uniqueness of real and imaginary parts of complex permittivity was observed and subsequently resolved, and appropriate values were predicted using the developed methodology. Based on the results presented in Table 4-3, the estimated dielectric constant values of Teflon, Lexan, Bakelite, and concrete are in agreement to reported values or within reported ranges. However, it should be emphasized that the values found using the proposed methodology for dielectric constants and loss factors do not exactly correlate with the reported values in the literature because of the differences in applied measuring techniques and frequency ranges used in experimental measurements. This is especially true for loss factor values. Note that in Table 4-3, not all loss factor comparisons could not be made because of the lack of information in the literature. Also, loss factor values are generally more sensitive to measurement frequency and experimental parameters.

4.6.1 Effect of Selected Frequency Bands in TDOA

Time difference of arrival estimates were obtained using the entire sets of measurements over the X- and Ku- bands. For potential practical applications of this methodology, the question arises as to what would be the optimum frequency band needed to provide a sound estimate for the dielectric constant. Table 4-4 presents a summary of different estimates of dielectric constant using time difference of arrival values that were calculated for various frequency bands. Calculations were conducted in 1 *GHz* intervals covering the range from 8 *GHz* to 18 *GHz*. After comparing the results presented in Table 4-4 with the dielectric constant estimates from Table 4-3, it is observed that estimates calculated from narrow frequency ranges may provide poor estimates for dielectric constant values. Accurate estimates using the TDOA technique may require the use of wide frequency ranges for uniquely identifying the dielectric constant that characterizes the specimen under investigation. The accuracy of such estimation is critical to the subsequent assessment of the loss factor.

Material	Frequency Range [GHz]									
	8 - 9	9 - 10	10 - 11	11 - 12	12 - 13	13 - 14	14 - 15	15 - 16	16 - 17	17 - 18
Teflon	1.42	5.80	1.89	1.89	2.37	1.18	1.32	2.28	2.28	2.34
Lexan	-	6.05	6.96	2.25	2.53	2.06	4.53	3.61	2.41	3.23
Bakelite	-	0.96	14.75	5.38	8.86	8.17	5.45	4.69	9.76	-
Concrete	4.80	6.03	6.64	5.30	5.01	4.66	8.04	6.76	5.99	4.47

Table 4-4 Estimates for dielectric constant using TDOA for different frequency ranges

4.6.2 Limitations of the Use of TDOA Information

From the results for the one-layer Tyfo® SEH-51A specimen, it was observed that the thickness of the sample critically affects the performance of TDOA technique. Thus, a minimum thickness limitation might be necessary to the accurate characterization of dielectric constant of construction materials using the proposed methodology. Based on the presented investigation, measurements of specimens of 6 *mm* or larger would provide acceptable results.

Another potential limitation of the use of TDOA information could be related the accuracy of the wave velocity approximation used in the theoretical development of the TDOA technique. From EM wave theory it is known that the wave (phase) velocity of EM waves is the function of the material's dielectric properties. For instance, the phase velocity, v_p for lossy materials within a medium is (Kong 1990):

$$v_p = \frac{\omega}{k_R} = \frac{1}{\sqrt{\mu\varepsilon}} \cdot \left[\frac{1}{2} \left(\sqrt{1 + \frac{\sigma^2}{\omega^2 \varepsilon^2}} + 1 \right) \right]^{-1/2} \tag{4.38}$$

where $k_R =$ real part of the complex wave number, $k = k_R + i \cdot k_I$. The first order expansion of v_p provides:

$$v_p \cong \frac{1}{\sqrt{\mu\varepsilon}} \cdot \left[1 + \frac{1}{8} \left(\frac{\sigma}{\omega\varepsilon} \right)^2 \right]^{-1} \tag{4.39}$$

For lossless materials the electrical conductivity, σ is zero, and the wave velocity then becomes:

$$v_p = \frac{1}{\sqrt{\mu\varepsilon}} = \frac{c}{\sqrt{\mu_r' \varepsilon_r'}} \tag{4.40}$$

For non-magnetic materials such as concrete, v_p becomes $c/\sqrt{\varepsilon_r'}$, which is the wave velocity representation used in the TDOA estimation. Eq. 4.29 is used in the TDOA procedure because of its simplicity, and it is considered as a convenient approximation of Eq. 4.38 when $\sigma/\omega\varepsilon \ll 1$. To investigate the accuracy of this approximation, a comparative study was performed. Wave velocities using Eqs. 4.38, 4.39, and 4.40 were calculated with respect to different values of $\sigma/\omega\varepsilon$ ranging from 0 to 20, as shown in Figure 4-17. It is observed that the differences between Eqs. 4.38 and 4.40 or between Eqs. 4.39 and 4.40 may be substantial when $\sigma/\omega\varepsilon$ is greater than 1. Nevertheless, in the range of investigation where $(\sigma/\omega\varepsilon)_{\max} = 0.1$ which applies to applications of construction materials, the mentioned differences are not significant as demonstrated in

Figure 4-17 (b). Hence, the use of Eq. 4.40 in the methodology for dielectric property characterization of construction materials is justified.

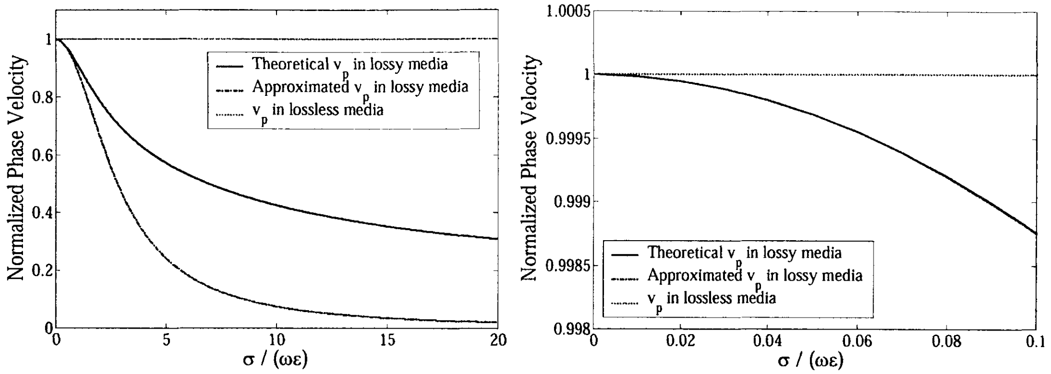

(a) $\sigma/\omega\varepsilon = 0 \sim 20$ (b) $\sigma/\omega\varepsilon = 0 \sim 0.1$

Figure 4-17 Comparative study of different phase velocity representations

Chapter 5

Radar Measurements of FRP-Confined Concrete

The objective of this chapter is to present an exploratory research effort dealing with the application of high resolution radar technologies for detecting and assessing defect and damage features in FRP-confined concrete specimens. The experimental program focused on inverse synthetic aperture radar (ISAR) measurements of various specimen configurations such as plain concrete, reinforced concrete, intact FRP-confined concrete, and defective or mechanically-damaged FRP-confined concrete. Measurements were conducted at X- and Ku- frequencies band to achieve high resolution and surface penetration. Frequency – angle, range – angle, and range – cross-range imagery was generated using the radar measurement data. Cross-correlation studies were also conducted to evaluate and compare radar measurements of intact and defective specimens. The first sections of this chapter are devoted to introducing concepts related to the fundamentals of radar, its parameters, SAR and ISAR methodologies, and basic signal processing techniques. Then, details of the exploratory experimental program for radar measurements of FRP-confined concrete specimens are presented. Analyses and discussions of measurement results are then provided.

5.1 Fundamentals of Radar

The main purposes of radar are detection and location of objects through the use of radio waves. Currently, new applications of modern radar extend to identification, classification, and imaging of target objects, weather detection, automobile speed detection, air traffic control, astronomy, and a variety of non-destructive evaluation techniques (Knott *et al.* 1993, Bungey and Millard 1996, Kingsley and Quegan 1999).

The four basic radar system elements are: a transmitter, an antenna, a receiver, and an indicator. The transmitter subsystem creates the required waveform to be transmitted and it is typically composed of a power supply, a modulator, and a radio-frequency (RF) amplifier. The types of transmitter and power source are selected depending on the power requirements, cost, and specific details of the application (Knott *et al.* 1993). The type of waveform is also selected depending on the specific application and it can range from an un-modulated continuous wave to a complex frequency, phase, and time code modulated wave as in the case of advanced radars (Rhim 1995). The antenna is the device which couples the energy between the transmission lines in the radar and the free-space. The RF energy is converted by the transmitting antenna into a beam of a given shape which will illuminate the desired target. The receiving antenna receives the EM signals from specific directions and guides that energy to the receiver. In most radar systems, the transmission and reception tasks are performed by the same antenna. The receiver subsystem performs the detection and signal processing tasks. The received RF signal is mixed down to a lower intermediate frequency (IF) for further data analysis and processing (Knott *et al.* 1993). The indicator is the final radar component which conveys the target information to the user or operator. Figure 5-1 shows a simplified block diagram of a coherent radar. Further discussions on radar systems are presented in Eaves and Reedy (1987), Edde (1993), Knott *et al.* (1993), Scheer and Kurtz (1993), and Kingsley and Quegan (1999).

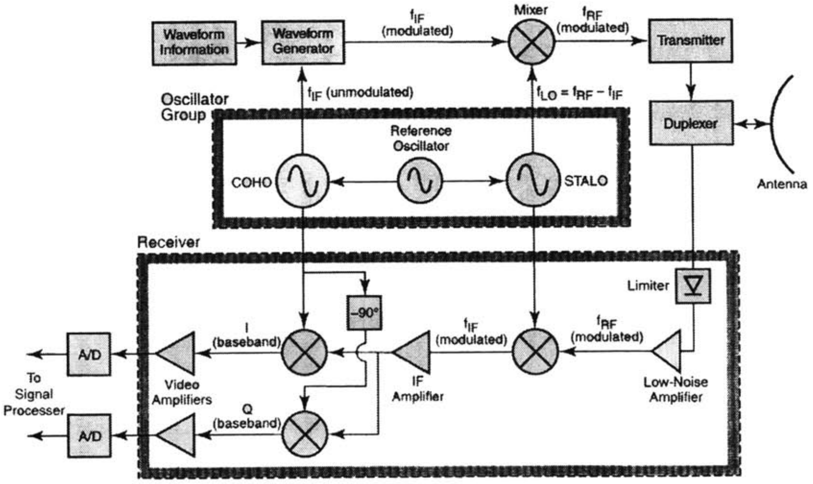

Figure 5-1 Block diagram of a typical coherent radar (Sullivan 2000)

5.1.1 Radar Parameters

Pulse Width and Bandwidth

A linear frequency modulated waveform generated by radar consists of a rectangular pulse of duration $T = t_2 - t_1$ as shown in Figure 5-2 (a). The carrier frequency f is swept over the pulse length by an amount B which represents the bandwidth, as shown in Figure 5-2 (b). For the case of a compression pulse length similar to T, the swept bandwidth and the achievable pulse are related by (Eaves and Reedy 1987):

$$T \approx \frac{1}{(f_2 - f_1)} = \frac{1}{B} \tag{5.1}$$

where f_1 and f_2 are the starting and ending frequencies, respectively.

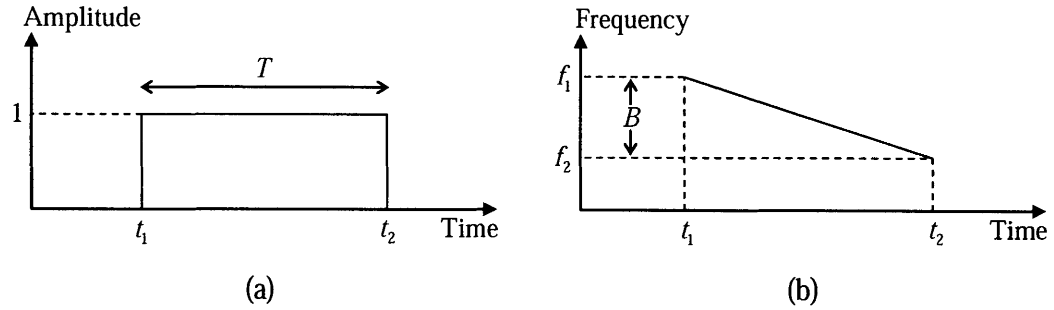

Figure 5-2 Linear frequency modulated pulse waveform

Range and Cross-Range Resolutions

Range resolution is related to the line-of-sight range, and it is often obtained by processing the transmitted pulse. *Cross-range* resolution is related to the resolution perpendicular to the line-of-sight of the radar along the target's surface, and it is obtained by integrating the reflected energy from the target medium as the radar sweeps alongside the area of illumination (Wehner 1995). The relationships for the range and cross-range resolutions associated with radar are given by the following expressions, respectively:

$$\rho_r \cong \frac{c}{2B} \tag{5.2}$$

$$\rho_{xr} \cong \frac{\lambda_c}{2\Delta\theta_{rad}} \tag{5.3}$$

where c = speed of light in free-space, B = bandwidth, λ_c = wavelength at center frequency, and $\Delta\theta_{rad}$ = angular rotation of the target during processing time. Eq. 5.2 is the commonly accepted measure of resolution. Precise expressions are dependent on more specific definitions of resolution (Mensa 1981). It is worth noticing that the range and cross-range resolutions expressed by Eqs. 5.2 and 5.3 are valid for free-space. Approximations of these equations when the medium under test is a dielectric material (*e.g.* concrete) are given by (Rhim 1995):

$$\rho_r \approx \frac{\left(\dfrac{c}{\sqrt{\varepsilon_r}}\right)}{2B} \tag{5.4}$$

$$\rho_{xr} \approx \frac{\left(\dfrac{c}{f_c\sqrt{\varepsilon_r}}\right)}{2\Delta\theta_{rad}} \tag{5.5}$$

where ε_r = dielectric constant of the dielectric medium and f_c = center frequency.

Polarization

Polarization is related to the orientations of the electric and magnetic fields and their variations with respect to time. In some applications, the polarization is referenced to the localization of the radar site itself. In other applications, the polarization is referenced to the characteristic dimension of the target under test (Knott *et al.* 1993). For the instance when the target under test is an infinite cylinder (treated as a two-dimensional structure), the incident field is referred to as VV-polarized or TM (transverse magnetic) when the electric field is parallel to the axis (infinite dimension) of the cylinder. The other polarization option is then HH-polarized or TE (transverse electric) when the electric field is perpendicular to such axis. For the case of a semi-infinite space and EM plane waves as shown in Figure 5-3, the mentioned polarizations are defined in terms of the plane of incidence. In Figure 5-3, the plane of incidence is denoted by the x-z plane. The incident electric field vector $\overline{E}_{incident}$ is perpendicular to the plane of incidence. Such incident wave is called TE wave or HH-polarized. When the incident electric field vector is parallel to the plane of incidence, such wave is called TM wave or VV-polarized. In the two mentioned polarization options, the orientation of the electric field does not change with increasing distance, thus, they are termed linear polarizations. Circular polarization, on the contrary, allows for the electric and magnetic field orientations to rotate about the direction of propagation with increasing distance. The availability of the HH and VV polarizations is a key advantage of radar methodologies for NDE applications on anisotropic materials whose properties are dependent on the direction of measurement (Rhim 1995).

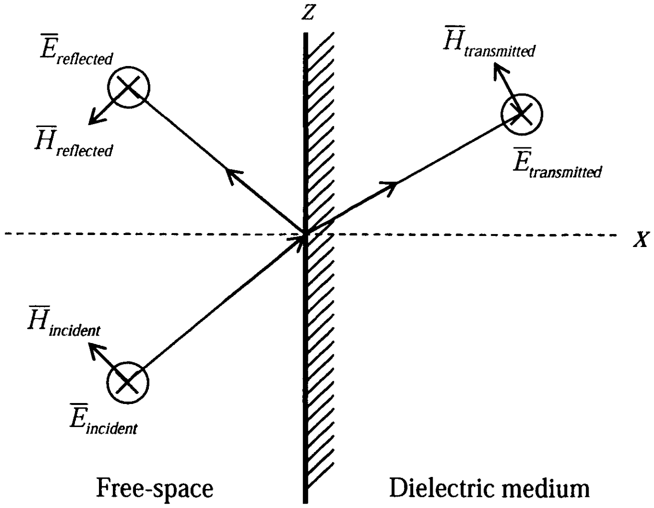

Figure 5-3 Reflection and transmission of a TE or HH-polarized wave in a semi-infinite medium

Decibel (dB)

In radar measurements, variability of radar parameters may extend over several orders of magnitude. For instance, transmitted signal powers could be on the megawatt range, while received signal powers could be on the picowatt range (Knott *et al.* 1993). In addition, visualization of wide dynamic range RCS (radar cross section) plots could become cumbersome for data sets expanding several orders of magnitude. Thus in radar work, a logarithmic unit referred to as decibel (dB) is used. Such unit expresses power ratios in the following manner:

$$P(dB) = 10\log_{10}\left(\frac{P}{P_0}\right) \qquad (5.6)$$

where P_0 = reference power level. For power measurements, reference units such as 1 watt and 1 milliwatt and their corresponding notations dBW and dBm are used. The common reference unit for RCS measurements is 1 m^2. A decibel referenced to 1 m^2 is designated as dBsm. Table 5-1 shows useful references for selected power ratios and their corresponding dB values which will be observed in the studies documented in this chapter.

Power Ratio	0.01	0.10	0.32	0.79	1.00	1.26	3.16	10	100
dB	-20	-10	-5	-1	0	1	5	10	20

Table 5-1 Selected power ratios and corresponding dB values

Radar Cross Section (RCS)

Estimation of the input signal strength received by a radar receiver requires the knowledge of the signal strength decay of radiated waves from transmitting sources, the excitation of a wave reflection by a remote obstacle, and the dispersion of the reflected waves by the obstacle. A single function σ, referred to as radar cross section (RCS) characterizes the obstacle reflection (Eaves and Reedy 1987). Formally, RCS is the defined as:

$$\sigma = \lim_{r\to\infty} 4\pi r^2 \frac{\left|\overline{E}^{scat}\right|^2}{\left|\overline{E}^{inc}\right|^2} \tag{5.7}$$

where $\overline{E}^{scat}$ and $\overline{E}^{inc}$ are the scattered and incident electric fields (Knott *et al.* 1987). By its definition, RCS provides information about the target's characteristics and removes the effects of the transmitted power, receiver sensitivity, and the relative distance between the transmitter and receiver.

Near Field and Far Field

Antenna patterns vary in shape depending on the distance from the antenna, noted as R, and with the look direction. In the extreme case of a large distance from the antenna, the shape of the antenna pattern over a sphere of constant radius is independent of R. A common accepted criterion for independence between the range and the pattern shape is when:

$$R > \frac{2D^2}{\lambda} \tag{5.8}$$

where D = diameter of the smallest sphere that completely contains the antenna or the target extent facing the radar and λ = wavelength of the transmitted wave (Eaves and Reedy 1987, Wehner 1995). Values of R larger than Eq. 5.6 are said to be in the far field of the antenna, while smaller values are said to be in the near field. For the latter case, antenna patterns vary significantly as the distance R decreases.

Coherent Radar

The characteristic feature of coherent radars is the generation of sinusoidal waveforms from a source within the radar (referred to as stable local oscillator, or STALO) that maintain a constant frequency over several pulses. Using the STALO phase information and the recorded phases of the returned pulses, relative phases between pulses can be calculated (Sullivan 2000). From a radar signals perspective, coherent processing of a sequence of pulses refers to the situation when their phase information at the carrier frequency is known and stable (Kingsley and Quegan 1999). Coherent radar systems are widely used, and their application becomes necessary when requiring precise radar measurements especially for target velocity estimations (Sullivan 2000).

5.1.2 Inverse Synthetic Aperture Radar (ISAR)

Synthetic aperture radar (SAR) is a radar mapping technique that generates high resolution maps in both range and cross-range. The SAR mapping is obtained through the processing of the reflectivity data collected as the radar device moves over the target of interest. Thus, this scheme resembles the function of several antennas that are arranged in a linear antenna array. The fundamental principle that underlies the SAR method is the relationship between the cross-range position of the target of interest and the instantaneous Doppler shift of the energy reflected and scattered by such target. Inverse synthetic aperture radar (ISAR) refers to a modification of the SAR scheme. ISAR techniques have been applied for the imaging of ships, aircrafts, space objects and the RCS evaluation of targets and target models (Wehner 1995). In the ISAR scheme, the backscattering data is collected while the target rotates and is illuminated by the radar beam. The ISAR scheme can be understood by visiting one particular scenario of SAR application called spotlight SAR. As shown in Figure 5-3, spotlight SAR is achieved when the radar antenna consistently tracks the target of interest. In this case, the radar antenna is moving along an angular section ψ around the target. Similar data could be obtained for the case when the target object rotates and the radar antenna remains static, which is what occurs in ISAR implementation. A potential application of spotlight SAR technique for non-destructive evaluation of civil infrastructure is that mentioned in Section 2.5.4. Currently, research on the development of the APS-CW technique is still at preliminary stages. A first step in the further development of such technique is the laboratory implementation of ISAR techniques to achieve the same non-destructive evaluation objectives of the APS-CW technique for damage and defect detection in FRP-confined concrete specimens.

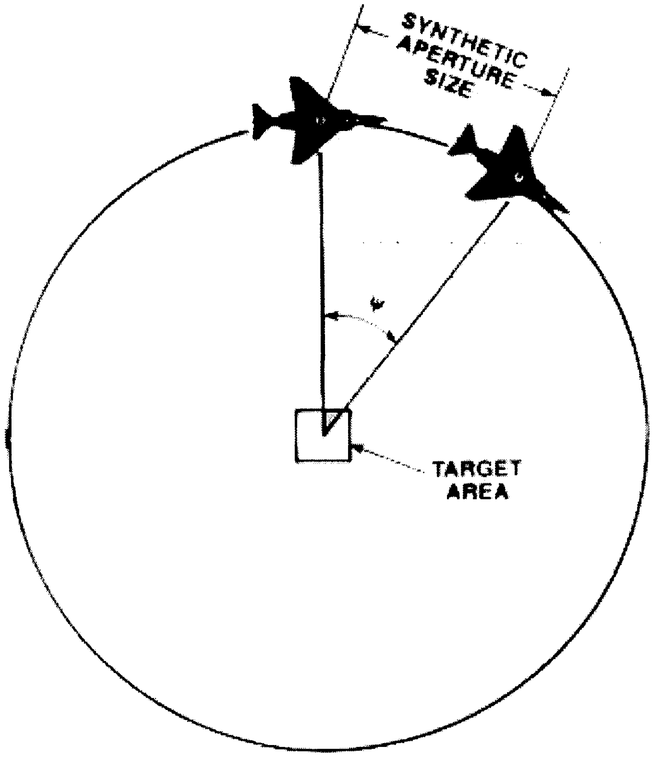

Figure 5-3 Spotlight SAR (Wehner 1995)

5.2 Important Issues related to ISAR Test Parameters

Before the implementation of the ISAR methodology for radar NDE measurements, range and cross-range resolution criteria need to be established. The resolution to be achieved using radar techniques is highly dependent on the specific problems at hand and the type of feature to be resolved. In NDE applications, ground penetrating radar techniques have been applied for the detection of defects in pavement and highway systems, tunnel linings, and the quantification of scour around bridge piers (refer to Section 2.4.2).For these cases, relatively low resolutions could be sufficient to detect defects of sizable configuration, and thus the use of low frequencies (large wavelengths) would be appropriate. However, other applications (*e.g.* the radar NDE case documented in this thesis) might require higher resolutions due to the smaller characteristic sizes of the defects under investigation, and thus the use of high frequencies (short wavelengths) would be required. From Eqs. 5.4 and 5.5, it is apparent that the key radar parameters to be considered when designing ISAR experiments are the central frequency f_c, the frequency bandwidth B, and the angle of rotation $\Delta\theta_{rad}$. Due to the inverse proportionality of these parameters to the range (ρ_r) and cross-range (ρ_{xr}) resolutions, high center frequency and frequency bandwidth values and large rotation angle values will improve the range and cross-range resolutions of the ISAR measurements. However in practical applications, there are important constraints to the values of these parameters that need to be considered.

5.2.1 Penetration Depth vs. Frequency

In lossy media, such as concrete, power is dissipated as the EM waves propagate through the media. For the case of a plane wave traveling in the z-direction, the power attenuation is related by:

$$\frac{P}{P_0} = e^{-\frac{2z}{d_p}} \tag{5.9}$$

where P_0 = incident power, z = depth inside the medium, and d_p = penetration depth. The penetration depth is defined as the depth at which the power attenuates by $1/e^2$. For the case of a slightly conductive medium, the penetration depth can be approximated by (Kong 1990):

$$d_p = \frac{2}{\sigma}\sqrt{\frac{\varepsilon'}{\mu}} \tag{5.10}$$

where ε', μ, and σ represent the dielectric properties of the medium at hand, namely the dielectric constant, permeability, and the conductivity, correspondingly. For the specific case of concrete, its dielectric properties have been found to be highly dependent on frequency as shown in Figure 5-4. It is worth noticing that the dielectric properties shown in Figure 5-4 developed by Rhim and Büyüköztürk (1998) were measured using a different methodology (open-ended coaxial probe) than that proposed in Chapter 4. The objective of the first study was to determine the frequency dependency of dielectric properties for concrete and mortar materials, while in the second study effective dielectric properties of several materials were determined over specific frequency bandwidths. For further comparison between the two particular methodologies, the reader is referred to Section 4.2. After observing the relatively decreasing behavior of the dielectric constant and the increasing behavior of the conductivity as functions of frequency, their compound effect would equate to decreasing values for the penetration depth. As a result, an optimization problem arises when choosing the center frequency and bandwidth. While higher frequencies could yield high resolutions radar measurements, radar wave penetration in dielectric lossy media such as concrete is negatively affected.

5.2.2 Bandwidth and Rotation Angle vs. Computational Cost

As already mentioned, data processing of large frequency bandwidths and rotation angles for ISAR measurements would yield improved range and cross-range resolutions. In applications where the target of interest presents symmetry properties (cylindrical configurations such as FRP-wrapped concrete columns), the need for measurement of large rotation angles could be reduced due to the axisymmetric characteristics of the specimen at hand. However, the improvements in resolution due to large frequency bandwidths and measured rotation angles also result in extensive number of measurements, time consuming data processing and imaging, and other related computational costs. These issues become significantly important when new technologies are being developed for field applications, where number of measurements and computational time directly translate into monetary costs. A balance between cost issues and the desired resolution achieved by radar measurements is required.

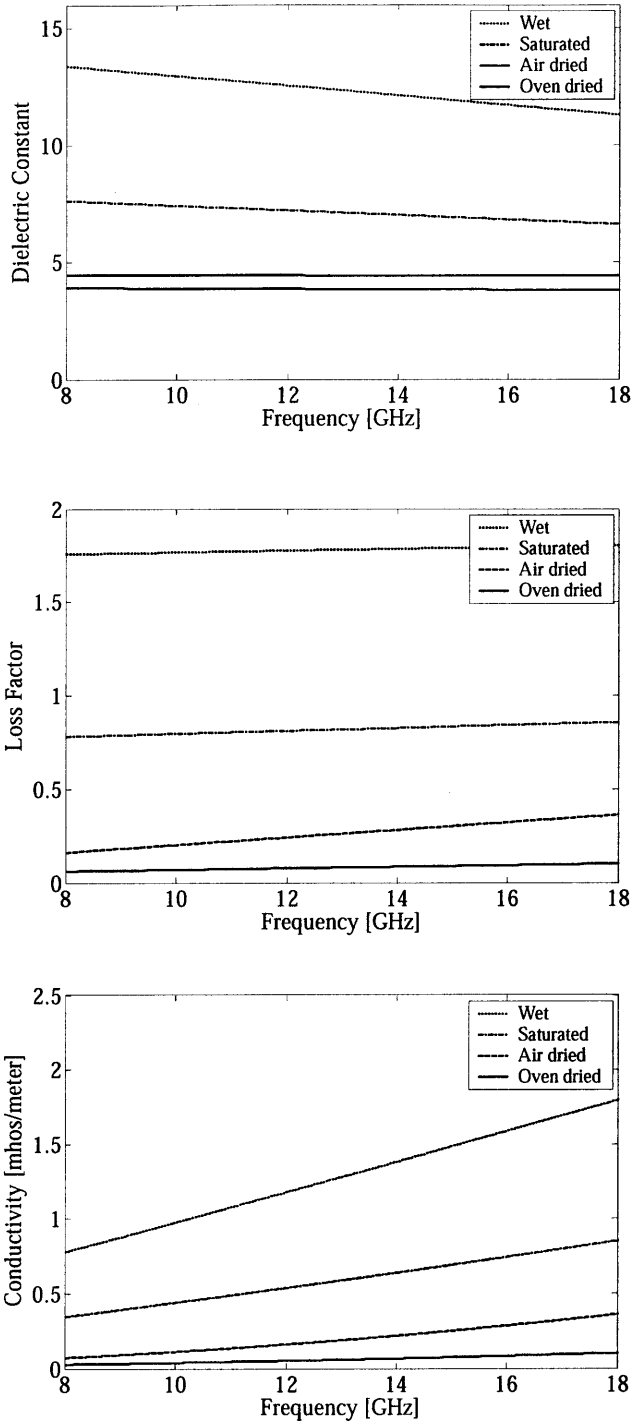

Figure 5-4 Dielectric constant, loss factor, and conductivity for concrete at X- and Ku-band frequencies (Rhim and Büyüköztürk 1998)

5.3 Signal Processing

5.3.1 Fourier Transform Method

The description of physical processes could be achieved mathematically in two distinct forms. In time domain, a process is quantified by a some quantity h as a function of time t, represented as $h(t)$. The same process could also be described in frequency domain where the process is quantified by an amplitude H (generally a complex number composed of magnitude and a phase component) as a function of angular frequency ω, represented as $H(\omega)$. The Fourier transform method allows a mathematical connection between the two different domain descriptions of the same process. The Fourier transform of h is a function of H depending on frequency (Strang 1986):

$$H(\omega)=\int_{t=-\infty}^{\infty}h(t)e^{-i\omega t}\,dt \qquad (5.11)$$

The inverse Fourier transform of H brings the original function h back by:

$$h(t)=\frac{1}{2\pi}\int_{\omega=-\infty}^{\infty}H(\omega)e^{i\omega t}\,d\omega \qquad (5.12)$$

For the case when the frequency domain description is given in cycles per second, the relation between ω and f is given by:

$$\begin{aligned}&\omega=2\pi f\\&H(\omega)=H(f)\big|_{f=\omega/2\pi}\end{aligned} \qquad (5.13)$$

and Eqs 5.11 and 5.12 become

$$H(f)=\int_{t=-\infty}^{\infty}h(t)e^{-2\pi ift}\,dt \qquad (5.14)$$

$$h(t)=\int_{f=-\infty}^{\infty}H(f)e^{2\pi ift}\,df \qquad (5.15)$$

When the Fourier transform method is applied to discrete processes in which a finite number of sample points are given, discrete Fourier transformation methods need to be applied. Fourier transformation processing is implemented for the radar measurement herein described (which are conducted in the frequency domain) in order to generate range-angle imagery, and thus investigate the detection of different types of defects and damage in FRP-confined concrete specimens.

5.3.2 Cross-Correlation

Correlation of signals is a technique often used in signal processing for estimating the frequency content of noisy signals, as well as detection of targets from radar signals. Two cases of correlation are encountered: autocorrelation, in which the correlation is performed on the original signal with itself, and cross-correlation, in which two different signals are correlated. Cross-correlation can be mathematically described by the following relationship (Phillips *et al.* 2003):

$$R_{xy}(p) = \sum_{m=-\infty}^{\infty} x(m) y(p+m) \tag{5.16}$$

which is similar to the definition of discrete-time convolution:

$$y(m) = \sum_{k=-\infty}^{\infty} x(k) h(n-k) = x(n) * h(n) \tag{5.17}$$

The maximum value in the correlation function determines a coefficient which is used in this study as a metric for correlating two signals. In the autocorrelation, the maximum value of the correlation function is normalized by itself, yielding a correlation coefficient of unity, whereas for the comparison of two different signals, the maximum value in the correlation function is normalized by that of the autocorrelation of the benchmark signal. Consequently, the correlation coefficient will be less than unity. For the case of correlation of two-dimensional arrays *A(Ma,Na)* and *B(Mb,Nb)*, the equation for two-dimensional discrete cross-correlation is (Mathworks 2005):

$$C(i,j) = \sum_{m=0}^{(Ma-1)} \sum_{n=0}^{(Na-1)} A(m,n) \cdot conj[B(m+i, n+j)] \tag{5.18}$$

For further information on correlation functions and cross-correlation, the reader is referred to Orfanidis (1996).

5.3.3 Backprojection Imaging Algorithm

Imaging algorithms used to treat SAR data are classified in two broad categories: Fast Fourier Transform (FFT) based methods, and backprojection (time domain) methods. While FFT methods are computationally less expensive, they suffer from several limitations: the method might not be universally applicable, assumptions are needed in terms of target motions, and data interpolation is required. Several of these deficiencies are overcome through the use of backprojection algorithms at the price of greater computational effort (Yegulalp 1999). Such algorithms are capable of producing high resolution range – cross-range imagery through the full utilization of the EM wave reflection and scattering response information embedded in SAR or ISAR measurements. A backprojection algorithm developed at MIT – Lincoln Laboratory was used in this work to generate ISAR imagery for selected specimens.

5.4 Radar Measurements of FRP-Confined Concrete

The objective of the exploratory experimental program described in the following sections is the application of high resolution ISAR radar technologies for the detection and assessment of defect and damage features in FRP-confined concrete specimens. The experimental set-up, description of test parameters, sample configurations, and data processing, analysis, and interpretation are discussed.

5.4.1 Radar Measurement Set-up

The radar measurements of FRP-confined concrete specimens were performed at MIT – Lincoln Laboratory using the Compact RCS/Antenna Range facility located in Building 1718. The experimental set-up consists of a horn antenna, stepped-frequency radar and network analyzer systems, and a Harris Dual-Shaped reflection system, Model 1606, designed for conducting far field studies. Photographs of this experimental facility are shown in Figure 5-5. The facility can achieve high signal-to-noise ratio measurements for a large frequency bandwidth ranging from UHF (0.7 GHz) to 100 GHz. This radar system is capable of producing a 20-m quiet zone, different antenna radiation patterns, and full polarimetric RCS measurements. Specimens are placed on top of a Styrofoam tower that is capable of fully rotating the target at predetermined angular steps. The measurements were conducted in stepped-frequency mode by sweeping from a starting frequency f_1 to an end frequency f_2 in 0.02 GHz increments at a fixed angle. The target is then rotated to the next angular step and the frequency sweeping is again performed. The ISAR measurement scheme herein described emulates the measurement scheme described in Section 2.5.4, namely the APS-CW technique in which the radar antenna is rotated around the specimen under test.

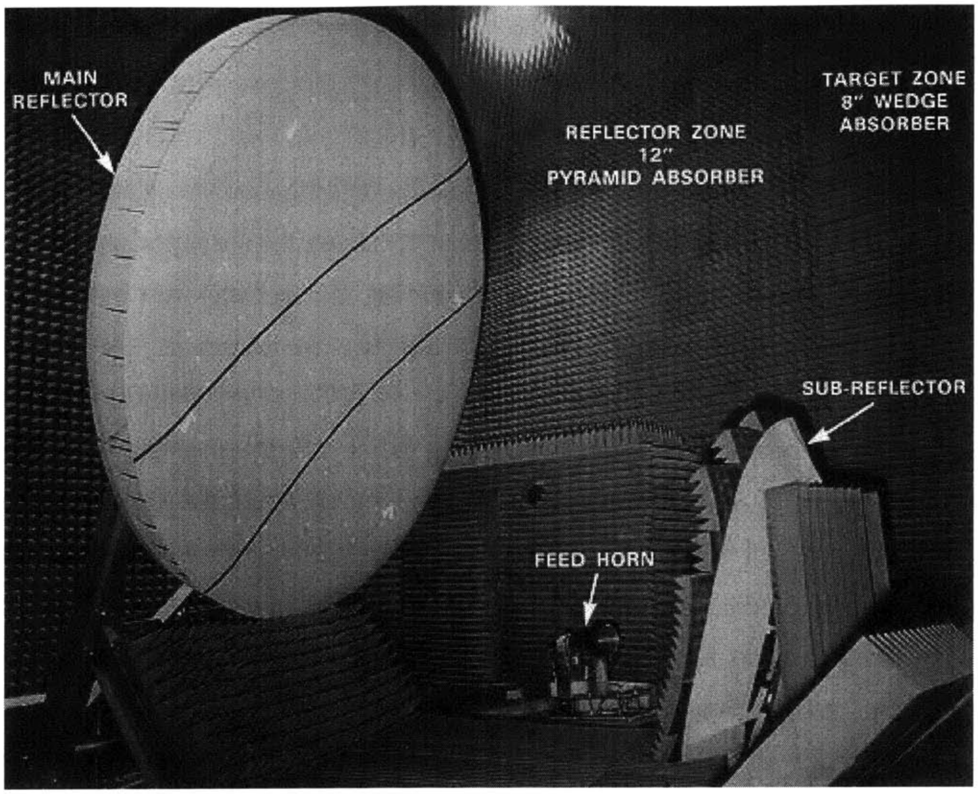

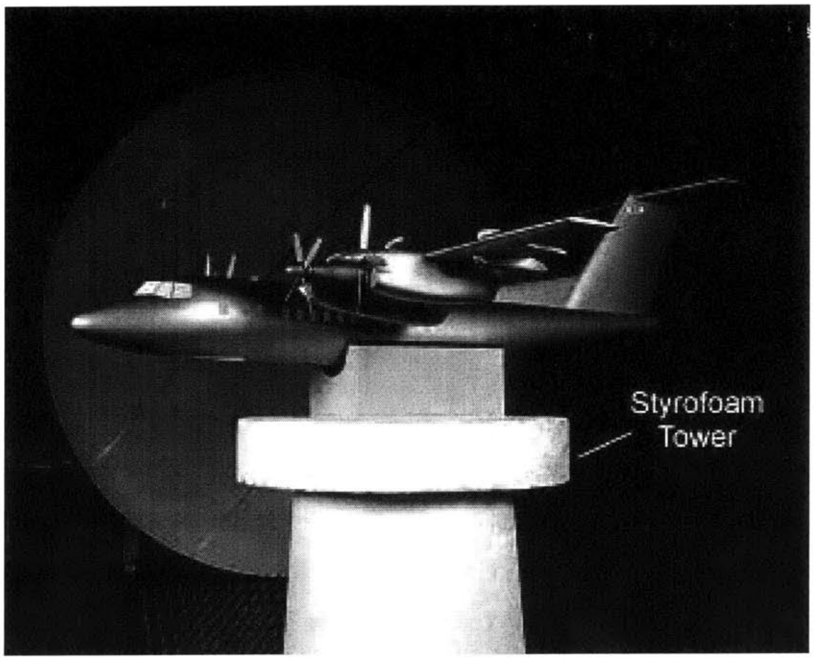

Figure 5-5 Photographs of the MIT- Lincoln Laboratory Compact RCS/Antenna Range facility, Building 1718: reflector and feed horn antenna (top), and Styrofoam tower (bottom) (Courtesy of Dennis Blejer)

5.4.2 Experiment Parameters

Measurement Schemes

For radar measurements, the cylindrical specimen under investigation was placed on top of a Styrofoam tower in two alternative orientations: 1) having the specimen rest on one of its ends, referred to as vertical position, and 2) having the specimen rest on its side, referred to as horizontal position. Schematics of the two measurement schemes are presented in Figures 5-6 (a) and (b). Because of the two different orientations in which the specimen can be measured, it is more precise to define the measurement scheme in terms of the EM wave relative angle of incidence, as seen in Figure 5-6 (c) and (d). In Figure 5-6 (c), the angle of incidence θ is at 90° with the lateral surface of the cylinder, thus the corresponding radar measurements are always made at normal incidence as the specimen is rotated around its z-axis. This measurement scheme is termed as normal incidence, and it corresponds to the scheme presented in Figure 5-6 (a). In Figure 5-6 (d), the angle of incidence ϕ will vary as the specimen is rotated around its y-axis. Only when the incident waves and the lateral surface of the specimen are perpendicular to each other (referred to $\phi = 90°$), normal incidence is achieved. For all other incidences, the wave will meet the specimens in an oblique fashion. Thus, this measurement scheme is termed as oblique incidence, and it corresponds to the scheme presented in Figure 5-6 (b). Both measurement schemes were designed to capture different EM wave scattering behaviors, and consequently investigate their effectiveness when radar techniques are applied for damage or defect detection in FRP-confined concrete elements.

Radar Parameters

Radar measurements were conducted at X- and Ku-band frequencies (8-12 and 12-18 GHz, respectively) to achieve optimized resolution and surface penetration capabilities. From Eq. 5.2, the range resolution is directly related to the bandwidth of processed radar signals. For X- and Ku- bands whose bandwidths are 4 and 6 GHz respectively, the corresponding achieved range resolutions are 38 mm and 25 mm. These resolutions are deemed as ultra-high for conventional radar applications. For cross-range resolution, the total angular rotation of the target $\Delta\theta_{rad}$, was determined as to obtain the same range and

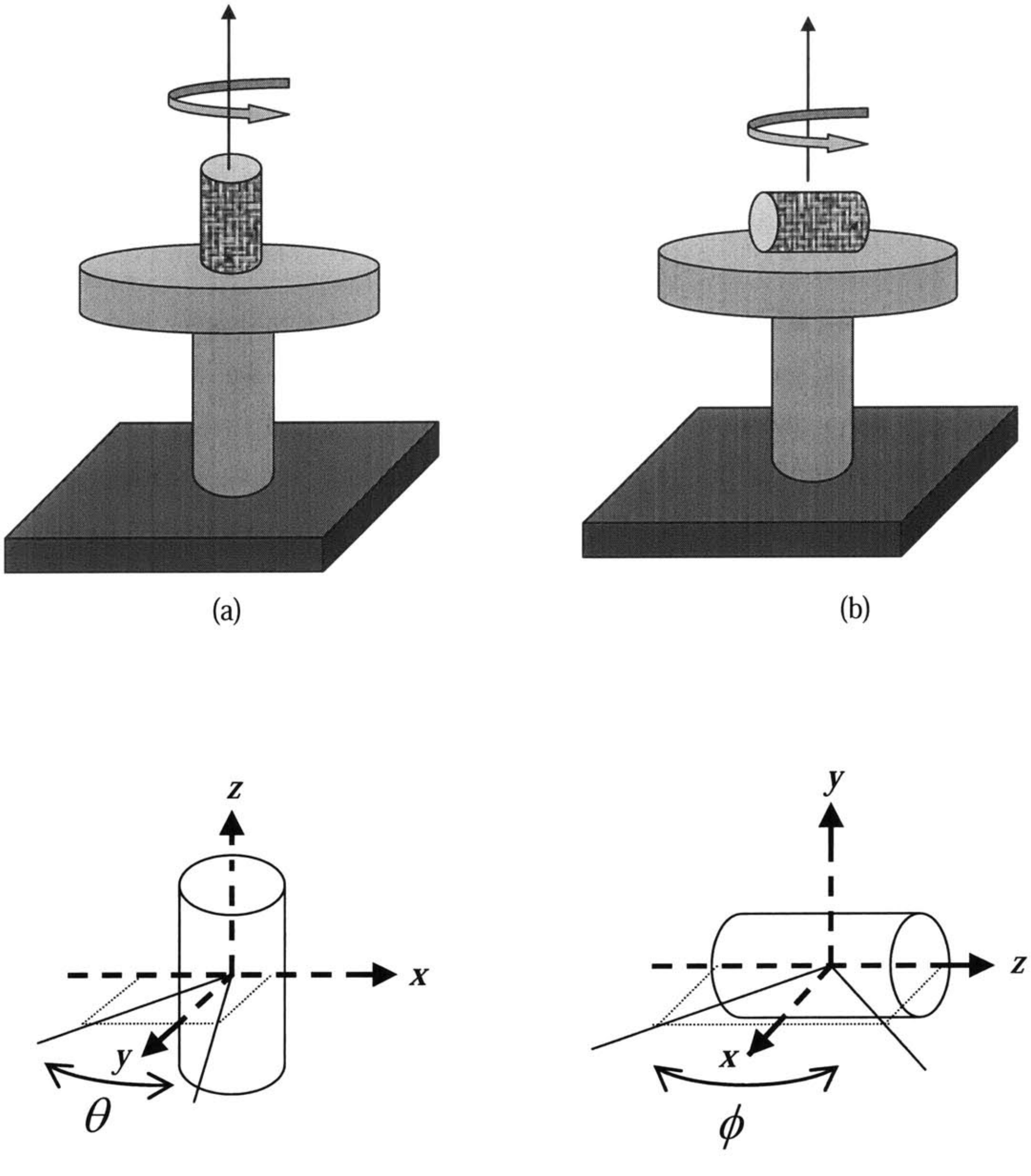

(a) (b)

(c) (d)

Figure 5-6 ISAR measurement schemes (a) sample resting on its end cap, (b) sample resting on its side. ISAR measurement scheme notations (c) normal incidence, (d) oblique incidence cross-range resolutions. For the X- and Ku- bands, the minimum angular rotation needed for ISAR imaging with high resolution was $22.92°$. The corresponding angle increment was $0.2°$. It is worth noticing that these computed space resolutions are valid in free-space. When EM wave propagates in dielectric media, such as the test specimens herein investigated, the resolution would actually be improved due to the effect of the dielectric constant of the media being greater than unity. This is mathematically expressed in Eqs. 5.4 and 5.5.

While the resolution achieved in the radar measurements is significantly high, the trade-off is evident in terms of penetration capabilities. Using the definition of penetration depth for a dielectric, non-magnetic material expressed in Eq. 5.10, the penetration depth is controlled by the permittivity of the material and the measurement frequency. When dielectric losses occur in the material due to conduction currents, the equivalent conductivity σ is expressed as (Rhim 1995):

$$\begin{aligned} \sigma &= \varepsilon'' \omega \\ \sigma &= 2\pi \varepsilon_r'' \varepsilon_0 f \end{aligned} \tag{5.19}$$

For the specific case of the specimens discussed in this chapter, the dielectric properties of the concrete material used for manufacturing the FRP-confined concrete specimens were characterized using the methodology described in Chapter 4. The results for dielectric constant and loss factor from the proposed dielectric property characterization methodology are 5.69 and 0.62, respectively. As a first approximation of penetration depth values, constant dielectric properties over the X- and Ku- bands are assumed. Using Eqs. 5.10 and 5.19, the estimated penetration depths are approximately 50 mm and 22 mm for 8 and 18 GHz frequencies, respectively. As mentioned in Section 5.2.1, the use of high frequency radar waves will result in shallow penetration depths as demonstrated by the previous calculations. However, the proposed X- and Ku- bands were originally selected in view of the need to detect near-surface defects, FRP-concrete delaminations, and mechanical damage in the concrete core regions close to the FRP jacket.

Two types of polarizations were used in the radar measurements: HH-polarization and VV-polarization. The purpose of using two different polarizations is to explore detection capabilities of damage or defect features oriented in different directions. This is especially important for rebar detection purposes in which stronger radar signatures are collected when the magnetic field is oriented parallel to the steel rebar.

One of the important features of the performed radar measurements is the application of the far field condition (refer to Section 5.1.1). The experimental set-up used in this study is inherently designed to achieve such condition since one of the key operational objectives of the Compact RCS/Antenna Range facility is to simulate radar measurements of airborne objects. Far field conditions simplify the wave propagation phenomena by reducing complex antenna radiation patterns to plane wave scenarios. From the perspective of this research work, it is intended to first demonstrate the applicability of radar NDE technologies for defect and damage detection in FRP-confined concrete elements for a well-established experimental scenario. The use of such technologies for potential field applications will require radar measurements in near field conditions, which are out of the scope of this thesis.

5.4.3 Test Program

Table 5-2 shows the test program of radar measurements. Several types of specimens were selected for radar measurements to investigate the following particular features of interest:

- *ME Series*: An aluminum cylinder was measured as an example of a metallic specimen.
- *PC Series*: A plain, intact concrete cylinder was measured as the first example of a dielectric specimen.
- *CC Series*: An intact FRP-confined concrete cylinder was measured as the first example of a dielectric specimen wrapped with a FRP composite jacket.
- *RE Series*: A plain concrete cylinder with steel rebar at different depth locations was investigated to explore the rebar detection capabilities of the proposed radar methodology.
- *AD Series*: Three specimens with distinctive defects were measured to test the capability of the radar methodology for detecting air cavities and delaminations in FRP-confined concrete specimens.

- *MD Series*: Three specimens with different levels of mechanical damage were measured to test the capability of the radar methodology for detecting cracking and volumetric deformation of FRP-confined concrete specimens.

Specimen dimensions, measurement scheme (normal or oblique incidence), and frequency band used for the measurements of each specimen are also provided in Table 5-2. All the concrete and FRP-wrapped concrete specimens were manufactured using the same materials, mixing ratios, and other procedures outlined in Chapter 3. For the AD series specimens, defects were artificially introduced by using Styrofoam inserts during the concrete casting procedures. Once the concrete cured, such inserts were removed, and the specimens were subsequently wrapped with GFRP fabric. Specimen CYL-AD3 shown in Table 5-2 was measured for future studies on EW wave simulations. Only limited analysis of this case is presented in subsequent sections. For the MD series, specimens were subjected to controlled compressive loads. Specimens MD1, MD3, and MD5 correspond to damage levels 1, 3, and 5 as described in Section 3.7.1. Consequently, specimen MD1 corresponds to intact FRP-confined concrete, MD3 corresponds to a zero net volumetric deformation (which is also related to the kink point in the axial stress – axial strain curve, see Section 3.3.2), and MD5 corresponds to a damage state close to ultimate failure. Schematics and photographs of selected specimen configurations are provided in Figures 5-7 and 5-8, respectively.

Specimen	Description	Dimensions		Measurement Setup	Frequency Band
		Length [mm]	Diameter [mm]		
CYL-ME	Aluminum cylinder, 6 mm thick wall	305	152	Normal Normal	X Ku
CYL-PC	Plain concrete cylinder	305	152	Normal Normal	X Ku
CYL-CC	FRP-confined concrete cylinder	305	152	Normal	X
CYL-RE	Plain concrete cylinder, rebar at different locations	380	152	Normal	X
CYL-AD1	FRP-confined concrete cylinder, 35mm x 35mm x 25 mm cavity	305	152	Normal Normal Oblique	X Ku X
CYL-AD2	FRP-confined concrete cylinder, 75mm x 75mm x 5 mm delamination	380	152	Normal Oblique	X X
CYL-AD3	FRP-confined concrete cylinder, 380 mm x 25 mm x 25 mm cavity	380	152	Normal	X
CYL-MD1	FRP-confined concrete cylinder, intact	380	152	Normal	X
CYL-MD3	FRP-confined concrete cylinder, mechanical damage (stage 3)	380	152	Normal	X
CYL-MD5	FRP-confined concrete cylinder, mechanical damage (stage 5)	380	152	Normal	X

Series: ME - metal, PC - plain concrete, CC - confined concrete, RE - rebar, AD - artificial damage, MD - mechanical damage

Table 5-2 Radar measurement test program

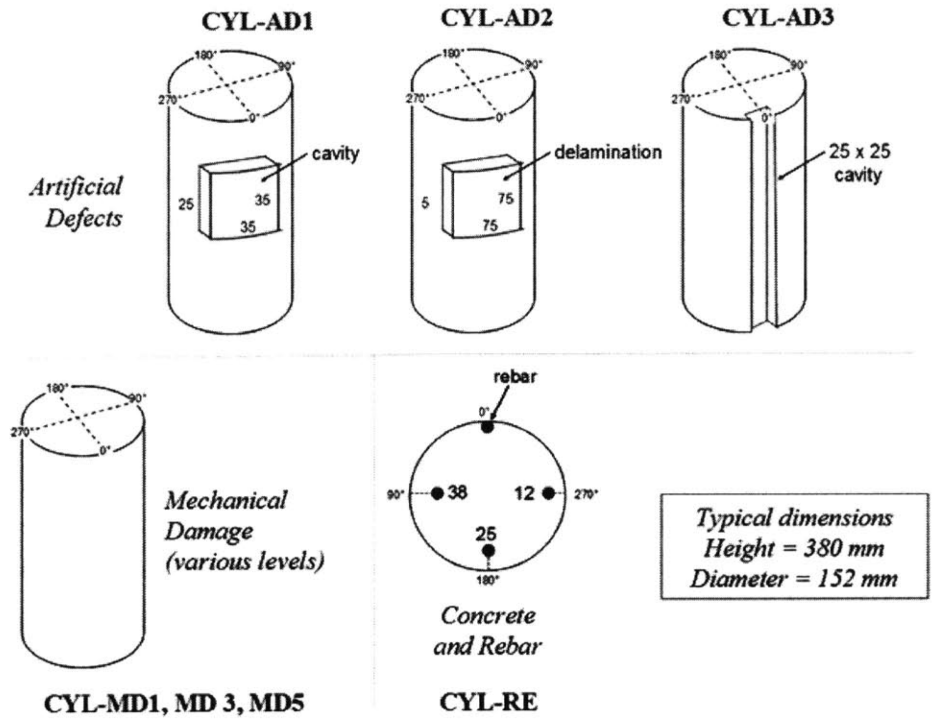

Figure 5-7 Specimen configurations (all dimensions are in *mm*)

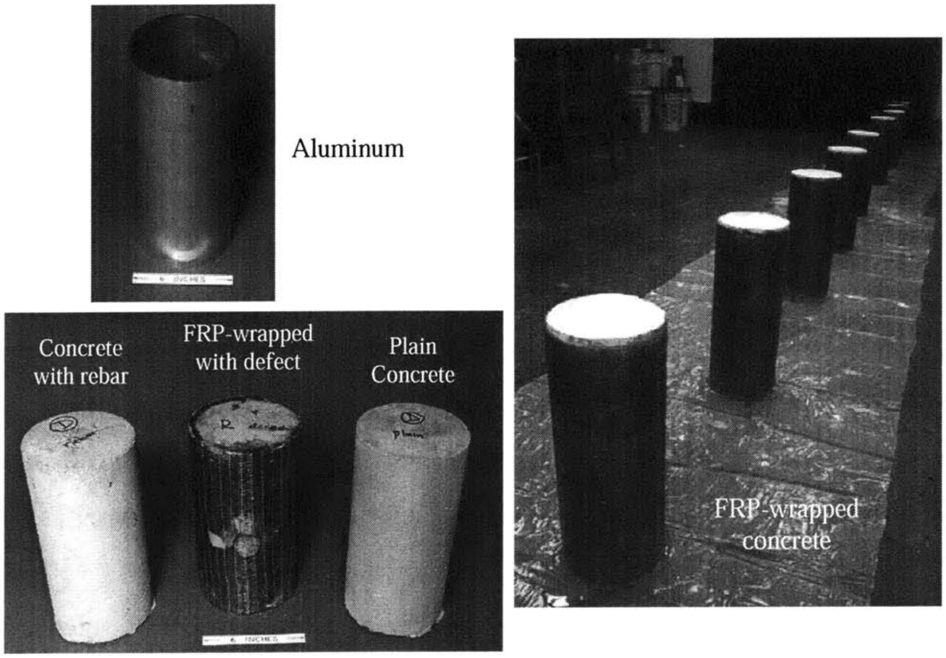

Figure 5-8 Photographs of selected specimens

5.4.4 Data Processing

The ISAR raw data collected at MIT – Lincoln Laboratory consisted of HH and VV polarization measurements as functions of frequency at fixed incident angles. For each polarization, an amplitude entry (A) and a phase entry (φ) were recorded at each frequency step. Table 5-3 shows a sample of raw data that was collected for specimen CYL-AD1 at oblique incidence during ISAR measurements. The data was then converted into complex number format using the following relations (Blejer, D., personal communication, 2005):

$$\begin{aligned} &P = 10^{\frac{A}{20}} \cdot \cos(\varphi) \quad ; \quad Q = 10^{\frac{A}{20}} \cdot \sin(\varphi) \\ &H = P + j \cdot Q \end{aligned} \tag{5.20}$$

Once the raw data was processed using Eq. 5.20, data analysis could be carried out using various methodologies, namely: frequency – angle imagery, cross-correlation functions, range – angle imagery, and ISAR imagery. Each of these methods could be thought of, in a hierarchical order due to their increased complexity in implementation, as means for processing and displaying the rich information embedded in the reflectivity measurements due to the EM wave scattering from the cylindrical specimens.

An important aspect regarding the interpretation of the results for each methodology is the correct understanding of the values for the incident angles for both normal and oblique incidences. For normal incidence measurements, θ describes the angular position of the specimen with respect to the radar antenna system. The convention for specimens measured in normal incidence was shown in Figure 5-7. Incidence angle $\theta = 0°$ is located in what is referred to as front surface. For FRP-wrapped concrete specimens, the location of the overlap is always in the back surface (*i.e.* $\theta = 180°$). Artificial defects were consistently centered around $\theta = 0°$ and at the mid-height of the specimens. For oblique incidence measurements, positive ϕ values describe measurements made on the specimen when the defect was facing the radar antenna system. This is referred as front surface. Negative ϕ values describe measurements made on the specimen on its non-defective side, referred to as back surface. As already mentioned, $\phi = \pm 90°$ refer to the unique situation when the incident waves hit the specimen under test in a perpendicular fashion.

		VV		HH	
Aspect (Deg)	Frequency (MHz)	Amp (dB)	Phase (Deg)	Amp (dB)	Phase (Deg)
-120.0	8000	-36.80	-24.00	-31.61	-58.33
-120.0	8020	-36.63	-28.11	-31.53	-60.04
-120.0	8040	-35.76	-34.64	-30.86	-62.40
-120.0	8060	-37.82	-48.02	-31.03	-64.90
-120.0	8080	-36.72	-54.69	-30.77	-65.89
-120.0	...	...	...	...	...
-119.8	8000	-35.03	-14.15	-31.12	-53.21

Table 5-3 A sample of raw data collected for CYL-AD1

5.5 Results of Radar Measurements

Due to the vast amount of ISAR measurements, this section is limited to the display of the results of the signal processing and imagery methodologies previously described. Corresponding analyses and discussions of these results are presented in a Section 5.6.

5.5.1 Frequency – Angle Imagery

Frequency – angle imagery refers to the graphical representation of the raw ISAR data as a function of frequency and incident angle. Thus, this method becomes the first and coarser data processing that can be carried out for ISAR data. While EM wave reflection and scattering information is presented in frequency domain, from which intuitive understanding of what the return signals might mean may not be easily drawn, direct comparisons could be established between the radar signatures of intact and defective specimens. Once the raw data is processed as explained in Section 5.4.4, the intensities of the EM wave return signals H (see Eq. 5.20) at specific frequencies and incident angles are calculated using Eq. 5.6 as follows:

$$Amplitude(dBsm) = \left[10\log_{10}\left(H \cdot H^*\right)\right]_{f=f_i,\theta=\theta_i} \tag{5.21}$$

where H^* is the conjugate pair of H. For each frequency – angle plot, measured amplitudes are normalized by the maximum amplitude in the data set. Frequency – angle imagery for selected measurement cases is presented in Figures 5-9 through 5-19. For a complete display of frequency – angle plots for all measured specimens, the reader is referred to Appendix A.

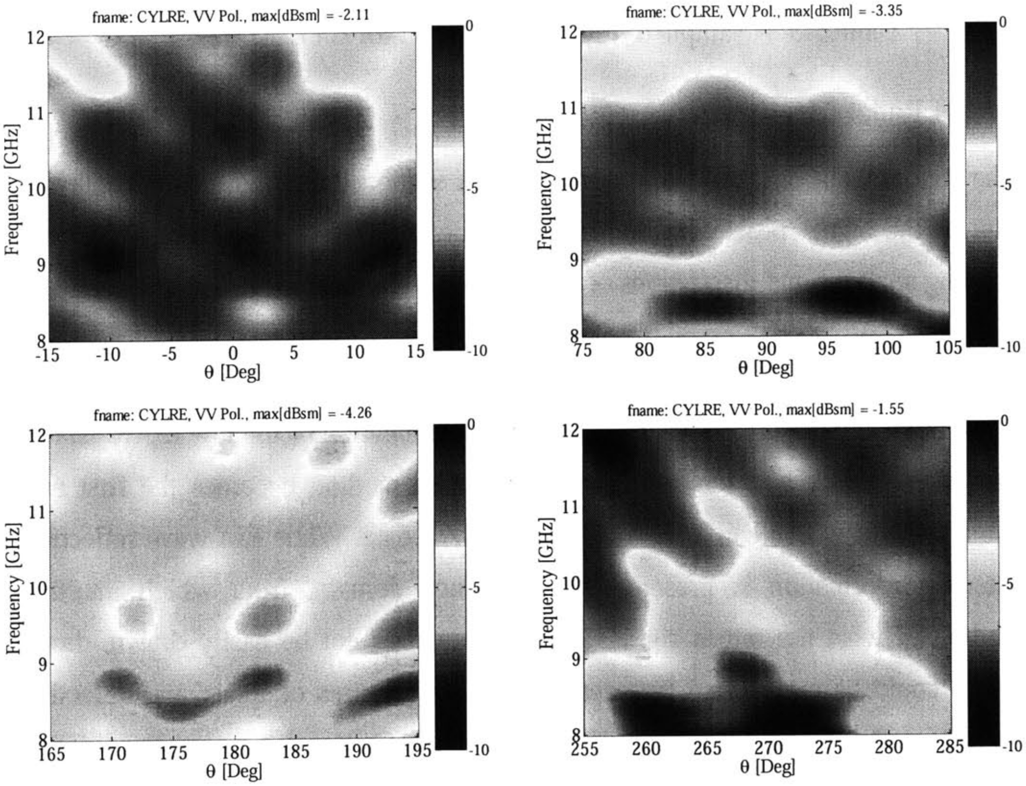

Figure 5-9 Frequency – angle imagery for specimen CYL-RE measured at normal incidence, X-band, VV polarization

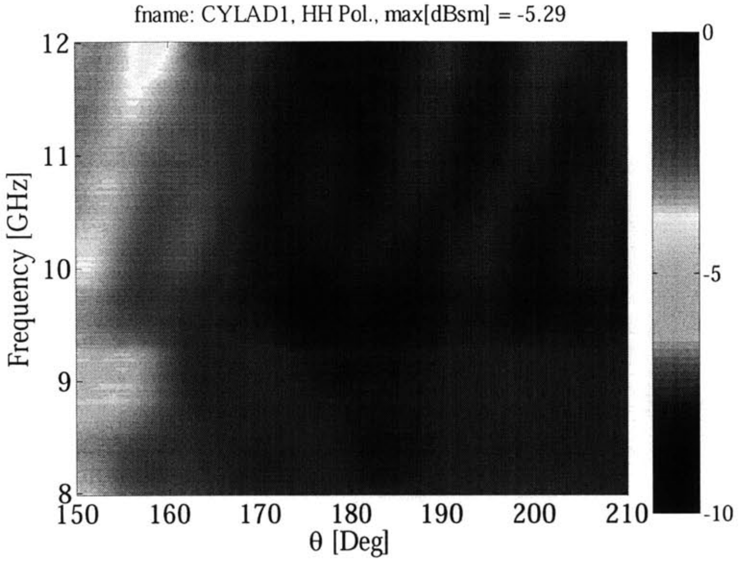

Figure 5-10 Frequency – angle imagery for specimen CYL-AD1 measured at normal incidence, X-band, HH polarization, back surface (no defect)

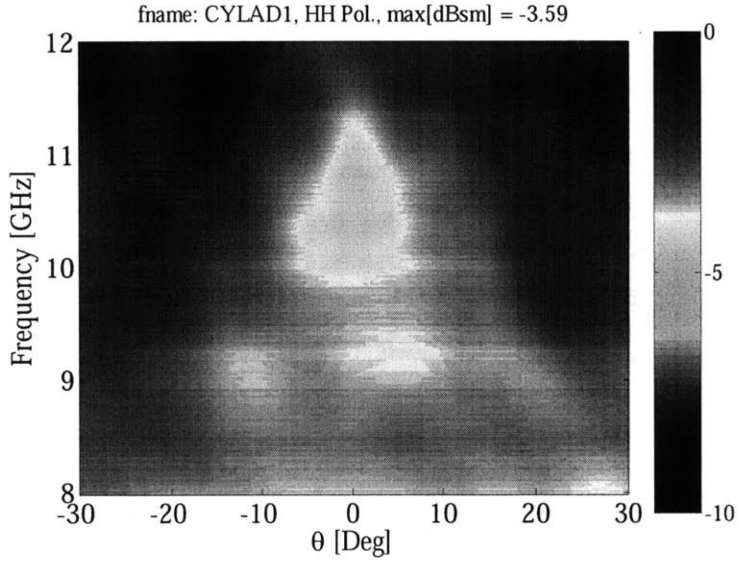

Figure 5-11 Frequency – angle imagery for specimen CYL-AD1 measured at normal incidence, X-band, HH polarization, front surface (with defect)

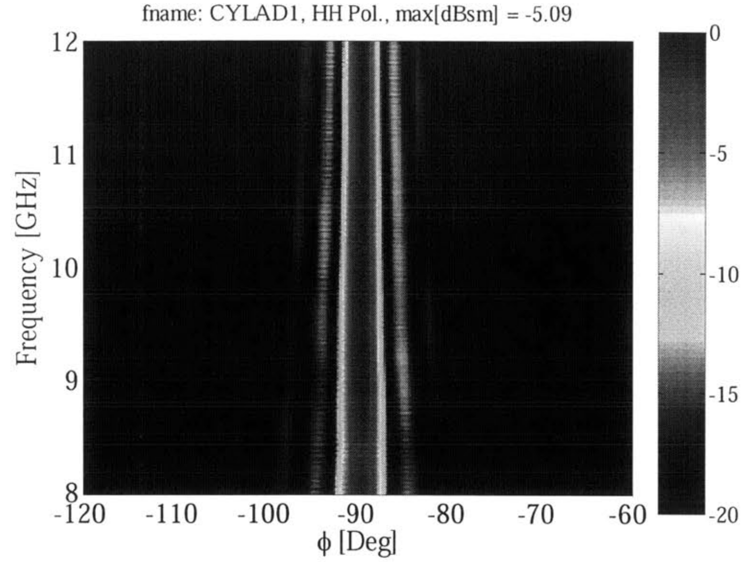

Figure 5-12 Frequency – angle imagery for specimen CYL-AD1 measured at oblique incidence, X-band, HH polarization, back surface (no defect)

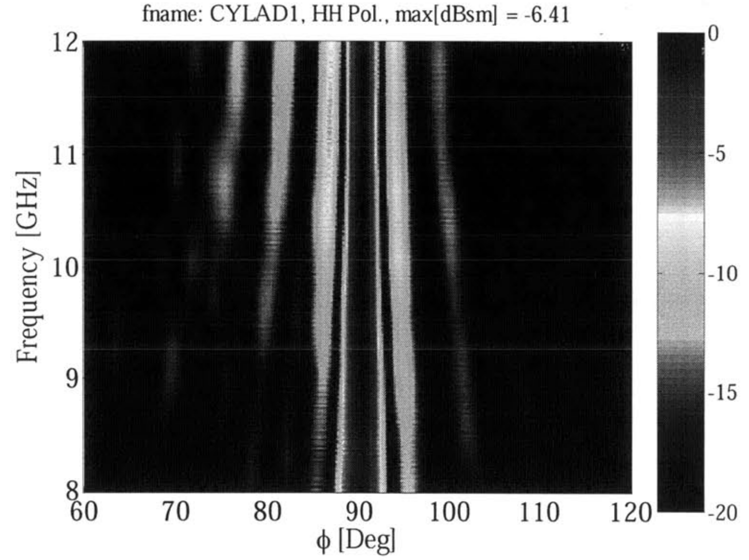

Figure 5-14 Frequency – angle imagery for specimen CYL-AD1 measured at oblique incidence, X-band, HH polarization, front surface (with defect)

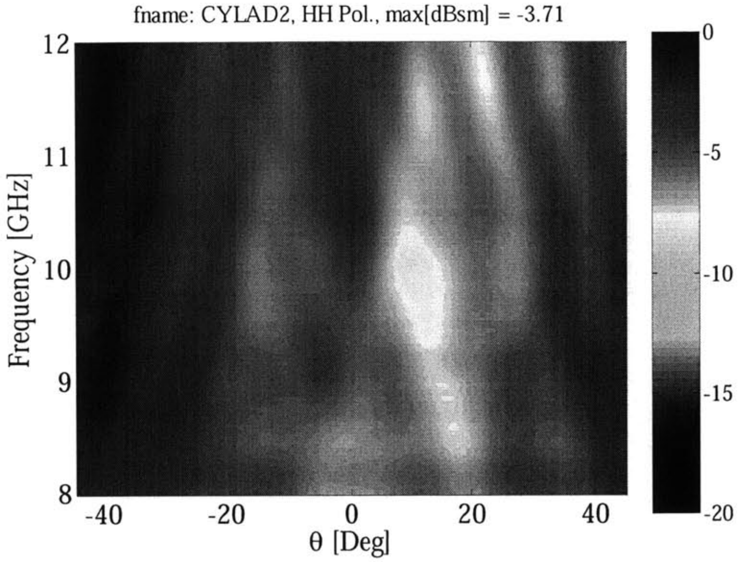

Figure 5-15 Frequency – angle imagery for specimen CYL-AD2 measured at normal incidence, X-band, HH polarization, front surface (with defect)

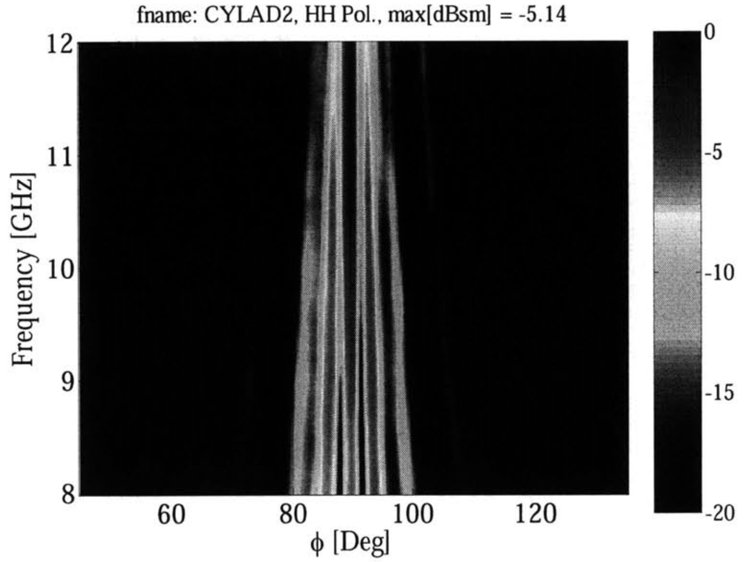

Figure 5-16 Frequency – angle imagery for specimen CYL-AD2 measured at oblique incidence, X-band, HH polarization, front surface (with defect)

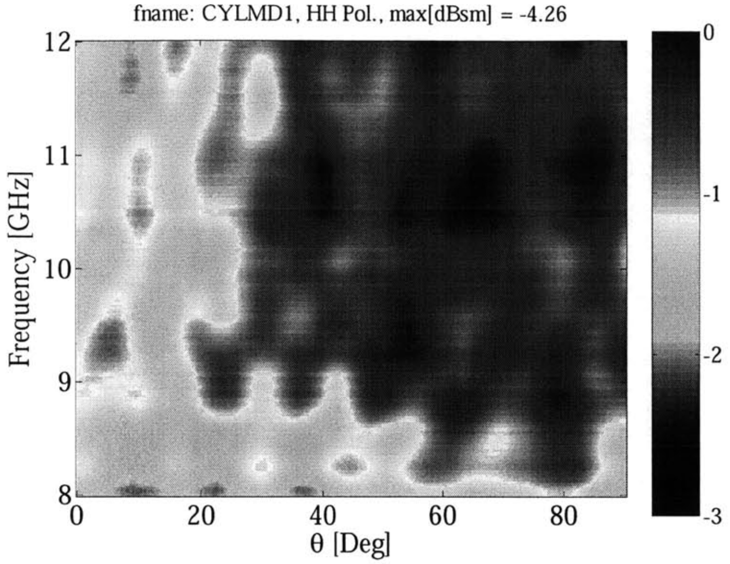

Figure 5-17 Frequency – angle imagery for specimen CYL-MD1 measured at normal incidence, X-band, HH polarization

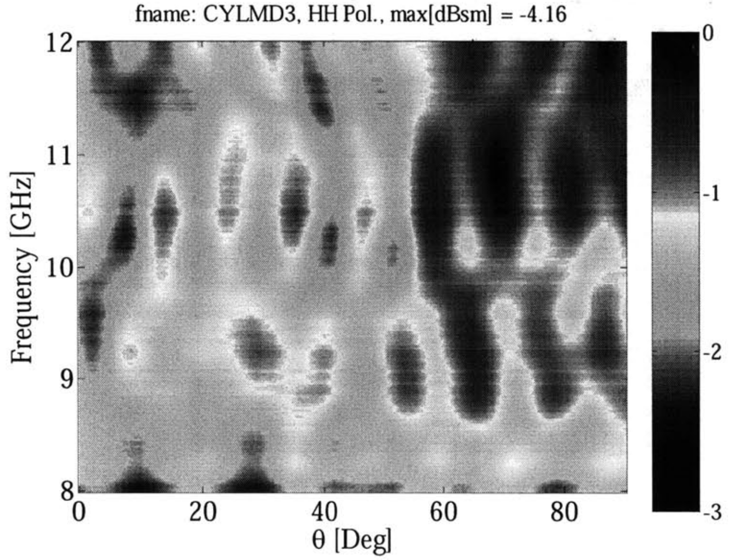

Figure 5-18 Frequency – angle imagery for specimen CYL-MD3 measured at normal incidence, X-band, HH polarization

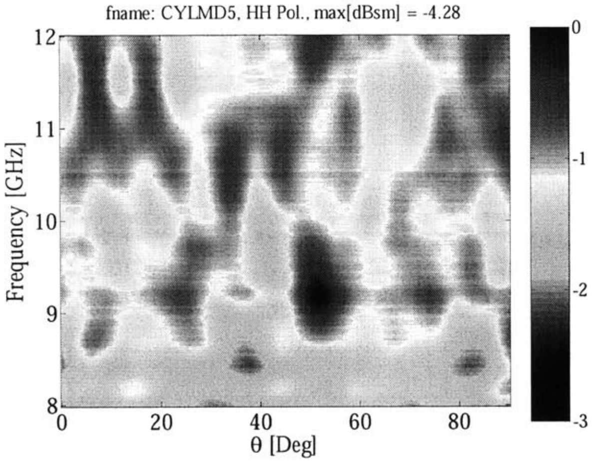

Figure 5-19 Frequency – angle imagery for specimen CYL-MD5 measured at normal incidence, X-band, HH polarization

5.5.2 Cross-Correlation Studies

Cross-correlation studies between intact and defective/damaged specimens were performed. Advanced signal processing tools available in MATLAB® computer software allowed the implementation of the two-dimensional cross-correlation calculations. First, an autocorrelation calculation was conducted for the two selected intact structures that served as benchmark for comparison, namely, CYL-AD1 specimen (back, non-defective surface) and CYL-MD1 specimen (intact FRP-confined concrete). The cross-correlation calculations were then performed for an array of cases which are listed in Table 5-4. The normalization procedures and the estimation of the cross-correlation parameter were discussed in Section 5.3.2. Sample plots of cross-correlation functions are presented in Figure 5-20.

Benchmark Region	Defective Region	Measurement Setup	Frequency Band	Polarization	Cross-Correlation
CYL-AD1 back surface	CYL-AD1 front surface	Normal	X	HH	0.274
				VV	0.261
		Normal	Ku	HH	0.308
				VV	0.294
		Oblique	X	HH	0.718
				VV	0.679
CYL-MD1	CYL-MD3	Normal	X	HH	0.817
				VV	0.816
CYL-MD1	CYL-MD5	Normal	X	HH	0.920
				VV	0.919

Table 5-4 Summary of cross-correlation studies

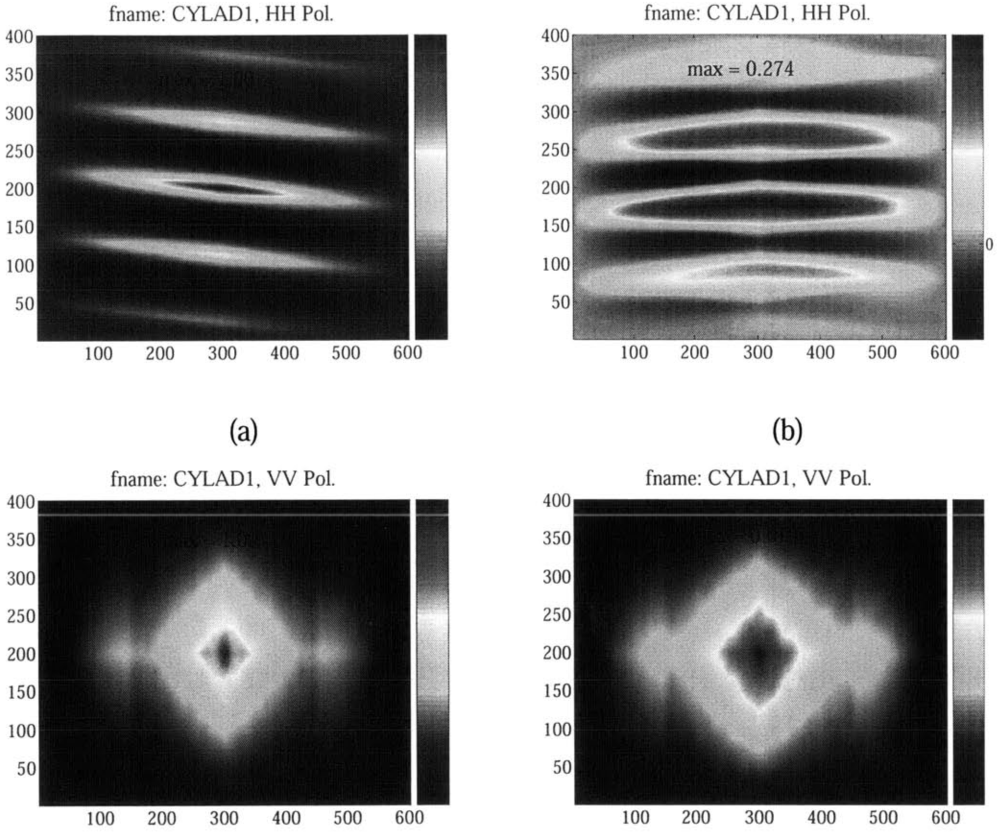

(a) (b)

(c) (d)

Figure 5-20 Autocorrelation and cross-correlation functions for selected cases: (a) and (b) for CYL-AD1 specimen measured in normal incidence, X-band, HH polarization, (c) and (d) for CYL-AD1 specimen measured in oblique incidence, X-band, VV polarization

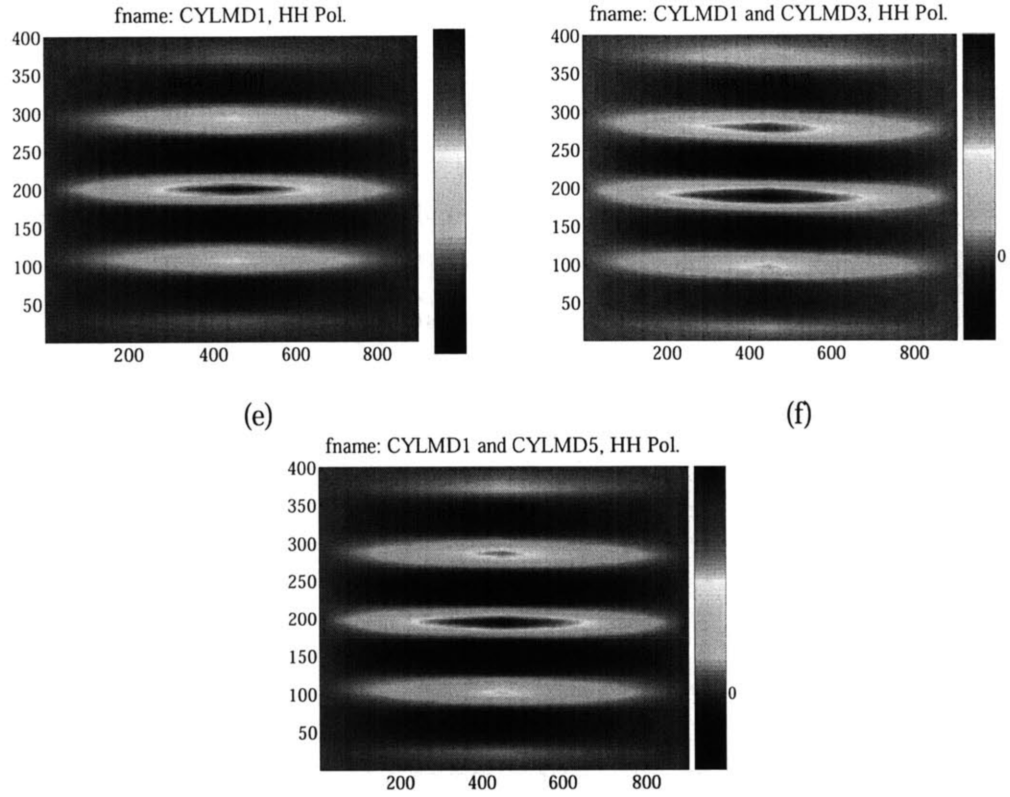

(e)

(f)

(g)

Figure 5-20 (continued) Autocorrelation and cross-correlation functions for selected cases: (e), (f), and (g) for CYL-MD series specimens measured in normal incidence, X-band, HH polarization

5.5.3 Range – Angle Imagery

Range – angle imagery was generated for selected cases from the proposed test program. This type of imagery is developed by the application of Fourier transform techniques, which process the frequency domain radar information into time domain information. Thus, range resolution is resolved for each incident angle. Using the results of raw data processing using Eq. 5.20, the radar measurements for HH and VV polarizations for either X- or Ku-band as functions of frequency are Fourier transformed into RCS amplitudes (in dBsm) as function of time. The time scale is then adjusted to range scale by factoring the velocity of light propagation, c in free-space (see Section 4.1). This process is repeated for each incident angle. The main response observed in the plots is related to the first reflection of the geometry under test. For all studied cases, the main response was shifted to $Range = 0m$. Due to the radar capability of processing phase information, time lags (or alternatively space separations) can be identified in the range – angle information, which in principle could be related to the presence of defective or damage features in specimen surfaces. Figures 5-21 and 5-22 show representative cases of range – angle imagery. In Figure 5-21, range – angle imagery of CYL-AD1 measured at HH polarization, normal incidence, and X-band is presented. In Figure 5-22, range – angle imagery of CYL-AD1 measured at HH polarization, oblique incidence, and X-band is presented. These two cases were selected due to the notorious differences in the radar scattering data and the resulting information and understanding that can be extracted from such data.

For all angles shown in Figure 5-21, there are minor differences in terms of RCS magnitude and space responses. This behavior, which will be further explained in Section 5.6, is directly related to the magnitude of the returned signals at normal incidence, or specular returns. For the case of normal incidence measurements, the receiving antenna records the wave reflection behavior from the specimen profile directly in front of the radar (in this case, such profile is a rectangular region of 380 by 152 mm^2). Being this profile constant throughout the ISAR measurements at normal incidence, any responses generated by the presence of defects, damage, or geometrical distortions must be of the same order of magnitude of the specular returns in order to be detected. As observed in Figure 5.21, the main responses are therefore dominated by specular returns and any other responses are of secondary order and do not appear significant. These results were consistent for all normal incidence measurements independent of the specific damage or defect feature under investigation.

For the selected case in Figure 5-22, the specular response is captured as well, however, oblique incident measurements show different signatures for recorded signals from the side with the defect (or front surface) and from the side with no defect (or back surface). The two selected cases displayed in this section are for HH polarization measurements. After examination of the entire data set using the proposed imagery technique, the use of different polarizations did not provide any additional enhancements in the data interpretation efforts. Further discussion of range – angle imagery results will be presented in Section 5.6.

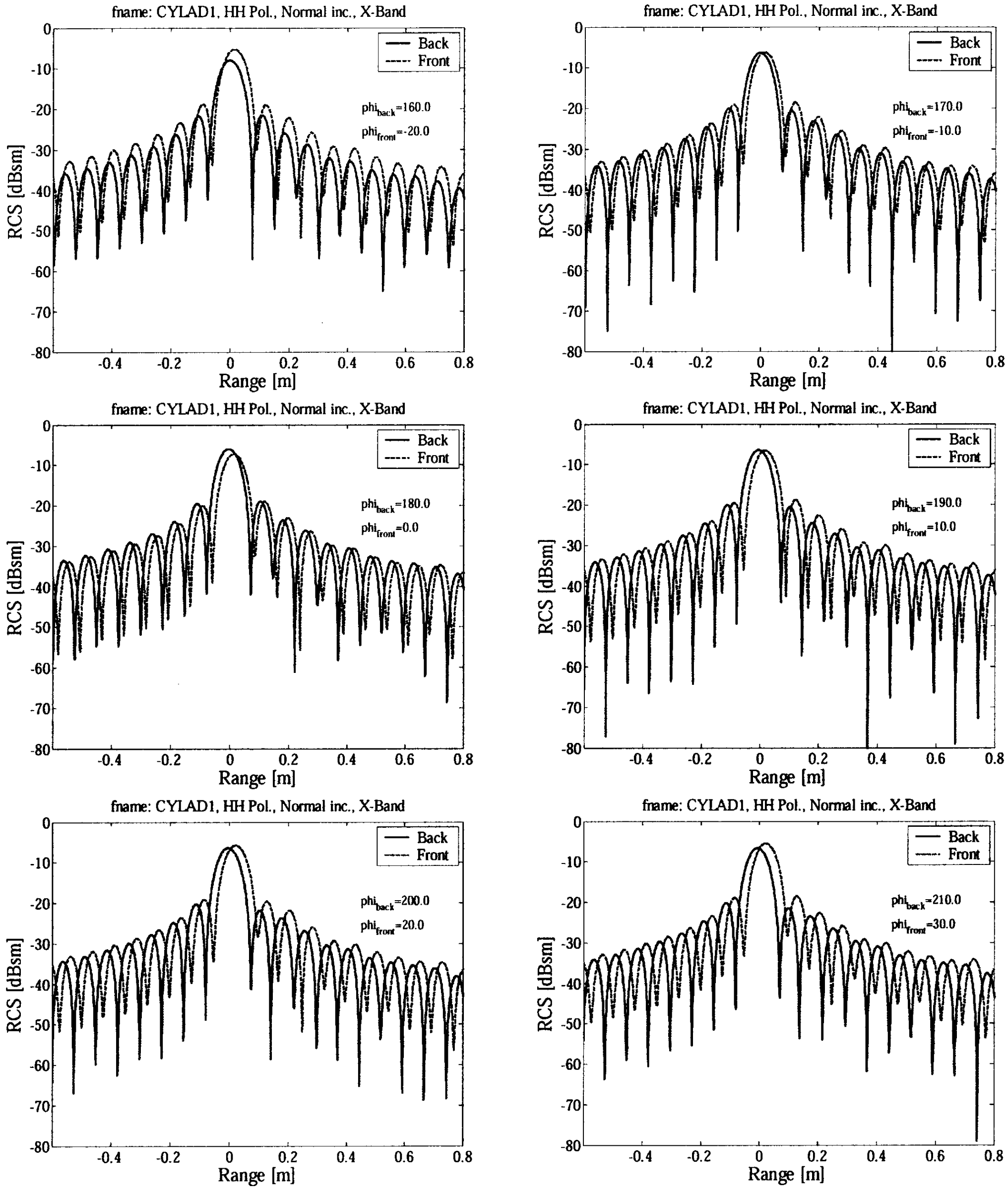

Figure 5-21 Range – angle imagery for specimen CYL-AD1 measured at normal incidence, X-band, HH polarization for different incident angles

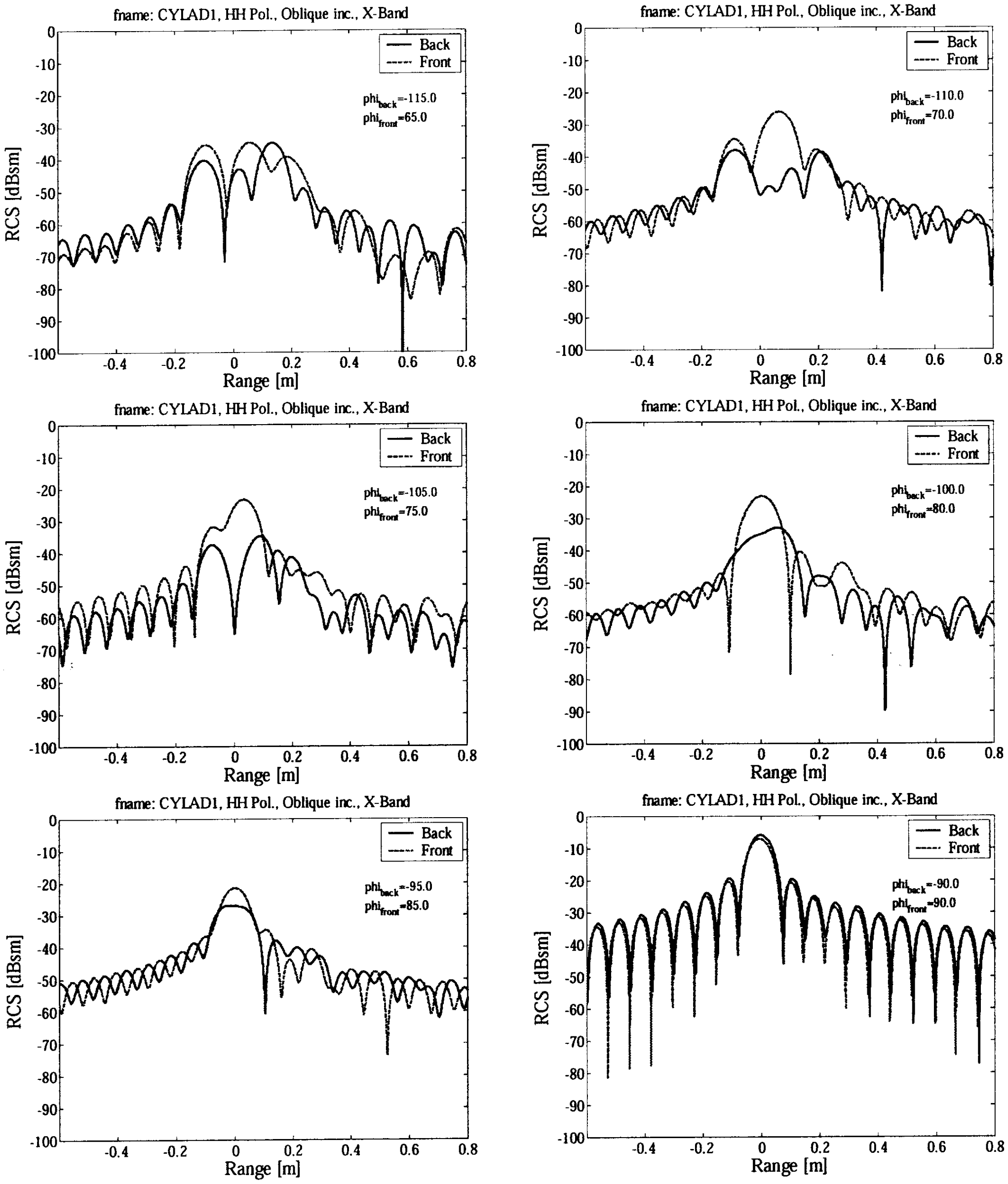

Figure 5-22 Range – angle imagery for specimen CYL-AD1 measured at oblique incidence, X-band, HH polarization for different incident angles

5.5.4 ISAR Imagery

ISAR imagery was produced for selected measurement cases. For this purpose, a backprojection algorithm developed at MIT – Lincoln Laboratory was used. ISAR imagery was exclusively processed by Dennis Blejer and Alex Eapen, both from MIT – Lincoln Laboratory. Specific details regarding the backprojection algorithm are out of the scope of this thesis. The reader is referred to the work by Yegulalp 1999 (see Section 5.3.3) for further details of the imaging formulation. As already mentioned in Section 5.3.3, the backprojection algorithm allows for a full utilization of the information embedded in the radar measurements in order to produce ultra high resolution imaging in range and cross-range. While the use of such signal processing methodology is extremely accurate, less computationally-intense algorithms could be used for implementation of radar NDE technologies in field applications.

Figures 5-23 through 5-27 show ISAR imagery results for selected measurement cases. In Figure 5-23, the case of rebar embedded in concrete was investigated. Figures 5-24 and 5-25 are related to the radar measurements for specimen CYL-AD1 (air cavity) for both normal and oblique incidence schemes, respectively. Finally, Figures 5-26 and 5-27 are related to the radar measurements for mechanically damaged specimens MD1 and MD5, respectively, for normal incidence. For the complete set of ISAR imagery generated for this thesis work, the reader is referred to Appendix B. Discussion of the ISAR imagery results is presented in Section 5.6.

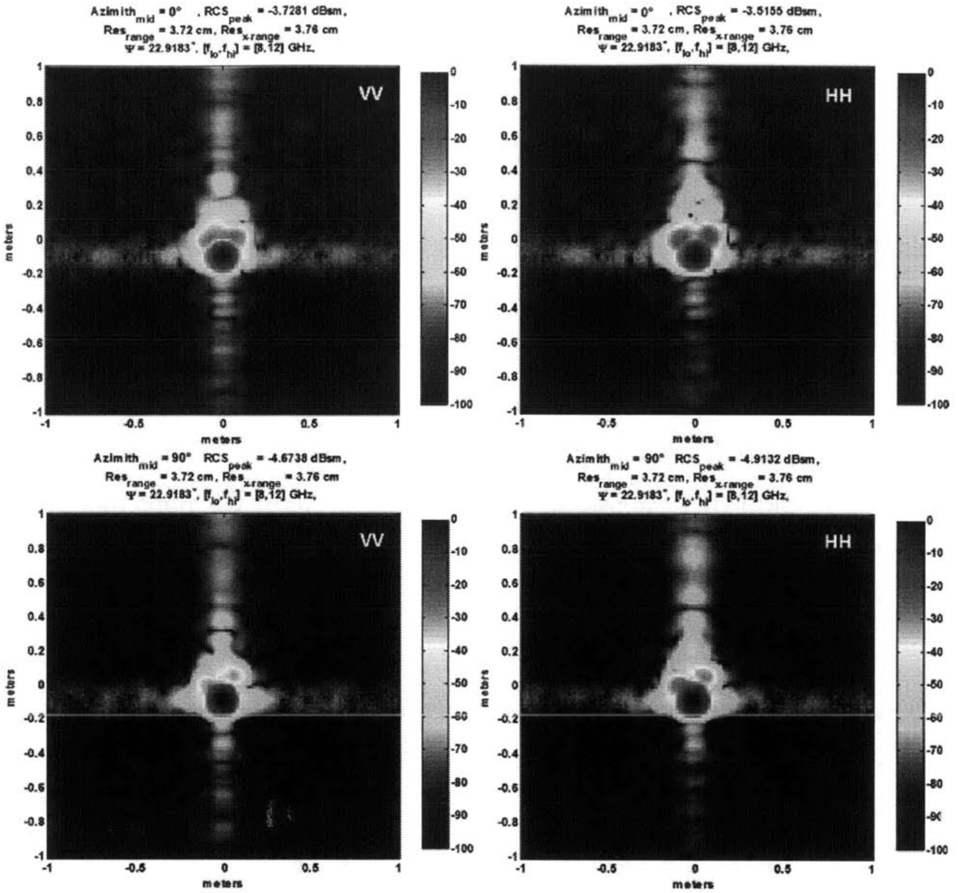

Figure 5-23 ISAR imagery for specimen CYL-RE measured at normal incidence, X-band, HH and VV polarizations at 0 and 90 deg incident angles

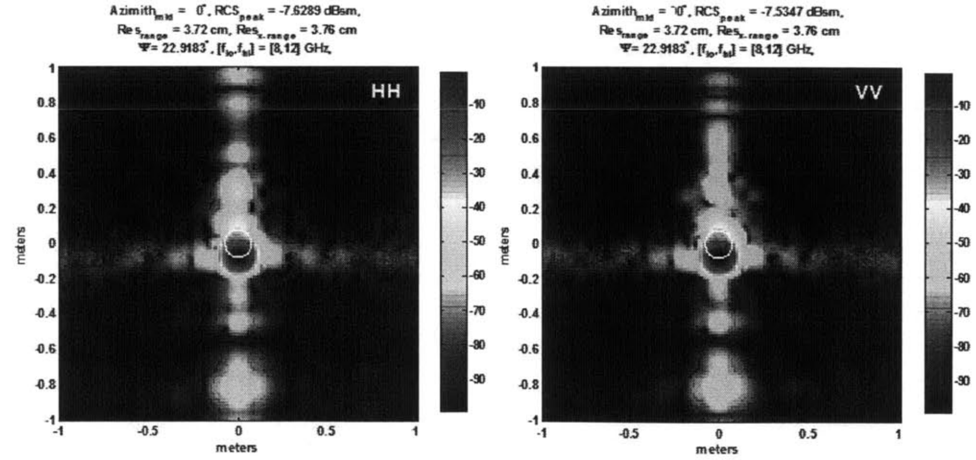

Figure 5-24 ISAR imagery for specimen CYL-AD1 measured at normal incidence, X-band, HH and VV polarizations, front surface (with defect)

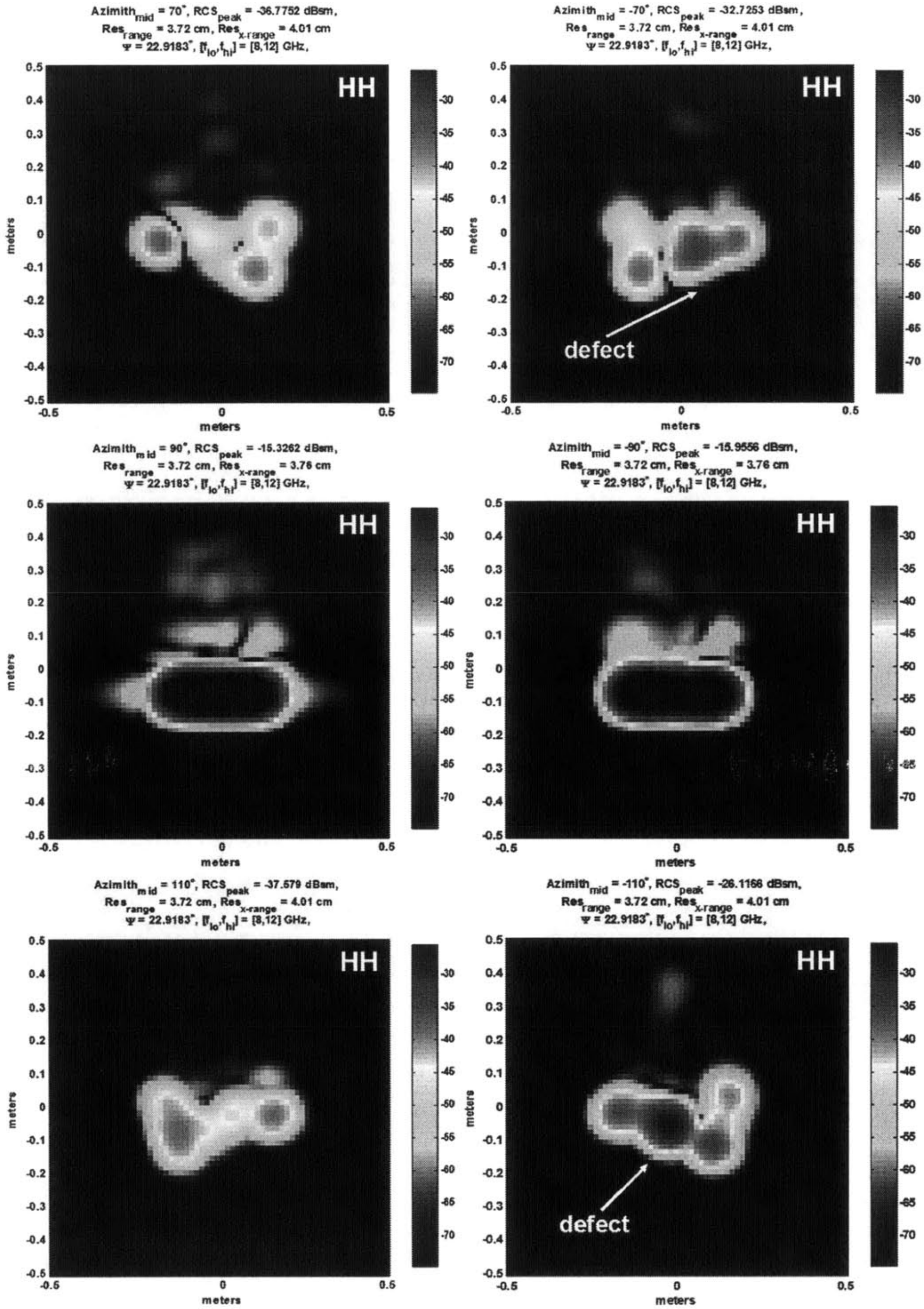

Figure 5-25 ISAR imagery for specimen CYL-AD1 measured at oblique incidence, X-band, HH polarization, back surface (no defect) and front (with defect) at different incident angles

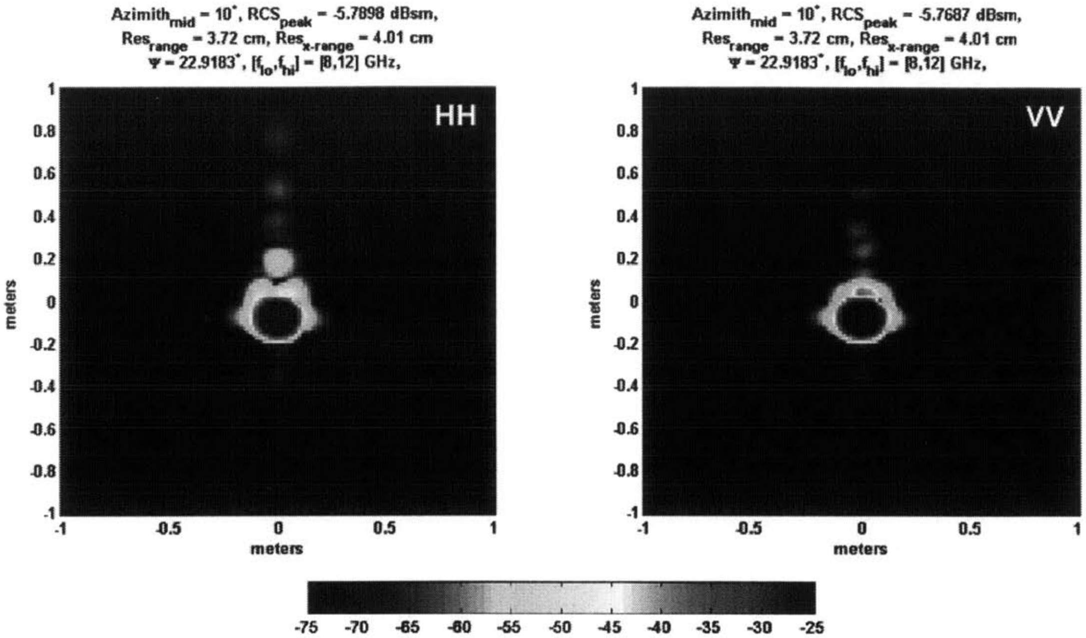

Figure 5-26 ISAR imagery for specimen CYL-MD1 measured at normal incidence, X-band, HH and VV polarizations

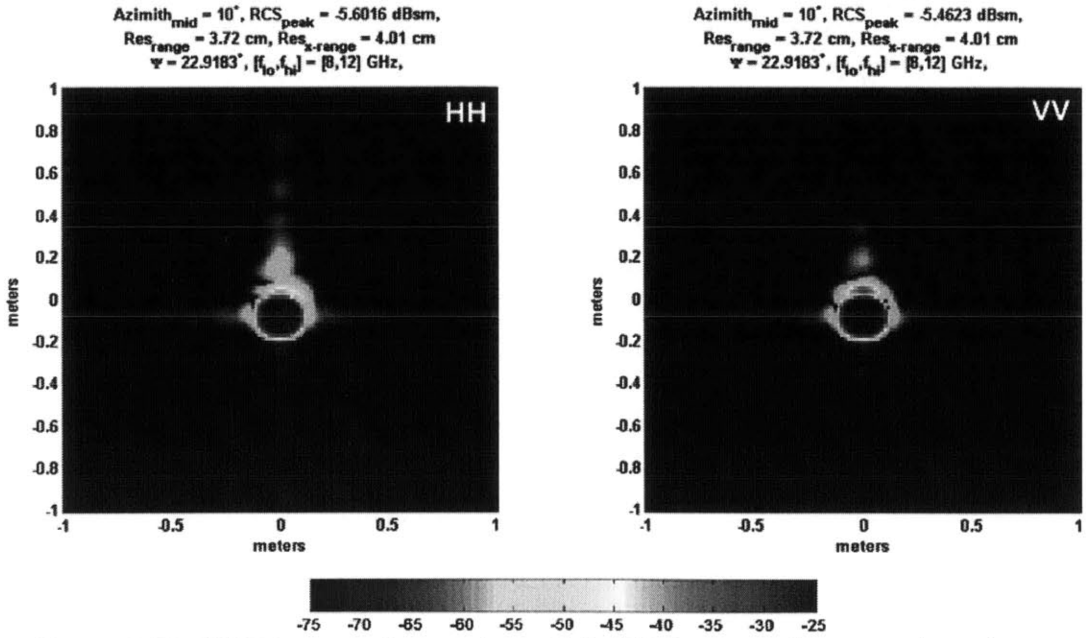

Figure 5-27 ISAR imagery for specimen CYL-MD5 measured at normal incidence, X-band, HH and VV polarizations

5.6 Discussion of Results

Due to the vast amount of radar measurements and the various data analysis and imagery techniques, only qualitative assessment of the ability of the proposed radar NDE technique for defect and damage detection in various concrete and FRP-confined concrete specimens is offered in this section. A stop-light chart, shown in Table 5-5, has been developed for such purposes. Aided by a color code, the chart provides a qualitative assessment of the success or failure of the NDE technique to detect the various defect and damage features under investigation as functions of the imagery technique, polarization, frequency band, and measurement scheme used. Green color labeling was used for the cases of positive detection of the features under investigation. Yellow color labeling was used for cases in which an inconclusive assessment was reached. Red color labeling was used for cases in which the features under investigation were not detected. Finally, gray color labeling was assigned to the cases for which no studies were conducted. Four distinctive features were coded: air cavity, delamination, deformation / microcracking (due to induced mechanical damage through compressive loads), and presence of rebar. For each available radar measurement, three types of imagery were developed: frequency - angle ($f-\phi$), range - angle ($\rho-\phi$), and range - cross-range or ISAR imaging ($\rho-\rho_{xr}$). The results of the cross-correlation studies are treated separately in subsequent sections.

In what follows, discussions on the effects of measurement parameters on the positive or negative detection of defective features or presence of rebar and evaluations of data analysis and imagery techniques used to interpret the developed ISAR measurements are provided.

5.6.1 Evaluation of Measurement Parameters

Measurement Schemes

As mentioned in Section 5.5.3, the magnitude of the specular return for normal incidence measurements, which could be interpreted as an interfering signal, overshadowed any possibilities of feature detection for all defective or mechanically-damaged specimens.

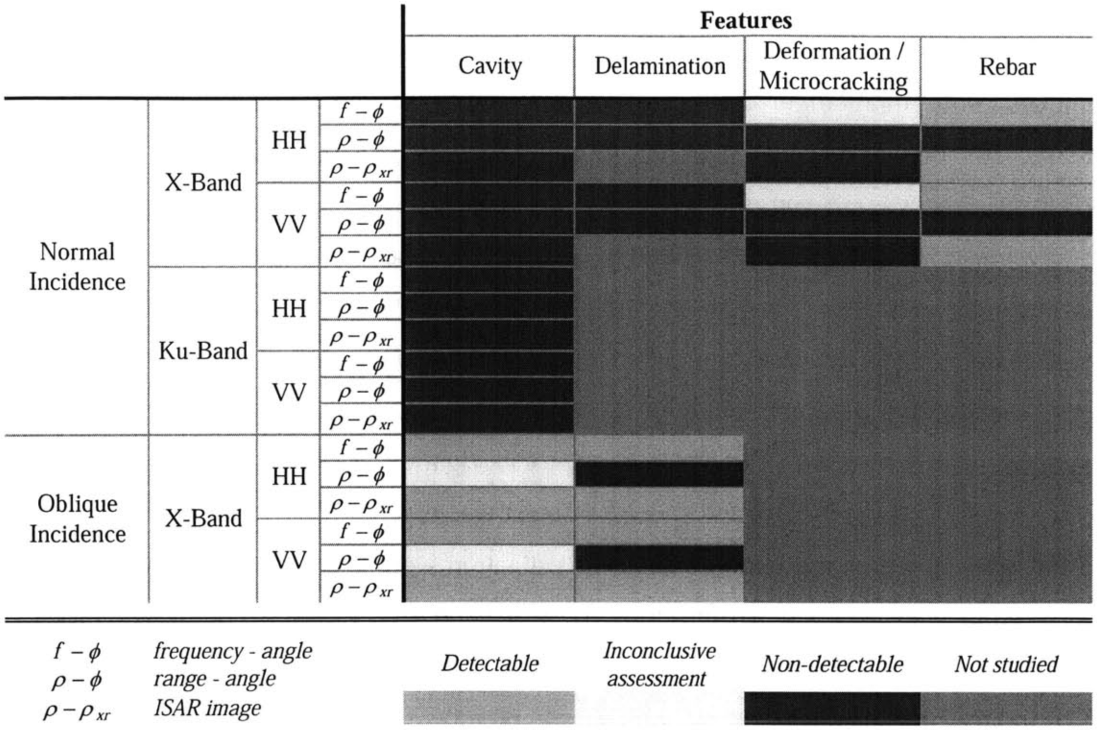

				Features			
				Cavity	Delamination	Deformation / Microcracking	Rebar
Normal Incidence	X-Band	HH	$f-\phi$	■	■	□	▒
			$\rho-\phi$	■	■	■	■
			$\rho-\rho_{xr}$	■	▓	■	▒
		VV	$f-\phi$	■	■	□	▒
			$\rho-\phi$	■	■	■	■
			$\rho-\rho_{xr}$	■	▓	■	▒
	Ku-Band	HH	$f-\phi$	■	▓	▓	▓
			$\rho-\phi$	■	▓	▓	▓
			$\rho-\rho_{xr}$	■	▓	▓	▓
		VV	$f-\phi$	■	▓	▓	▓
			$\rho-\phi$	■	▓	▓	▓
			$\rho-\rho_{xr}$	■	▓	▓	▓
Oblique Incidence	X-Band	HH	$f-\phi$	▒	▒	▓	▓
			$\rho-\phi$	□	■	▓	▓
			$\rho-\rho_{xr}$	▒	▒	▓	▓
		VV	$f-\phi$	▒	▒	▓	▓
			$\rho-\phi$	□	■	▓	▓
			$\rho-\rho_{xr}$	▒	▒	▓	▓

$f-\phi$	*frequency - angle*	*Detectable*	*Inconclusive assessment*	*Non-detectable*	*Not studied*
$\rho-\phi$	*range - angle*				
$\rho-\rho_{xr}$	*ISAR image*	▒	□	■	▓

Table 5-5 Stop-light chart: summary of radar measurement results

While additional studies need to be conducted, oblique incidence measurements showed potential to better resolve the presence of defect or damage features.

X- and Ku-Bands

Based on early studies of CYL-ME, CYL-PC, and CYL-AD1 specimen series, it was observed that measurements using Ku-band frequencies did not enhance the detection capabilities of the proposed radar NDE technique. Results of such measurements were significantly scattered, and therefore, allowed for limited interpretation of the measurements.

Polarization

For the majority of measured cases, small differences in terms of imagery and cross-correlation results were observed between HH and VV polarizations. While for the case of rebar detection in which the VV polarization was expected to yield better results due to the specific alignment of the EM wave fields with the vertically oriented rebar, both polarizations showed successful rebar detection.

5.6.2 Feature Detection

Cavities and Delaminations

As already mentioned before, large specular returns were the main factors affecting the delectability of defect or damage features for normal incidence measurements. Being the characteristic sizes of the air cavity and delamination defects smaller than the specimen largest cross-section, measurements in normal incidence were dominated by specular returns. While additional studies and measurements need to be conducted, oblique incidence measurements could overcome this difficulty, as they already showed success in detecting the two mentioned near-surface defects.

Deformation / Microcracking

Using previous arguments, measurements under normal incidence were dominated by specular return signals. For the case of mechanical damage in FRP-confined concrete specimens previously subjected to particular compressive load levels, damage detection was not positively determined. As discussed in Section 3.8, the mechanical damage induced on the concrete core seemed to be defined by microcracking development or other small-scale processes. Measurements using the oblique incidence scheme could provide potential opportunities for delectability of this type of damage.

Rebar

Rebar detection measurements were conducted for normal incidence only. While the specular return has been the dominant effect frustrating damage detection in all other measured cases at normal incidence, rebar was detected for both HH and VV polarizations. VV polarization was expected to yield improved results compared to the HH polarization due to the specific alignment of electric fields with the vertically oriented rebar. However from ISAR imagery, HH and VV polarization measurements showed positive feature detection when compared to the intact specimen case. At this point, adequate interpretation of the observed responses in the ISAR imagery is pending due to the complex rebar arrangement in only one specimen and the newness of such type of measurement, *i.e.* radar measurements of a dielectric material combined with metallic objects at different positions. Such scenario is of great interest to the civil and radar engineering communities due to the potential benefits of locating buried metallic objects or rebar detection in concrete structural elements.

5.6.3 Evaluation of Data Interpretation Techniques

Frequency – Angle, Range – Angle, and ISAR Imagery

From Table 5-5, it is observed that for the measured cases in which positive detection is confirmed, both frequency – angle and ISAR imagery show similar positive results. Range – angle imagery did not yield the same level of certainty when assessing the presence of defects after comparing radar signatures of intact and defective specimens. A distinction between frequency – angle and ISAR imagery must be made due to significant differences in computational effort. In view of potential applications of this radar NDE methodology for field studies, adequate interpretation of frequency – angle data would be ideal due to the inexpensive data processing involved. Additional radar measurements for other significant test cases may result advantageous for building a database of radar signatures for different types of damage features and enhance their adequate interpretation.

Cross-Correlation

As mentioned before, cross-correlation studies need to be further extended for enhancing the data interpretation aspects of this technique. From the results presented in Section 5.5.2, clear differences were registered between intact and defective or damaged specimens. Cross-correlation parameter thresholds have not been established to directly relate such metric to specific types of damage. However, the application of cross-correlation techniques for contrasting radar signatures is extremely important, especially in view of potential applications of the proposed radar NDE technology for field studies. For instance, for the case in which an operator would be conducting measurements of a large column element with unknown damage characteristics, change detection techniques could be applicable. Radar signatures of the measured element may not be directly linked to the level of damage present in the element; however, the presence of damage could, in principle, be detected if a minimum number of measurements are conduced. Having scanned the structural element at various locations, cross-correlation techniques could be applied to contrast the radar signatures obtained from different surfaces.

An example of this hypothetical scenario is presented in Figure 5-28 using the data for one of the measured cases: specimen CYL-AD1 measured at normal incidence, X-band. Specific incident angles serve as autocorrelation signals, and for this specific example, one dimensional cross-correlation is performed since frequency domain information at individual incident angles is selected. Data for all remaining incident angles is then cross-correlated with the benchmark signals. As observed in Figure 5-28, the cross-correlation parameter varies significantly as a function of incident angle for two cases with different reference incident angles: 160° and $0°$. For the first case, measurements in the back surface ($150° < \theta < 210°$ where no defect is present) gave cross-correlation values of approximately 0.8, while in the front surface ($-30° < \theta < 30°$ where the air cavity is present) cross-correlation values were approximately 0.6. Similar qualitative results are observed for the second case in which the incident angle of references is $0°$. For envisioned field applications, this methodology could be potentially successful for vertical scans of FRP-wrapped concrete column elements with the radar antenna positioned for oblique incidence measurements. Similar change detection and cross-correlation techniques used in this example could be applied to such cases.

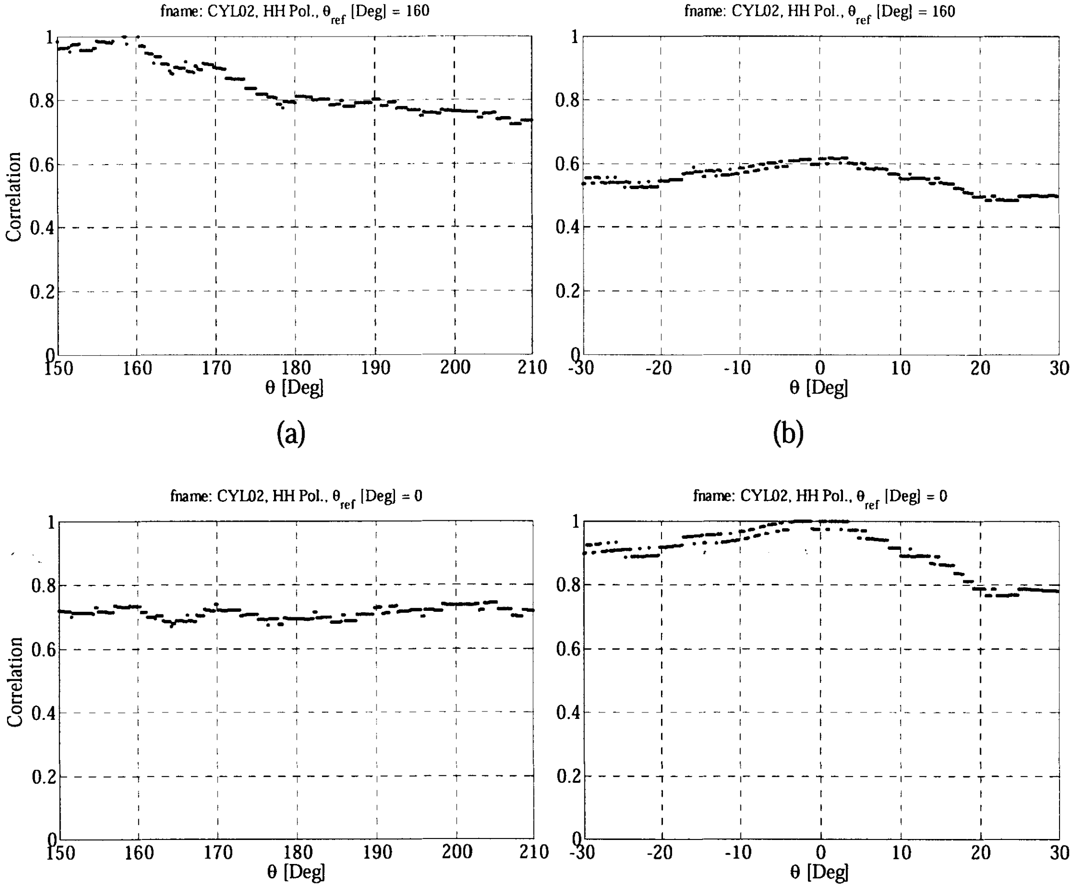

(a) (b)

(c) (d)

Figure 5-28. Example of application of change detection and cross-correlation techniques for detection of defects in FRP-confined confined concrete.

For (a) and (b), autocorrelation signal is frequency data for $\theta_{ref} = 160°$.

For (c) and (d), autocorrelation signal is frequency data for $\theta_{ref} = 0°$.

Chapter 6

Summary, Conclusions, and Future Work

6.1 Summary

This thesis represents an interdisciplinary research effort aimed at establishing part of the fundamental knowledge required for developing a robust NDE methodology for the assessment of FRP-confined concrete column elements using radar technologies. In particular, the two main objectives of this research are investigating the mechanics and damage behavior of FRP-confined concrete subjected to compressive loads and developing a methodology for dielectric property characterization of low-loss materials such as concrete and certain FRP composites using free-space radar measurements. Additionally, exploratory research on radar measurements for a variety of concrete, reinforced concrete, and FRP-wrapped concrete specimens was conducted for the detection of rebar, defects such as air cavities and delaminations, and mechanical damage.

Research on mechanics and damage behavior of FRP-confined concrete subjected to compressive loadings involved a thorough literature review on the current understanding of the subject and the execution of a comprehensive experimental program. In the literature review, characteristic behaviors of active and passive confined concrete systems were investigated and compared to the state-of-the-art behavioral understanding for FRP-confined concrete column elements. Research findings regarding the load-deformation behavior exhibited by FRP-confined concrete under compressive loads, observed failure modes, and applied damage monitoring techniques were examined from across current research to shed light on the damage processes that occur in FRP-confined concrete subjected to compressive loads. The experimental program involved the characterization of the mechanical behavior of plain and FRP-wrapped concrete specimens. A comparative study between the obtained experimental data and various analytical models was also performed. The experimental program was then extended to the characterization of specific damage stages through the use of a consistent metric based on volumetric deformation measurements. Visual observations of the concrete core after bisection of selected specimens and microscopic observations of the concrete microstructure were also conducted to enhance the understanding of damage extent and evolution in the investigated FRP-confined concrete system.

Research on the characterization of dielectric properties for concrete and FRP composite materials involved the development of an integrated methodology for estimating their complex permittivity and that of low-loss materials in general using experimental measurements of EM wave transmission. Such development required theoretical modeling of EM wave propagation phenomena through dielectric media and experimental measurements of EM transmission coefficients for various materials. The estimation procedure of the complex permittivity consisted of two components: (1) implementation of a time difference of arrival (TDOA) technique for estimating the dielectric constant (or real part of the complex permittivity), and (2) a root-searching procedure involving parametric system (SI) identification and an error sum of squares (SSE) criterion for estimating the loss factor (or imaginary part of the complex permittivity). The proposed methodology was validated for Teflon, Lexan, and Bakelite materials for which their dielectric properties are established in the literature. Implementation of the methodology to low-loss construction materials such as concrete and glass FRP was accomplished. Applicability and limitations of the proposed methodology were discussed. In addition to the scope of the experimental measurements for dielectric property characterization, measurements of EM wave transmission for various types of FRP materials were performed to evaluate which types of FRP jacket systems commonly used for strengthening and retrofitting of concrete columns could be potentially assessed through the application of radar technologies.

Exploratory research on the assessment of FRP-confined concrete involved the application of high resolution ISAR technologies for detecting defects and damage features in FRP-confined concrete cylindrical specimens. The experimental program was carried out with the collaboration of MIT – Lincoln Laboratory. Radar measurements were conducted at X- and Ku- frequency bands to achieve high resolution and adequate surface penetration. Two ISAR measurement schemes were used: normal incidence, and oblique incidence. Several types of specimens (plain concrete, reinforced concrete, intact FRP-confined concrete, and defective or damaged FRP-confined concrete) were measured to investigate various features of interest such as rebar location, air cavities, FRP/concrete delaminations, and mechanical damage. Specimens having predetermined levels of mechanical damage were manufactured based on the expertise developed through the mechanics and damage behavior characterization studies for FRP-confined concrete subjected to compressive loads. Various signal processing and imagery techniques were applied for interpreting the ISAR measurements. Evaluations of radar parameters and types of damage/defect features, as well as advantages and limitations of measurement schemes and data interpretation techniques were discussed.

6.2 Conclusions

Based on the results of mechanical testing of FRP-confined concrete specimens, dielectric properties characterization, and preliminary radar measurements for NDE of the FRP-confined concrete, the following conclusions are drawn:

6.2.1 Mechanics and Damage Behavior of FRP-Confined Concrete

- While extensive efforts have been made by the research community for understanding ultimate stages of damage in FRP-confined concrete column elements, there exists a lack of definitive understanding regarding the mechanics and damage behavior of such structural elements for damage levels other than ultimate failure or structural collapse.
- Deformation behavior information could serve as a metric for relating corresponding compressive load levels applied to the structural element to the degree or extent of damage existing in its concrete core. Consistent volumetric deformation behavior was observed in experiments performed for GFRP-confined concrete cylindrical specimens subjected to monotonic compressive loads. The volumetric strain development was linked to important features observed in common axial stress –

axial strain tests such as the ultimate compressive strength of plain concrete and the kink point.

- The previously mentioned experiments also revealed no apparent signs of exterior damage on the FRP jacket until ultimate failure had taken place. However from visual observation studies of specimen cross-sections obtained by bisection procedures, it was inferred that significant residual volumetric strains could be present in the concrete core after a specimen had been loaded to levels close to its ultimate load capacity. Release of the FRP jacket for specimens that had been loaded to such load levels provoked severe cracking in the concrete core. No definitive assessments were made regarding the extent of damage in FRP-confined concrete specimens loaded to various compression load levels through the use of optical microscopic observations. Further work needs to be pursued in this area.

6.2.2 Characterization of Dielectric Properties

- An integrated methodology for the characterization of dielectric properties (dielectric constant and loss factor) of low-loss materials using radar measurements of EM wave transmission was developed. The methodology is on measurements of transmission coefficients in free-space for a broad band of frequencies.
- The proposed methodology was evaluated using various benchmark materials providing acceptable dielectric property estimates comparable to those from existing literature.
- Measurements on construction materials such as concrete and GFRP fabric were also conducted. The estimated values for complex permittivity of concrete were in good agreement with previous research. However, the methodology was not applicable to thin slabs as in the case of a one-ply GFRP specimen. Consequently, the proposed methodology needs further evaluation for adequate criteria to be established regarding minimum acceptable specimen dimensions.
- The proposed methodology has great potential for in situ applications due to the flexibility of the experimental set-up. In principle, this methodology could be used for assessing bulk dielectric properties of complex materials systems such as concrete or masonry walls and slabs.

6.2.3 Radar Measurements of FRP-Confined Concrete

- Preliminary ISAR measurements of FRP-confined concrete specimens having various levels of mechanically-induced damage and various types of near-surface defects such as air cavities and delaminations were conducted. Additionally, measurements aiming at the detection of rebar in concrete were also conducted.
- Various imagery and data analysis techniques were implemented for processing and interpreting radar measurement data. Frequency-angle imagery was found to be advantageous as a first tool to interpret data even though it is the coarser imagery technique from those implemented.
- Radar measurements taken at oblique incidence angles were found optimal for detection of near-surface defects. Measurements at normal incident angles were dominated by specular returns, resulting in poor damage/defect detection capability.
- Although measured at normal incidence, detection of rebar in plain concrete cylinders was feasible. However, understanding of the measured radar signals and corresponding imagery of this test case requires further work.

6.3 Future Work

The research activities recommended to expand this present work are the following:

- Implementation of advanced techniques such as epoxy-dye impregnation in combination with scanning electron microscopy (SEM) observations could reveal what are the mechanisms involved in the deterioration and damage of the concrete matrix in FRP-confined concrete subjected to compressive load levels other than ultimate conditions.
- Investigations of mechanics and damage behavior of FRP-confined concrete column elements should be conducted for other alternative loading scenarios such as eccentric and cyclic compressive loadings to better simulate important service conditions found in actual concrete infrastructure.
- Further validation of the proposed dielectric property characterization technique is needed. A parametric study with specimens of varying thickness would be required to

establish adequate criteria for specimen dimensions in view of potential field applications.

- The results from the exploratory radar NDE studies showed promising opportunities for the methodology to be used in field applications. Various important research issues related to radar parameters, measurement schemes, and data processing and imagery were established. Future research activities should involve additional radar measurements of specimens subjected to various degrees of mechanical damage levels. Specifically, these measurements should be performed using oblique measurement schemes which proved to be optimal for detection of near-surface defects. Additionally, analytical studies and numerical simulations of EM wave propagation could result advantageous for complementing, validating, and interpreting the results from experimental ISAR radar measurements.

References

1. Ahmad, S. H. and Shah, S. P. (1982) "Stress-Strain Curves of Concrete Confined by Spiral Reinforcement." *ACI Journal*, Vol. 79, No. 4, pp. 484-490.
2. Al-Qadi, I.L., Hazin, O.A., Su, W., Riad, S.M. (1995) "Dielectric Properties of Portland Cement Concrete at Low Radio Frequencies." *Journal of Materials in Civil Engineering*, ASCE, Vol. 7, No. 3, pp. 192-198.
3. American Society for Testing and Materials, ASTM (2002) *ASTM C192/C192M - 02: Standard Practice for Making and Curing Concrete Test Specimens in the Laboratory*, manual.
4. American Society for Testing and Materials, ASTM (2003) *ASTM C617 - 98: Standard Practice for Capping Cylindrical Concrete Specimens*, manual.
5. American Society for Testing and Materials, ASTM (2004) *ASTM C39/C39M - 04: Standard Test Method for Compressive Strength of Cylindrical Concrete Specimens*, manual.
6. Ammouche, A., Riss, J., Breysse, D., and Marchand, J. (2001) "Image Analysis for the Automated Study of Microcracks in Concrete." *Cement and Concrete Composites*, Vol. 23, pp. 267-278.
7. Arai, M., Binner, J.P.G., and Cross, T.E. (1995) "Estimating Errors due to Sample Surface Roughness in Microwave Complex Permittivity Measurements obtained using a Coaxial Probe." *Electronics Letters*, Vol. 31, No. 2, pp. 115-117.
8. ASCE (2005) *Report Card on America's Infrastructure*. American Society of Civil Engineers, http://www.asce.org/reportcard/2005/index.cfm.
9. ASTM Subcommittee D09.12. (2001) *American Society for Testing and Materials Standards Vol. 10.02*, ASTM International, West Conshohocken, Philadelphia.
10. Au, C. (2001) *Behavior of FRP-Confined Concrete Structures*. S.M. Thesis, Massachusetts Institute of Technology, Cambridge, Massachusetts.
11. Au, C. (2005) *Moisture Degradation in FRP Bonded Concrete Systems: An Interface Fracture Approach*. PhD Thesis, Massachusetts Institute of Technology, Cambridge, Massachusetts.
12. Au, C. and Büyüköztürk, O. (2005) "Effect of Ply Orientation and Ply Mix on Fiber Reinforced Polymer - Confined Concrete." *Journal of Composites for Construction, ASCE*, in press.
13. Au, C. and Büyüköztürk, O. (2006) "Peel and Shear Fracture Characterization of Debonding in Fiber Reinforced Polymer Plated Concrete Affected by Moisture." *Journal of Composites for Construction*, Vol. 10, No. 1, (in print).
14. Aurand, J.F. (1995) "Measurement of Transient Electromagnetic Propagation through Concrete and Sand." *Sandia Report 96-2254*, Sandia National Laboratory, New Mexico.

15. Baker-Jarvis, J., Geyer, R.G., Grosvenor, J.H. Jr., Janezic, M.D., Jones, C.A., Riddle, B., Weil, C.M. (1998) "Dielectric Characterization of Low-Loss Materials – A Comparison of Techniques." *IEEE Transactions on Dielectrics and Electrical Insulation*, Vol. 5, No. 4, pp. 571-577.

16. Barbero, E. J. (1999) *Introduction to Composite Materials Design.* Taylor & Francis, Philadelphia.

17. Berthelot, J. M. and Robert, J. L. (1987) "Modeling Concrete Damage by Acoustic Emission." *Journal of Acoustic Emission*, Vol. 6, No. 1, pp. 43-60.

18. Blitz, J. and Simpson, G. (1996) *Ultrasonic Methods of Non-destructive Testing.* Chapman and Hall, London.

19. Bungey, J. H. and Millard, S. G. (1996) *Testing of Concrete in Structures, 3th Edition.* Blackie Academic and Professional, London, UK.

20. Bungey, J., Millard, S., Thomas, C., Soutus, M. and Shaw, M. (1995) "Radar assessment of river-bed scour at bridges." *Proc. Int. Syrup. Non-destructive Testing in Civil Engineering (NDT-CE),* eds G. Schickert and H. Wiggenhanser, Vol. 1, pp. 69-76.

21. Büyüköztürk, O. (1998) "Imaging of concrete structures." *NDT & E International.* Vol. 31, No. 4, pp. 233.

22. Büyüköztürk, O. and Rhim, H. C. (1994) "Simulation of Wideband Radar Measurements for Concrete." *Proc. of Structural Materials Technology,* Atlantic City, NJ, pp. 339-344.

23. Büyüköztürk, O. and Rhim, H. C. (1995a) "Modeling of Electromagnetic Wave Scattering by Concrete Specimens." *Cement and Concrete Research*, Vol. 25, No. 5, 1011-1022.

24. Büyüköztürk, O. and Rhim, H. C. (1995b) "Radar Imaging of Concrete Specimens for Non-destructive Testing." *Proc. Int. Conf. on Structural Faults and Repair-95,* ed. M. C. Forde, London, UK, Vol. 2, pp. 307-310.

25. Büyüköztürk, O., Yu, T. Y., and Ortega, J. A. (2005) "A Methodology for Determining Complex Permittivity of Construction Materials Based on Transmission-only Coherent, Wide-bandwidth Free-space Measurements." Submitted to *Journal of Cement and Concrete Composites.*

26. Carino, N. J., and Sansalone, M. (1990) "Flaw Detection in Concrete Using the Impact-Echo Method." *Bridge Evaluation, Repair and Rehabilization,* Nowak, A.S., Ed., pp. 101-118.

27. Cartz, L. (1995) *Nondestructive Testing,* ASM International, Ohio.

28. Chen, W. F. and Han, D. J. (1988) *Plasticity for Structural Engineers.* Springer-Verlag, New York.

29. Chung, T., Carter, C. R., Masliwec, T. and Manning, D. G. (1992) "Impulse Radar Evaluation of Asphalt-Covered Bridge Decks." *1EEE Trans. Aerospace Elec. Sys.*, Vol. 28, No. 1, 125-137.

30. Cullen, A.L. (1987) "A New Free-wave Method for Ferrite Measurement at Millimeter Wavelengths." *Radio Science*, Vol. 22, No. 7, pp. 1168-1170.

31. Davidson, N., Padaratz, I. and Forde, M. (1995) "Quantification of Bridge Scour using Impulse Radar." *Proc. Non-destructive Testing in Civil Engineering (NDT-CE)*, eds G. Schickert and H. Wiggenhauser, Vol. 1, pp. 61-68.

32. De Lorenzis, L. and Tepfers, R. (2003) "Comparative Study of Models on Confinement of Concrete Cylinders with Fiber-Reinforced Polymer Composites." *Journal of Composites for Construction*, ASCE, Vol. 7, No. 3, pp. 219-237.

33. Demers, M. and Neale, K. W. (1999) "Confinement of Reinforced Concrete Columns with Fibre-reinforced Composite Sheets – An experimental Study." *Canadian Journal of Civil Engineering*, Vol. 26, pp. 226-241.

34. Deshpande, M.D., Reddy, C.J., Tiemsin, P.I., and Cravey, R. (1997) "A New Approach to Estimate Complex Permittivity of Dielectric Materials at Microwave Frequencies using Waveguide Measurements." *IEEE Transactions on Microwave Theory and Techniques*, Vol. 45, No. 3, pp. 359-365.

35. Eaves, J. L. and Reedy, E. K. (1987) *Principles of Modern Radar.* Van Nostrand Reinhold Company, New York, New York.

36. Edde, B. (1993) *Radar: Principles, Technologies, Applications.* Prentice Hall, Upper Saddle River, New Jersey.

37. Feng, M. Q., De Flaviis, F., and Kim, Y. J. (2002) "Use of Microwave for Damage Detection of Fiber Reinforced Polymer – Wrapped Concrete Structures." *Journal of Engineering Mechanics.* Vol. 128, No. 2, pp. 172-183.

38. Fenning, P. J. and Brown, A. J. (1995) "Ground Penetrating Radar Investigation." *Construction Repair*, Vol. 9, No. 6, 17-21.

39. Fyfe Co. LLC (2005) Project Details, *The Fibrwrap® Company Website*, http://www.fyfeco.com/index.html.

40. Fyfe Co. LLC (1999) *Design Manual for the Tyfo® Fibrwrap® System*, Rev. 2.

41. Fyfe Co. LLC (2002) *Tyfo® SEH-51A Composite using Tyfo® S Epoxy*, material specifications sheet.

42. Fyfe Co. LLC (2005) *Quality Control Manual for the Tyfo® Fibrwrap® System*, Rev. 6.

43. Gere, J. M. (2000) *Mechanics of Materials, 5th Edition.* Brooks/Cole, Pacific Grove, California.

44. Gershon, D.L., Calame, J.P., Carmel, Y., Antonsen, T.M., and Hutcheon, R.M. (1999) "Open-ended Coaxial Probe for High-temperature and Broad-band Dielectric Measurements." *IEEE Transactions on Microwave Theory and Techniques*, Vol. 47, No. 9, pp. 1640-1648.

45. Ghodgaonkar, D.K., Varadan, V.V., and Varadan, V.K. (1989) "A Free-space Method for Measurement of Dielectric Constants and Loss Tangents at Microwave

Frequencies." *IEEE Transactions on Instruments and Measurement*, Vol. 37, No. 3, pp. 789-793.

46. Gunes, O. (2004). *A Fracture Based Approach to Understanding Debonding in FRP Bonded Structural Members*. PhD Thesis, Massachusetts Institute of Technology, Cambridge, Massachusetts.
47. Halmshaw, R. (1991) *Non-Destructive Testing*, 2nd edn, Edward Arnold, London.
48. Harries, K. A. and Kharel G. (2003) "Experimental Investigation of the Behavior of Variably Confined Concrete." *Cement and Concrete Research Journal*, Vol. 33, pp. 873-880.
49. Harrington, R. F. (2001) *Time-Harmonic Electromagnetic Fields*, John Wiley & Sons, Inc., New York.
50. Holloway, L. (1993) *Polymer Composites for Civil and Structural Engineering*. Chapman and Hall, London.
51. Hornain, H., Marchand, J., Ammouche, A., Commene, J. P., and Moranville, M. (1996) "Microscopic Observation of Cracks in Concrete – A New Sample Preparation Technique using Dye Impregnation." *Cement and Concrete Research*, Vol. 26, No. 4, pp. 573-583.
52. Howie I. and Karbhari V. M. (1995) "Effect of Tow Sheet Composite Wrap Architecture on Strengthening of Concrete Due to Confinement: I – Experimental Studies." *Journal of Reinforced Plastics and Composites*, Vol. 14, pp. 1008-1030.
53. Hsu, T.T.C., Slate, F. O., Sturman, G. M., and Winter, G. "Microcracking of Plain Concrete and the Shape of the Stress-Strain Curve." *Journal of the American Concrete Institute (ACI)*, Vol. 60, No. 2, pp. 203-229.
54. Hull, D. and Clyne, T. W. (1996) *An Introduction to Composite Materials*, Cambridge University Press, Cambridge, UK.
55. IEEE (1984) *Standard Letter Designations for Radar-Frequency Bands, IEEE Standard 521-1984*, Institute of Electrical and Electronics Engineers, New York.
56. Imran, I. and Pantazopoulou, S. J. (1996) "Experimental Study of Plain Concrete under Triaxial Stress." *ACI Materials Journal*, Vol. 93, No. 6, pp. 589-601.
57. IST Group (2005) *Infrastructure Science and Technology Group*. Website, http://web.mit.edu/istgroup.
58. Jalinoos, F. and Olson, L. D. (1995) "Use of Combined Acoustic Impact Echo and Crossmedium Tomography Methods for Defect Characterization in Concrete Civil Structures." *Proc. of the Sixth Int. Conf. on Structural Faults and Repair*, ed. M. C. Forde, Vol. 2, pp. 43-49.
59. Jang, B. Z. (1994) *Advanced Polymer Composites: Principles and Applications*. ASM International, Ohio.
60. Jose, K.A., Varadan, V.V., Hollinger, R.D., Tellakula, A., Varadan, V.K. (2000) "Non Contact Broadband Microwave Material Characterization at Low and High

Temperatures." C. Nyugen, ed., *Proceedings of SPIE in Subsurface Sensing Technologies and Applications II*, pp. 324-331.

61. Kak, A. C. and Sianey, M. (1988). *Principles of Computerized Topographic Imaging*, IEEE Press, New York.
62. Karbhari, V. M. and Gao, Y. Q. (1997) "Composite Jacketed Concrete under Uniaxial Compression – Verification of Simple Design Equation." *Journal of Materials for Civil Engineering*, Vol. 4, No. 9, pp. 185-193.
63. Karihaloo, B. L. and Jefferson, A. D. "Looking into Concrete." *Magazine of Concrete Research*, Vol. 53, No. 2, pp. 135-147.
64. Kingsley S. and Quegan S. (1999) *Understanding Radar Systems*. SciTech Publishing, Inc., Mendham, New Jersey.
65. Knott, E. F., Shaeffer, J. F., and Tuley, M. T. (1993) *Radar Cross Section, 2th Edition*. Artech House, Inc., Norwood, Massachusetts.
66. Kong, J. A. (1990) *Electromagnetic Wave Theory, 2nd edn*, John Wiley, New York.
67. Kotsovos, M. D. and Newman, J. B. (1977) "Behavior of Concrete under Biaxial Stresses." *ACI Journal*, Vol. 66, No. 8, pp. 656-666.
68. Krause, M., Maierhofer, C. and Wiggenhauser, H. (1995) "Thickness Measurement of Concrete Elements using Radar and Ultrasonic Impulse Echo Techniques." *Proc. Int. Conf. on Str. Faults and Repair-95*, ed. M. C. Forde, London, UK, Vol. 2, pp. 17-24.
69. Lam, L. and Teng, J. G. (2003) "Design-oriented Stress-Strain Model for FRP-confined Concrete." *Construction and Building Materials Journal*, Vol. 17, pp. 471-489.
70. Lam, L. and Teng, J. G. (2004) "Ultimate Condition of Fiber Reinforced Polymer – Confined Concrete." *Journal of Composites for Construction, ASCE*, Vol. 8, No. 6, pp. 539-548.
71. Lau, K. and Zhou, L. (2001) "The Mechanical Behavior of Composite-wrapped Concrete Cylinders Subjected to Uniaxial Compression Load." *Journal of Composite Structures*, Vol. 52, pp. 189-198.
72. Ljungberg, S. A. (1994) "Infrared Techniques in Buildings and Structures: Operation and Maintenance. *Infrared Met. and Tech.*, ed. X. P. V. Maldague, Vol. 7, pp. 211-252.
73. Martz, H. E., Roberson, G. P., Skeate, M. F., Schneberk, D. J. and Azevedo, S. G. (1991). "Computerized Tomography Studies of Concrete Samples." *Nuclear Instr. Meth. Phys. Res.*, B58, pp. 216-226.
74. Maurens, M., Priou, A., Brunier, P., Aussudre, S., Lopez, M., and Combes, P. (1992) "Free-space Microwave Measurement Technique for Composite Minerals." A. Priou, ed., *Progress in Electromagnetics Research (PIER) 06*, pp. 345-385.
75. McIntire, P., ed. (1986) *Nondestructive Testing Handbook, 2nd Ed.* American Society of Nondestructive Testing, Vol. 4.

76. Mensa, D. L. (1981) *High Resolution Radar Imaging.* Artech House, Inc., Dedham, Massachusetts.

77. Millard, S.G., Davis, J., Huang, Y., and Bungey, J.H (2002) "A Wide Band System for Measuring Dielectric Properties of Concrete." S. Koppenjan and H. Lee, eds., *Proceedings of the Ninth International Conference on Ground Penetrating Radar,* pp. 416-421.

78. Mills, L. L. and Zimmerman, R. M. (1970) "Compressive Strength of Plain Concrete under Multiaxial Loading Conditions." *ACI Journal,* Vol. 67, No. 10, pp. 802-807.

79. Mirmiran, A. and Yunmei, W. (2001) "Damage Assessment of FRP-encased Concrete using Ultrasonic Pulse Velocity." Journal of Engineering Mechanics, Vol. 127, No. 2, pp. 126-135.

80. Mirmiran, A., Shahawy, M., and El Echary, H. (1999) "Acoustic Emission Monitoring of Hybrid FRP-Concrete Columns." *Journal of Engineering Mechanics,* Vol. 125, No. 8, pp. 899-905.

81. Mitchell, T. M. (1991) Radioactive/nuclear methods. *CRC Handbook on Nondestructive Testing of Concrete,* eds. V. M. Malhotra and N. J. Carino, CRC Press, Boca Raton, pp. 227-252.

82. Nanni A. (1993) *Fiber-Reinforced-Plastic (FRP) Reinforcement for Concrete Structures: Properties and Applications.* Elsevier, Amsterdam.

83. Nanni, A. and Bradford, N. M. (1995) "FRP Jacketed Concrete under Uniaxial Compression." *Journal of Construction and Building Materials,* Vol. 9, No. 2, pp. 115-124.

84. Nicholson, A.M. and Ross, G.F. (1970) "Measurement of the Intrinsic Properties of Materials by Time Domain Techniques." *IEEE Transactions on Instrumentation and Measurements,* Vol. IM-19, pp. 377-382.

85. Orfanidis, S. J. (1996) Optimum Signal Processing, An Introduction, 2nd Edition, Prentice-Hall, Englewood Cliffs, New Jersey.

86. Palaniswamy, R. and Shah, S. P. (1974) "Fracture and Stress-Strain Relationship of Concrete under Triaxial Compression." *Journal of Structural Division, ASCE,* Vol. 100, No. ST5, pp. 901-916.

87. Pantazopoulou, S. J. (1995) "Role of Expansion on Mechanical Behavior of Concrete." *Journal of Structural Engineering, ASCE,* Vol. 121, No. 12, pp. 1795-1805.

88. Pantazopoulou, S. J. and Mills, R. H. (1995) "Microstructural Aspects of the Mechanical Response of Plain Concrete." *ACI Materials Journal,* Vol. 92, No. 6, pp. 605-616.

89. Peters, S. T. (Ed.) (1998) *Handbook of Composites,* Chapman & Hall, New York.

90. Phillips, C. L., Parr, J. M., and Riskin, E. A. (2003) *Signals, Systems, and Transforms, 3rd Edition,* Prentice Hall, Upper Saddle River, New Jersey.

91. Power Corporation (1996) *Lexclad Insulation Systems Brochure #PC-025.* Severn, Maryland.

92. Priestley, M. J. N. and Seible, F. (1996) *Seismic Design and Retrofit of Bridges.* John Willey & Sons, Ldt., New York.

93. Rhim, H. C. (1995) *Nondestructive Evaluation of Concrete using Wideband Microwave Techniques.* PhD Thesis, Massachusetts Institute of Technology, Cambridge, Massachusetts.

94. Rhim, H. C. and Büyüköztürk, O. (1998) "Electromagnetic Properties of Concrete at Microwave Frequency Range." *ACI Materials Journal,* Vol. 95, No. 3, pp. 262-271.

95. Richart, F. E., Brandtzaeg, A., and Brownm R. L. (1928) "A Study of the Failure of Concrete under Combined Compressive Stresses." *Engineering Experiment Station Bulletin No. 185,* University of Illinois, Urbana.

96. Richart, F. E., Brandtzaeg, A., and Brownm R. L. (1929) "The Failure of Plain and Spirally Reinforced Concrete in Compression." *Engineering Experiment Station Bulletin No. 190,* University of Illinois, Urbana.

97. Richart, R. M. and Abbott, B. J. (1975) "Versatile Elastic-Plastic Stress-Strain Formula." *Journal of Engineering Mechanics,* ASCE, Vol. 101, No. 4, pp. 511-515.

98. Scheer, J. A. and Kurtz, J. L. (1993) *Coherent Radar Performance Estimation.* Artech House, Inc., Norwood, Massachusetts.

99. Schwartz, M. M. (1992) *Composite Materials Handbook, 2^{nd} Ed.* McGraw-Hill, New York.

100. Schwartz, M. M. (1997) *Composite Materials, Volume I: Properties, Nondestructive Testing, and Repair.* Prentice Hall, New Jersey.

101. Seo, I.S., Chin, W.S., and Lee, D.G. (2004) "Characterization of Electromagnetic Properties of Polymeric Composite Materials with Free Space Method." *Journal of Composite Structures,* Vol. 66, pp. 533-542.

102. Sika Group (2005) The Sika Construction Business, *Sika Global Website,* http://www.sika.com/construction/cc-our-business.htm.

103. Staelin, D. H., Morgenthaler, A. W., and Kong, J. A. (1994) *Electromagnetic Waves.* Prentice Hall, New Jersey.

104. Stanley, C. and Balendran, R. V. (1994) "Non-destructive Testing of the External Surfaces of Concrete Buildings and Structures in Hong Kong using Infra-red Thermography." *Conc. London,* Vol. 28, No. 3, pp. 35-37.

105. Starnes, M. A., Carino, N. J., and Kausel, E. A. (2003) "Preliminary Thermography Studies for Quality Control of Concrete Structures Strengthened with Fiber-Reinforced Polymer Composites." *Journal of Materials in Civil Engineering,* ASCE, Vol. 15, No. 3, June, pp. 266-273.

106. Stone, W.C. (1996) *Non-line-of-sight (NLS) Construction Metrology.* NIST Construction Automation Program Report No. 1, National Institute of Standards and Technology, Maryland.

107. Strang, G. (1986) *Introduction to Applied Mathematics.* Wellesley-Cambridge Press, Wellesley, Massachusetts.

108. Sullivan, R. J. (2000) *Microwave Radar: Imaging and Advanced Concepts.* Artech House, Inc., Norwood, Massachusetts.

109. Tam, K. C. (1988) "Limited-angle Image Reconstruction in Non-Destructive Evaluation." *Signal Processing and Pattern Recognition in Nondestructive Evaluation of Mat.,* NATO ASI Series, Vol. F-44, pp. 205-229.

110. Tanigawa, Y., Yamada, K., and Kiriyama, S. (1977) "Frequency Characteristics of AE in Concrete." *Proceedings of Japanese Concrete Institute,* Tokyo, Vol. 2, pp. 129-132.

111. Teng, J. G. and Lam, L. (2004) "Behavior and Modeling of Fiber Reinforced Polymer – Confined Concrete." *Journal of Structural Engineering,* Vol. 130, No. 11, pp. 1713-1723.

112. Teng, J. G., Chen, J. F., Smith, S. T., and Lam, L. (2003) "Behavior and Strength of FRP-strengthened RC Structures: A State-of-the-Art Review." *Journal of Structures and Buildings,* Vol. 156, No. 1, pp. 51-62.

113. The MathWorks, Inc. (2005) Support, MATLAB. December 3. http://www.mathworks.com/access/helpdesk/help/techdoc/matlab.shtml

114. Toutanji, H. A. (1999) "Stress-Strain Characteristics of Concrete Columns externally Confined with Advanced Fiber Composites." *American Concrete Institute Journal,* Vol. 96, No. 3, pp. 397-404.

115. Tuttle, M. (2004) *Structural Analysis of Polymeric Composite Materials.* Marcel Dekker, Inc., New York.

116. Van Den Einde, L., Zhao, L., and Sible (2003) "Use of FRP Composites in Civil Structural Applications." Journal of Construction and Building Materials, Vol. 17, pp. 389-403.

117. van Mier, J. G. M. (1984) "Complete Stress-Strain Behaviour and Damaging Status of Concrete under Multiaxial Conditions." *Proceedings of RILEM/CEB/CNRS International Conference on Concrete under Multiaxial Conditions,* Toulouse, France.

118. van Mier, J. G. M. (1991) "Mode I Fracture of Concrete: Discontinuous Crack Growth and Crack Interface Grain Bridging." *Cement and Concrete Research,* Vol. 21, pp. 1-15.

119. van Mier, J. G. M. (1997) *Fracture Processes of Concrete: Assessment of Material Parameters in Fracture Models.* CRC Press, Inc., Boca Raton.

120. Venkatesh, M. S. and Raghavan, G. S. V. (2005) "An Overview of Dielectric Properties Measuring Techniques." *Canadian Biosystems Engineering*, Vol. 47, pp. 7.15-7.30.

121. Venkatesh, S.R. and Dahleh, M.A. (2001) "On System Identification of Complex Systems from Finite Data." *IEEE Transactions on Automatic Control*, Vol. 46, No. 2, pp. 235-257.

122. Ward, I. M. and Sweeney, J. (2004) *An Introduction to the Mechanical Properties of Solid Polymers, 2nd Ed.* John Willey & Sons, Ldt., West Sussex.

123. Wehner D. R. (1995) *High Resolution Radar, 2nd Edition.* Artech House, Inc., Norwood, Massachusetts.

124. Xiao, Y. and Wu, H. (2000) "Compressive Behavior of Concrete Confined by Carbon Fiber Composite Jackets." *Journal of Materials in Civil Engineering, ASCE*, Vol. 2, No. 12, pp. 139-146.

125. Xiao, Y., Sheikh, S. A., and Li, Z. X. (2001) "Applications of FRP Composites in Concrete Columns." *FRP Composites in Civil Engineering, Vol. I*, J. G. Teng, Ed., pp. 731-739.

126. Yang, X., Nanni, A., and Chen, G. (2001) "Effect of Corner Radius on the Performance of Externally Bonded FRP Reinforcement." *Proceedings of FRPRCS-5*, Cambridge, UK.

127. Yegulalp, A. F. (1999) "Fast Backprojection Algorithm for Synthetic Aperture Radar." *IEEE National Radar Conference - Proceedings*, pp. 60-65.

128. Zhang, J. and Huang, Y. (1999) "Extraction of Dielectric Properties of Building Materials from Free-space Time-domain Measurement." *Proceedings IEEE High Frequency Postgraduate Student Colloquium*, pp. 127-132.

129. Zoughi, R. and Bakhtiari, S. (1990) "Microwave Nondestructive Detection and Evaluation of Disbonding and Delamination in Layered-Dielectric-Slabs." *IEEE Transactions on Instrumentation and Measurement*, Vol. 39, No. 6, pp. 1059-1063.

Appendix A

Frequency – Angle Imagery for All Measured Specimens

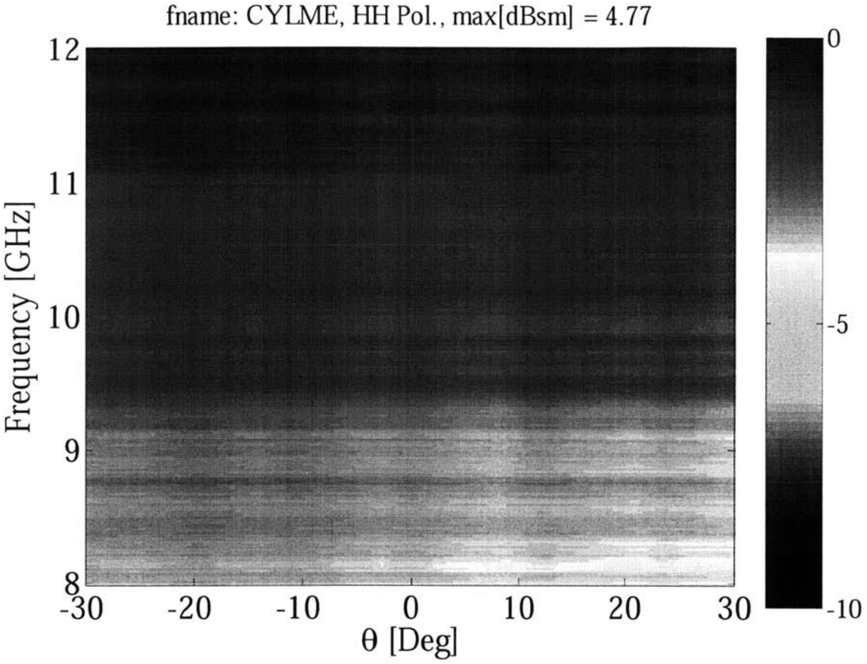

Figure A-1 Frequency – angle imagery for specimen CYL-ME measured at normal incidence, X-band, HH polarization

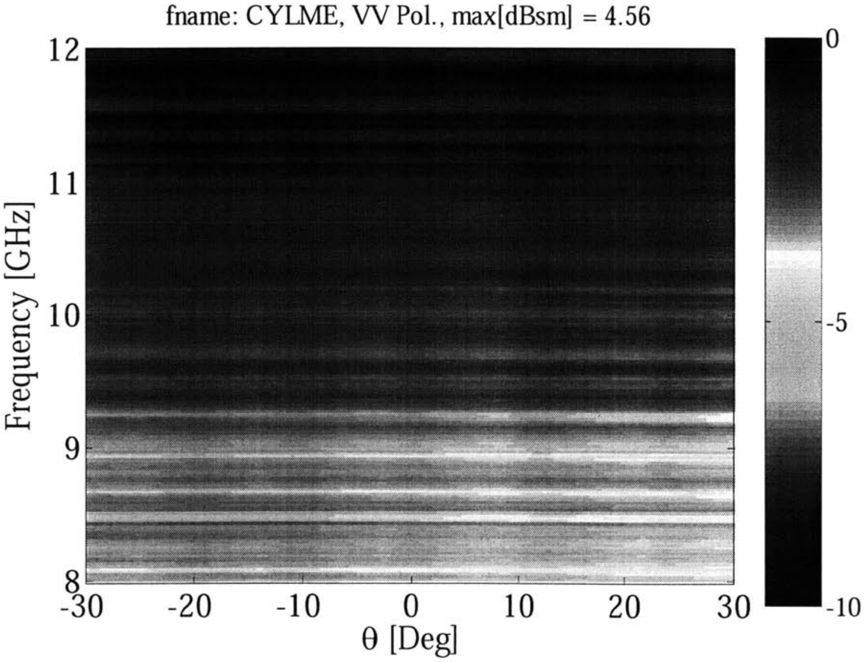

Figure A-2 Frequency – angle imagery for specimen CYL- ME measured at normal incidence, X-band, VV polarization

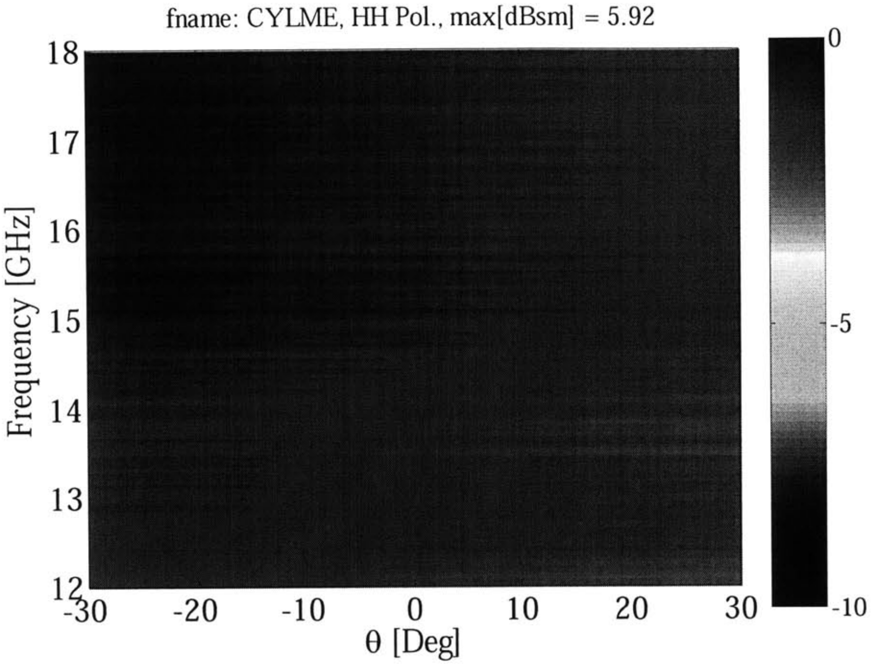

Figure A-3 Frequency – angle imagery for specimen CYL- ME measured at normal incidence, Ku-band, HH polarization

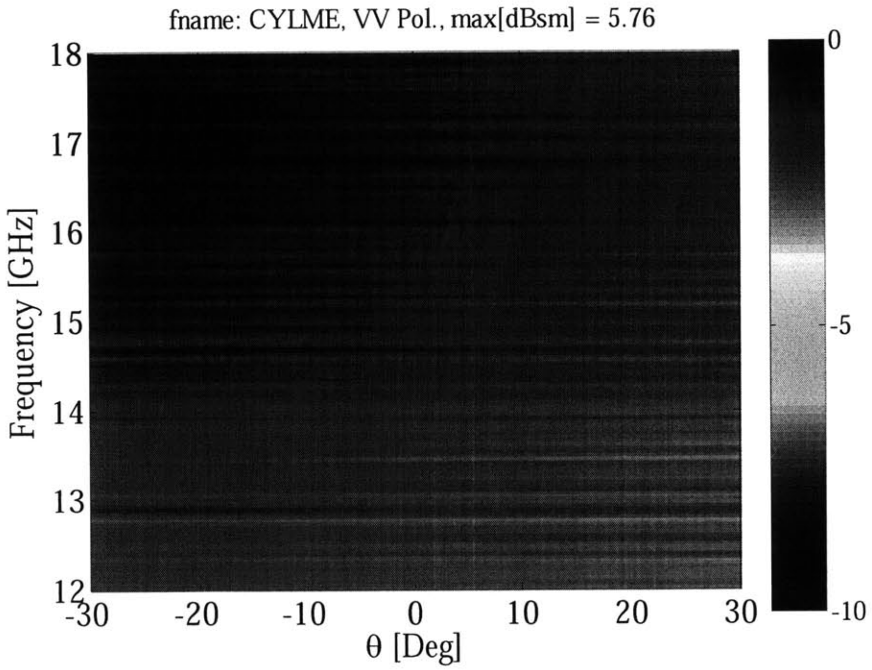

Figure A-4 Frequency – angle imagery for specimen CYL- ME measured at normal incidence, Ku-band, VV polarization

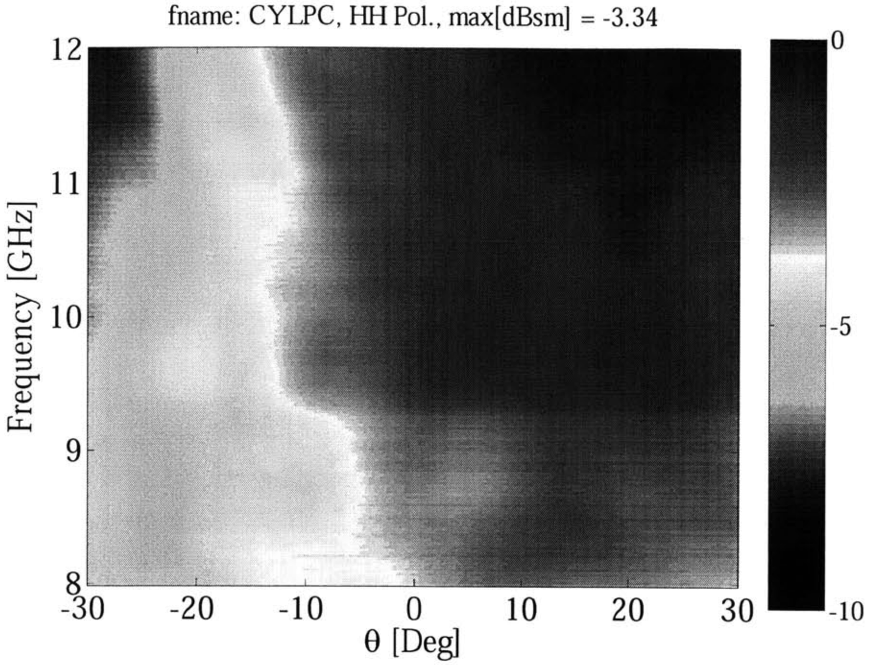

Figure A-5 Frequency – angle imagery for specimen CYL-PC measured at normal incidence, X-band, HH polarization

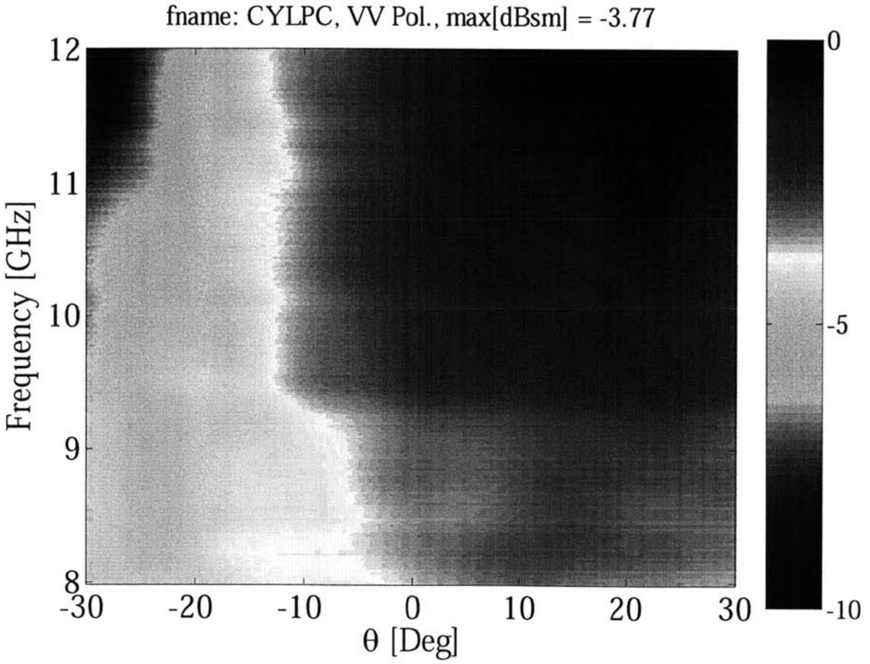

Figure A-6 Frequency – angle imagery for specimen CYL-PC measured at normal incidence, X-band, VV polarization

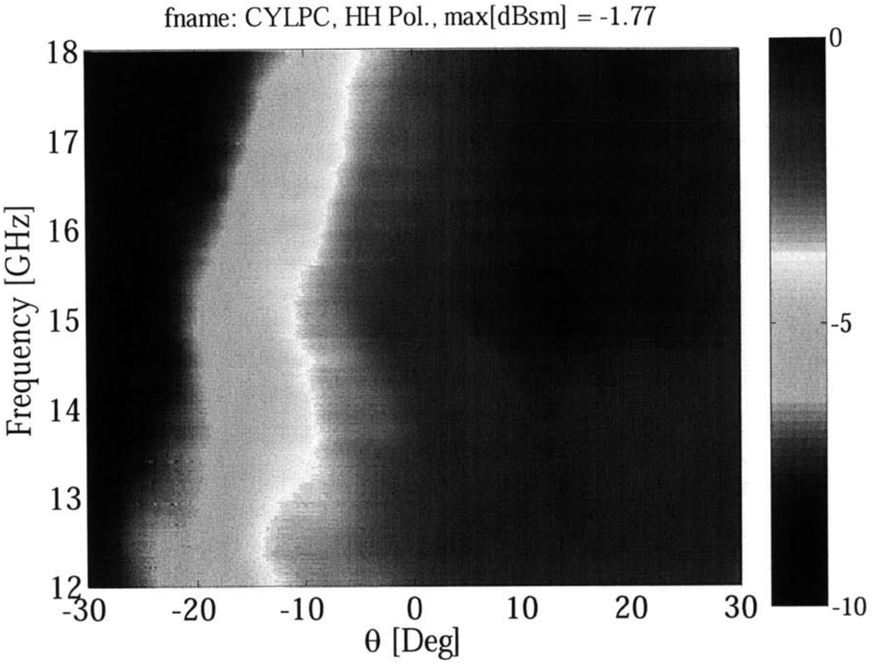

Figure A-7 Frequency – angle imagery for specimen CYL-PC measured at normal incidence, Ku-band, HH polarization

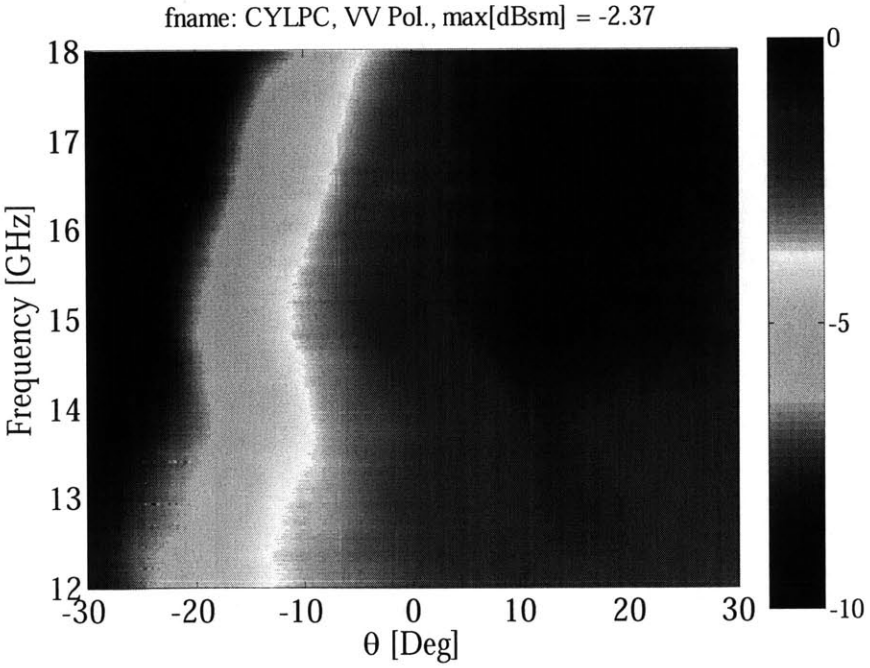

Figure A-8 Frequency – angle imagery for specimen CYL-PC measured at normal incidence, Ku-band, VV polarization

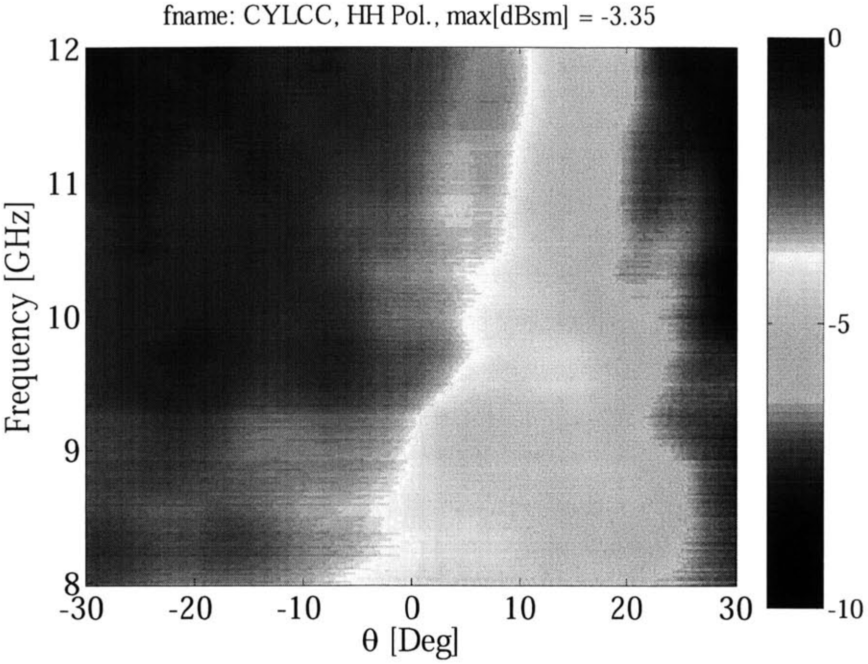

Figure A-9 Frequency – angle imagery for specimen CYL-CC measured at normal incidence, X-band, HH polarization

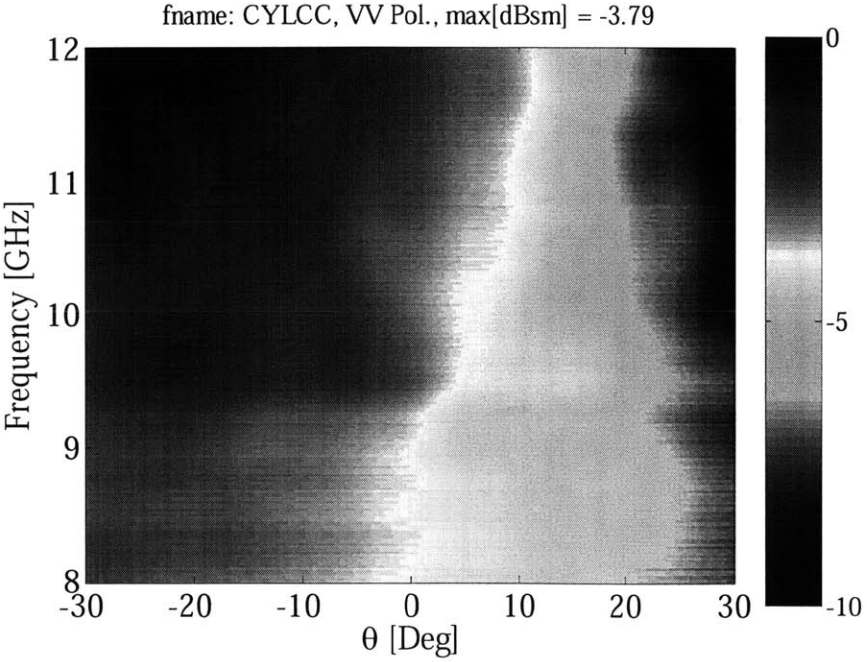

Figure A-10 Frequency – angle imagery for specimen CYL-CC measured at normal incidence, X-band, VV polarization

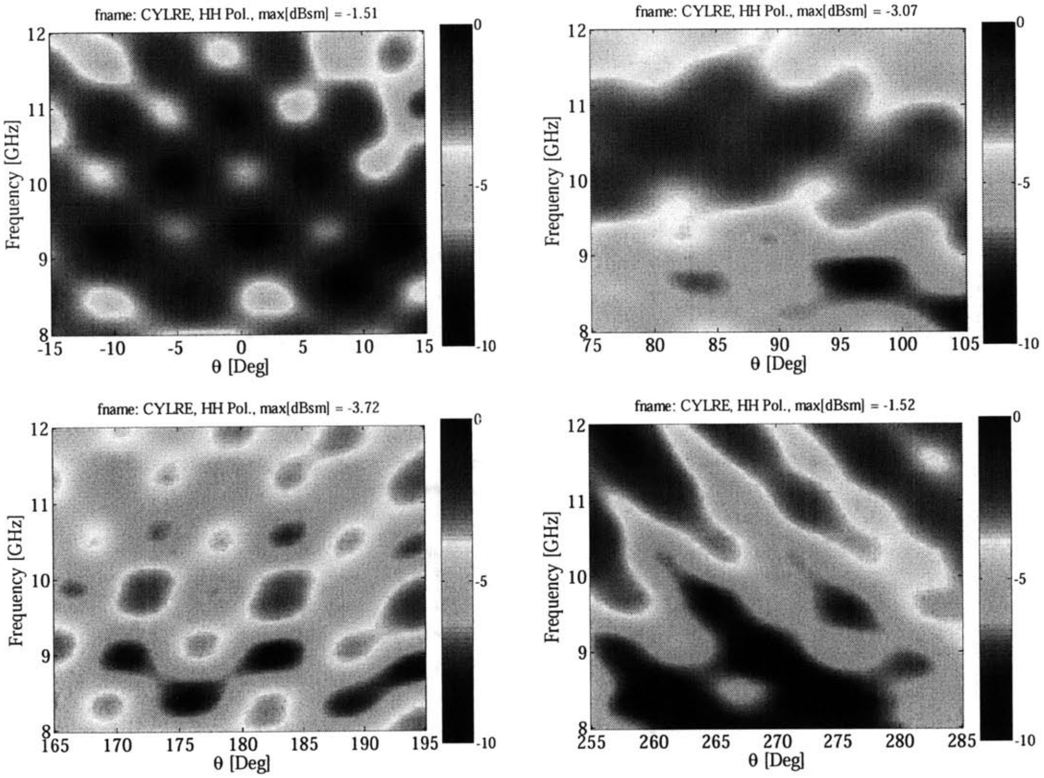

Figure A-11 Frequency – angle imagery for specimen CYL-RE measured at normal incidence, X-band, HH polarization

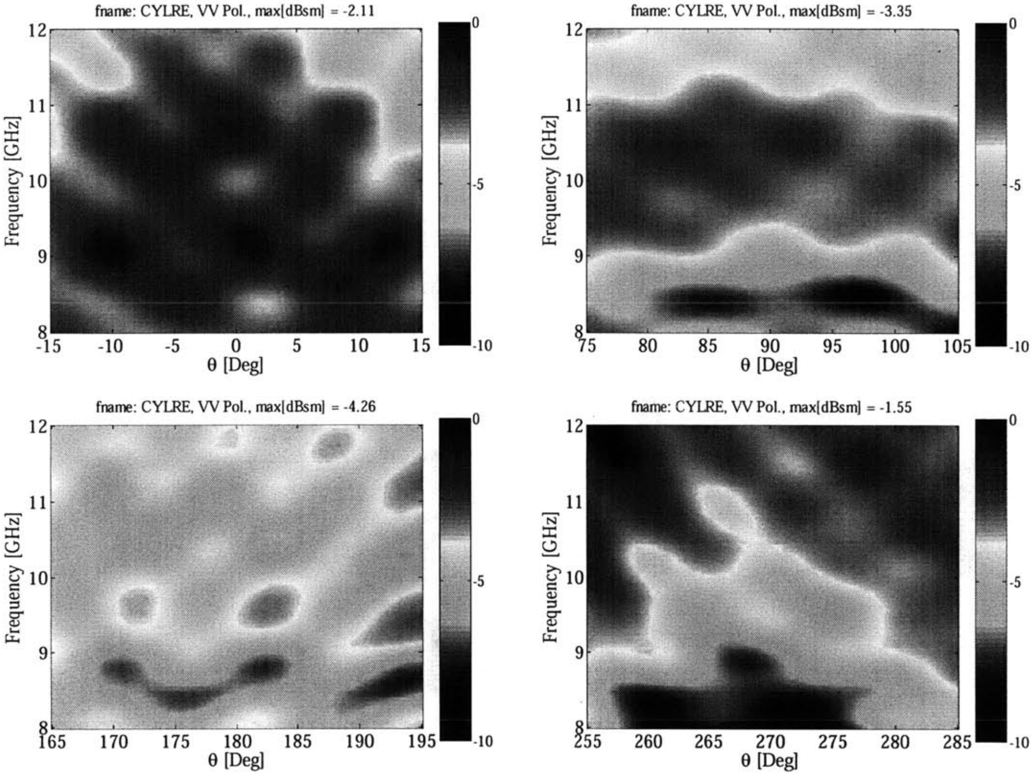

Figure A-12 Frequency – angle imagery for specimen CYL-RE measured at normal incidence, X-band, VV polarization

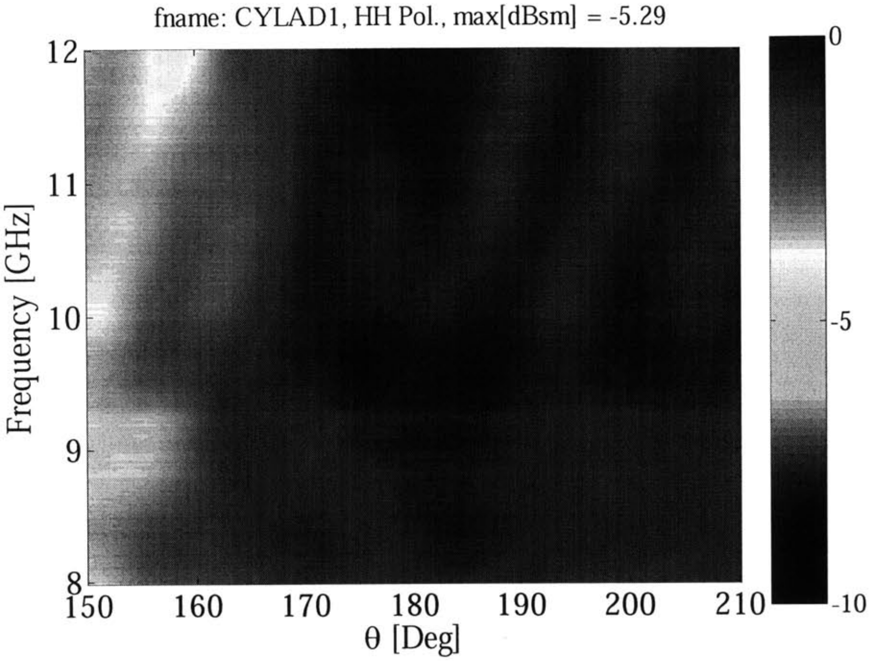

Figure A-13 Frequency – angle imagery for specimen CYL-AD1 measured at normal incidence, X-band, HH polarization, back surface (no defect)

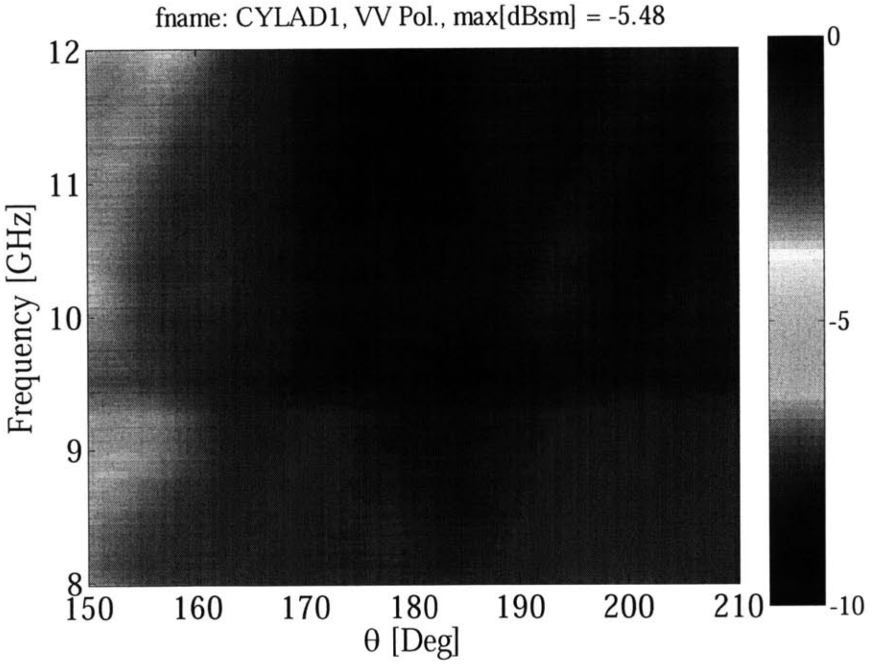

Figure A-14 Frequency – angle imagery for specimen CYL-AD1 measured at normal incidence, X-band, VV polarization, back surface (no defect)

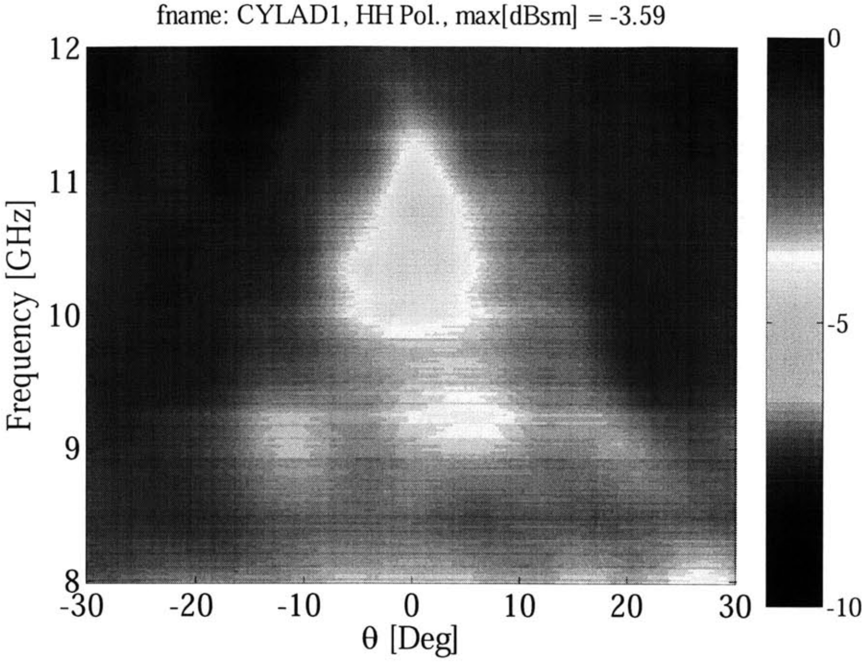

Figure A-15 Frequency – angle imagery for specimen CYL-AD1 measured at normal incidence, X-band, HH polarization, front surface (with defect)

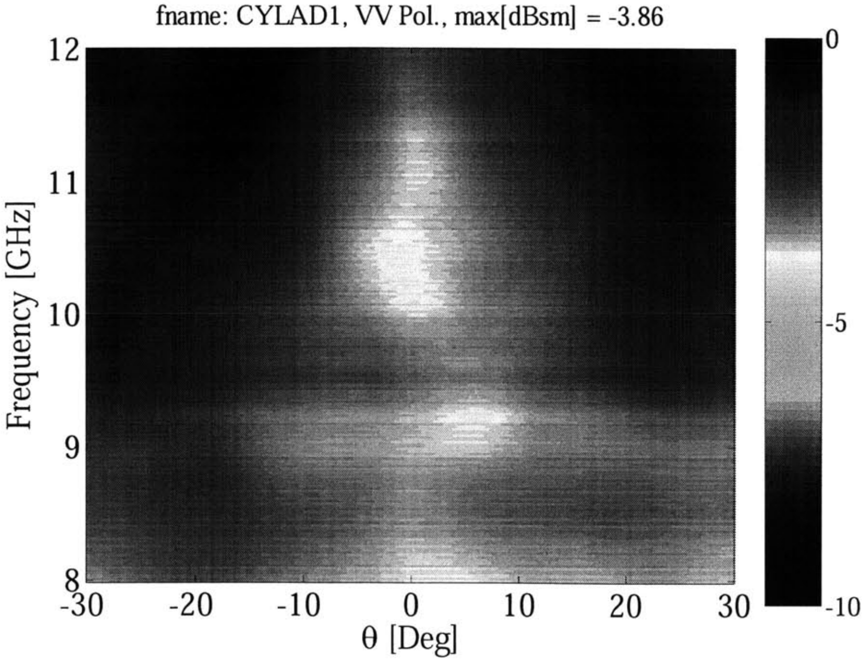

Figure A-16 Frequency – angle imagery for specimen CYL-AD1 measured at normal incidence, X-band, VV polarization, front surface (with defect)

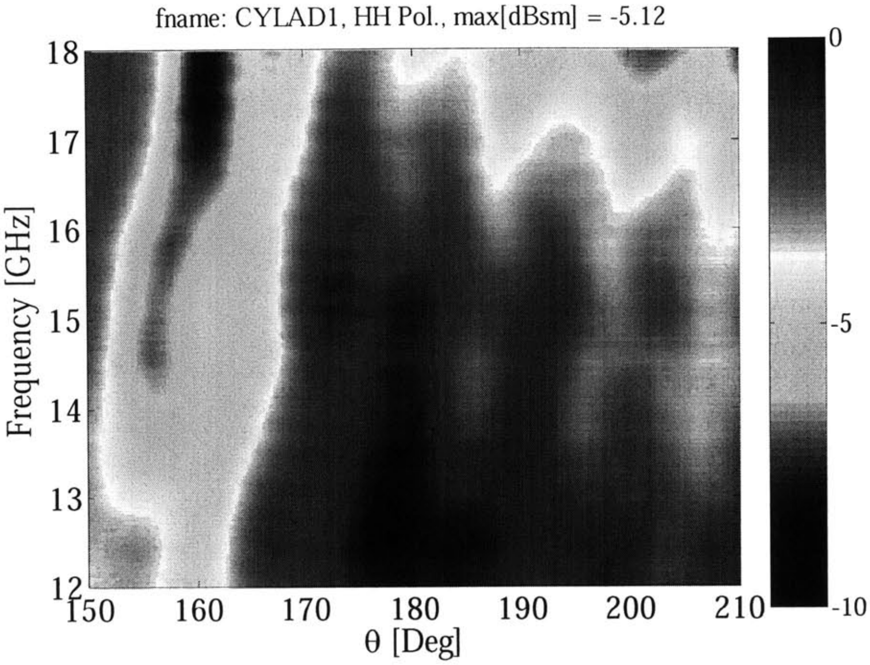

Figure A-17 Frequency – angle imagery for specimen CYL-AD1 measured at normal incidence, Ku-band, HH polarization, back surface (no defect)

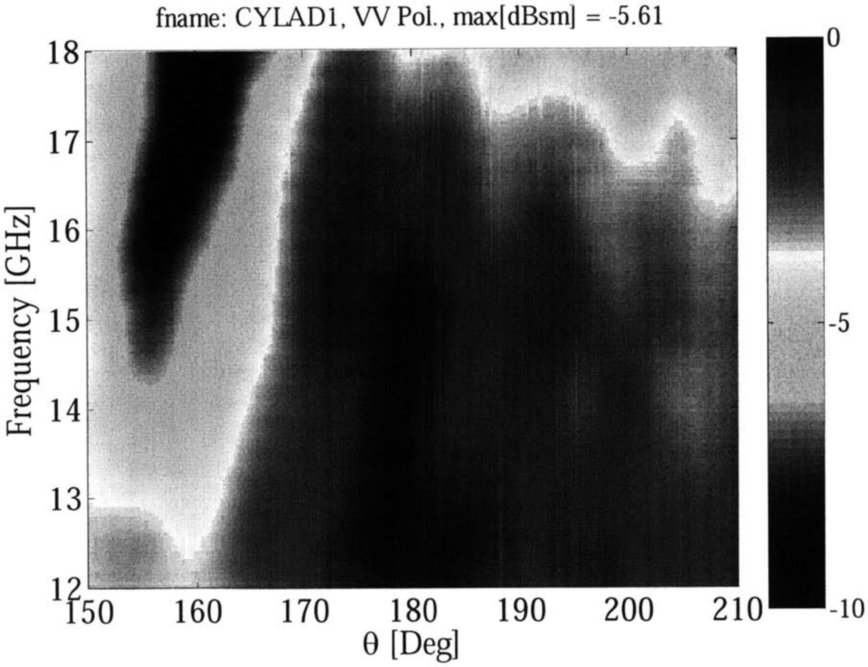

Figure A-18 Frequency – angle imagery for specimen CYL-AD1 measured at normal incidence, Ku-band, VV polarization, back surface (no defect)

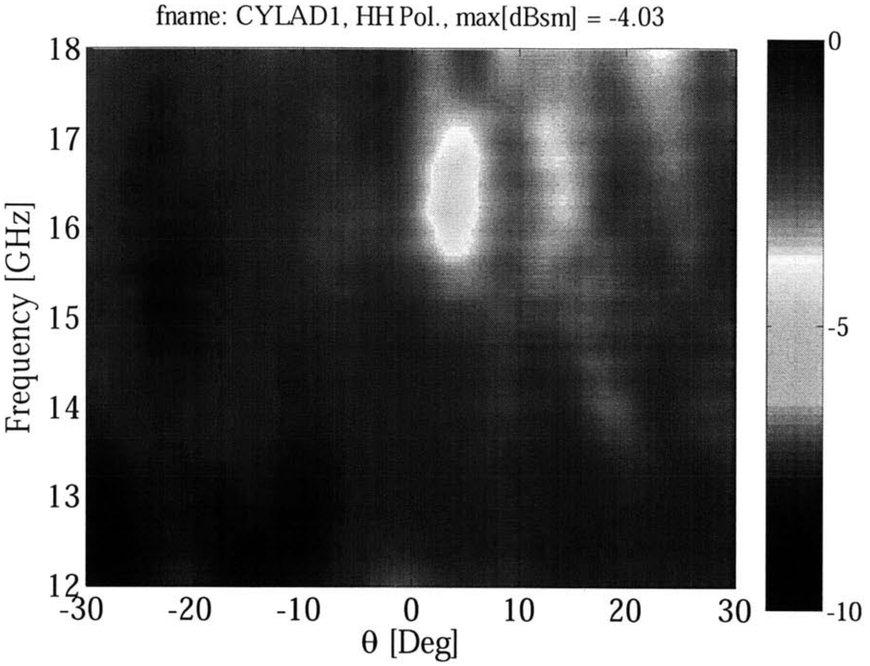

Figure A-19 Frequency – angle imagery for specimen CYL-AD1 measured at normal incidence, Ku-band, HH polarization, front surface (with defect)

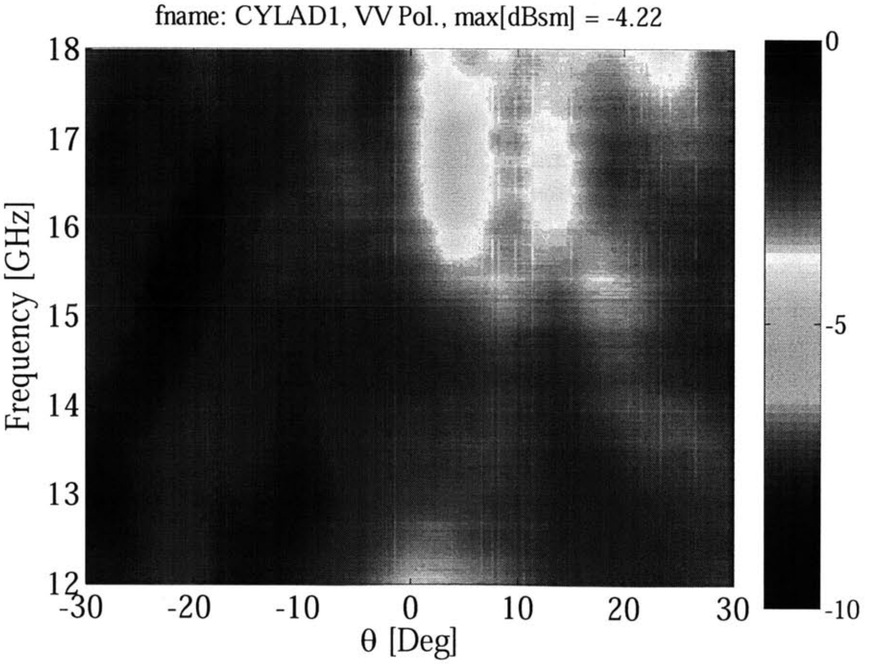

Figure A-20 Frequency – angle imagery for specimen CYL-AD1 measured at normal incidence, Ku-band, VV polarization, front surface (with defect)

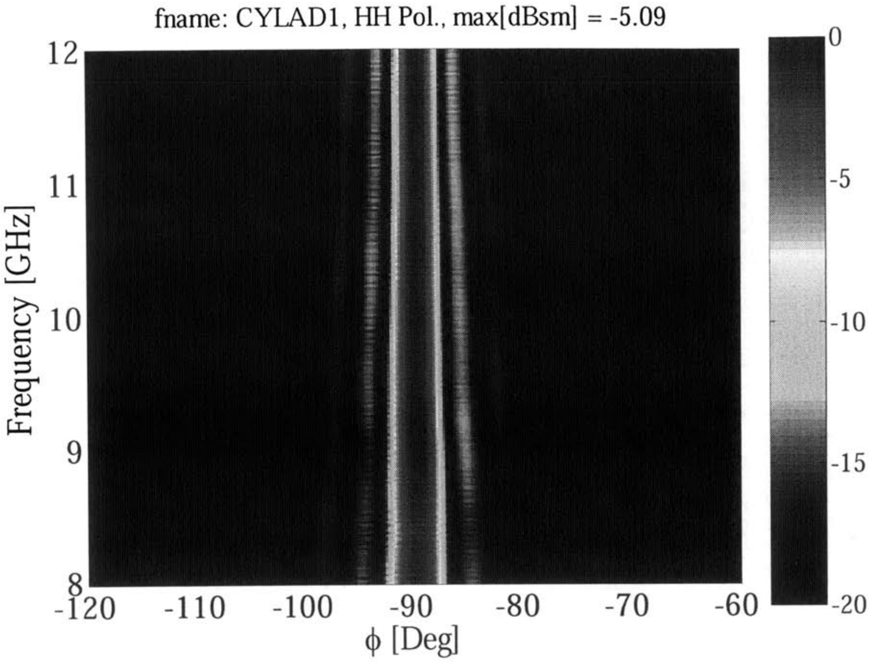

Figure A-21 Frequency – angle imagery for specimen CYL-AD1 measured at oblique incidence, X-band, HH polarization, back surface (no defect)

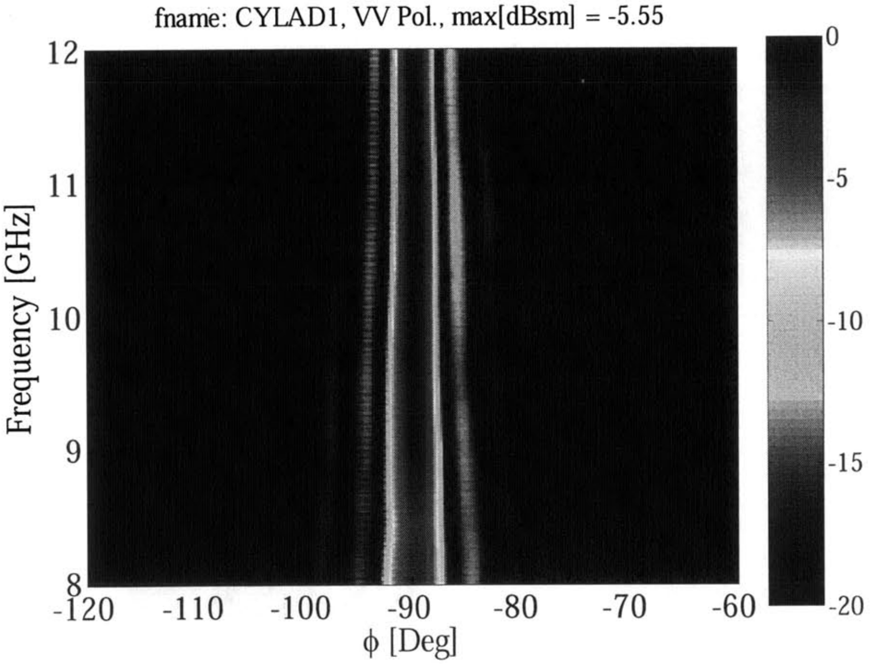

Figure A-22 Frequency – angle imagery for specimen CYL-AD1 measured at oblique incidence, X-band, VV polarization, back surface (no defect)

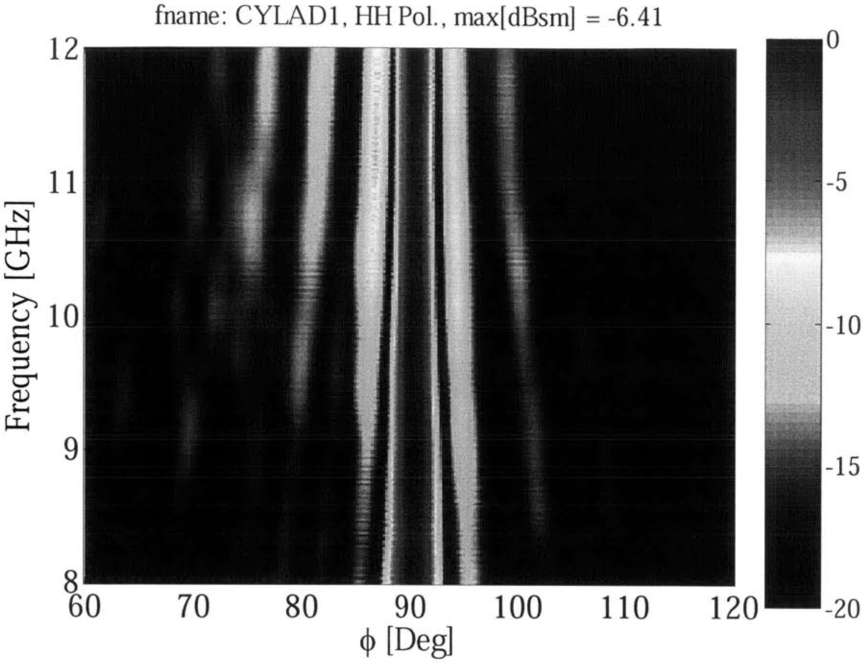

Figure A-23 Frequency – angle imagery for specimen CYL-AD1 measured at oblique incidence, X-band, HH polarization, front surface (with defect)

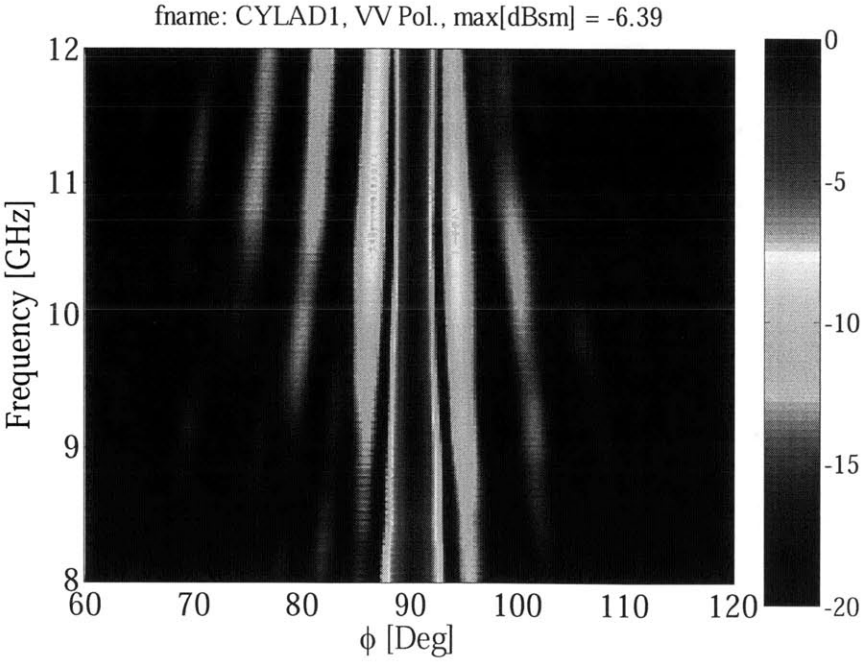

Figure A-24 Frequency – angle imagery for specimen CYL-AD1 measured at oblique incidence, X-band, VV polarization, front surface (with defect)

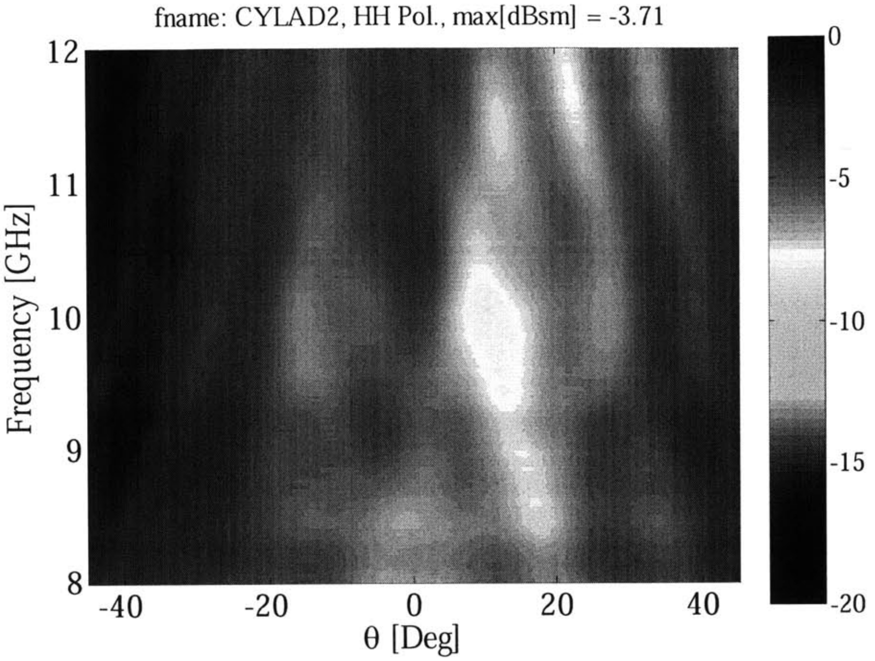

Figure A-25 Frequency – angle imagery for specimen CYL-AD2 measured at normal incidence, X-band, HH polarization, front surface (with defect)

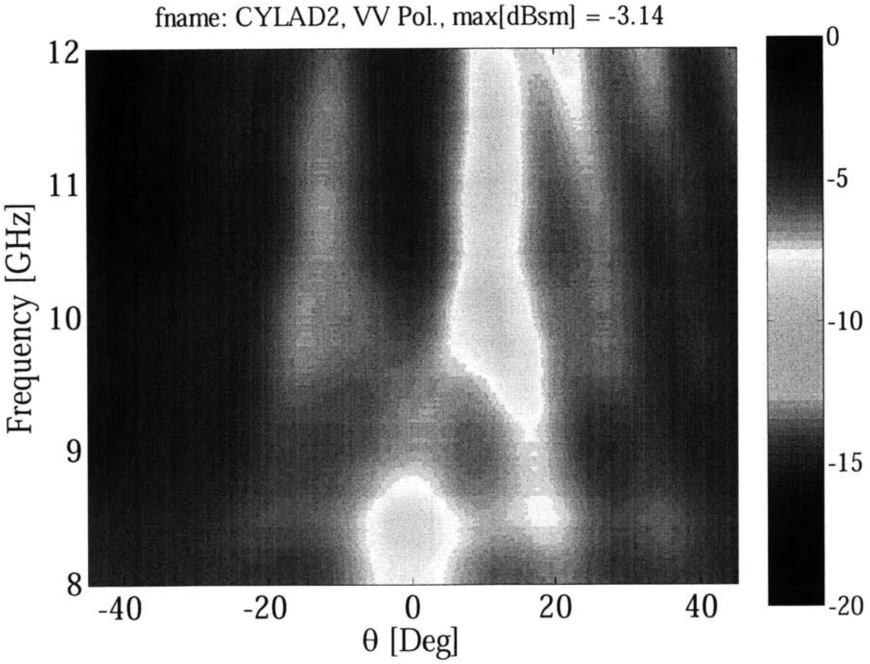

Figure A-26 Frequency – angle imagery for specimen CYL-AD2 measured at normal incidence, X-band, VV polarization, front surface (with defect)

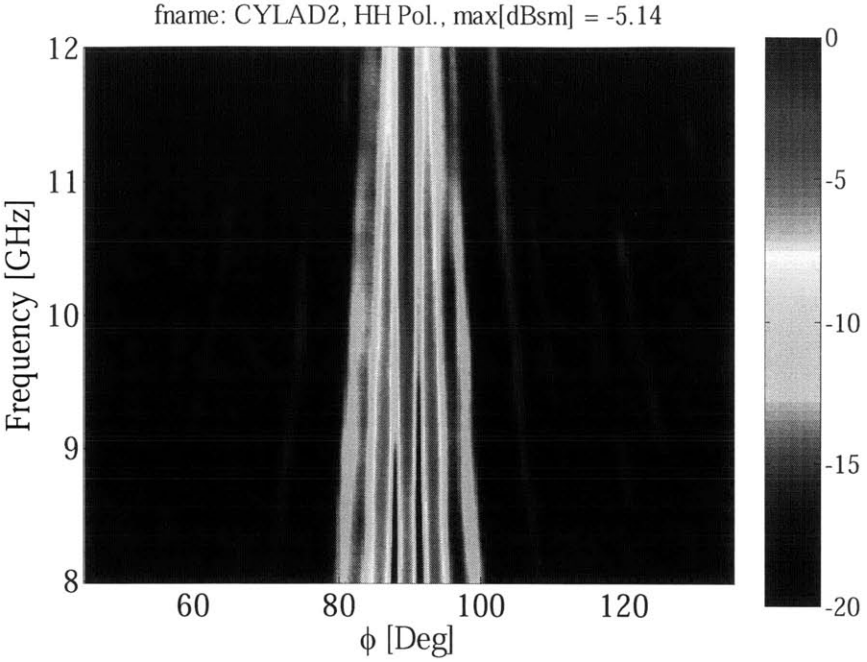

Figure A-27 Frequency – angle imagery for specimen CYL-AD2 measured at oblique incidence, X-band, HH polarization, front surface (with defect)

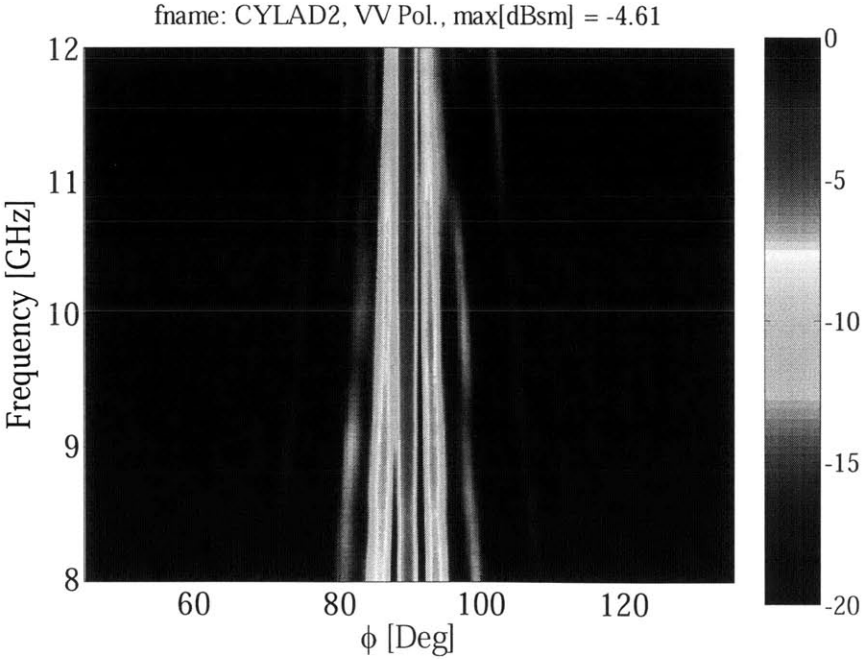

Figure A-28 Frequency – angle imagery for specimen CYL-AD2 measured at oblique incidence, X-band, VV polarization, front surface (with defect)

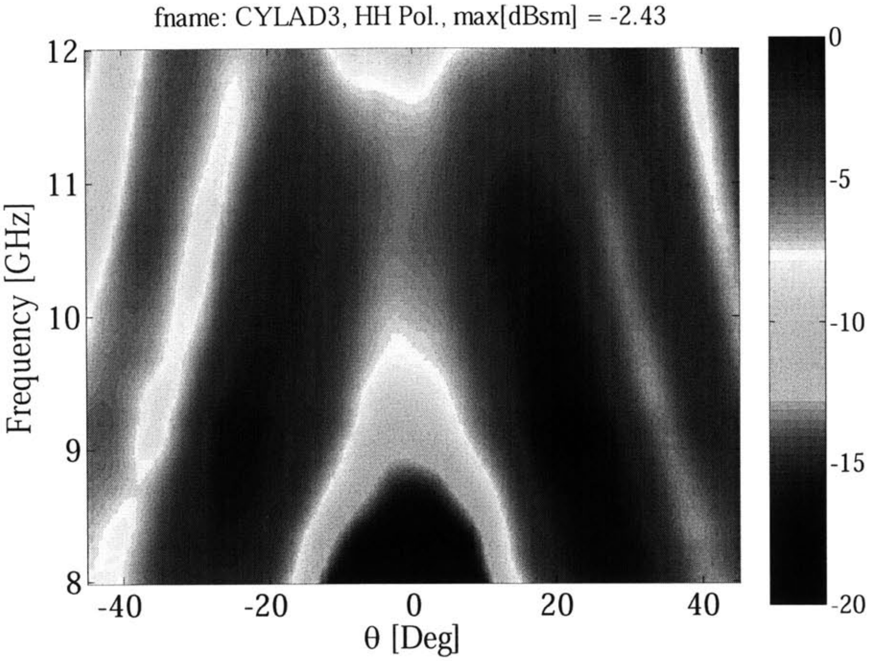
fname: CYLAD3, HH Pol., max[dBsm] = -2.43

Figure A-29 Frequency – angle imagery for specimen CYL-AD3 measured at normal incidence, X-band, HH polarization

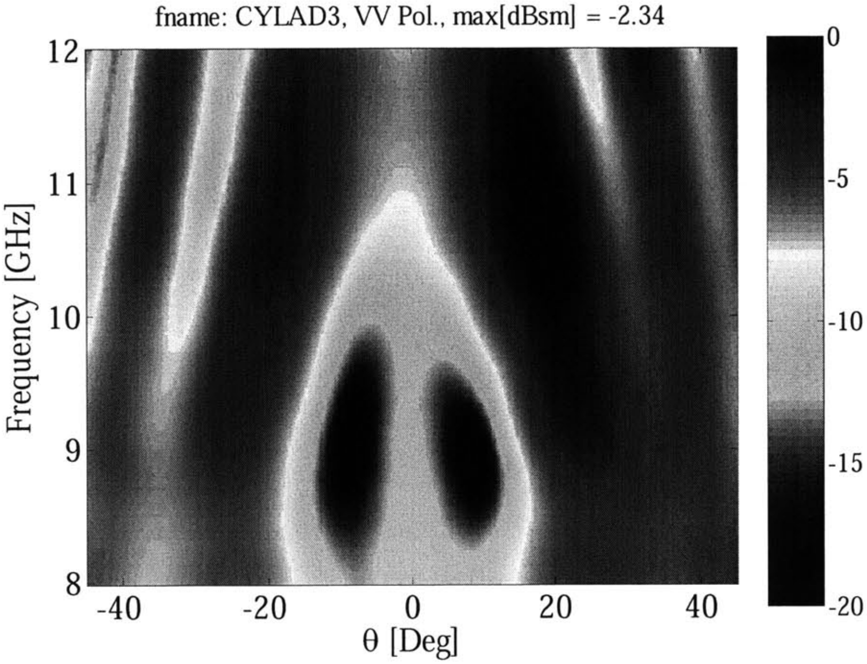
fname: CYLAD3, VV Pol., max[dBsm] = -2.34

Figure A-30 Frequency – angle imagery for specimen CYL-AD3 measured at normal incidence, X-band, VV polarization

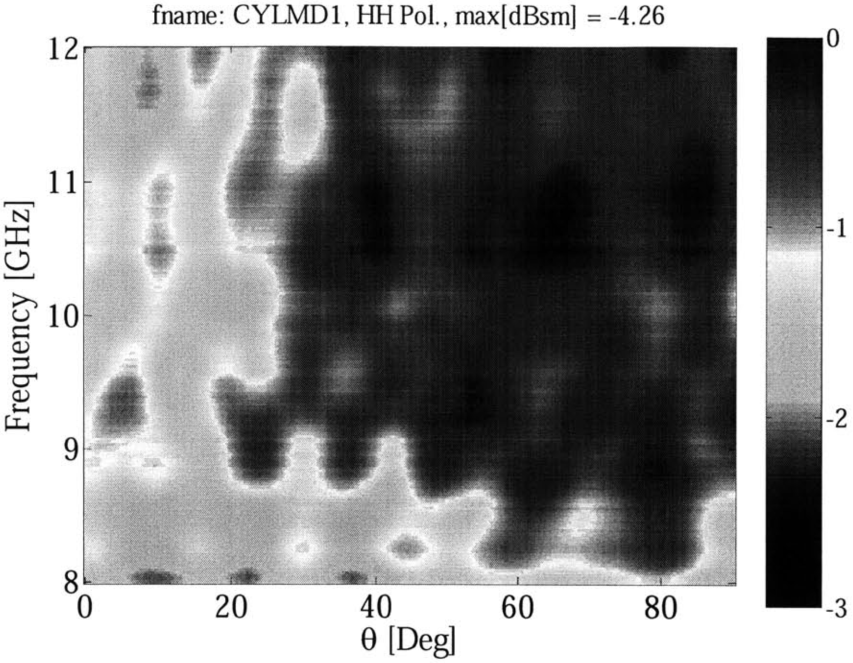

Figure A-31 Frequency – angle imagery for specimen CYL-MD1 measured at normal incidence, X-band, HH polarization

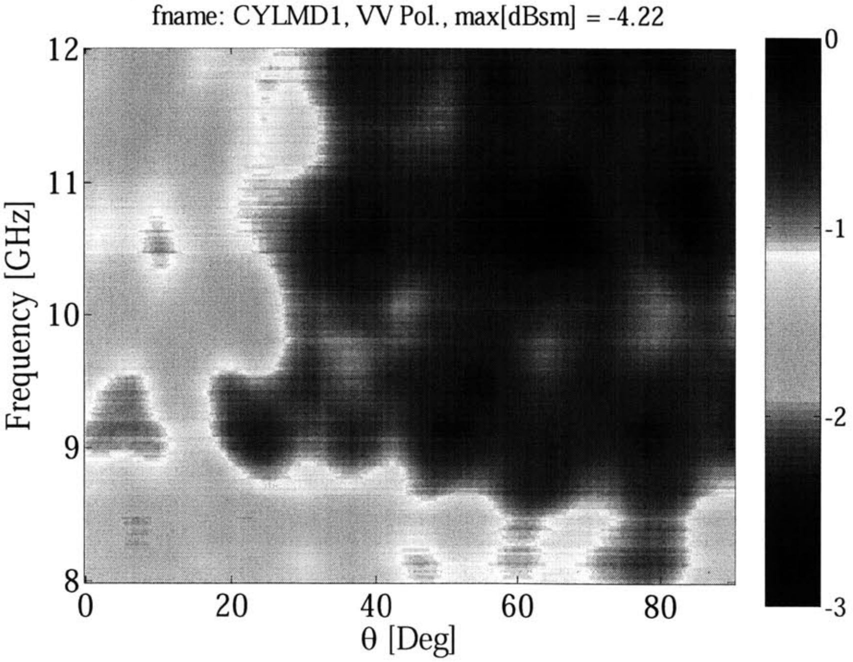

Figure A-32 Frequency – angle imagery for specimen CYL-MD1 measured at normal incidence, X-band, VV polarization

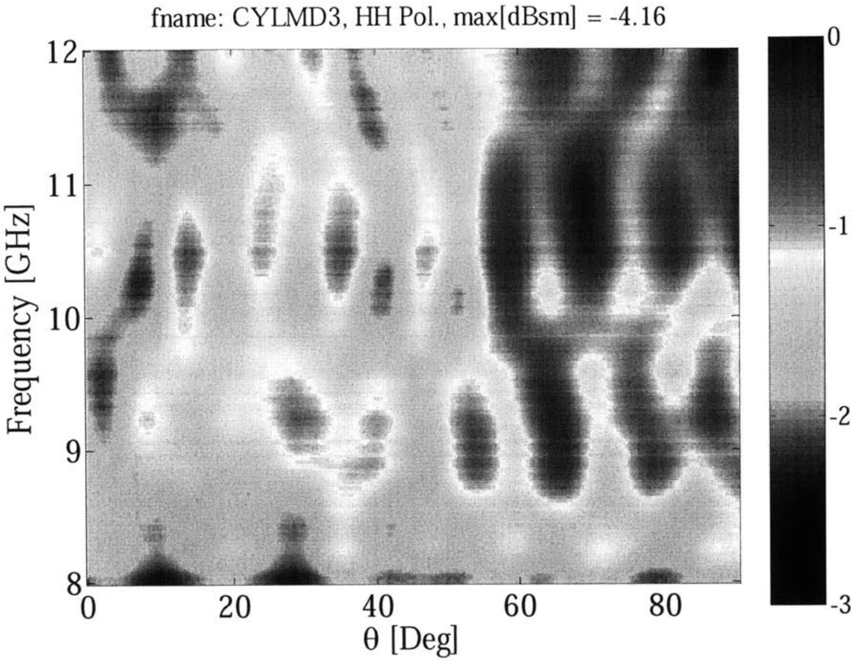

Figure A-33 Frequency – angle imagery for specimen CYL-MD3 measured at normal incidence, X-band, HH polarization

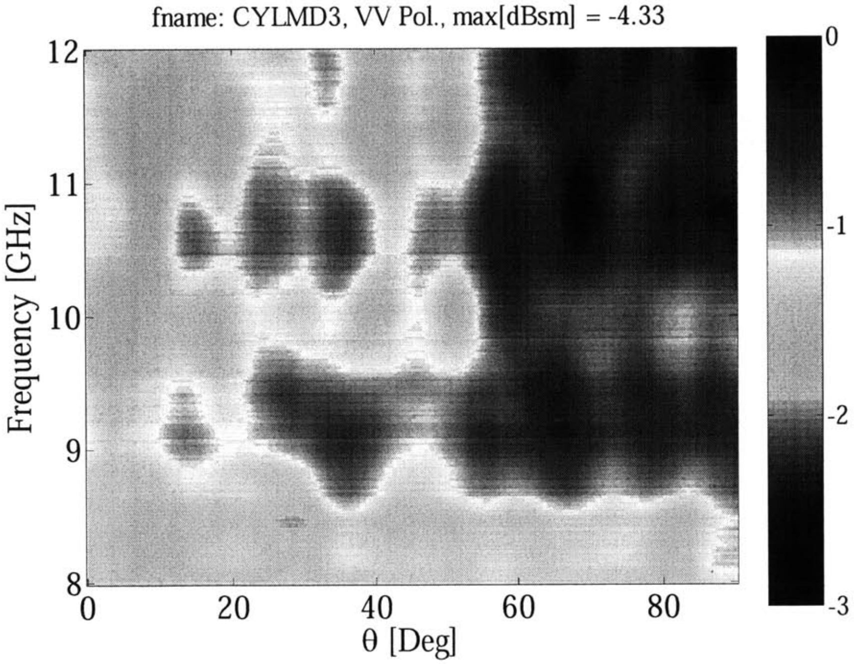

Figure A-34 Frequency – angle imagery for specimen CYL-MD3 measured at normal incidence, X-band, VV polarization

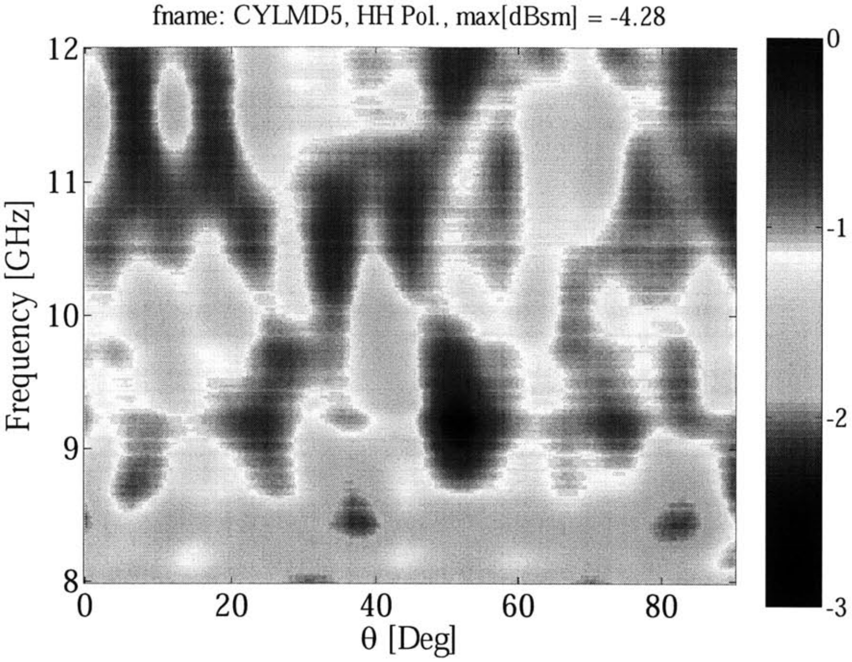

Figure A-35 Frequency – angle imagery for specimen CYL-MD5 measured at normal incidence, X-band, HH polarization

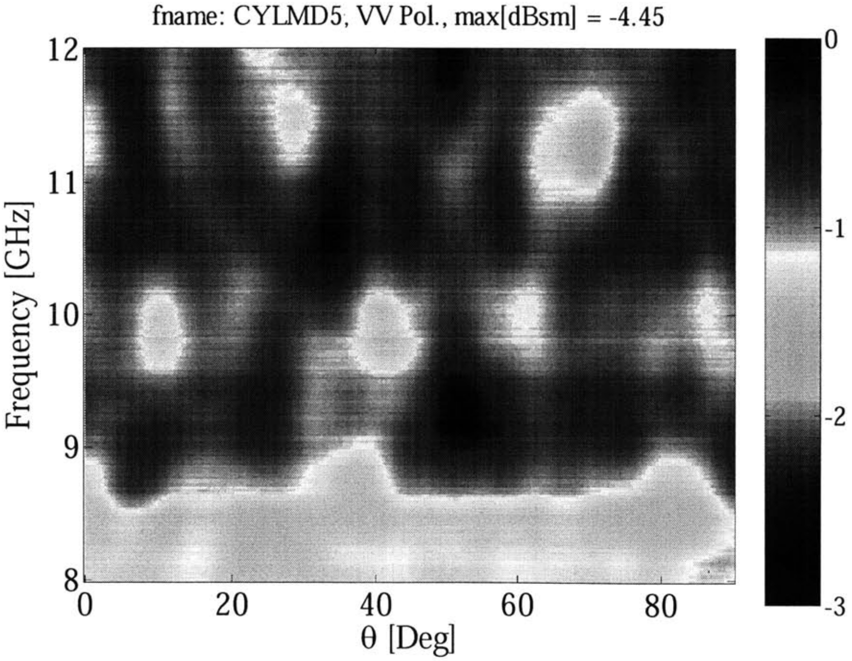

Figure A-36 Frequency – angle imagery for specimen CYL-MD5 measured at normal incidence, X-band, VV polarization

Appendix B

ISAR Imagery for Selected Specimens

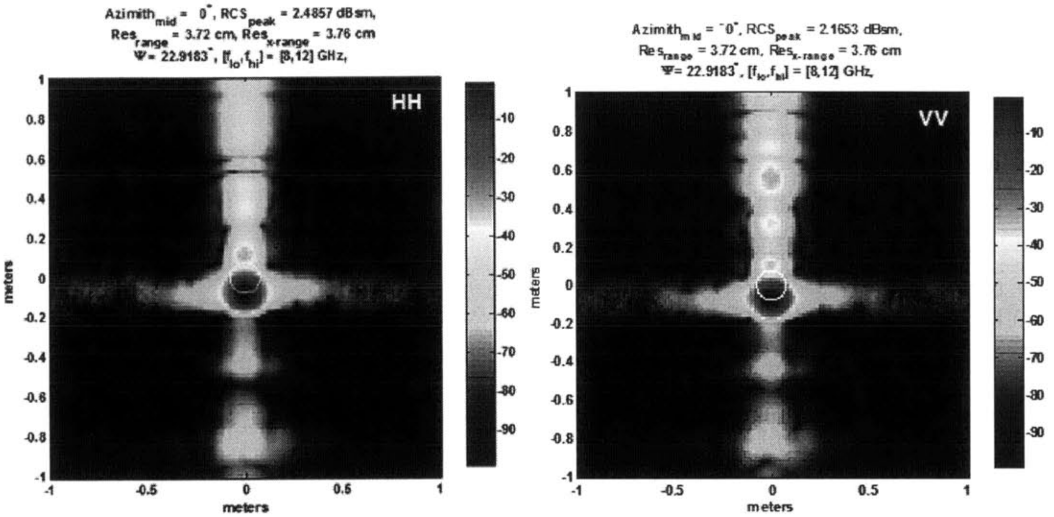

Figure B-1 ISAR imagery for specimen CYL-ME measured at normal incidence, X-band, HH and VV polarizations

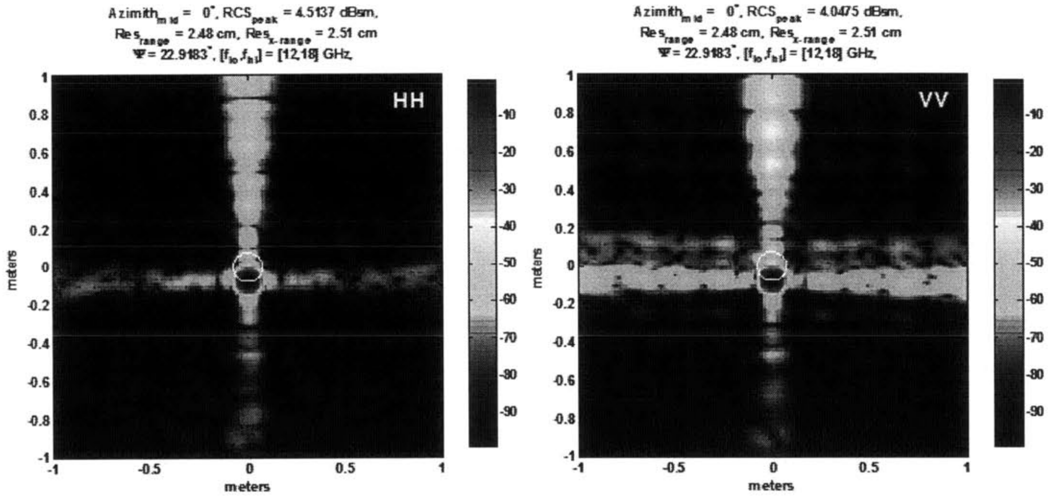

Figure B-2 ISAR imagery for specimen CYL- ME measured at normal incidence, Ku-band, HH and VV polarizations

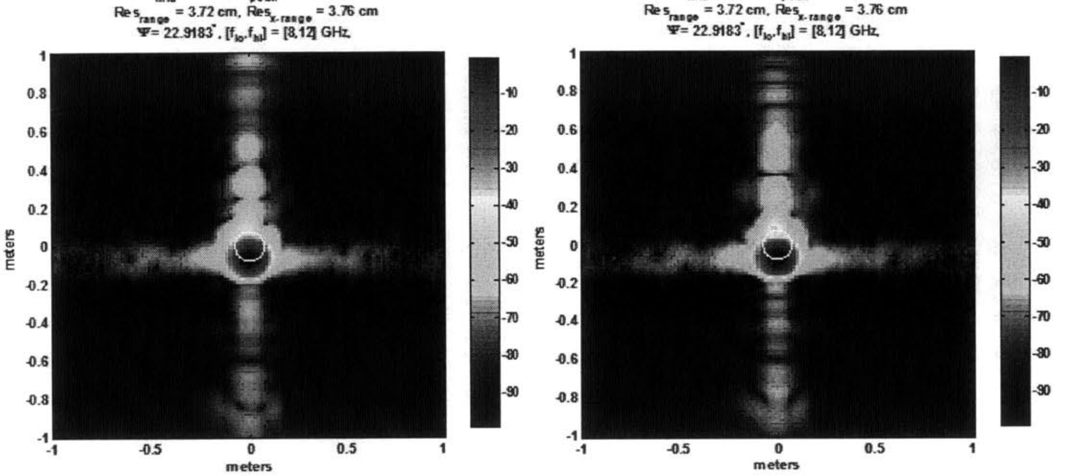

Figure B-3 ISAR imagery for specimen CYL-PC measured at normal incidence, X-band, HH and VV polarizations

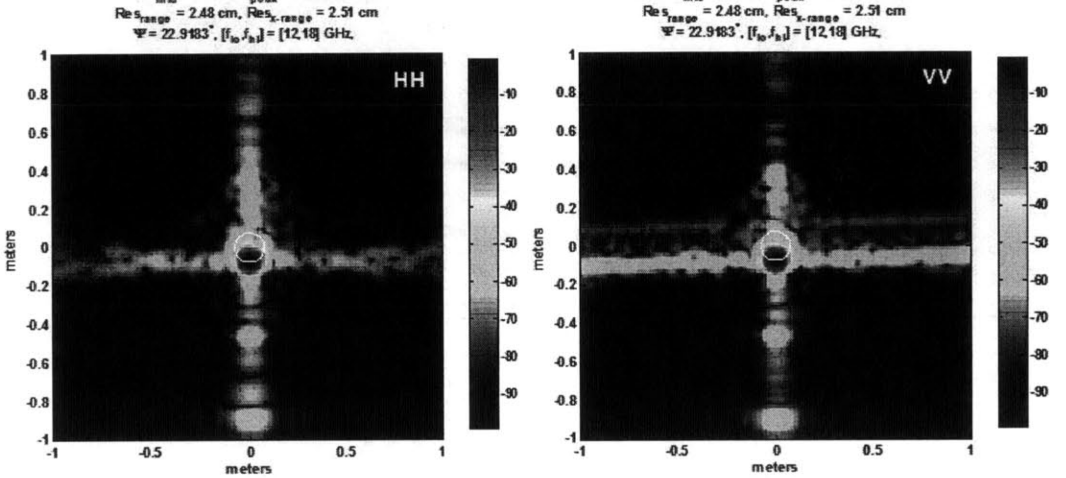

Figure B-4 ISAR imagery for specimen CYL-PC measured at normal incidence, Ku-band, HH and VV polarizations

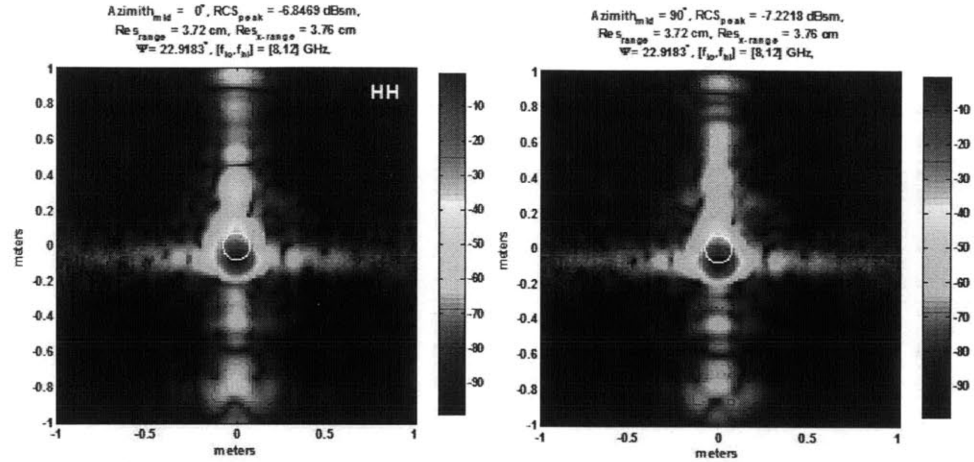

Figure B-5 ISAR imagery for specimen CYL-CC measured at normal incidence, X-band, HH and VV polarizations

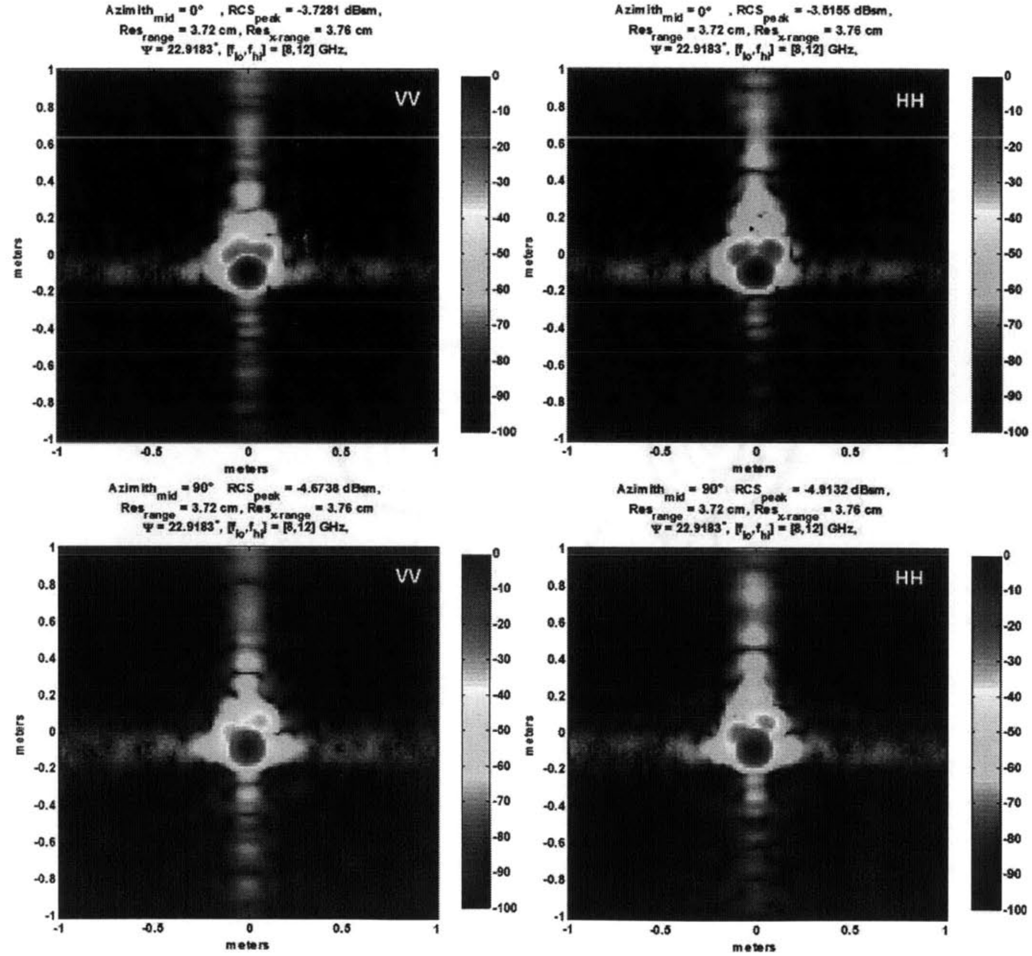

Figure B-6 ISAR imagery for specimen CYL-RE measured at normal incidence, X-band, HH and VV polarizations at 0 and 90 deg incident angles

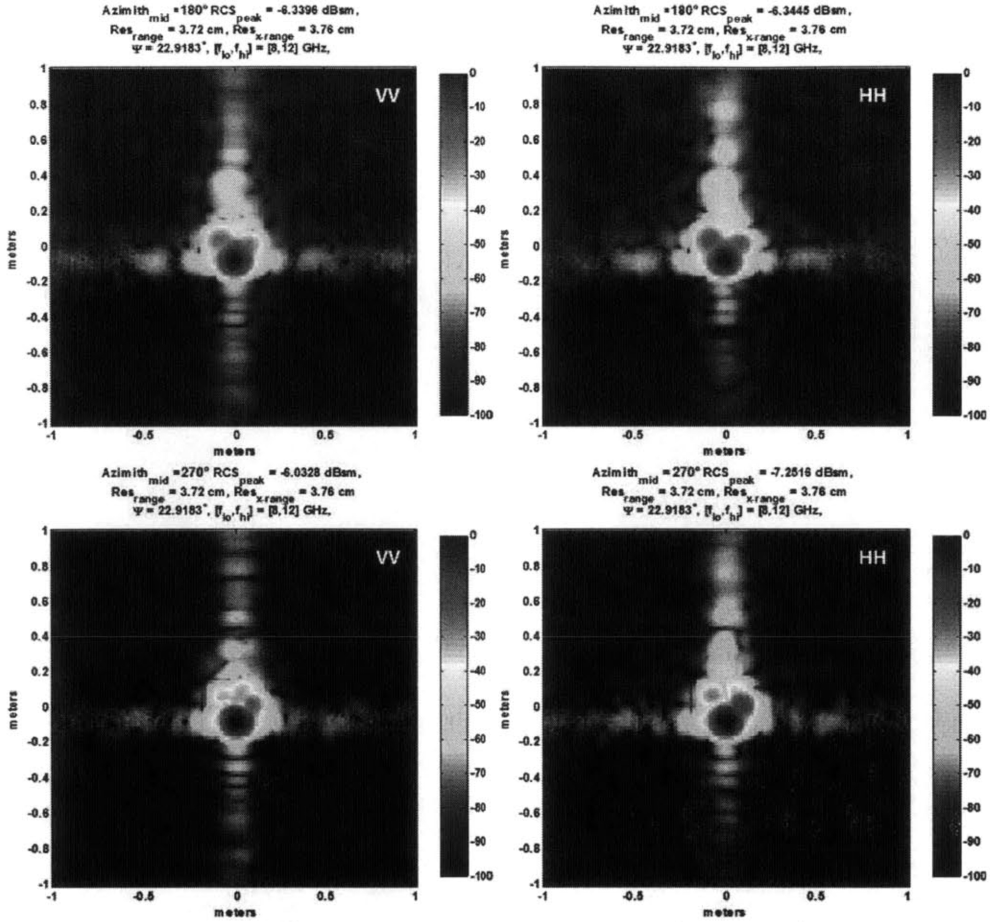

Figure B-7 ISAR imagery for specimen CYL-RE measured at normal incidence, X-band, HH and VV polarizations at 180, and 270 deg incident angles

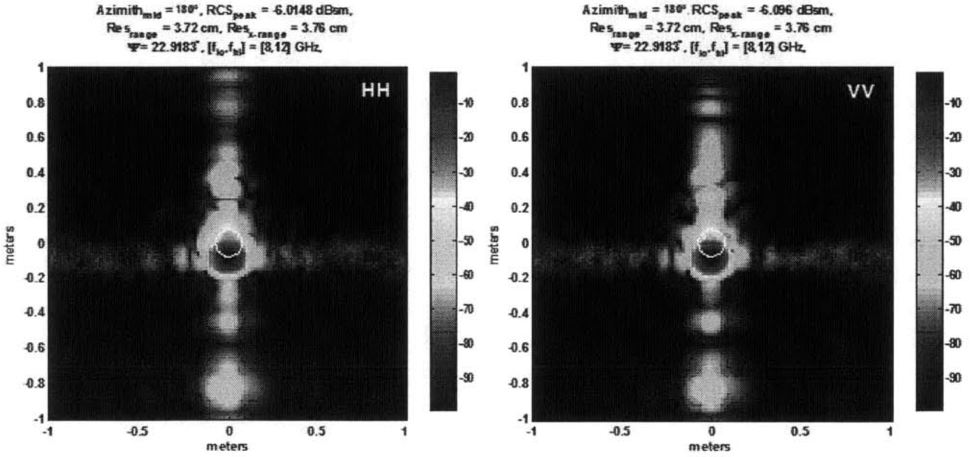

Figure B-8 ISAR imagery for specimen CYL-AD1 measured at normal incidence, X-band, HH and VV polarizations, back surface (no defect)

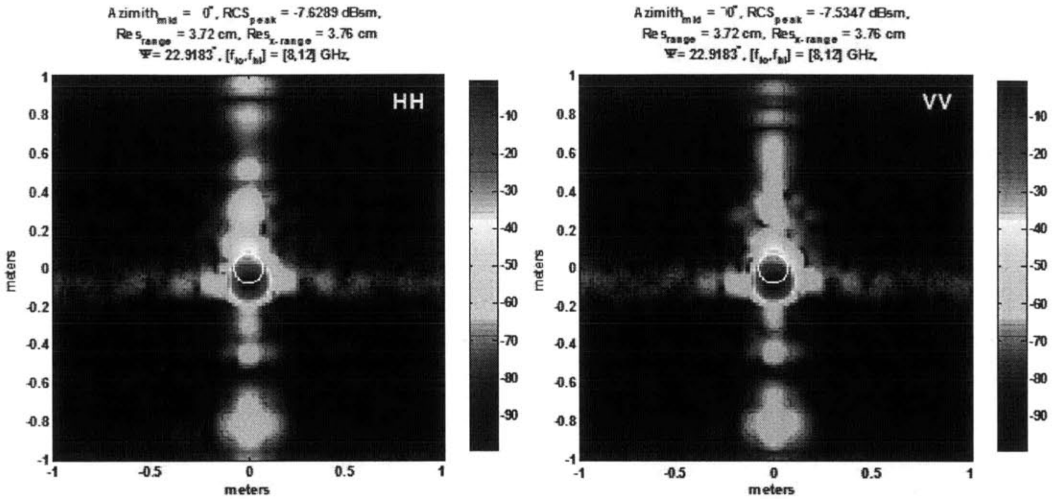

Figure B-9 ISAR imagery for specimen CYL-AD1 measured at normal incidence, X-band, HH and VV polarizations, front surface (with defect)

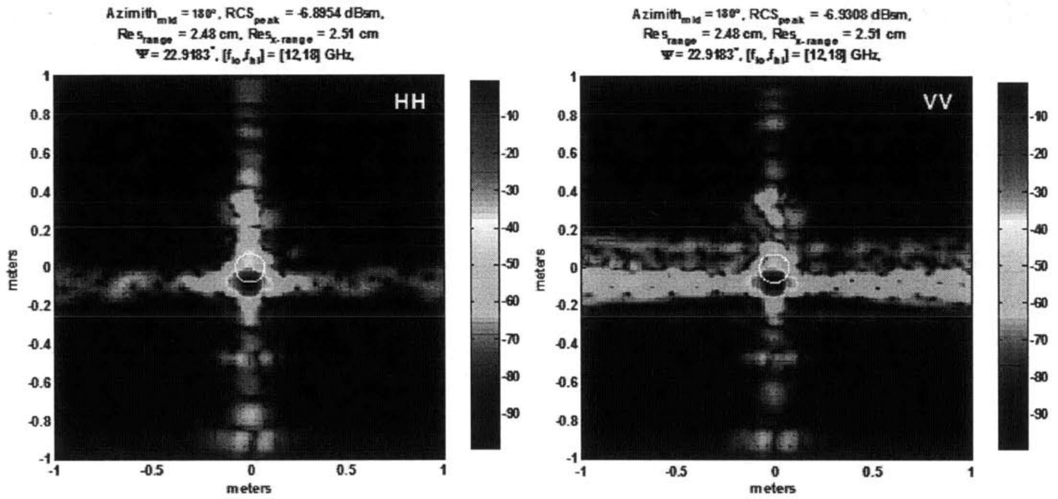

Figure B-10 ISAR imagery for specimen CYL-AD1 measured at normal incidence, Ku-band, HH and VV polarizations, back surface (no defect)

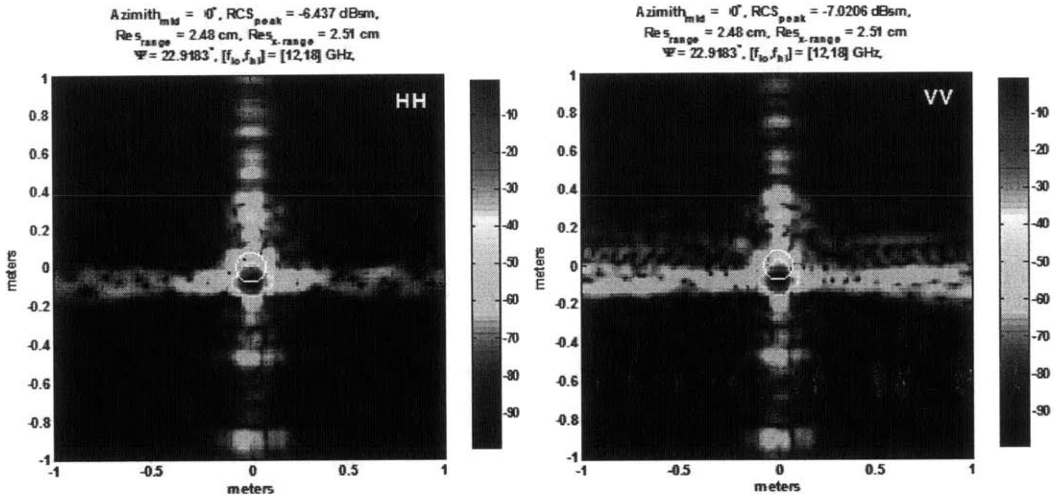

Figure B-11 ISAR imagery for specimen CYL-AD1 measured at normal incidence, Ku-band, HH and VV polarizations, front surface (with defect)

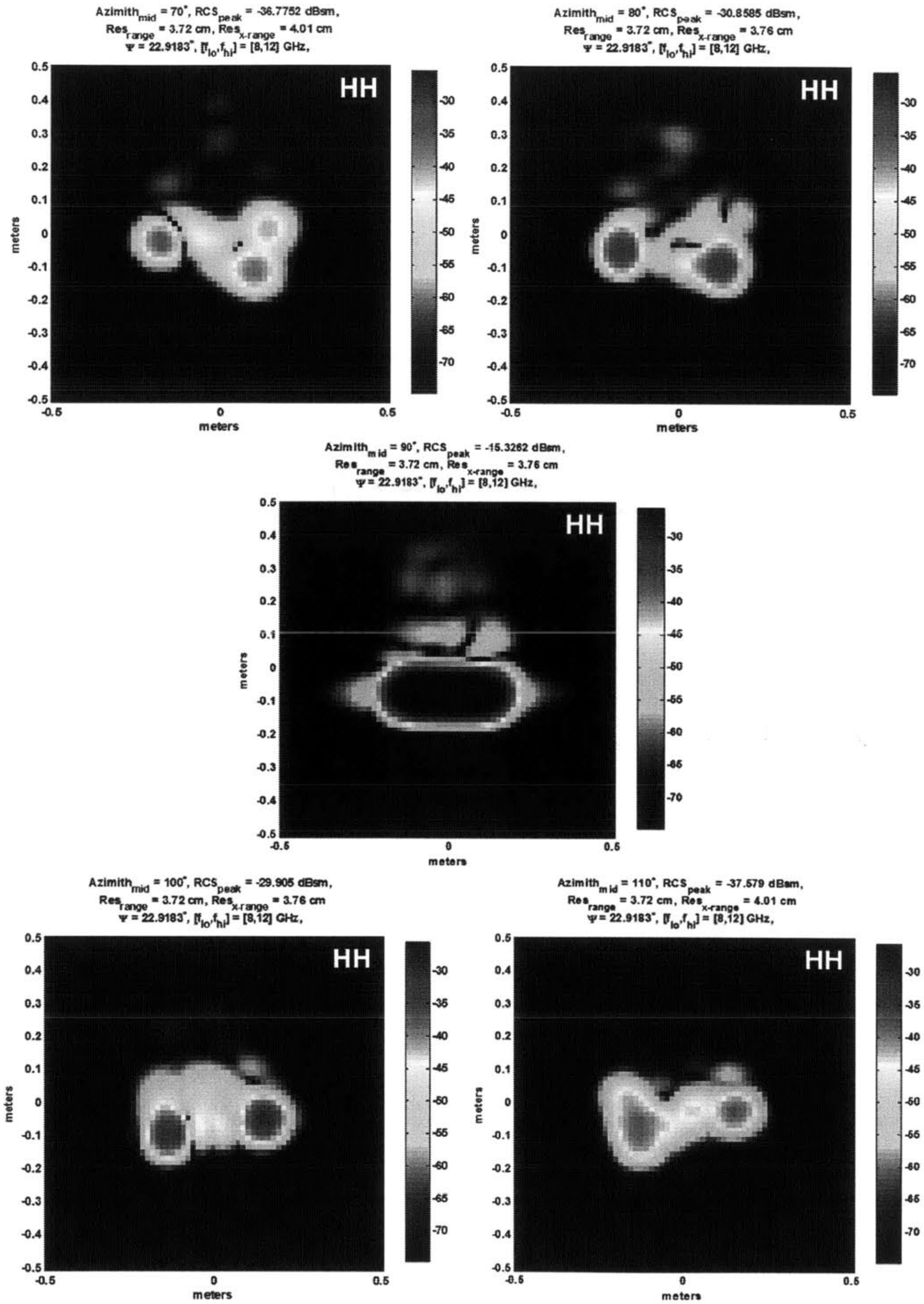

$\text{Azimith}_{mid} = 70^\circ$, $\text{RCS}_{peak} = -36.7752$ dBsm, $\text{Res}_{range} = 3.72$ cm, $\text{Res}_{x\text{-}range} = 4.01$ cm $\Psi = 22.9183^\circ$, $[f_{lo}, f_{hi}] = [8,12]$ GHz,

$\text{Azimith}_{mid} = 80^\circ$, $\text{RCS}_{peak} = -30.8585$ dBsm, $\text{Res}_{range} = 3.72$ cm, $\text{Res}_{x\text{-}range} = 3.76$ cm $\Psi = 22.9183^\circ$, $[f_{lo}, f_{hi}] = [8,12]$ GHz,

$\text{Azimith}_{mid} = 90^\circ$, $\text{RCS}_{peak} = -15.3262$ dBsm, $\text{Res}_{range} = 3.72$ cm, $\text{Res}_{x\text{-}range} = 3.76$ cm $\Psi = 22.9183^\circ$, $[f_{lo}, f_{hi}] = [8,12]$ GHz,

$\text{Azimith}_{mid} = 100^\circ$, $\text{RCS}_{peak} = -29.905$ dBsm, $\text{Res}_{range} = 3.72$ cm, $\text{Res}_{x\text{-}range} = 3.76$ cm $\Psi = 22.9183^\circ$, $[f_{lo}, f_{hi}] = [8,12]$ GHz,

$\text{Azimith}_{mid} = 110^\circ$, $\text{RCS}_{peak} = -37.579$ dBsm, $\text{Res}_{range} = 3.72$ cm, $\text{Res}_{x\text{-}range} = 4.01$ cm $\Psi = 22.9183^\circ$, $[f_{lo}, f_{hi}] = [8,12]$ GHz,

Figure B-12 ISAR imagery for specimen CYL-AD1 measured at oblique incidence, X-band, HH polarization, back surface (no defect) at different incident angles

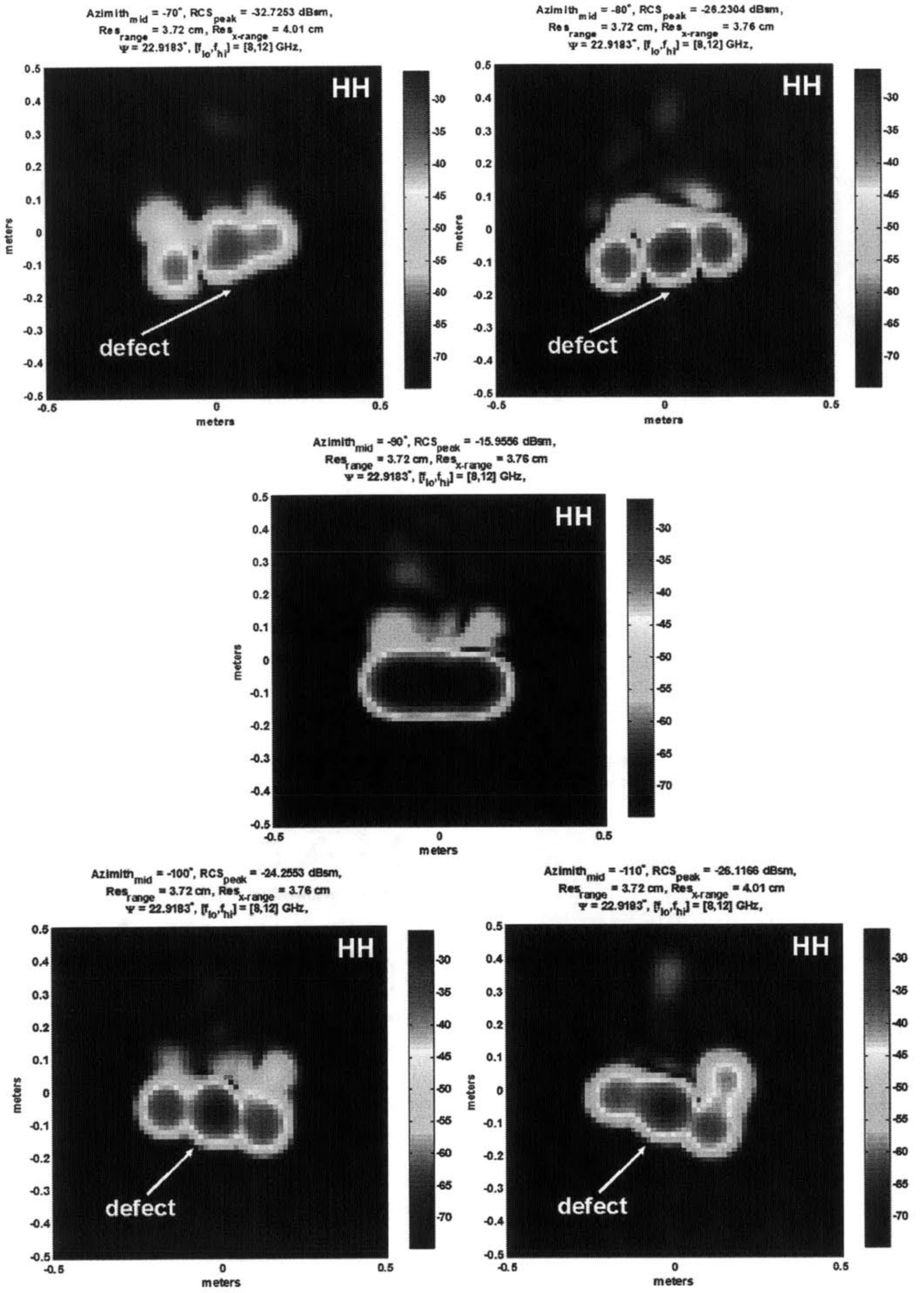

Figure B-13 ISAR imagery for specimen CYL-AD1 measured at oblique incidence, X-band, HH polarization, front surface (with defect) at different incident angles

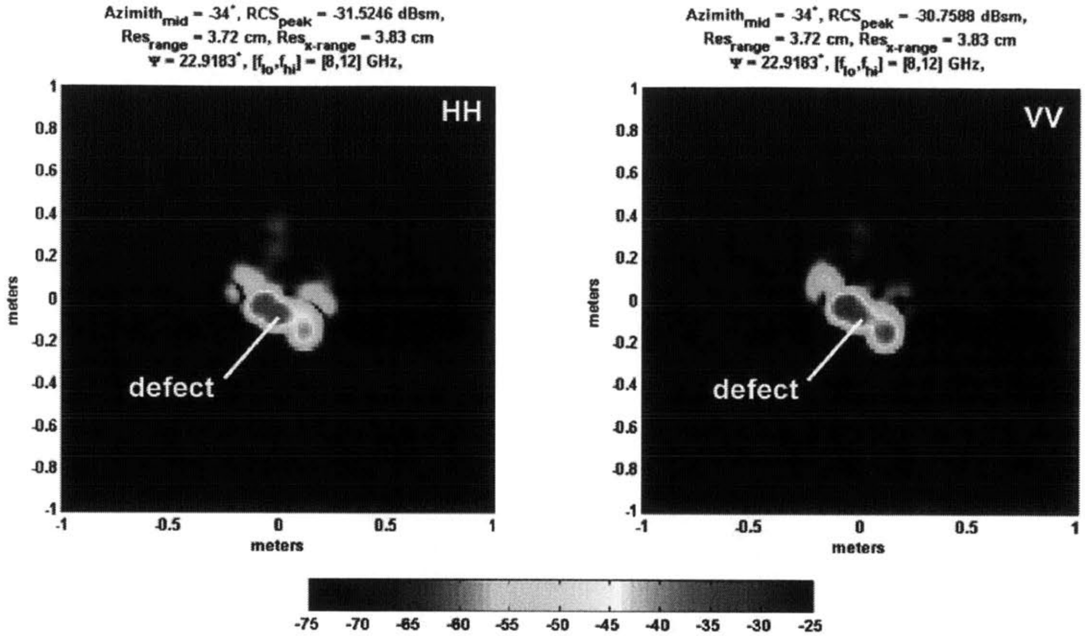

Figure B-14 ISAR imagery for specimen CYL-AD2 measured at oblique incidence, X-band, HH and VV polarizations, front surface (with defect)

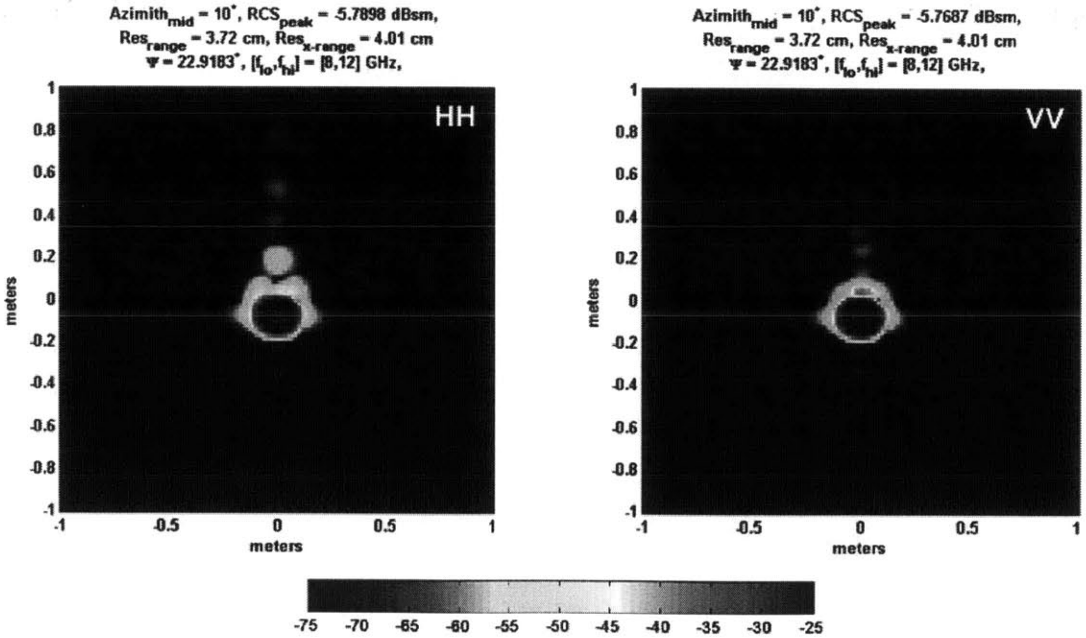

Figure B-15 ISAR imagery for specimen CYL-MD1 measured at normal incidence, X-band, HH and VV polarizations

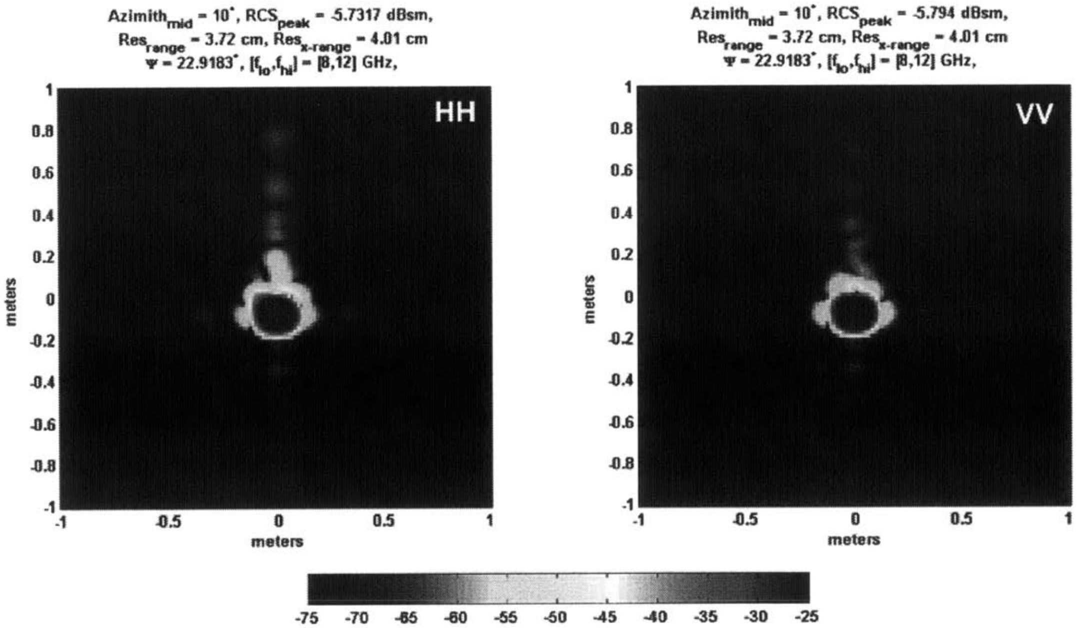

Figure B-16 ISAR imagery for specimen CYL-MD3 measured at normal incidence, X-band, HH and VV polarizations

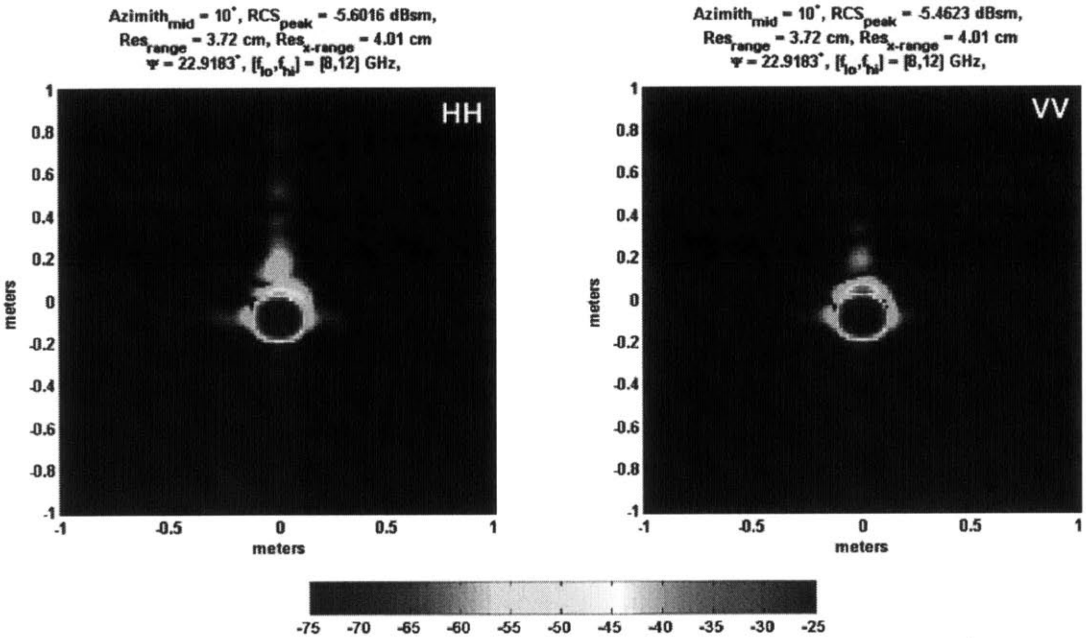

Figure B-17 ISAR imagery for specimen CYL-MD5 measured at normal incidence, X-band, HH and VV polarizations